Growth and Characterization of InGaN by Plasma-assisted Molecular Beam Epitaxy

by

Kamruzzaman Khan

A dissertation submitted in partial fulfillment
of the requirements for the degree of
Doctor of Philosophy
(Materials Science and Engineering)
in the University of Michigan
2023

Doctoral Committee

Assistant Professor Elaheh Ahmadi, Co-Chair
Assistant Professor Robert Hovden, Co-Chair
Dr. Stacia Keller, University of California, Santa Barbara
Professor Emmanuelle Marquis
Professor Zetian Mi

Kamruzzaman Khan

kkhans@umich.edu

ORCID ID: 0000-0001-7631-7977

Dedication

To my parents

Jamsed Ali Khan and Sahida Akhter

Without their support, dedication, and sacrifices

I would not be here today

Acknowledgements

My years as a Ph.D. student have been a period of learning and discovery that I will treasure the rest of my life. It is therefore my pleasure to acknowledge the exceptional individuals that made this possible.

I am indebted to my advisor and first epitaxy mentor Prof. Elaheh Ahmadi to take me in her group as her first Ph.D. student even without any prior experience in epitaxy and III-nitrides. I have learned many aspects of life from her and consider myself fortunate to have her as an advisor and mentor. Her ideas, advice, and critical feedback have been central to my growth both intellectually and personally. I want to thank her for assigning me several projects, which challenged both my patience and intellect! She set a new standard of patience to me during my Ph.D. and was open to ideas about growth during this whole time period. She taught me not only the importance of relaxed InGaN but also the importance of relaxation during MBE growth, maintenance, and life! I cannot appreciate her enough for believing in me with setting up two molecular beam epitaxy (MBE) systems along with refurbishment and maintenance of them. Being taken into her research group strengthened my belief that all things including some breakdown in experimental (MBE) setup, happens for the best! Big thanks to Elaheh for checking my slides and reading my journal papers, conference papers, and thesis along with giving me critical feedback in her busy schedule.

I would like to thank Prof. Robert Hovden, for guiding me through my tough times in my first two years of Ph.D. I am thankful to him for giving me lecture about training in tools and working with people. His continuous energy to explain transmission electron microscopy (TEM) results, encouragement, and feedback on my presentation and slides helped to shape much of my communication skills. I would like to thank Prof. Zetian Mi to for his continuous encouragement and support during my work with MBE. Without his group's help with MBE, pre-commissioning, commissioning, setup, refurbishment, and maintenance would be impossible. I appreciate him and his group members' support with the MBE. I thank Prof. Marquis for being on my committee and sharing his ideas and thoughts with me during the meetings. It has been a great pleasure to work with Dr. Stacia Keller on porous GaN projects and MOCVD regrowth of MQWs. Her knowledge

and insight into materials growth and semiconductors have helped shape much of my porous work. I have been deeply influenced by her love for science, and the high standards she sets for experimental research.

Moreover, I would like to thank Elaheh for sending me to University of California, Santa Barbara to learn epitaxial growth by MBE, which was a great learning experience in heaven (after living in Midwest gloomy weather and snow for 4 years) for ten months! Most importantly, I met Prof. Umesh Mishra who taught me both to have fun and to work hard in life. Without his initial help to use his MBE system, it would be impossible to get the initial results on InGaN growth on ZnO substrate. His unique way of dealing with students and leading his group by walking and talking is mind-blowing. He imparted valuable lessons of life and device physics (when he had excess time!). It was a unique experience to work in his MBE lab and with his Ph.D. students. During my last few months at UCSB, I came to know him more closely. He taught me the importance of communicating well in only one 2 hours session and changed my view on the importance of presentation.

I want to thank Dr. Kai Sun for looking at numerous (almost infinite!) samples with InGaN SASL structure in timely manner and showing extreme energy to explain the scanning transmission electron microscopy (STEM) results. I appreciate Prof. Parag Deotare's research group for their help and agreeing to collaborate on photoluminescence properties of the SASL structure.

I am grateful to the professors who taught my classes, Prof. Zhaohui Zhong, Prof. Pallab Bhattacharya, Prof. Elaheh Ahmadi, Prof. Umesh Mishra from My Ph.D. Back home, I would like to thank all my professors from Bangladesh University of Engineering and Technology and University of Toledo, Ohio (especially my M.Sc. advisor Prof. Daniel Georgiev and Prof. Robert Collins). Without their inspiration and support, I could have not come all this way today. I also want to thank my teachers in school for giving the best and also the cheapest education in the world. Especially, I am grateful to my high school teacher, late Abdul Khalek for changing my life goal from being a cricketer to being an academic/researcher.

I cannot thank Christian, Richard, and Kelsey enough for teaching me with great care, passion, and patience about MBE regular operation, maintenance, and opening. I appreciate their excitement to show me materials characterization methods too. I am grateful to Islam, Niru, Wenjian and Weiyi for helping me with substrate treatment during different time in first few years

of my Ph.D. I would like to thank Shubhra and Christian for doing materials characterization when I had too many samples before leaving UCSB. Thanks to Chirag, Aditya, Athith, Emmanuel, Shubhra, and Nirupam for maintaining a great lab atmosphere. I enjoyed my conversations with them during my stay and later virtually.

All the members of Elaheh's group were great and kind to me. Ashley joined Elaheh's group at same time as I did. Her continuous energy and fun-loving attitude to research helped me to push my boundaries and grow as a researcher. Sandra taught me documentation and how to train people. She helped me a lot during first the few years of MBE maintenance and regular checkups. Her critical feedback helped me to change my behaviors. During my Ph.D. and after coming from UCSB, I met Subhajit and he taught me a lot about device physics. He asked a lot of questions and helped to solve a lot of my questions about my research. His hard work and views towards research set a new standard for me. I enjoyed my conversations with these three people about research, life and politics especially during USA election times. Additionally, I want to thank my other MBE buddies (Irfan, Zhuoqun, Ruby, Majid, and Mahitosh) for sharing my pain during all the maintenance, which built our character (according to me!). I enjoyed training them and chatting with them during the training process. I enjoyed working with Subhajit, Oguz, and Irfan in last few months of my Ph.D. I would like to thank Subhajit and Oguz for explaining a lot of fabrication process and challenges that came during the process to me. They also explained a lot about different measurement techniques during their measurements. I would like to thank other lab members in the lab with their high energy Ruby, Zhuoqun, Xin, Irfan, Harsh, Stefan, Oguz. I enjoyed my conversation with them will miss them in the upcoming days. I want to thank my friends (Mirza, Kawser, Walid, Tanjil (Late), Riyad (Late), Prinon, Fuad, Wasequl, Rabbi, Riyad etc.) from home and abroad for cheering me up with their bad and lame jokes the whole time.

I am grateful to Dennis, an extended member of the MBE lab, who played a pivotal role in setting up two MBE system and their pre-commissioning, commissioning, and maintenance. I want to thank Xianhe Liu, Yuanpeng, Ping, and Ayush for discussing nanowire growth with me and to help me explain my nanowire results. I am indebted to other MBE growers at Umich (Ayush, Ping, Dejiu, Anthony, Arthur, Navid, Ding, Yakshita, and David) for their good heart and intention to help me as a fellow MBE grower with MBE setup, refurbishment, and maintenance. Big thanks to Dan and John for helping me during MBE maintenance by responding to my emails promptly. Kanak helped me a lot in my project by studying optical properties of InGaN. I would like to thank

Boyu, Henry, Nirupam, Christian, and Shubhra for helping me with epi-growth and porous pseudo-substrates. Without Stacia and Vineeta, MQW re-growths on porous GaN would not be possible.

Thanks to Shawn for installing ozone treatment in a short notice, which helped me in different experiment. I appreciate all other cleanroom staffs (Pilar, Sandrine, Brian etc.), MSE staff (Sahar, Ying and Tim etc.) and MC^2 (Haiping, Nancy and Bobby etc.) keeping the instruments up and running even during holidays. Thanks to all the administrative people in EECS (Michelle, Alex, and Kim etc.) and MSE (Shelley and Renee) for helping me with paperwork and people, EECS Dock (Dan) to shipping and delivering expensive items to our lab.

I am thankful to Cindy for helping me with materials characterization (AFM, XRD) on zillions of samples with great patience and energy. I also want to thank Ian, Zhaobo, Sophia for helping me with materials characterization. I enjoyed mentoring them on different characterization systems. I am grateful to Ian, one of my undergrad mentees, and Nocona, one of my friends from materials science at Umich, for reading my thesis and giving me feedback on typos, grammatical errors and sentence structure. I would like to thank Harsh and Stefan for agreeing to look at it.

I must thank my parents for their endless sacrifices and support in sending me to a university as first-generation college student. I would not be able to be a doctor (probably not the kind of doctor my parents and family wanted me to be!!!) of philosophy with their immense support, care and love. I cannot thank them enough to give me the all the opportunity from my childhood even when I was hopeless and busy playing cricket inside and outside home. Without them I would never have made it to the point where I am now. No matter what the financial situation is, they have always provided the best for me. Their blessings and inspiration gave me the desire to do things in my own way, eight thousand miles away from them! I wish you were here! I also thank my two siblings, Zarin and Zarif, for their love and support when I was away from home pursuing my graduate studies. I would like to thank my uncles, aunts and grandparents (who would be happy to see me succeed) for supporting my free spirit at my early age.

I feel lucky to meet my friend, partner in crime and now wife, Mou. I am grateful to her for accompanying me in this challenging journey of Ph.D. with great patience even in her crazy schedule. Nothing would have been possible without her encouragement, support, and unconditional love. She changed and enhanced my life in ways I could have never imagined!

Table of Contents

List of Tables

List of Figures

Abstract

There has been a great deal of interest in developing relaxed InGaN pseudo-substrates for the fabrication of efficient red/amber/green light emitting diodes (LEDs) and laser diodes (LDs) for augmented/virtual reality applications. Additionally, relaxed InGaN pseudo-substrates can be potentially advantageous to further increase the operating frequency of GaN-based high electron mobility transistors (HEMTs) that are being used for high-power RF applications. However, it has been widely believed that achieving full or even partial relaxation of an InGaN layer via abrupt growth of InGaN film on GaN is not feasible due to the formation of a high density of defects.

My Ph.D. thesis was focused on the development of relaxed InGaN pseudo-substrates by using novel approaches such as growth on alternative substrates (e.g. ZnO or compliant porousified GaN). For this purpose, plasma-assisted molecular beam epitaxy was utilized for the epitaxial growth of InGaN films. I used several characterization techniques, including X-ray diffraction (XRD), atom probe tomography (APT), transmission electron microscopy (TEM), and atomic force microscopy (AFM).

In the process of developing InGaN pseudo-substrates, I discovered certain growth conditions that lead to the spontaneous formation of superlattice (SL) structures, composed of InGaN layers with different compositions. I then further investigated the impact of GaN polarity, In flux, growth temperature, and strain on the formation of self-assembled super lattice (SASL) structures. I also showed that the formation of such SASL structures allowed the growth of InGaN films beyond their critical thickness coherently strained to the underlying GaN. This discovery can have potential applications for the fabrication of various optoelectronic devices such as photovoltaic cells, photo-detectors, LEDs, and LDs.

Therefore, to achieve relaxed InGaN films, a unique approach, an epitaxial growth on O-face ZnO substrates was also studied, as ZnO is lattice matched to $In_{0.2}Ga_{0.8}N$. For this purpose, atomically smooth GaN films, showing step edges, were first developed at low temperatures to suppress the interfacial reaction between nitrides and the ZnO substrate at elevated temperatures using metal-enhanced epitaxy. InGaN films as thick as 1 μm were grown. Although using the low-

temperature GaN interlayer was shown to improve the InGaN structural quality, the dislocation density remained high.

To achieve relaxed-InGaN with high structural quality, growth on porosified GaN was then explored as an alternative approach. The impact of InGaN thickness and different compositionally graded structures on InGaN relaxation grown on tiled porous-GaN pseudo-substrates (PSs) was studied. In addition, the impact of the degree of porosification on the In incorporation and relaxation of InGaN was examined. 82% relaxed 1µm thick $In_{0.18}Ga_{0.82}N$, which is equivalent to a fully relaxed In-composition of 15%, on porous GaN PS, was obtained. Additionally, multi-quantum wells (MQWs) grown on the MBE InGaN-on-porous GaN base layers by MOCVD showed ~85 nm redshift in comparison with MQWs grown on planar GaN.

There can be several practical applications for the spontaneous formation of SASL in solar cells and optoelectronics (LEDs, lasers, photodetectors, and etc.). Additionally, next-generation electronic devices, including hot electron transistors (HETs) [1], InGaN-channel HEMTs could potentially benefit from relatively high temperature (690 °C) growth of high-quality InGaN and spontaneous formation of InGaN/GaN SASL. Moreover, high-quality relaxed InGaN with high In content can be utilized to get efficient red LEDs, especially micro-LED displays. Porous GaN can be used as a pseudo-substrate for both (Al,Ga)N and (In,Ga)N related alloys to cover whole visible spectrum.

Chapter 1 Introduction

1.1 Material Properties of InGaN

III-nitrides refer to GaN, InN, AlN, and their ternaries along with their quaternary alloys [2,3]. Among the ternary III-nitride materials, InGaN ternary alloys have tremendous possibilities in different optoelectronics and electronics applications e.g., lighting [4], displays, lasers, photodetectors, and solar cells [5]. (In,Ga)N alloy system has been considered one of the most important materials for light-emitting diode (LEDs). Moreover, InGaN alloys could be useful for some electronic applications. These applications need the unique optical and electrical properties of InGaN. Most of these properties are related to the crystal structures and wide energy bandgap.

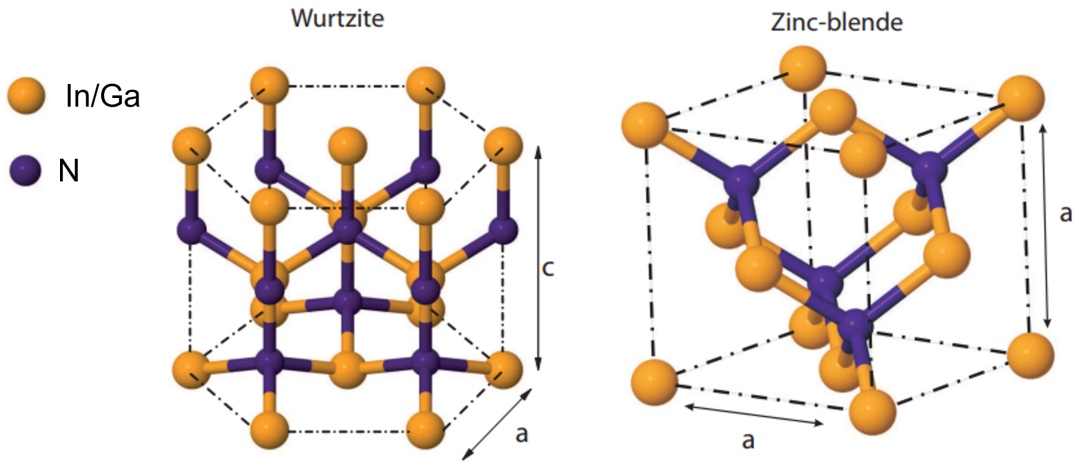

Figure 1.1 Schematic illustration of InGaN wurzite and zinc-blende crystal structure. The small (blue) and large (yellow) spheres indicate N and In/Ga, respectively ***Courtesy: W. M. Linhart [9]****.*

1.1.1 Crystal Structure

InGaN can be of different crystal structures e.g., wurtzite (WZ) and zinc blende (ZB) [6,7]. The interaction between the orbitals results in sp^3 hybridization, leading to tetrahedrally bonded (and vice versa) configurations of In/Ga and N atoms in both WZ and ZB structures [8,9]. The WZ and ZB structures of InGaN are shown in **Figure 1.1** [9]. WZ is the thermodynamically stable phase of nitrides under ambient condition. ***The focus of this thesis is on III-nitrides with wurtzite crystal structure.*** The WZ structure has a hexagonal unit cell and thus two lattice constants, c and a. It consists of six atoms of metal Ga/In, depending on their composition, and nitrogen atoms. InGaN with WZ crystal structure consists of two interpenetrating hexagonal close-packed (hcp) sub-lattices each with one III atom, offset along the c axis by 5/8 of the cell height (5c/8).

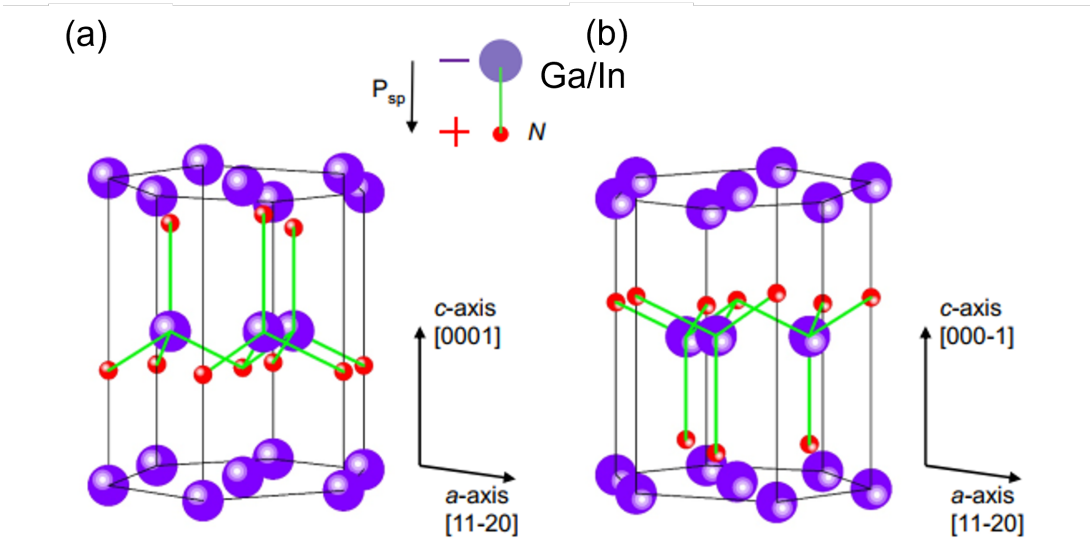

Figure 1.2 (a) Ga-polar and (b) N-polar III-nitride wurtzite crystal structure showing spontaneous polarization ***Courtesy: E. Ahmadi [8].***

The WZ InGaN thin films lack inversion plane perpendicular to the c-axis, and therefore, depending on the crystal orientation and surface termination, InGaN can have metal-polarity or N-polarity **(Figure 1.2 (a) and (b))** [8]. Since nitrogen is more electronegative than other group-V

elements, III-nitrides usually have a higher degree of ionicity. This high electronegativity of the nitrogen atom also contributes to the stability of the wurtzite phase of III-nitrides.

Furthermore, due to the lack of inversion symmetry and the partially ionic bond of III-N, wurtzite III-nitrides e.g., InGaN exhibit unique polarization effects along the c-axis (**Figure 1.2**). Moreover, when strained along the c-direction, they show piezoelectric effects. The total polarization is a sum of the spontaneous and piezoelectric polarization in the film. The electric polarization in InGaN results in unique electronic properties (e.g., band diagrams and charge distributions) in (Al,Ga,In)N heterostructures [10]. These heterostructures are essential for the demonstration of electronics and optoelectronics applications.

1.1.2 Bandgap

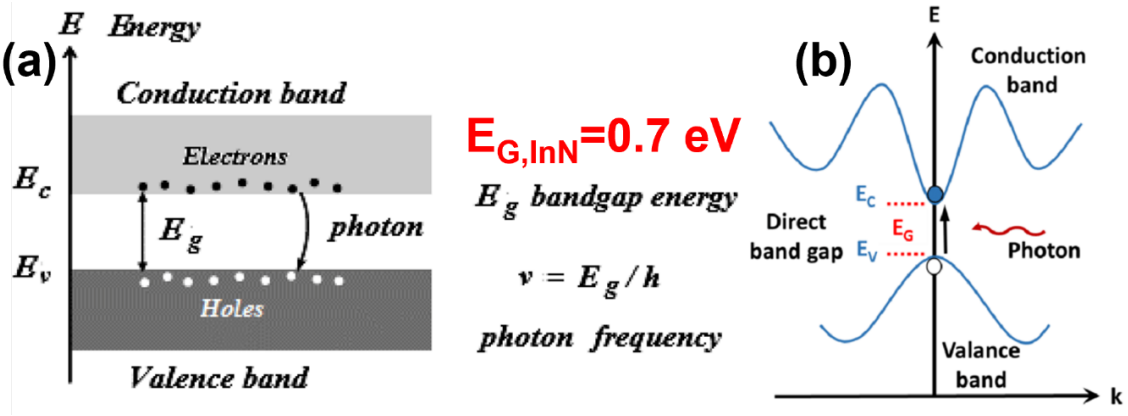

Figure 1.3 (a) A schematic of energy band diagram with valence band, conduction band and energy band gap. (b) E-K diagram showing direct band gap of InN with e-h recombination and photon emission ***Courtesy: A. C. Sparavigna [14].***

(In,Ga)N has a direct bandgap gap within the whole composition range, which is essential for optoelectronics applications e.g., light-emitting diodes, lasers, and solar cells [4,5]. Its wide bandgap makes $In_xGa_{1-x}N$ an excellent candidate for devices operating at high temperatures and in extremely harsh environments. Early investigation of InN indicated that the bandgap of InN was

in the range of 1.7-3.1 eV [11,12]. However, at that time the material was usually grown by sputtering, resulting in a polycrystalline and inhomogeneous film with high defects and electron density leading to inaccuracy in InN bandgap measurements. With the development of epitaxial growth techniques such as, MBE and MOCVD, InN film quality significantly improved. In addition, an understanding of the Burstein-Moss effect in highly doped InN helped to explain the increase in InN bandgap. Burstein-Moss effect refers to the increase in band-gap energy in degenerate semiconductors, which is associated with the effect that some states close to the conduction band can be populated due to degenerate electron distribution. These discoveries have led to the community accepting a lower value of ~0.7 eV [13] for the InN band-gap energy.

The narrow band-gap of InN is due to the electron configuration of In ($1s^2 2s^2 2p^6 3s^2 3p^5 4d^{10} 5s^2 5p^1$) and N ($1s^2 2s^2 2p^3$) atoms and interactions between orbitals [13]. The repulsion between N 2p valence band and shallow In 4d inner core-shells moves the valence band maximum to a higher energy state. In addition, the large difference in both ionic size and the higher electronegativity of nitrogen lowers the energy of the N 2s orbital. These characteristics lead to a narrowing effect between In 4d and N 2p orbitals and this leads to an increase in p-d repulsion effect. The p-d repulsion effect also occurs in other III-nitrides e.g, GaN where the bandgap is 3.4 eV since the repulsion for GaN is much smaller than that for InN due to the large Ga 3d and N 2p orbital separation.

InN has an E-K diagram with a conduction band minimum and valence band maximum at the same K-value [14] (**Figure 1.3**). Therefore, InN has a direct bandgap, which results in efficient e-h recombination. The band-gap can be tuned from 0.7 eV to 3.4 eV by alloying GaN with InN and can be measured by photo-luminescence technique. ***In Chapter 2 and Chapter 4****, Ga-polar InGaN grown Ga-polar GaN template on sapphire substrates showed strong luminescence*

properties. In contrast, in ***Chapter 3****, N-polar InGaN grown on bulk GaN substrates surprisingly showed no light emission.*

1.1.3 Pseudo-morphic Growth and Critical Thickness

InGaN epitaxially grown on GaN template can be referred to as heteroepitaxial growth since their in-plane lattice constant is different [15,16]. During hetero-epitaxial growth, a small amount of strain can be managed by elastic formation of the unit cells or lattice in the out-plane direction to compensate the decrease in in-plane lattice parameter. During epitaxial growth of InGaN with low In content, the in-plane lattice constant can be forced to stay similar to the substrate in-plane lattice constant, which is referred to as pseudo-morphic growth. A hetero-epitaxial InGaN film can be grown pseudo-morphically on a GaN substrate below a certain film thickness, which is known as the critical thickness [17–21]. With an increase in In content in InGaN, the critical thickness decreases due to an increase in strain. An InGaN thin film grown on a GaN substrate beyond critical thickness relaxes by the formation of dislocations and defects. *Critical thickness is explained in detail in* ***section 2.1.1 of Chapter 2****. In* ***chapter 2 and chapter 3,*** *both Ga-polar and N-polar InGaN on GaN substrate was grown beyond critical thickness by formation of self-assembled superlattices consisting of* $In_xGa_{1-x}N/In_yGa_{1-y}N$.

1.1.4 Polarization

The difference in the electronegativity between the III-site atoms and the N atoms results in an ionic bond in III-nitrides [15,22]. Due to the absence of inversion symmetry and the ionic bonding, III-nitrides, including InGaN, show spontaneous polarization, a built-in electric polarization absent in other conventional semiconductors e.g., GaAs and ZnSe. In a WZ crystal structure, where c/a=1.633, the polarization vectors nullify each other and net polarization in the lattice is zero.

However, in III-Ns, the ratio deviates from the ideal value, resulting in a net polarization along the $\vec{c}$ axis e.g., (0001) or $(000\bar{1})$ direction. Additionally, tensile or compressive stress in the lattice produces additional polarization called piezoelectric polarization. Piezoelectric polarization in non-polar directions e.g., $\overrightarrow{a}$ and $\overrightarrow{m}$ axis are zero, but piezoelectric polarization toward the $\vec{c}$ axis is non-zero.

Therefore, the net polarization ($\vec{P}_{net}$) in each layer is the summation of spontaneous ($\vec{P}_{sp}$) and piezoelectric ($\vec{P}_{pz}$) polarization shown in **Equation 1-1**

$$\vec{P}_{net} = \vec{P}_{sp} + \vec{P}_{pz}$$

Equation 1-1

1.1.5 Phase Diagram of (In,Ga)N and Phase Separation

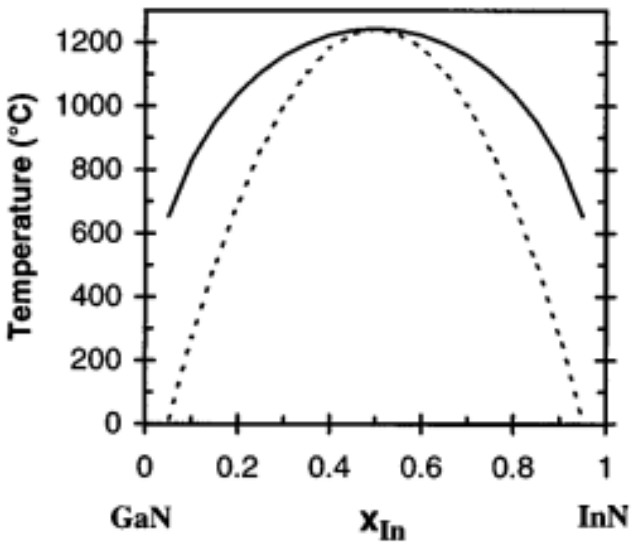

Figure 1.4: Binodal (solid) and spinodal (dashed) curves for the InxGa1-xN system, calculated assuming a constant average value for the solid phase interaction parameter ***Courtesy: Ho and Stringfellow et. al. [23].***

$In_xGa_{1-x}N$ (x is the InN mole fraction) growths have always been challenging and intimidating due to complexities e.g., phase separation, inhomogeneity [23–25]. These are due to the solid phase miscibility gap, which results from the large difference in interatomic spacing between GaN and InN. Ho and Stringfellow [23] reported the temperature dependence of binodal

and spinodal boundaries in InGaN system with an updated valence force field model **(Figure 1.4).** They calculated the extent of the miscibility gap and determined that the equilibrium In mole fraction in GaN is less than 6% at 800° C, the maximum temperature typically used for epitaxial growth by molecular beam epitaxy (MBE) or metal-organic chemical vapor deposition (MOCVD). The phase diagram also shows a critical temperature of 1250 °C for phase separation.

These results show that InGaN alloys are unstable over most of the composition range at the normal growth temperature. Thus, the miscibility gap is one of the significant challenges for the epitaxial growth of InGaN alloys [26,27]. However, epitaxial growth techniques e.g., MOCVD and MBE were designed with the capability to grow materials in supersaturated conditions where the equilibrium phase diagram does not apply usually. This leads to the possibility of the growth of metastable InGaN alloys. Indeed, once the InGaN has been formed, growth kinetics help to prevent phase separation. However, due to the miscibility gap, InGaN shows composition fluctuation and the formation of localized In rich clusters, which make the crystalline quality of the layer comparatively worse. ***In Chapter 2****, it was shown that a self-assembled superlattice consisting of* $In_xGa_{1-x}N/In_yGa_{1-y}N$ *has been formed due to vertical spinodal decomposition toward the growth direction and strain.*

1.2 InGaN Pseudo-substrates for Optoelectronics Applications

Lighting consumes about 20% of total global electricity production and contributes to carbon emission that is equivalent to approximately 70% of the amount produced by the global automobile industry [28–32]. The most widely used source of lighting is incandescent light, a technology that has not been improved since the 19th century. To replace incandescent lights, there are several energy-saving alternatives e.g., halogen light bulbs, fluorescent light bulbs, and LEDs. In recent years, rapid advancements in the development of high brightness light-emitting diodes

(LEDs) based on III-nitrides have introduced the concept of solid-state lighting (SSL) and led to the possibility of replacing incandescent bulbs with LEDs [33–36]. Advancements in SSL technology are transforming the lighting industry due to its compactness and, longer lifetime (20,000 hours for LEDs compared to 2000 hours for incandescent light) while consuming only a small fraction of the electrical power for the same luminous intensity. Additionally, this includes the benefit of robustness, anti-vibration-free, flexible design, and reduced carbon emission. Given the widespread application of SSL, I. Akasaki, H. Amano and S. Nakamura were awarded the Physics Nobel prize in 2014 for their work on bright and efficient blue LEDs.

Furthermore, with the increasing use of portable, wearable, and other consumer electronics, the standards of displays have risen exponentially, and the demand for better displays has gained dramatic attention in both academia and industry [29]. The use of electronic devices has become essential component and has infiltrated our daily lives, from smartphones/tablets and laptops to automotive displays and large TV monitors [32,37,38]. Due to the huge application of smart displays, market research companies forecast the display panel market will grow by more than 30 billion USD from 2019 to 2024 globally. With these recent demands in display technology, a new display technology referred to as micro-LED is currently being recognized as the ultimate solution to next-generation display technology [39,40]. Global tech giants are putting a lot of effort into micro-LED on a variety of products like wearable displays, high speed augmented reality (AR)/virtual reality (VR) displays, pen projectors, ultra-high-definition and high brightness/contrast large flat panel displays, and TVs as well as visible light communications [41–44]. A huge demand in consumer electronics for micro-LEDs is a major driving force of the development of recent innovations in technology and products related to micro-LED. According to a report from MarketWatch, “The global MicroLED market valuation was 170 million USD in

2018 and is expected to reach 17 billion USD by the end of 2025, growing at a compound annual growth rate (CAGR) of 78.3% during 2019-2025." The growth percentage is much larger than the overall display panel market [40].

In nitrides-based LEDs for SSL and displays, a smaller bandgap material (In,Ga)N sandwiched by larger bandgap material GaN creates an InGaN/GaN quantum well, which is often referred to as an active layer. Therefore, (In,Ga)N is an essential part of any nitride-based optoelectronics device. N. Yoshimoto et al. [45] demonstrated light emission from high-quality InGaN grown by MOCVD in 1991. Later in the 1990s, S. Nakamura et al. [36,46,47] worked extensively on InGaN as an active layer for blue and green LED. A blue LED is used to stimulate the yellow phosphor, converting the blue emission to yellow or green emission for commercially available white LEDs.

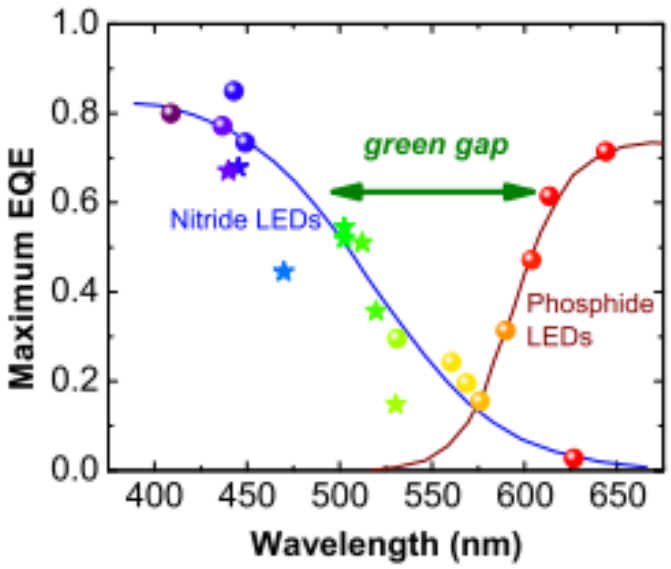

Figure 1.5: The green gap. Maximum external quantum efficiency (EQE) of different commercial nitride and phosphide LEDs (spheres), illustrating the green gap problem. The lines are guides to the eye ***Courtesy: M. A. d. Maur et. al. [48].***

However, this conversion leads to an inefficient energy loss defined as Stokes' loss, which makes device performance below 75%. The loss mechanism can be eliminated by substituting the

phosphor-based down-conversion with direct color-mixing, combining the light emission from different LEDs at a different wavelength. The most important challenge of phosphor-fee SSL is the **green gap**. The green gap refers to a severe drop in efficiency in LEDs emitting green or yellow light compared to blue or red ones for III-nitride and III-phosphide technology, respectively [48]. **Figure 1.5** shows the maximum external quantum efficiency (EQE) of different commercial nitride-and phosphide-based LEDs showing the green gap problem. High efficiency of green LEDs is particularly important since the phosphor-free SSL based on color mixing needs a green emitter with an emission wavelength ~540 nm. Besides, integrating red LEDs based on phosphides with green and blue LEDs based on nitrides has been a challenging task. Due to these issues, obtaining ultra-efficient InGaN-based green and red LEDs is of paramount importance.

Growing high-quality InGaN with high In content has been challenging for the last few decades. This is due to the low miscibility of In in InGaN, the vapor pressure of InGaN being lower than that of GaN, and large lattice mismatch of InN and GaN (~10%). For MOCVD, it was shown that the In content needs to be below 20%-25% to maintain good quality. Higher In content InGaN layers showed phase separation [24,25,49] due to the miscibility gap [48].

Moreover, InN and GaN thermal stabilities and vapor pressures are quite different. InN starts decomposing at 500 °C due to its low vapor pressure [50] whereas the ideal GaN growth temperature is about 700 °C in plasma-assisted molecular beam epitaxy (PAMBE) [51]. To achieve large In contents, the substrate temperature during InGaN growths needs to be decreased below 600 °C, which reduces the Ga adatom mobility, resulting in a rougher surface and inhomogeneity in the ternary alloys. Additionally, at typical InGaN growth temperatures, the In desorption rate is lower than the In–N bond decomposition rate, leading to the accumulation of metal In droplets on the surface [52]. Furthermore, for InGaN/GaN QWs, at lower GaN growth

temperatures, surface quality degrades drastically due to nitrogen deficiency [53]. Due to the presence of the Quantum Confined Stark Effect (QCSE) (**discussed in Chapter 5**) in the c-plane, InGaN/GaN QWs can emit in the green region with In content lower than 20% by increasing the well-width. Unfortunately, this reduces electron-hole overlap in the QW region, resulting in a decrease in quantum efficiency and poor performance [30,31]. Additionally, conventional AlInGaP-based red light-emitting diodes (LEDs) showed high efficiency in regular devices with 0.1 mm^2 but the μLEDs devices had low external quantum efficiency (EQE) with low device dimensions and showed a decrease thermal stability at a high temperature. These is due to Shockley-Read-Hall (SRH) nonradiative recombination due to sidewalls damage and a higher surface recombination velocity. This is a challenging issue since these issues are related to intrinsic AlInGaP materials property. It has been explored that InGaN μLEDs can be an alternative to solve EQE size effect by sidewalls passivation. InGaN μLEDs has a robust thermal stability in commercial InGaN blue and green LEDs as well. Therefore, InGaN red μLEDs can be a promising candidate for μLEDs display application.

The availability of relaxed bulk InGaN pseudo-substrate can offer the ultimate solution to the problems discussed above e.g., high strain and QCSE. By using a relaxed $In_xGa_{1-x}N$ layer as a pseudo-substrate, the growth of the $In_zGa_{1-z}N$ based structure where z>x can be attainable [54,55]. This can reduce the lattice mismatch between $In_zGa_{1-z}N$ and the pseudo-substrate compared to the lattice constant between $In_zGa_{1-z}N$ and a GaN substrate or a compressively strained $In_xGa_{1-x}N$. Thus, the pseudo-substrate can accommodate higher In incorporation by increasing the critical thickness of $In_zGa_{1-z}N$ film and lowering the piezoelectric component for polarization. ***In Chapter 5****, it has been demonstrated that $In_xGa_{1-x}N/In_yGa_{1-y}N$ MQW grown on relaxed InGaN pseudo-substrate by MBE showed ~85 nm redshift compared to MQW grown on planar InGaN pseudo-*

substrate by MBE, which confirms a relaxed InGaN pseudo-substrate can increase the In incorporation MQW. Besides, the light emission intensity from MQW grown on relaxed InGaN is much higher than that from MQW grown on planar InGaN. This is associated with mitigation of the QCSE by relaxation of InGaN and increase in e-h recombination efficiency.

1.3 InGaN Pseudo-substrates for Electronic Applications

Table 1-1: Essential parameters of Si and III-nitrides with Johnson's figure of merit Courtesy: E. Johnson et. al. [56]

	Si	**GaAs**	**SiC**	**GaN**	**AlN**	**InN**
E_g (eV)	1.1	1.4	3.2	3.4	6.2	0.7
m_e	0.2	0.067	0.29(m_l) 0.42(m_t)	0.2	0.4	0.05
E_{bk} (V/cm)	$3x10^5$	$4x10^5$	$20x10^5$	$20x10^5$	$20x10^5$	$25x10^3$
v_s (cm/s)	$6x10^6$	$1.0x10^7$	$2.0x10^7$	$2.0x10^7$	$2.5\ x10^7$	$4.2x10^7$
μ (cm^2/Vs)	1000	8000	500	1000	135	4400
K (W/m-°C)	150	43	490	130	285	176
$^*(E_{bk}v_s/\pi)^2$	1	7	282	282	441	

* Johnson's figure of merit for power-frequency performance of discrete devices
All figures of merit are normalized to silicon. K is the thermal conductivity.

The material properties of GaN, such as its large critical electric field and high electron mobility, make it an attractive material system to fabricate devices for high power millimeter-wave power amplifiers. **Table 1-1** summarizes material parameters of III-nitrides and their related alloys commonly used for high power and high-frequency amplifiers. The Johnson's figure of merit

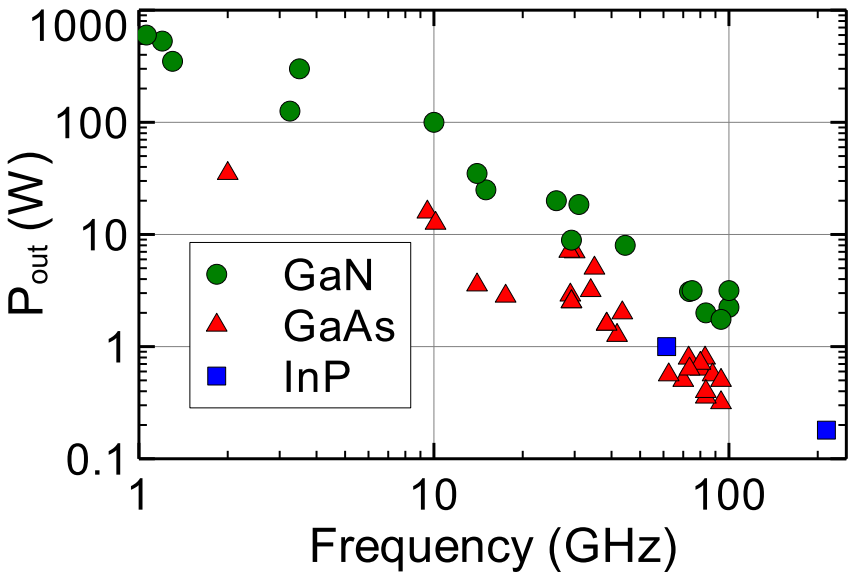

Figure 1.6 A comparison of output power vs Freq. for different material systems [Courtesy: Brian Romanczyk]

(JFOM), listed in **Table 1-1,** is commonly used to determine the suitability of a semiconductor for high-frequency high power transistors [56]**.**

As shown in **Figure 1.6**, GaN-based HEMT devices have demonstrated superior power performance over a wide frequency range when compared to alternative device technologies. To realize large-output power devices even at higher frequencies for sub-Terahertz application, channels with higher electron velocity must be utilized.

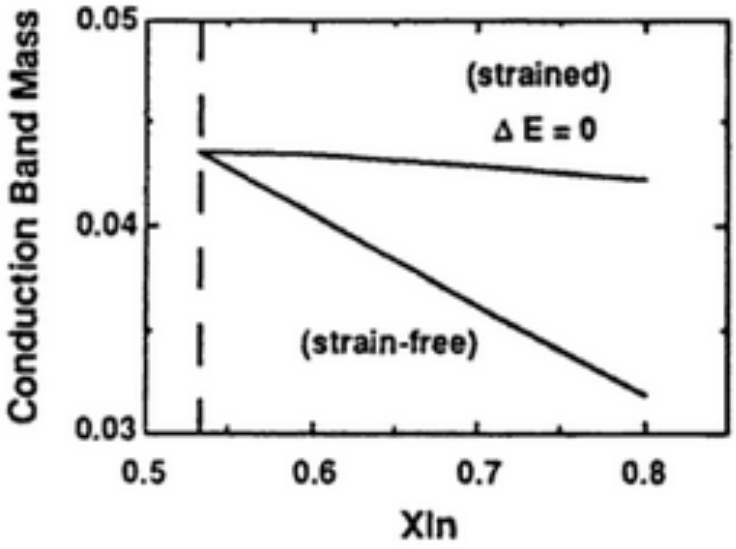

Figure 1.7: Calculated conduction band effective mass for strained and bulk (strain-free) InGaAs as a function of InAs mole fraction Xin ***Courtesy: T. Matsuno et. al. [65]***

One way of achieving a combination of higher electron velocity and large band-gap is using ***relaxed InGaN or strained GaN on relaxed InGaN as the channel material,*** which provides a reduced electron effective mass, critical in reducing electron scattering and enhancing electron velocity [57]. There is always a trade-off between the enhanced scattering introduced by the InGaN through alloy scattering over the binary GaN and the reduced scattering rate because of the reduced electron effective mass. This same trade-off is played out in the relaxed $Al_{.48}In_{.52}As/In_{.53}Ga_{.47}As$ on InP system wherein the benefits of reducing the effective mass (**Figure 1.7**) relative to GaAs

overcomes the increase in alloy scattering [58]. The 2DEG mobility in an $In_{0.2}Ga_{0.8}N$ channel has been predicted by Yarar et al. to be more than 5000 cm^2/Vs at room temperature and 10,000 cm^2/Vs at low temperature as calculated (**Figure 1.8**) [59]. Experimentally, electron mobility values as high as 3570 cm^2/Vs were measured for InN films with an electron carrier density of 1.5 x 10^{17} cm^{-3} compared to values around 600 cm^2/Vs for GaN films with similar carrier densities [60]. Theoretically, it has been reported that InN can exhibit the higher peak overshoot velocity compared to AlN, or GaN e.g., has a peak drift velocity of ~5 x 10^7 cm / s at an electric field strength of 32 KV / cm [57]. The highest calculated value for low field mobility of unintentionally doped InN is ~14,000 cm^2/V s at room temperature. InGaN has been explored as a HEMT channel material [61–65], where they have reported a maximum 2DEG mobility of ~1300 cm^2/V with a sheet carrier density of ~10^{13} cm^{-3}. However, this is much lower than conventional 2DEG mobility from GaN channel structures, which is typically 1000-1500 cm^2/V s resulting in high sheet resistance due to either low mobility or low carrier density. This is due to the alloy disorder scattering in InGaN and significant interface roughness scattering. To re-iterate for emphasis, relaxation of the InGaN channel is required since an InGaN channel coherently grown on GaN substrate does not provide an effective mass commensurate with the In mole fraction. This is because the lattice constant and hence the Brillouin Zone and conduction band curvature of the strained InGaN is more akin to GaN, as previously observed for strained and relaxed InGaAs **(Figure 1.7)** [58]. This is where the ability to grow relaxed InGaN buffer layers would play a very important role in enabling high-frequency devices for high power applications.

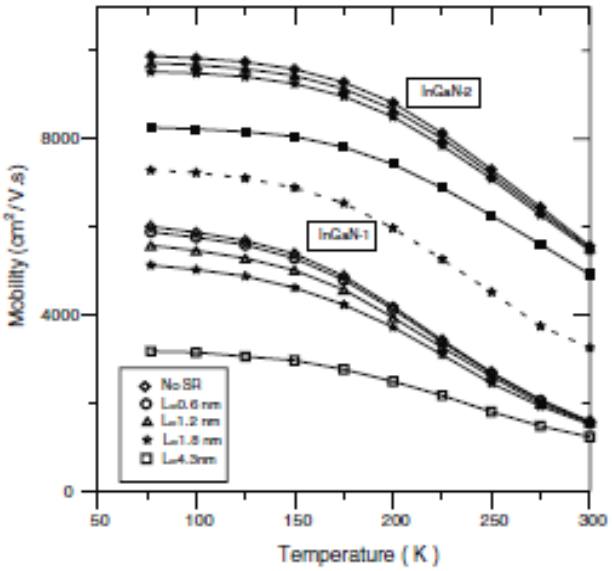

Figure 1.8: Electron mobility in $In_{0.2}Ga_{0.8}N$ film sandwiched between two GaN layers. InGaN-2 and InGaN-1 are electron mobility calculated assuming m = 0.04 and m* = 0.07 for InN, respectively* ***Courtesy: Z. Yarar et. al. [59].***

1.4 Relaxed InGaN Buffer as Pseudo-substrate

Several research groups have attempted to grow relaxed InGaN buffers using different approaches. One of these approaches is multi-step or graded InGaN films on GaN buffer layers [51,52]. A fully relaxed $In_{0.1}Ga_{0.9}N$ layer on the GaN layer was achieved on GaN by PAMBE growth with a grading of 2% In incorporation increase per 100 nm containing a GaN interlayer in every 100 nm. The GaN interlayer in every 100 nm was grown for the sustaining high-quality InGaN layer since the temperature needs to be raised from low InGaN growth temperature to a higher temperature helps to desorb the excess metallic In accumulated on the surface during the growth of the previous 100 nm of InGaN. The excess In on the InGaN layer is coming from metal rich growth condition of InGaN. However, this method is slow, since each GaN interlayer cycle (GaN growth, temperature ramp up, temperature ramp down) takes an extra ~25 min every cycle. To reach 20% In content in InGaN, 10 cycles of these InGaN/GaN layers will be necessary, which will be typically ~4h of growth time. In addition, due to low InGaN growth temperature, Ga

adatom mobility is low, resulting in low crystalline quality for the GaN interlayer. Thus, low-quality GaN interlayer can lead to the following InGaN layer with low structural quality.

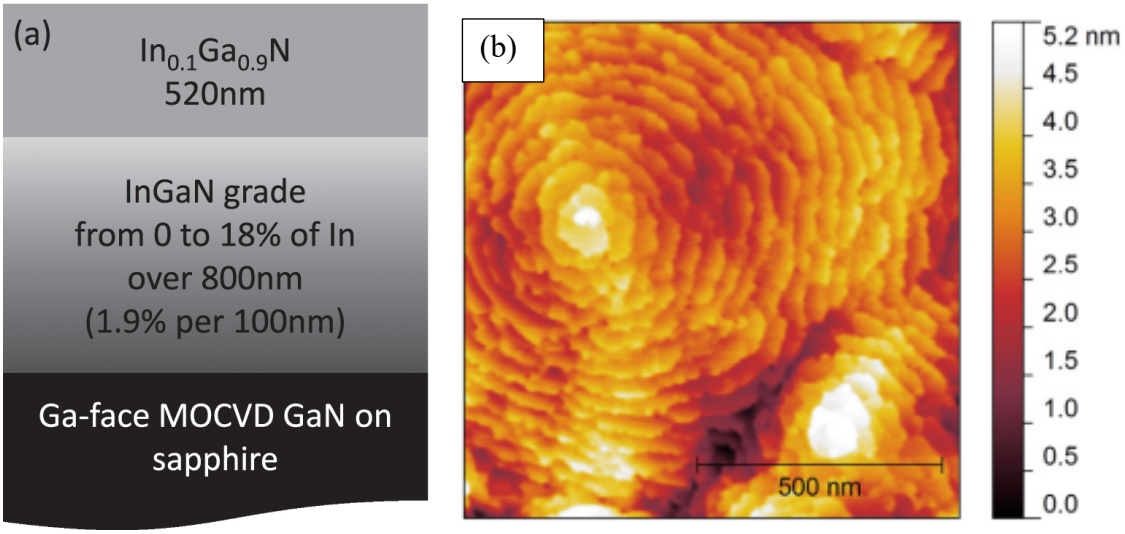

Figure 1.9 (a) Scheme of the structure grown to achieve a relaxed $In_{0.1}Ga_{0.9}N$ layer (b) 2x2 µm² AFM image of the surface, exhibiting spiral growth. The rms surface roughness is 0.75 nm ***Courtesy: K. Hestroffer et. al. [66]***

So, to solve these problems related to slow process and GaN interlayer, K. Hestroffer et al. [66] demonstrated a fully relaxed $In_{0.1}Ga_{0.9}N$ layer by plasma-assisted molecular beam epitaxy (MBE) on c-plane GaN using a grading technique without any GaN interlayer. This technique consisted of two parts: (i) a graded InGaN buffer and (ii) a thick InGaN layer with constant composition **(Figure 1.9(a)**). The In content in the graded InGaN buffer increased 1.8% every 100 nm. This technique could provide a quick and continuous epitaxial growth procedure due to growing InGaN buffer near the stoichiometric region of the growth diagram. This results in a smooth surface without accumulation of In droplets. **Figure 1.9 (b)** shows the 2x2 μm^2 AFM image of the relaxed InGaN sample surface after growth. The sample surface had clear spiral hillocks, which is characteristic of step-flow growth mode associated with threading dislocation. However, TEM **(Figure 1.10**) revealed that the relaxation occurred through the formation of dislocations and defects. A high density of threading dislocations (~3×10^{10} cm^{-2}) was observed

from TEM, which is two orders of magnitude larger than the dislocation density of the GaN template on sapphire substrate.

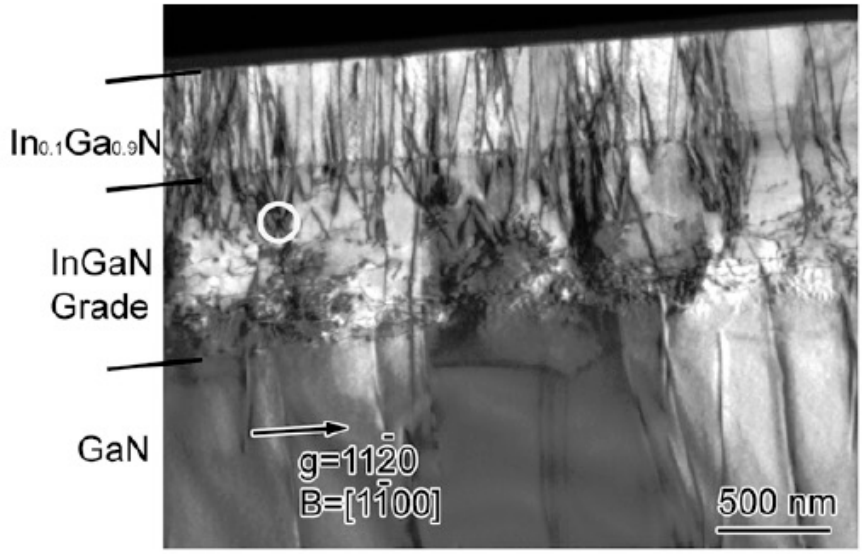

Figure 1.10 TEM image illustrating the high density of threading dislocations that spread through the graded InGaN buffer and the top thick $In_{0.1}Ga_{0.9}N$ layer ***Courtesy: K. Hestroffer et. al. [51].***

Alternatively, InGaN pseudo-substrates have been fabricated via coalescence of relaxed nano-feature arrays e.g., nano-stripes and nano-pillars [68,69]. S. Keller et. al. [68] reported a uniaxially relaxed, coalesced InGaN growth over a nano stripe array of InGaN/GaN multi-quantum well (MQW) by MOCVD. The MQW nano strip arrays with a height-to-width aspect ratio of 0.5 and 1 were fabricated from strained planar MQW **(Figure 1.11).** After the fabrication, MQW is relaxed perpendicular to the stripe direction, resulting in a $a_{\perp}$ lattice constant perpendicular to the strip direction where it is larger than that of the GaN base layer. They showed that a stripe aspect ratio of 1 is required to induce elastic relaxation of the MQW stripes after (In,Ga)N growth. A stripe aspect ratio of 0.5 plastically relaxes after the (In,Ga)N cap layer growth, which shows light emission with lower intensity. However, the main challenges of this method is the necessity of

multi-step lithography to make the MQW nano strip array and the relaxation is dependent on the aspect ratio.

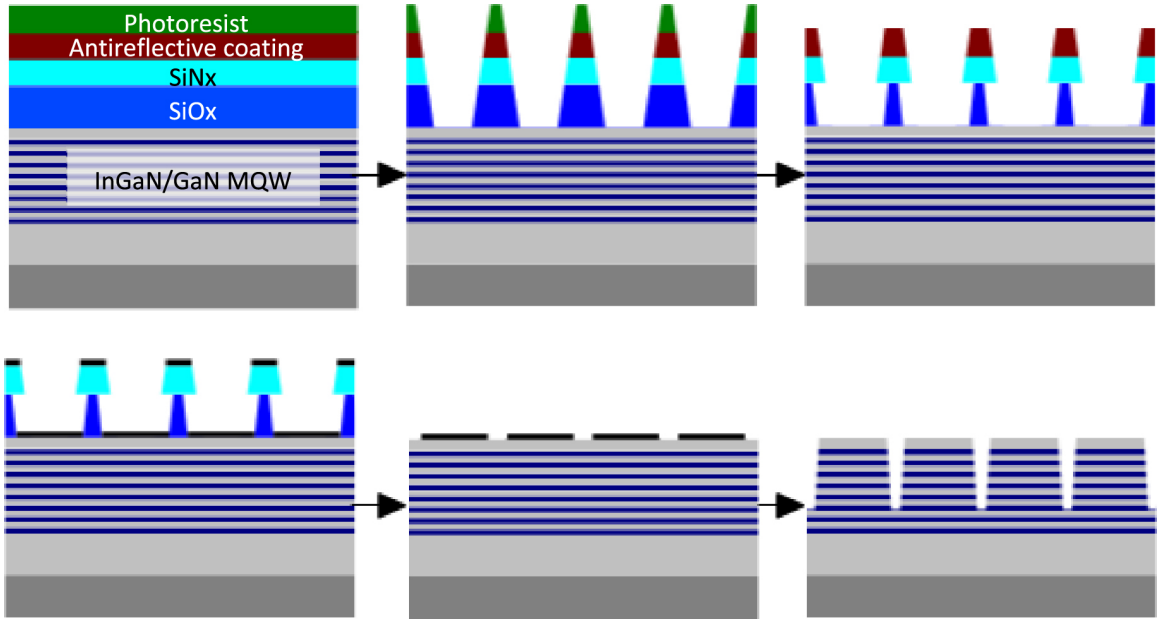

Figure 1.11 Schematic process flow for nanostripe array fabrication. 1) O_2 and Si_3N_4 mask layers were first deposited via plasma-enhanced chemical vapor deposition (PECVD) onto the planar MQW samples, and then an anti-reflective coating and photoresist were spun on. 2) Using holographic lithography, a stripe pattern was defined. 3) After development, a series of dry etches was performed in order to transfer the stripe pattern onto the SiO_2 and Si_3N_4 mask layers. 3) An HF undercut etch was used to define the fill factor of the stripe pattern, 4) a nickel hard mask was deposited to protect the GaN surface where the stripes would be. 5) After removal of the SiO_2 and Si_3N_4 masks, 6) a final dry etch was performed to etch the stripe pattern into the InGaN/GaN MQWs and the nickel mask was removed ***Courtesy: Stacia Keller et. al. [68]****.*

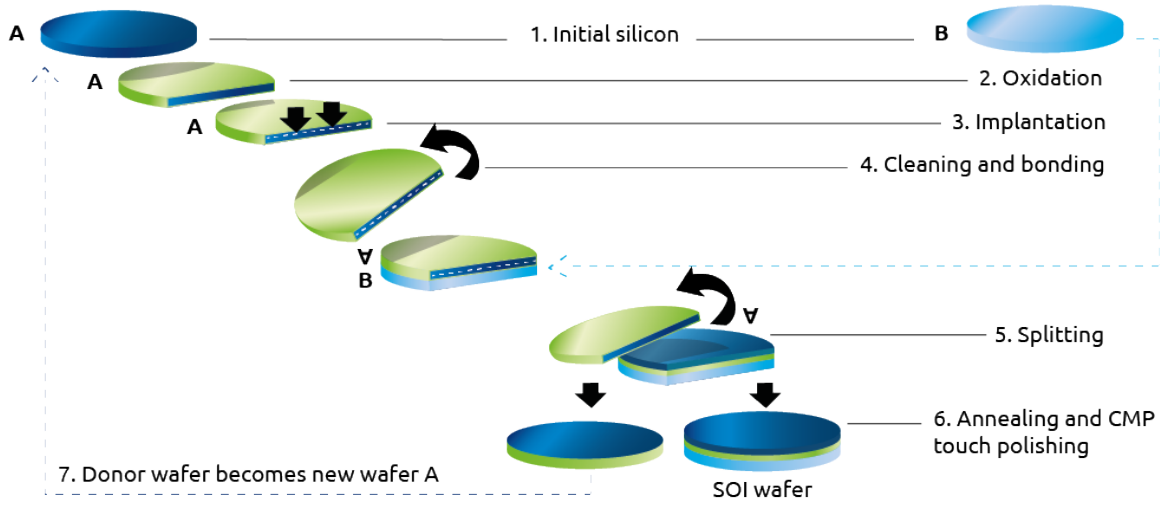

Figure 1.12 Schematic of different steps in the Smart cut TM process ***Courtesy: Soitec S.A. [70]***

Soitec S.A. has developed a InGaN pseudo-substrate (InGaNOS) based on their SmartCut technology for relaxation of InGaN [70]. In this technique, the process is initiated by wafer bonding an InGaN layer grown on GaN to a second substrate. Afterwards, the InGaN is removed from its native substrate using the Smart Cut technology **(Figure 1.12)** and the InGaN layer is patterned and annealed for relaxation. InGaNOS substrate, which has a thin relaxed InGaN layer, can be used for III-nitride growth by MOCVD and MBE. However, the largest in-plane lattice constant of the InGaN layer has been less than that of fully relaxed InGaN with an equivalent In composition of 5%, which is relatively low.

More recently, P. Chan et al. [71] showed a highly relaxed InGaN buffer layer on a full two-inch c-plane sapphire substrate by MOCVD by a single growth technique **(Figure 1.13).** 100 nm GaN decomposition stop layer (DSL) on a 3nm thick InGaN with a high In incorporation decomposition layer (DL) was grown. The first 30nm of GaN DSL was grown at a low temperature similar to InGaN growth temperature so that InGaN does not dissociate. Afterward, 70nm of GaN was grown with a temperature ramp to 1000 °C to ensure higher crystal quality for the following layer. The InGaN DL went through thermal decomposition at 1000 °C resulting in voids to relax

the subsequent InGaN grown over the GaN DSL layer. A 200 nm $In_{0.04}Ga_{0.96}N$ buffer grown on GaN decomposition stop layer showed 85% biaxial relaxation. However, the surface morphology was relatively poor and deep pits were observed, which may be detrimental for device fabrication.

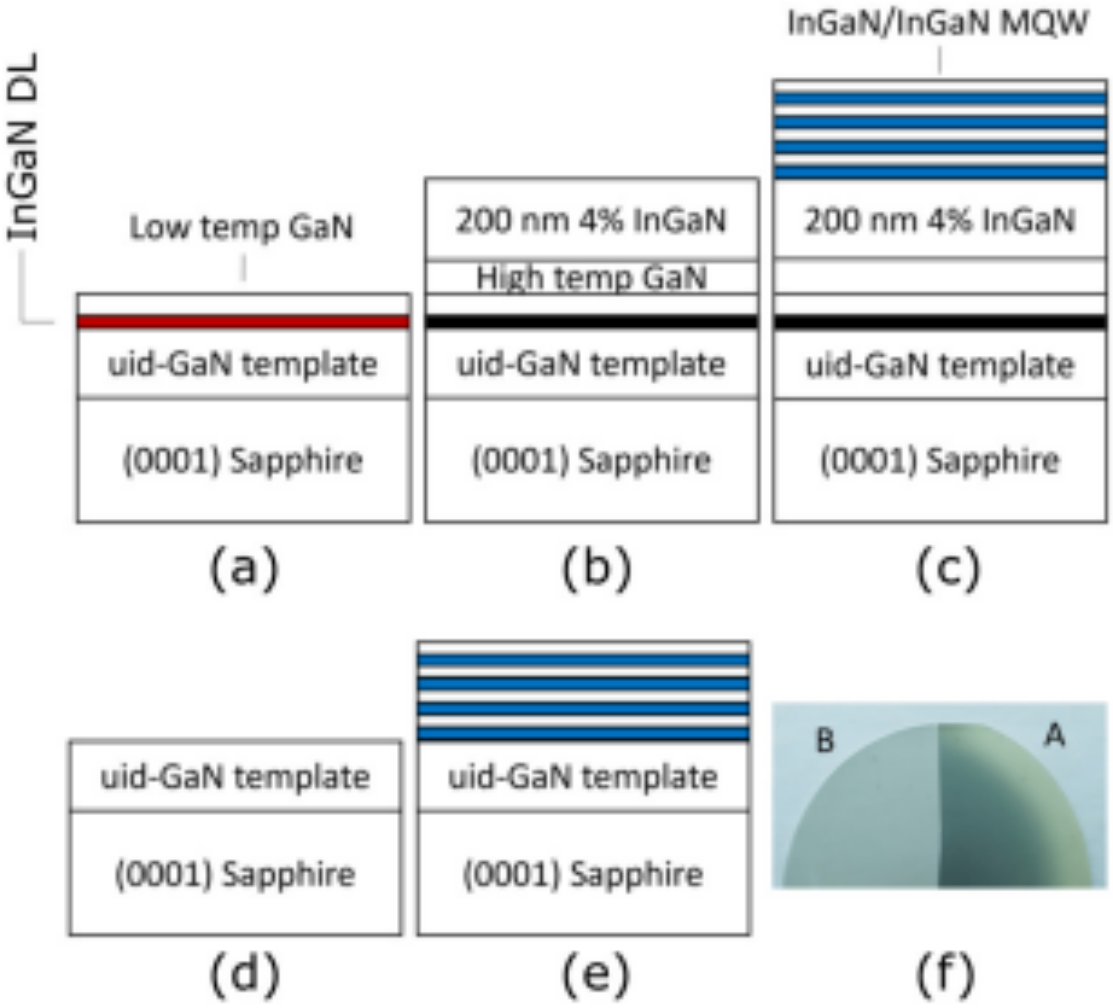

Figure 1.13 Growths performed in this study. (a)–(c) The growths of a relaxed InGaN pseudo-substrate and MQW regrowth on sample A. In (a), a UID-GaN template and high-In composition InGaN DL are grown and capped with low-temperature GaN. After this, the temperature is increased to decompose the InGaN DL, and an InGaN buffer layer is grown (b). Finally, a MQW was regrown (c) co-loaded with sample B. (d)–(e) The reference sample B. First, a UID-GaN template was grown on sapphire (d) and then co-loaded for MQW regrowth (e). Subfigure (f) shows a photograph of samples A and B side by side ***Courtesy: P. Chan et al. [71].***

Alternatively, there have been several attempts to grow InGaN on ZnO [72–75] and $ScAlMgO_4$ [76,77] substrates since $In_{0.18}Ga_{0.82}N$ is lattice matched to these substrates. $ScAlMgO_4$ [76,77] substrate known as SCAM is an alternative for InGaN growth. SCAM has a rhombohedral

crystal structure ($R\bar{3}m$) consisting of alternating stacks of wurtzite (Mg,Al)O (0001) and rocksalt ScO (111). The lattice parameters are a=0.3249 nm and c=2.5195 nm, where the latter corresponds to the length of three formula units of (Mg,Al)O and ScO. SCAM is transparent up to 196nm, which is essential for visible and (UV) optoelectronics. However, the high n-type conductivity of InGaN grown on $ScAlMgO_4$ substrates has made epitaxial growth efforts on SCAM substrates very challenging.

ZnO is in-plane lattice-matched with $In_{0.18}Ga_{0.82}N$ and has the same crystal structure (wurtzite) as (In,Ga)N with identical stacking order. Regardless, one of the challenges in utilizing ZnO as a substrate is inconsistency in the surface morphology due to its chemical mechanical polishing. ***In Chapter 4,*** *a substrate treatment method consisting of ozone treatment, and BHF etching followed by high temperature annealing is described.* Another challenge for using ZnO as an alternative substrate for the growth of nitrides is H_2 back etching of ZnO substrate at high growth temperatures in MOCVD reactors [75]. Ammonia (NH_3) is used as the N source during MOCVD GaN growth, which is the main source of H_2 during the InGaN growth on ZnO by MOCVD. Another common issue in InGaN growth on ZnO by MBE and MOCVD is hetero-valency at the III-nitride/ZnO interface forming intermediate phases e.g., In_2O_3 or Ga_2ZnO_4. This interfacial layer has shown poor crystalline quality and can diminish the advantage of the lattice-matched ZnO substrates. To avoid the formation of an interfacial layer, several methods such as Al_2O_3 passivation of ZnO and using N_2 as a carrier gas have been proposed for MOCVD growth. However, the quality of surface morphology has not improved to the expected standard. ***In Chapter 4,*** *a low-temperature GaN nucleation layer by metal enhanced epitaxy (MEE) was introduced, which can help to stop the interfacial interaction between InGaN and ZnO at high*

growth temperature. Besides, InGaN grown on ZnO substrate using two monolayers GaN by MEE led to a sharp interface between InGaN and ZnO and strong luminescence properties.

Recently, S. S. Pasayat et al. demonstrated fully or partially relaxed micron-sized InGaN via porosification of underlying Si doped GaN layer [78–80]. The elastic relaxation of (In,Ga)N layer beyond the critical thickness is enabled by the low stiffness of the porous GaN:Si layer. A buried n-type Si-doped GaN layer was embedded in unintentionally doped (UID) GaN or InGaN as a protection layer. The GaN:Si was porosified via electrochemical (EC) etching using oxalic acid from the sidewalls of etched mesa tiles [81,82]. This technique will be discussed in more detail in **Chapter 5.**

However, most of the InGaN re-growths on porosified GaN substrates were done by MOCVD [83–86]. Since InGaN growth by PAMBE needs lower growth temperatures than that by MOCVD, In incorporation can be increased by growing InGaN on porous GaN by PAMBE. Before I started my PhD, there was no study on InGaN re-growth on porous GaN by PAMBE. Very recently, C. Wurm et. al demonstrated relaxed InGaN by growing on porosified GaN-on-sapphire by PAMBE [87]. In collaboration with him and the team at UCSB, I studied PAMBE growth of InGaN on porosified GaN-on-Si template, which is discussed in **Chapter 5.**

1.5 Molecular Beam Epitaxy

Molecular beam epitaxy and metal-organic chemical vapor deposition (MOCVD) are two common growth techniques used for epitaxial growth of III-nitrides. Both of these techniques can control the layer thickness with a resolution of monolayers.

MOCVD can give higher growth rates than that of MBE, and the maintenance of MOCVD equipment is relatively cheaper than that for MBE. These make MOCVD a preferred method in commercial applications and industry. Nonetheless, MBE offers a unique advantage over

MOCVD, especially for academic research purposes. The ultrahigh vacuum (UHV) environment (pressure of 10^{-7} Torr) of MBE leads to less unintentional incorporation of impurities such as H, C, and O. Additionally, the growth temperature is comparably lower in MBE compared with that in MOCVD. This makes MBE advantageous for growth of high In-content (In,Ga)N films since the lower growth temperature helps to incorporate more indium in the film.

An MBE system usually consists of three connected stainless-steel vacuum chambers capable of reaching ultrahigh vacuum (UHV), including load/lock, buffer, and growth chambers. The load/lock chamber is used to load the sample and after the pressure reaches a desired low value, the sample will be transferred to the buffer chamber, where it will be baked to remove residual water. After baking, the wafer is then transferred to the growth chamber, where the epitaxial growth occurs. The growth chamber is typically held at the lowest pressure using a combination of multiple pumps including a turbo pump, a cryo-pump, and an ion pump. Additionally, to further help with reducing the pressure, the growth chamber is equipped with a cryo-panel around its walls, which is filled with liquid nitrogen to absorb impurities.

In a nitride MBE, Knudsen effusion cells are typically used for Ga, In, Al, Mg, and Si sources. This atomic flux of solid sources is simply controlled thermally and can be measured in-situ using an ion gauge. Mechanical shutters in front of each effusion cell allow for precise control of incorporating desired elements in the film, resulting in sharp interfaces and doping profiles.

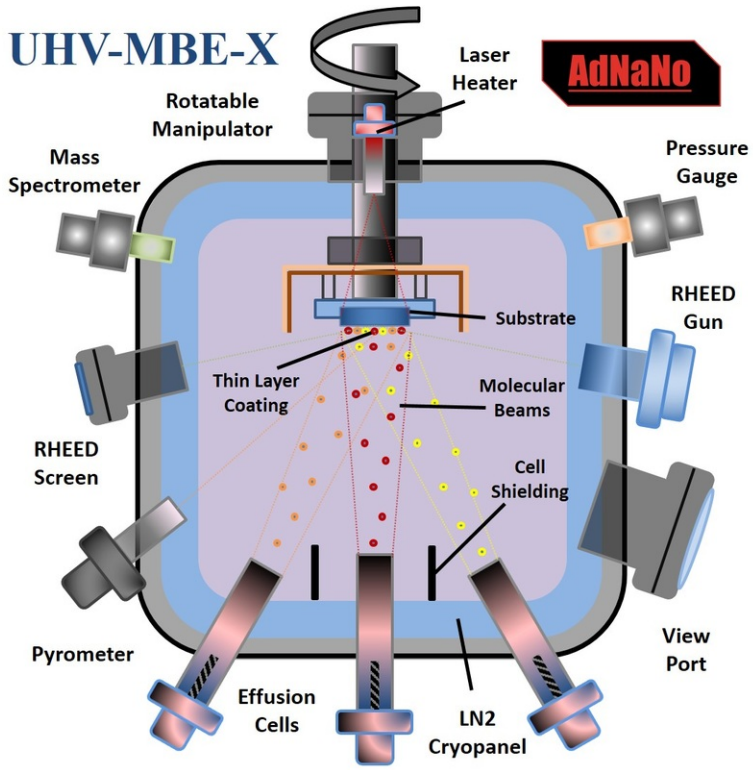

Figure 1.14 Schematic of a PAMBE machine, showing Knudsen effusion cells, RGA and RHEED gun and rf plasma source for providing active N ***[Courtesy: Adnanotek]***

The nitrogen anion must be supplied from a gas source for the growth of III-nitrides. Two different sources are being used to supply active nitrogen in an MBE; radio frequency (RF) plasma and ammonia (NH_3). The former, RF-MBE, utilizes molecular nitrogen N_2 as the anion source, and a radio frequency plasma is required to break the strong molecular nitrogen dimer bond. This results in a variety of metastable and excited atomic states into the plasma afterglow. These excited atomic nitrogen species then can then bond with the metal ions. The latter, ammonia MBE (NH_3-MBE), relies upon the thermal decomposition of an ammonia molecule on the growing III-nitride surface to supply nitrogen to the crystal, requiring a higher growth temperature than the PAMBE. **Figure 1.14** illustrates a schematic of PAMBE, showing Knudsen effusion cells, RF plasma source and the substrate.

In contrast to the other growth methods e.g., liquid phase epitaxy or MOCVD where crystal growth happens under quasi-equilibrium condition, growth in an MBE system occurs in a non-equilibrium process. This is usually a surface kinetic limited process. Due to the vacuum environment, the mean free path of a particle from the cells in the chamber is an order of magnitude larger than the distance between the crucibles and the sample holder. This leads to atoms or molecules not interacting with each other in the chamber until they reach the sample surface. This is the essence of MBE growth, leading to the growth of metastable materials, which cannot be synthesized by other methods due to thermodynamic stability.

The crystal growth on the substrate surface happens through a few elementary steps. In the most common cases, the steps are: i) trapping of arriving atoms on physisorption states on the sample surface known as adsorption, ii) diffusion of adatoms on the sample surface, iii) desorption of adatoms from the physisorption states into the vacuum system, and iv) chemical bonding between adatoms leading to crystal lattice sites (chemibsorption).

1.6 Synopsis of the Thesis

The objective of this dissertation is studying the growth and characterization of relaxed (In,Ga)N using PAMBE. In the process of developing relaxed InGaN films on GaN template, self-assembled superlattice (SASL) structures consisting of $In_xGa_{1-x}N/In_yGa_{1-y}N$ were observed. This accidental discovery motivated me to further investigate the impact of growth conditions and polarity on the spontaneous formation of such superlattice structure. These results are discussed in **Chapter 2** and **Chapter 3.** I then studied growth of InGaN on ZnO to (i) examine the impact of strain on the formation of SASL structures and (ii) develop relaxed $In_{0.2}Ga_{0.8}N$ since ZnO is in-plane lattice matched InGaN film with 20% In content. For this purpose, first, a technology to achieve a smooth surface with the desired surface morphology for both Zn-face and O-face ZnO

was developed. Additionally, I developed a low temperature growth technique for growth of GaN and InN to suppress formation of interfacial interlayer. I showed that low temperature GaN interlayer helped to improve the structural quality of InGaN films grown on ZnO, The results of this part of my project are discussed in **Chapter 4**. The density of threading dislocations remained relatively high in InGaN films grown on ZnO, which is not desired for fabrication of electronic and optoelectronic devices. Therefore, as an alternative, I investigated growth of relaxed InGaN on porousified GaN, which is presented in **Chapter 5**. As a side project, I also looked into selective area growth of nanowires on N-polar GaN template, which can be used as an alternative method for growth of high In-content InGaN as well as high Al-content AlGaN films on GaN templates. This work is discussed in **chapter 6.**

Chapter 2 Self-assembled Superlattice in Ga-polar InGaN Grown by Molecular Beam Epitaxy

2.1 Introduction

The InGaN alloy system, due to its direct bandgap, is attractive for a variety of optoelectronic applications, including laser diodes (LDs) [88–90], light-emitting diodes (LEDs) [32,91,92], solar cells [93–96], and photo-detectors [97,98]. Its direct bandgap can be tuned within a large range (0.7–3.4 eV) by changing In content in InGaN, which can cover the full solar spectrum. Increasing absorption in solar cells covering the full solar spectrum has gained immense attention in the scientific community for high efficiency photovoltaic applications [99]. Additionally, InGaN has high absorption coefficient (10^5), high thermal/chemical stability, and better radiation hardness, which make it a perfect candidate for space and terrestrial applications [99–101]. For achieving efficient absorption in solar cells from the incident light, the thickness of the active InGaN layer should be thicker than at least 300 nm with an average 10% In content. InGaN films can be grown pseudo-morphically on GaN below a critical thickness, which reduces sharply as the InN mole fraction in InGaN increases due to 11% lattice mismatch between InN and GaN. As the thickness increases beyond the critical thickness, InGaN film relaxes by formation of defects and dislocations to relieve the strain. Depending on the growth technique and growth conditions (e.g., growth temperature), the relaxation may occur through different mechanisms, such as the formation of V-defects [102–105], threading dislocations [106], pyramidal slip through the Matthews-Blakeslee mechanism [107,108], and basal slip of misfit dislocation [109,110].

2.1.1 Critical Thickness of InGaN

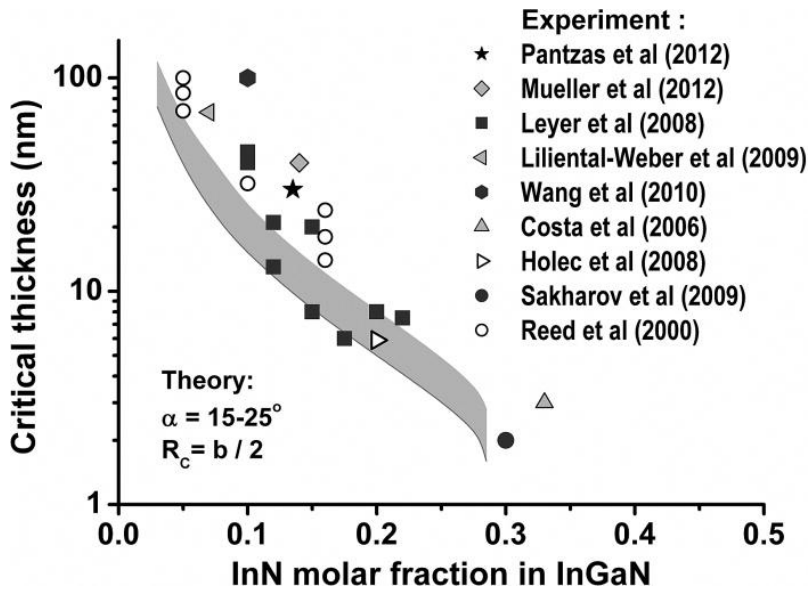

Figure 2.1 Critical thickness versus InGaN composition: gray shadow indicates theoretical predictions for Rc = b/2 and angle α varied from 15° to 25°, symbols are the experimental data from different papers ***Courtesy: A. V. Lobanova et al. [112].***

In 2007, D. Holec et al. [19,111] calculated critical thickness for InGaN/GaN system using the energy balance model with consideration of the proper hexagonal symmetry of wurtzite (InGa)N materials. Recently, A. V. Lobanova et al. [112] claimed the stress relaxation of InGaN/GaN layers occurs by V-shaped edge type dislocation half-loops (HLs) formation. They reported that 1) the half loops were first produced in the growth surface and propagated to the InGaN/GaN interface confirmed by transmission electron microscopy (TEM), ii) they result in stress relaxation confirmed by Xray diffraction reciprocal space mapping (XRD-RSM). They also explained the stress relaxation by formation of misfit dislocation (MD) in the interface similar to D. Holec et al. [19,111]. This mechanism can result in non-zero resolved normal stress to give the climb of the HLs in the m-plane of the wurtzite crystal. The climb needs consumption of point

defects that can propagate from the growth surface and the stress relaxation is expected to be intensified by InGaN low growth temperature. **Figure 2.1** shows theoretical prediction by A. V. Lobanova et al. [112] of critical thickness versus InGaN composition with experimental results by different research groups. These models [19,111,112] considered that misfit dislocation generates when the force because of misfit stress is equal to the dislocation line tension. This is called force balance model. However, Fischer et al. [113] suggested the Peierl's force should be added since

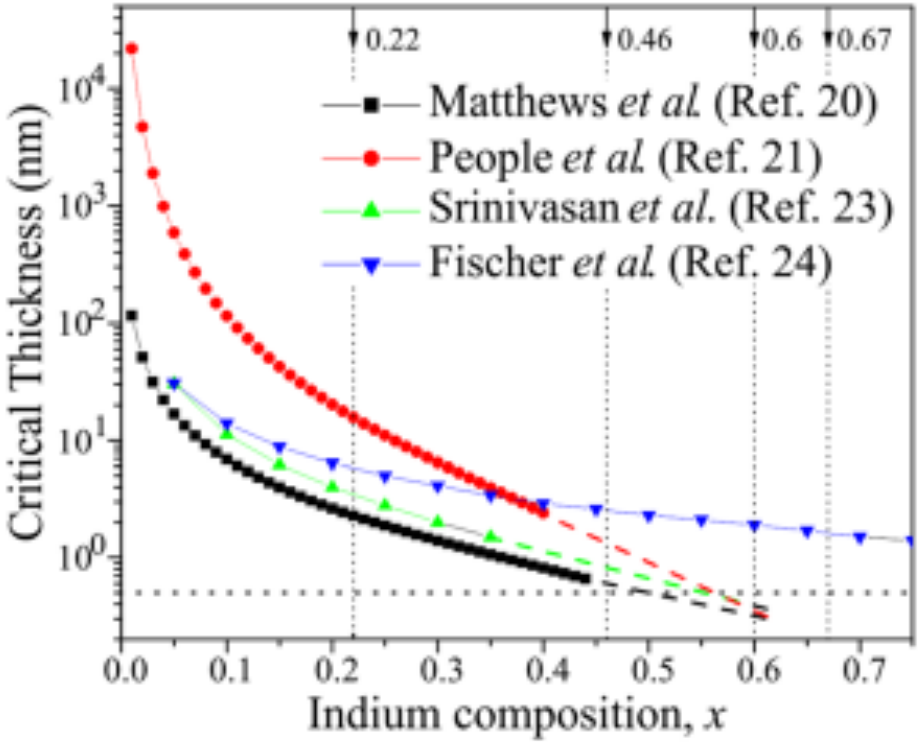

Figure 2.2 Critical thickness vs. indium content x for the In_xGa_{1-x}/GaN system using various models. The critical thickness of one lattice period c (horizontal dotted line) happens at x~0.55 ***Courtesy: Fischer et al. [113]***

the growth temperature and threading dislocation density is low for InGaN growth with high In content.

Figure 2.2 compares critical thickness with different In content for InGaN/GaN system using various models by different research groups. Fischer et al. [113] observation is also consistent with the experimental values of critical thickness for dislocation generation for epitaxy of InGaN on GaN (0001). They took into account the bulk material parameter and reasoned that,

due to the large lattice mismatch, the material is unstable until a sufficient number of atoms are available for the material to acquire its own identity, where it crystalizes with its own lattice parameter and misfit dislocation appear spontaneously. This can happen when the critical thickness for plastic relaxation is of the order of a few monolayers, with a periodic network of misfit dislocations. For such thin films, consideration of dislocation glide on the crystal plane is not necessary. The subsequent growth after relaxation then happened under relaxed conditions, leading to a low defect density.

2.1.2 Self-assembled Superlattice Structures

The superlattice (SL) structure of III-nitrides (InGaN/GaN) can be used to tune electrical and optical properties. The SL structure can result in periodic potential in their growth direction due to their periodicity, which are different from their consisting layers. SL can be obtained naturally or from self-assembly. Self-assembled or natural SL can be formed by either phase separation or atomic ordering [114,115]. The unique properties of SL can be used in optoelectronic devices e.g, solar cells[116–119]. One approach for both increasing the efficiency of concentrator PV cells and improving the efficiency with temperature is utilizing multi-quantum wells or SL. Quantum well or SL can increase the cell absorption at photon energies below the bulk host material bandgap. Therefore, it can increase the current to a degree that is more than compensation from any associated voltage loss. It has been reported SLs based solar cells can achieve greater carrier lifetimes and better carrier absorption. SLs can be valuable in the sub-cell based multi-junction solar cells because their bandgap can be engineered to optimum values. SASL can be useful to grow lattice matched SLs to the substrate and to avoid grain formation resulting in better crystal quality as well as PV performance.

SASL structures formed by chemical ordering have been widely reported in ternary and quaternary conventional III-V semiconductors [115,120], and have been also observed in AlGaN and InGaN [121–123]. Northrup et al [124,125] proposed that chemical ordering observed in InGaN alloys is because In atoms preferably incorporate at step edges ($(10\bar{1}1)$ micro facets) during growth on Ga-polar or N-polar surfaces. While most of the reported SASL structures are formed by chemical ordering [122,126], there have been only a few reports on the formation of SASL structure by phase separation [114,115] on III-V alloys whose compositions lay within the miscibility gap at the growth temperature.

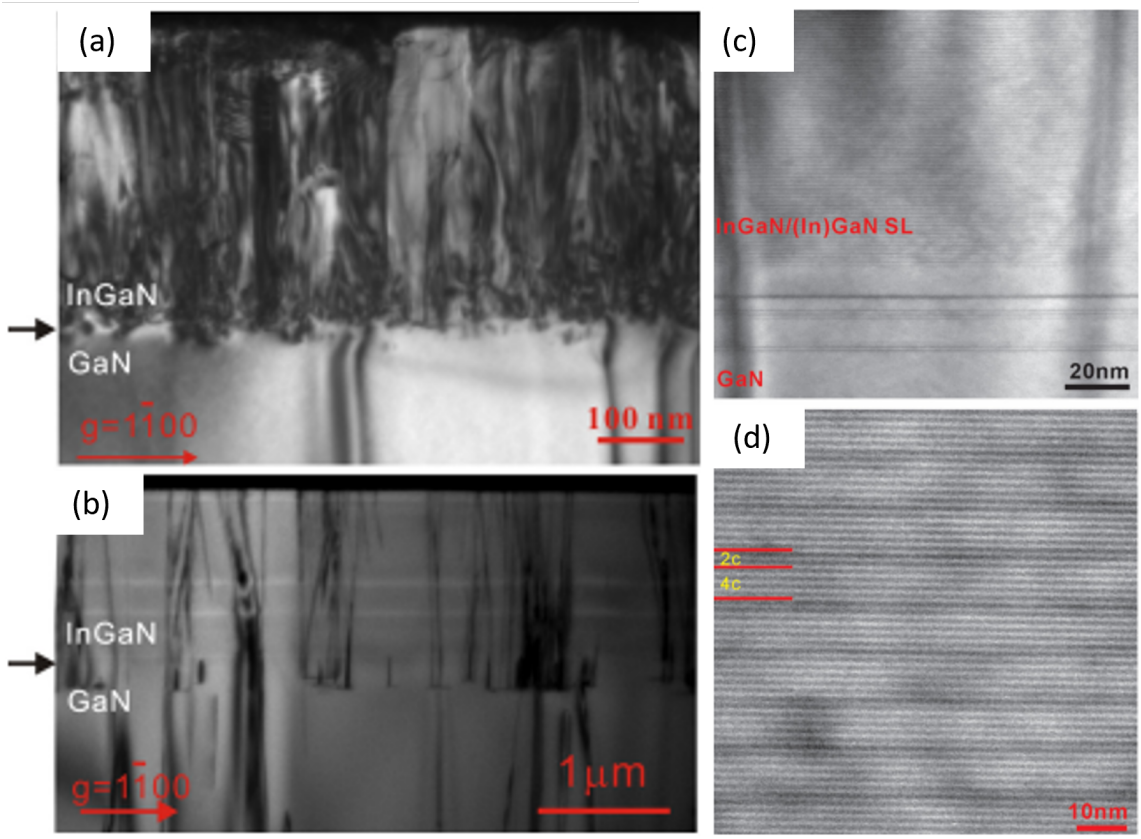

Figure 2.3 Bright-field cross-sectional TEM images of the $In_{0.1}Ga_{0.9}N$ films grown at growth rates of (a) 1.0 Å/s and (b) 3.6 Å/s, taken along the [$11\bar{2}0$] projection with g=[$1\bar{1}00$]. (c) Magnified TEM image for the $In_{0.1}Ga_{0.9}N$ film grown at 3.6 Å/s, showing the formation of periodic SL structure. (d) High resolution TEM image for the SL structure ***Courtesy: Z H Wu et al. [127]***

In 2011, it was shown [127] that using a high growth rate (~1.3 μm/hr) in PAMBE can enhance the structural quality of 350 nm-thick InGaN films with an average 10% In content compared with those grown using a conventional growth rate (~360 nm/hr). In this study, a self-assembled superlattice (SASL) structure was observed only in the faster-grown sample. **Figure 2.3 (a) and (b)** shows the low magnification cross sectional TEM images of the $In_{0.1}Ga_{0.9}N$ films grown with growth rate of 1.0 and 3.6 Å/s, respectively, taken along the the $[11\bar{2}0]$ projection with g=$[1\bar{1}00]$. The superior structural quality of the fast-grown sample was attributed to the surface roughness suppression caused by kinetic limitation and the inhibition of the Frank–Read dislocation generation mechanism within the spontaneously formed SL structure. Frank-Read dislocation cannot be generated within the SL structure since the dislocation HLs, which are formed at the surface cannot cross from one layer in SL to another. The InGaN grown with lower growth rate of ~360nm/hr had higher surface roughness, which resulted in a high local stress. The local stress points can decrease the barrier energy for formation of dislocations, leading to an increase in dislocation density. **Figure 2.3 (c)** shows the magnified TEM images around InGaN/GaN interface region of the film grown with 3.6 Å/s**.** A self-assembled superlattice structure with a 3.2 nm period was formed in the entire InGaN film independent of the position and location of threading dislocations. However, no SASL was observed in the films grown with lower growth rate (1 Å/s). **Figure 2.3 (d)** shows a high-resolution TEM image for a typical ordered region with sharp and abrupt interface between InGaN barrier and well layers. The SASL structure observed in this work was composed of 2 monolayers and 4 monolayers of InGaN films with different In contents. However, the In content in each layer was not determined.

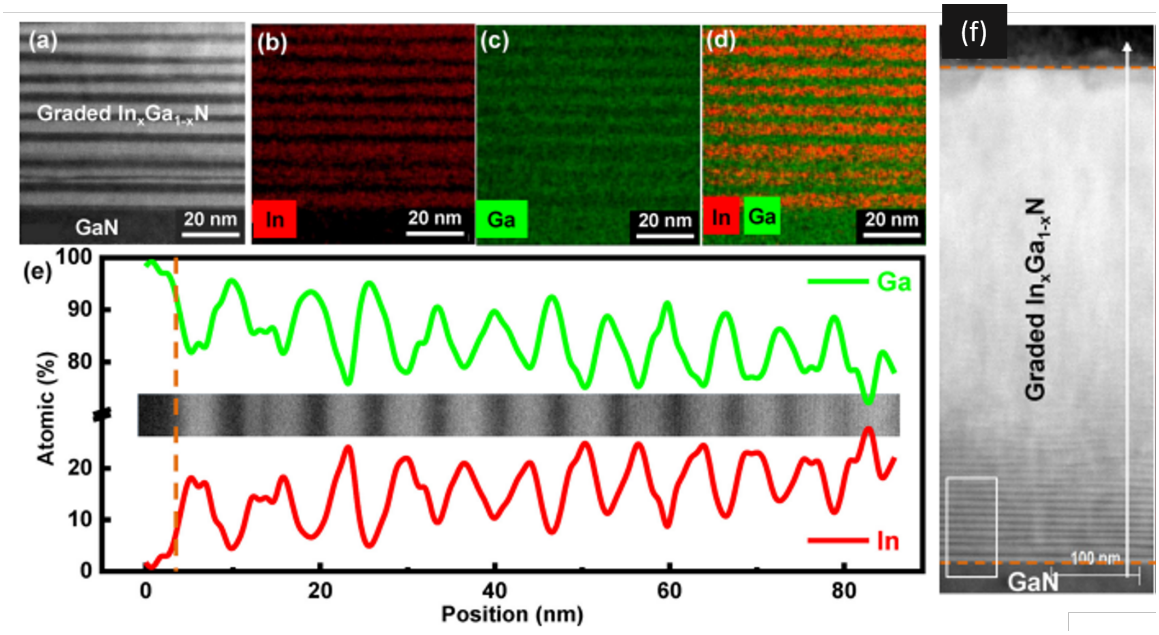

Figure 2.4 (a) HAADF-STEM image of graded MQW-like structures from the squared area in (f). (b)–(d) Corresponding EDS mapping of In, Ga, and In+Ga mixture. (e) EDS line scan profiles recorded from MQW-like structures. The inset shows the HAADF-STEM image of the MQWs (f) HAADF-STEM image of the graded $In_xGa_{1-x}N$ ***Courtesy: Zheng et al. [128]***

Zheng et al. [128] observed composition modulation in a graded InGaN film grown by MBE by changing growth temperature and metal fluxes. **Figure 2.4 (f)** shows periodic structure observed in initial region of the $In_xGa_{1-x}N$ film. The interfaces of the InGaN MQWs showed clear and sharp interfaces near the initial stage of the growth and became blurry with the increase in thickness. High magnification HAADF-STEM and EDS were recorded in the white square portion. **Figure 2.4 (a)** shows the high magnification HAADF-STEM image of graded MQWs and confirms the In composition modulation and periodicity. **Figure 2.4 (a)-(d)**, shows alternating In composition of InGaN, and EDS line scan shows the In incorporation in the InGaN well and barrier is about 0.18 and 0.03, respectively. Subsequently, In composition shows a gradual increase along the growth direction in both the wells and barriers.

However, the In modulation in this work was irregular, weakened as the thickness increased beyond 100 nm and eventually vanished. The reason for formation of SL structure can

be attributed to the release of strain coming from lattice mismatch between InN and GaN (~11%). Strain relaxation can be associated with the generation of dislocations, 3D growth, formation of self-assembled superlattice structures and so on.

To the best of our knowledge, there is no other report on the observation of SASL structures in InGaN films. In this work, in contrast, 700 nm-thick nominal "InGaN" film composed of a spontaneously formed superlattice (SL) structure made of 3nm-thick $In_{0.2}Ga_{0.8}N$/3nm-thick GaN layers was reported. This allowed to grow 700 nm-thick InGaN with an average InN mole fraction of ~8% with excellent structural quality. Using similar growth conditions, "InGaN" was also grown on a ZnO substrate, which is in-plane lattice-matched to $In_{0.2}Ga_{0.8}N$. The nominal "InGaN" films grown on GaN and ZnO were structurally characterized to investigate the impact of strain on the formation of self-assembled superlattice (SASL) structure. It is proposed that the vertical phase separation observed in the SASL structure is caused by high-temperature growth and intensified by strain.

2.2 Observation of Self-assembled InGaN/GaN Superlattices in Nominal "InGaN" Films on Ga-polar GaN Template

2.2.1 Experimental Details

Epitaxial Growth

All samples were grown in a Veeco GENxplor MBE system equipped with conventional Al, Ga, and In effusion cells and a radio-frequency (RF) plasma source to supply active nitrogen. The N source consisted of ultrahigh-purity (99.9995%) N_2 gas flowing at 1 SCCM through the RF-plasma source with 350 W RF power, which corresponded to a growth rate of 6 nm/min for metal-rich GaN layers. To ensure uniform temperature during the growth, 500 nm- thick Ti was deposited on the backside of the substrate via e-beam evaporation. The substrates were first solvent cleaned (acetone, methanol, and isopropanol for 4 min each) to remove organic residues from the surface, and then mounted on a Si substrate by In-bonding before being loaded in the MBE exit-entry chamber. An hour of baking was performed at 400 °C in a buffer chamber to remove any water prior to transferring the substrate to the growth chamber. During the growth, the substrate temperature was measured and monitored using a thermocouple. The growth was monitored in situ via Reflection high-energy electron diffraction (RHEED).

1 cm x 1cm Ga-polar GaN-on-sapphire templates were used. The growth was initiated with a 200 nm thick GaN in metal-rich growth regime at 730 °C using a Ga beam equivalent pressure (BEP) of 3.8×10^{-7} Torr to ensure a smooth and clean surface. The excess Ga was desorbed every 20 min by closing the Ga shutter while keeping the nitrogen shutter open for 40s [67,129] The substrate temperature was then reduced to 600 °C, and growth was interrupted for 15 min to stabilize the substrate temperature. A 700 nm-thick InGaN film was then grown on sample A in In-rich growth regime using Ga and In fluxes of 3×10^{-7} Torr and 1.7×10^{-7} Torr, respectively. It is

worth noting that several InGaN samples were first grown to optimize In and Ga fluxes to achieve smooth surface morphology prior to the growth of samples discussed here.

Structural Characterization

A Bruker NanoMan atomic force microscope (AFM) was employed to characterize the surface morphology of the samples. High-resolution x-ray diffraction (HRXRD) ω-2θ scans and (ω-2θ)-ω reciprocal space maps (RSM) were recorded on a triple-axis Philips X'pertPro Panalytical Pixel 3D materials research diffractometer. Cross-sectional specimens for transmission electron microscopy (TEM) study were prepared by in-situ focused ion beam (FIB) lift-out methods using a Thermo-Fisher G4 650 Xe Plasma-FIB (P-FIB). Utilizing a Xe plasma ion source instead of a regular Ga source prevents redistribution of Ga atoms or change of Ga concentration in InGaN films. For final thinning, a 5 keV energy and 10pA current beam were used. Needle-like cross-sectional specimen for atom probe tomography (APT) were also made using the same P-FIB. A JEOL JEM-3100R05 electron microscope with a cold-field emission gun equipped with both a probe and an imaging corrector was used for atom-resolved imaging that was operated in scanning transmission electron microscopy (STEM) mode. Both high-angle annular dark-field (HAADF) and bright-field images were taken simultaneously.

Optical Characterization

The lateral composition uniformity of InGaN was characterized by employing a steady state and time resolved photoluminescence (PL) spectroscopy setup. The samples were excited with a diffraction-limited spot using 405 nm pulsed laser (~30 ps pulse width, 40 MHz repetition rate) at room temperature using 60X 0.95 NA dry objective ((NIKON CFI PLAN APO λ 60X / 0.95). For steady state photoluminescence (PL) the sample emission was analyzed using a high-resolution spectrometer (Princeton Instruments IsoPlane SCT 320) coupled to a highly sensitive

CCD camera (Princeton Instruments Pixis: 400). The slit-width at the spectrometer entrance was kept at 250 μm with the spectrometer integration time set to 1.0 second. The PL scans were performed by keeping the laser excitation spot at a fixed position and scanning the sample on a piezo-nano-positioner stage in ~200 nm steps. For time resolved photoluminescence (TRPL) measurement, the sample emission was collected using a highly sensitive avalanche photodiode (APD) (MPD PDM series). The output of the APD was analyzed with a timing module (PicoQuant HydraHarp 400) synchronized to the laser diode module.

2.2.2 Results and Discussions

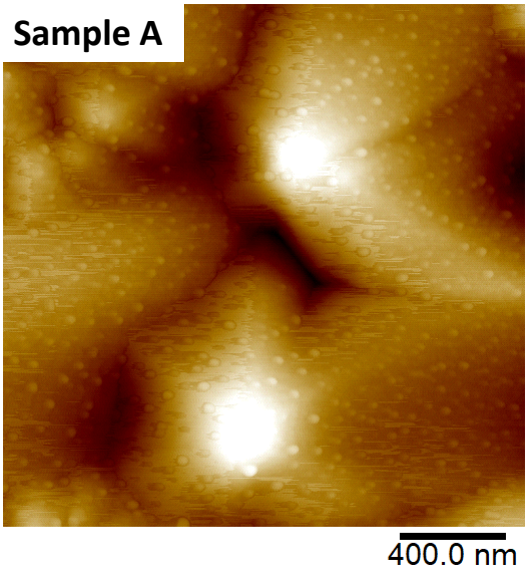

Figure 2.5 2x2 μm2 AFM image of samples A and B showing RMS roughness of ~3nm and 4.45nm, respectively.

AFM image of sample A is shown in **Figure 2.5**. A relatively smooth surface (for such thick InGaN films) with root-mean-square (RMS) roughness of ~3 nm was measured on sample A. The surface shows the density of spiral hillocks, which are associated with mixed (edge and screw) and screw threading dislocations [130].

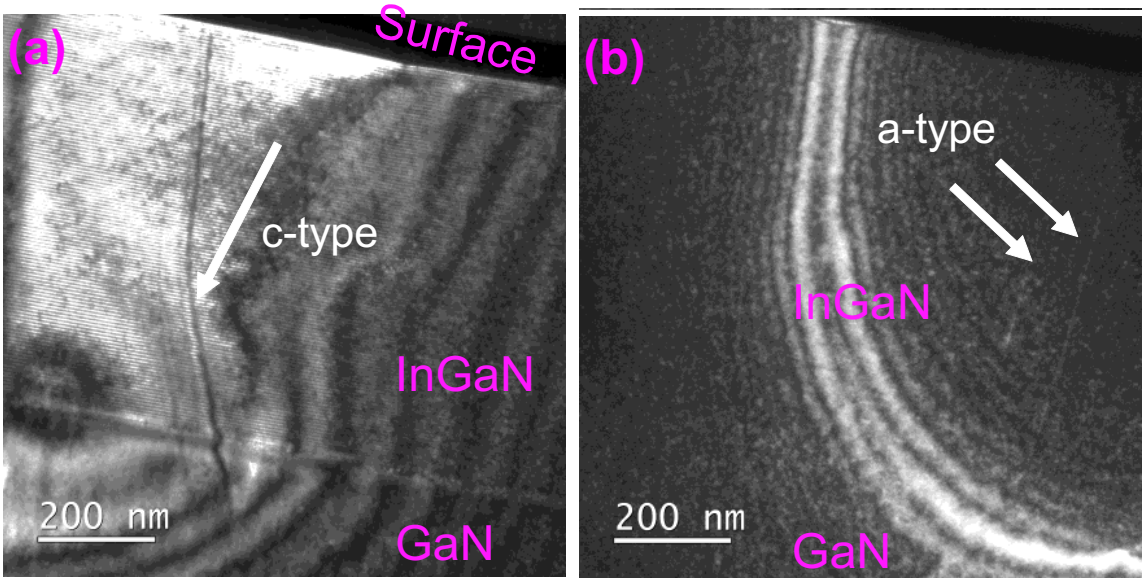

Figure 2.6 Bright field scanning transmission electron microscopy (STEM) images showing (a) edge type (a-type), (b) screw type (c-type) and mixed (c+a type) dislocation.

Figure 2.6 shows weak beam dark field (WBDF) TEM images of this sample Near $< 2\bar{1}10 >$ zone axis under two-beam condition. **Figure 2.6** (a) was recorded using $g = 01\bar{1}0$ in which only a-type dislocations are visible, while **Figure 2.6** (b) was recorded using $g = 0002$ in which only c-type or mixed with c-type component dislocations are visible. These images suggest that threading dislocations observed in the InGaN layer are propagated from the underlying GaN film and new threading or misfit dislocations did not generate in the InGaN layer.

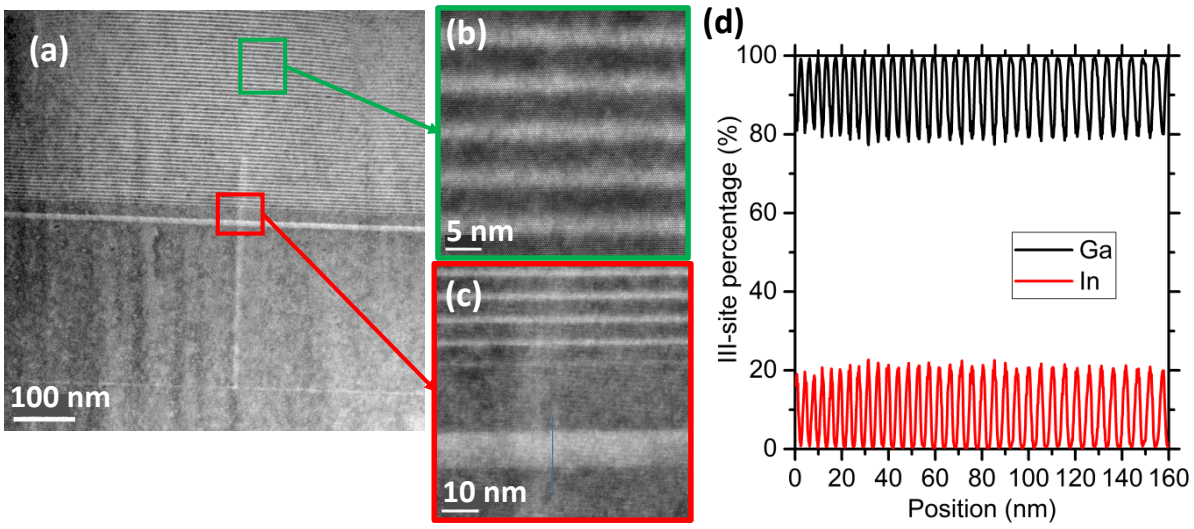

Figure 2.7 STEM-HAADF image of sample A (b) showing SASL structure (c) magnified STEM-HAADF image of sample A near the interface with GaN showing three distinctive regions of (i) InGaN film (ii) GaN layer (iii) layer with a superlattice structure. (d) In and Ga concentration profiles measured by APT showing a periodic variation of In content from 0% to 20%.

A superlattice structure on the nominal "InGaN" film grown on sample A is evident from STEM-HAADF images shown in **Figure 2.7(a)-(c)**. Three distinctive layers can be observed from the high-resolution STEM image taken from the region close to the GaN-"InGaN" interface **(Figure 2.7 (c))**: (i) a 10 nm-thick InGaN layer followed by (ii) a ~17 nm-thick GaN layer, followed by (iii) a superlattice structure for the remaining of the growth. It is important to emphasize that all shutters were kept open, and fluxes were not changed during the 2 hours growth of the "InGaN" film. No fluctuations in the Ga/In effusion cells and substrate temperatures was observed. The substrate temperature was monitored during the growth using a thermocouple. Additionally, the interface abruptness observed from STEM-HAADF images from this sample rules out temperature fluctuations as the cause for the formation of the SL structure. This means that the formation of the superlattice structure by In composition modulation is via a self-assembling process. **Figure 2.7 (a)** also reveals that the self-assembled superlattice (SASL) structure has a high structural quality with no newly generated dislocations or structural defects in

this layer. STEM-HAADF image was also recorded over a larger area, which showed a sharp interface and InGaN/GaN SL structure with high structural quality as well (**Figure 2.8**). To quantify In-content in the SL structure observed on sample A, APT was performed and In, Ga, N concentrations were recorded and are demonstrated in **Figure 2.7 (d)**. A periodic variation in In content from 0% to 20% was determined by APT.

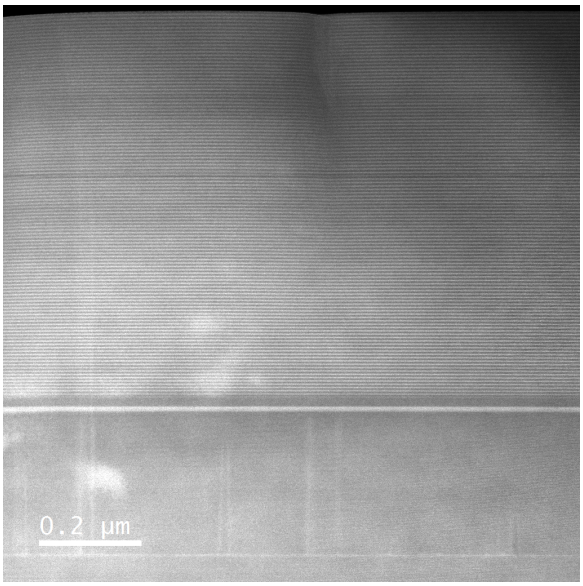

Figure 2.8 STEM-HAADF image of sample A over a large area showing similar sharp GaN and InGaN interface and a superlattice structure with high structural quality

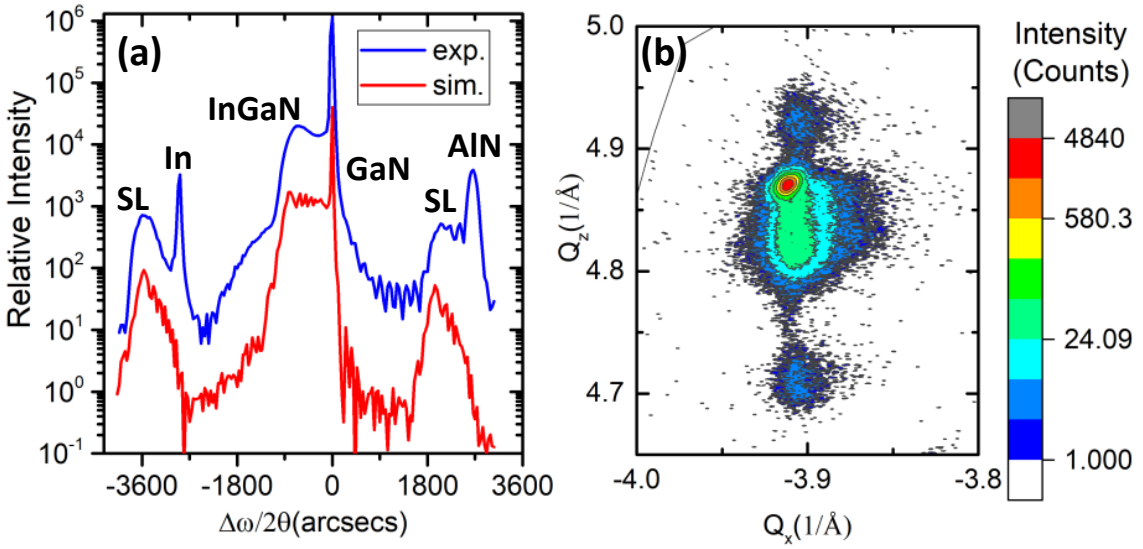

Figure 2.9 (a) XRD ω-2θ scan around GaN (0002) reflection and (b) XRD-RSM scan around GaN ($\bar{1}\bar{1}4$) reflection recorded on sample A.

XRD ω-2θ scan around GaN (0002) reflection was recorded on sample A and is shown in **Figure 2.9 (a)**. The AlN peak observed in the XRD ω-2θ scan of sample A corresponds to the AlN nucleation layer in the GaN-on-sapphire template purchased commercially. XRD ω-2θ scan of the template shows similar AlN peak. The In peak is due to excess In accumulated on the surface, which has been commonly observed on InGaN films grown in In-rich regime by PAMBE [50]. XRD ω-2θ profile of sample A suggests a graded InGaN film with the layer peak corresponding to an InGaN film with an average In content of ~8%. It is important to note that only the average In content can be determined from the XRD measurement. Therefore, a "graded composition" observed in the XRD ω-2θ scan could be due to an increase in In content, an increase in the thickness of InGaN well, or a decrease in the thickness of the GaN barrier. As an example, the red profile shown in **Figure 2.9 (a)** was simulated assuming a 3nm-thick InGaN/3nm-thick GaN superlattice with In content in the InGaN layer increasing from 2% to 18%, which matches closely

with the experimental data and is consistent with the InN mole fraction measured by APT on the top 160 nm of the SL.

XRD-RSM scan around GaN ($\bar{1}\bar{1}4$) reflection was also recorded on sample A and is shown in **Figure 2.9 (b)**. The RSM data indicates that the 700nm-thick InGaN film with an average 8% In content is only 12% relaxed. This is three times thicker than the critical thickness of $In_{0.08}Ga_{0.92}N$, so a significantly higher amount of relaxation through defect formation is expected [19,20,131]. This suggests that the formation of a self-assembled InGaN/GaN superlattice structure helps in managing the strain due to large lattice-mismatch between InGaN and GaN, and consequently leads to an enhancement in the critical thickness of InGaN film grown on GaN. Slight relaxation could be due to an increase in the height of hillocks as the InGaN thickness increases during the growth and therefore local elastic relaxation due to a 3D morphology can occur similar to what happens in nanowires [132,133]. The lateral widening of the RSM (**Figure 2.9 (b)**) can be related to different In incorporation on the facets of hillocks compared with that on the c-plane or asymmetric strain relaxation similar to that observed in nanowire [133].

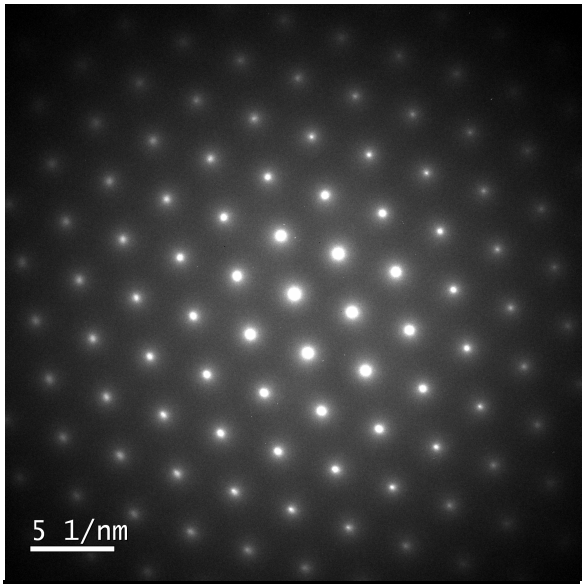

Figure 2.10 SAED pattern taken from sample A along [0001] direction

If the formation of SASL structures presented here was due to ordering, one would expect to see extra diffraction spots or strike lines in the selected area electron diffraction (SAED) pattern [134,135]. However, the SAED pattern recorded on sample A **(Figure 2.10)** has only very sharp ordered diffraction spots from the crystal, suggesting that InGaN layers in the SASL structure are not ordered. These results also indicate that the SASL structure presented here forms only in InGaN films grown at higher temperatures. For instance, the SASL was absent in the InGaN film grown at 560 °C **(Figure 2.11)**. This observation suggests that the formation of the SASL structure may be due to vertical phase separation at higher growth temperatures.

Therefore, the formation of SASL structure is a natural way for the system to manage the strain. Consequently, 700 nm-thick InGaN film with an average In content of 8% and high structural quality can be grown on GaN, which is several times larger than the critical thickness of $In_{0.08}Ga_{0.92}N$.

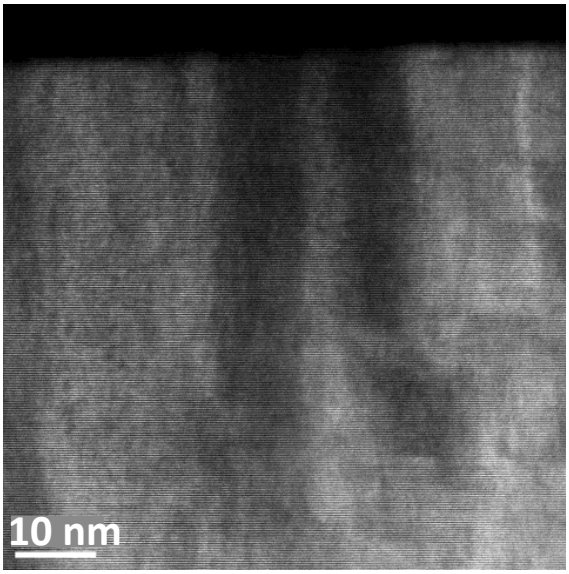

Figure 2.11 STEM-HAADF image of $In_{0.25}Ga_{0.075}N$ film grown on GaN at 560 °C.

It is important to note that what is reported in this work is different from self-assembled superlattice structures formed by chemical ordering that has been previously reported in AlGaN and InGaN films [121,123,136] and was attributed to In atoms' preference to incorporate at step edges ($(10\bar{1}1)$ micro-facets) during growth on Ga-polar or N-polar surfaces [124,125]. In this work, superlattice structures consist of $In_xGa_{1-x}N$ and $In_yGa_{1-y}N$ layers repeated periodically. One explanation is that the spontaneous formation of SL is due to spinodal decomposition of InGaN, which involves the formation of step bunches with alternating composition and thickness during the step flow growth by MBE as theoretically predicted by J. Tersoff [137] as a method for the system to lower its free energy nearly to its equilibrium value. His analysis suggested that the bunch size is controlled by a competition between thermodynamics and kinetics. Formation of SASL structure has been also reported on Ga-polar InGaN films grown on GaN by PAMBE [127]. In that study, the formation of the SASL structure was attributed to a high growth rate (~1.3 μm/hr). Moreover, SASL structures have been previously reported on Ga-polar InGaAlN quaternary alloys [120]. According to the explanation described by N. A. El-Masry et al. [120], InGaN SASL

formation is due to the formation of the excess metal melt, because of metal-rich growth condition, resulting in low In content region and the dilution of the metal melt resulting in high In content region. G. Grenet et al. [138] claimed the observed composition modulation happens as the result of an equilibrium between: (i) a decrease in an intrinsic alloy strain energy with a phase separation, (ii) the introduction of an extrinsic alloy strain energy by the mismatch between alloy phases and substrate, and (iii) a surface roughening leading to an increase in the surface energy but allowing both an intrinsic and extrinsic strain relaxation via step edges. However, further studies are required to understand the impact of In content, In/Ga fluxes, growth regime (metal-rich vs N-rich), and the miscut angle on the formation and periodicity of the SASL structures.

2.3 Impact of Strain on the Formation of Self-assembled (In,Ga)N Superlattice Structures

To study the impact of strain, ~1 μm-thick InGaN films with In content of ~20% and ~26% were grown at 600 °C and 580 °C, respectively, on ZnO.

2.3.1 Experimental Details

Commercial O-face ZnO (0001) substrates of size 10 × 10 mm^2 grown by the hydrothermal method were used. A UV ozone treatment followed by annealing of the substrate at 1050 °C was performed on ZnO substrates to obtain atomically smooth surface morphology with step edges. The details of substrate pretreatment [139] are discussed in **Chapter 4**. The growth of samples B and C was initiated with the growth of ~2 ML-thick low-temperature GaN at 440 °C by metal-enhanced epitaxy (MEE) to suppress chemical reaction between In/Ga adatoms and the ZnO substrate as well as formation of a poor-quality interfacial oxide layer. More details about this [139] is also discussed in **Chapter 4** . The substrate temperature was then increased to 600 °C (sample B) and 580 °C (sample C), and growth was interrupted for 15 min to ensure the substrate temperature was stabilized. 1μm-thick InGaN was subsequently grown using In and Ga fluxes similar to those used for sample A, which was discussed in **Section 2.2**

2.3.2 Results & Discussions

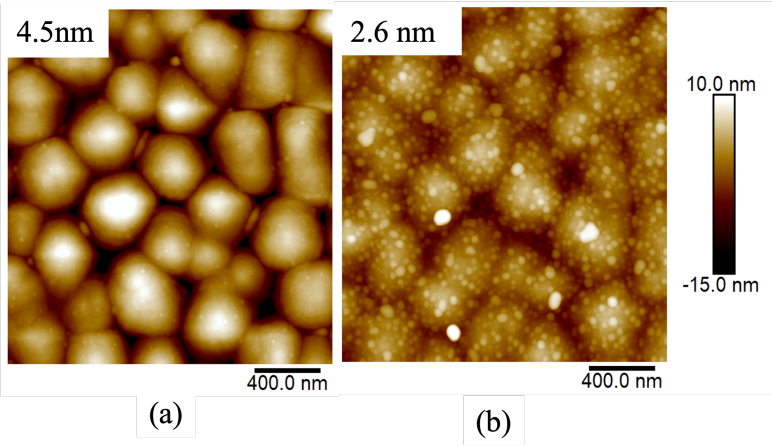

Figure 2.12 2x2 μm² AFM image of samples A and B showing RMS roughness of ~ 4.5nm and 2.6 nm, respectively.

AFM images of samples B and C are shown in **Figure 2.12**. A relatively smooth surface (for such thick ~1μm InGaN films) with root-mean-square (RMS) roughness of 4.5 and 2.6 nm were measured on sample A and B, respectively. However, the density of spiral hillocks, which are associated with mixed (edge and screw) and screw threading dislocations [130], increased significantly on InGaN film grown on ZnO, indicating an increase in the threading dislocation density (TDD). A higher TDD in both samples B and C could be due to formation of a low-quality interfacial layer due to chemical reaction between In or Ga atoms with ZnO. As mentioned earlier, the growth of sample B was initiated with the growth of ~2 ML-thick low-temperature GaN at 440 °C by MEE to suppress this chemical reaction. However, 2ML GaN may not be thick enough to fully cover the ZnO surface, leading to regions with poor quality interfacial layer and consequently a high density of threading dislocations. These will be discussed in detail in **Chapter 4.**

To study the impact of strain, the STEM-HAADF was also recorded on sample B **(Figure 2.13 (a))** and revealed a SASL structure on the nominal InGaN film grown on ZnO. However, there is significantly less compositional modulation between the layers of SASL structure formed on "InGaN" film grown on ZnO (sample B) compared with that grown on GaN (sample A described in section 2.2.2). The superlattice peaks are also visible in the HRXRD ω-2θ scan on sample B shown in **Figure 2.13 (b)**. Simulations conducted using Epitaxy and Smoothfit software revealed a good fit between the HRXRD ω-2θ profile with $In_{0.19}Ga_{0.81}N$ (3 nm)/$In_{0.23}Ga_{0.87}N$ (3 nm) superlattice structures, which is also consistent with the small compositional modulation observed in STEM image **(Figure 2.13 (a))**.

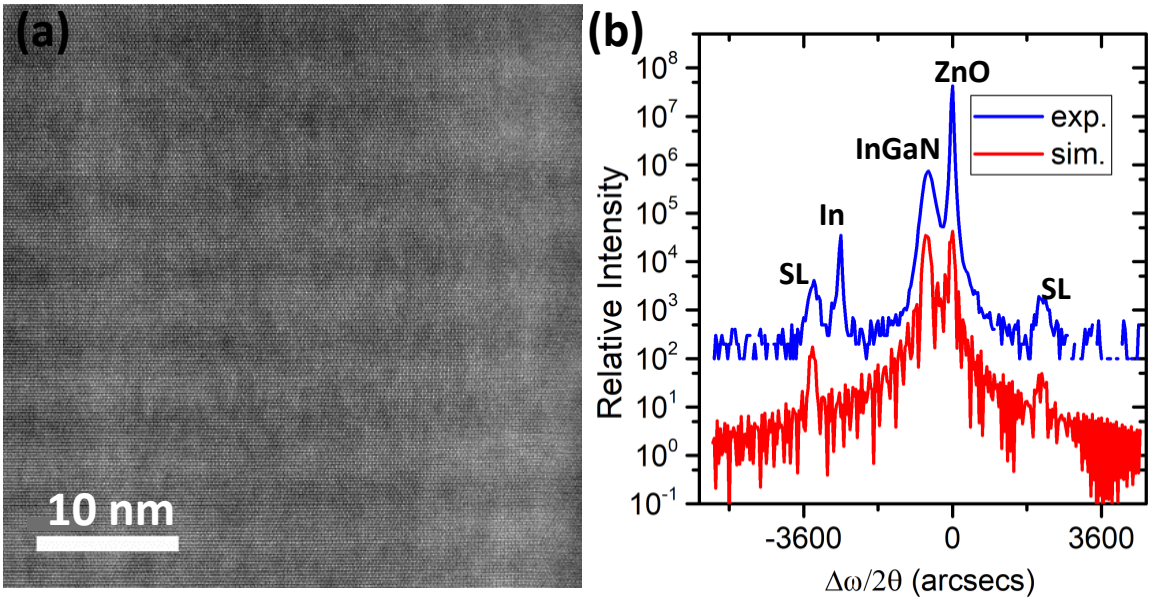

Figure 2.13 (a) STEM-HAADF image of "InGaN" film grown on ZnO (b) HRXRD ω-2θ scans of InGaN on ZnO substrate around ZnO (0002) reflection showing $In_{0.19}Ga_{0.81}N$ (3 nm)/$In_{0.23}Ga_{0.87}N$ (3 nm) superlattice (SL), respectively.

It is worth noting that although SASL structure can be observed on both sample A and B from STEM images, the In content modulation in sample A ranges from 0% to 20%, whereas there is only a small variation (19% to 23%) in the In content of SASL structure grown on ZnO (sample B and sample C described below). While there is ~2.2% lattice mismatch between $In_{0.2}Ga_{0.8}N$ and

GaN, $In_{0.2}Ga_{0.8}N$ is in-plane lattice-matched to ZnO. This indicates that the compressive strain built up in the InGaN film grown on GaN intensifies the vertical phase separation, and the formation of SASL structure is a natural way for the system to manage the strain.

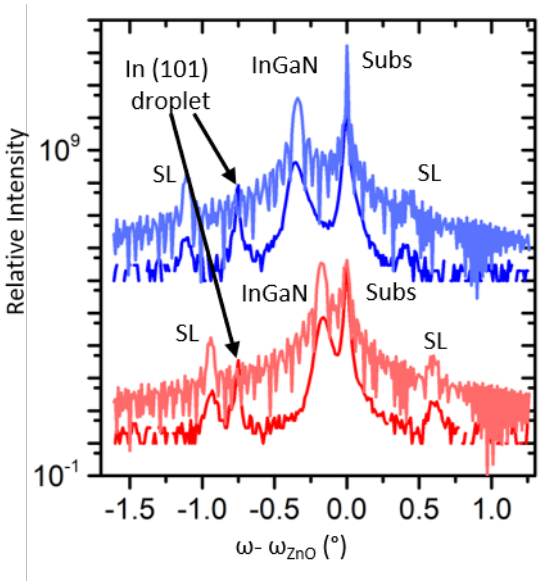

Figure 2.14: HRXRD ω-2θ scans of InGaN on ZnO substrate around ZnO (0002) for sample B, grown at 600 °C (red) and sample C, 580 °C (blue), reflection showing $In_{0.19}Ga_{0.81}N$ (3 nm)/$In_{0.23}Ga_{0.87}N$ (3 nm) and $In_{0.26}Ga_{0.84}N$ (3 nm)/$In_{0.28}Ga_{0.82}N$ (3 nm) superlattice (SL), respectively. The darker and lighter shades show experimental and simulated results, respectively.

To study the impact of temperature on formation of SASL during growth of InGaN on ZnO, HRXRD ω-2θ scans were carried out on both of the samples. The HRXRD ω-2θ scans shown in **Figure 2.14** revealed superlattice peaks on both samples B and C similar to $In_{0.18}Ga_{0.82}N$/GaN SASL observed on GaN template. As mentioned earlier, Ga, In, and N shutters were kept open during the growth of both InGaN film, and growth of a superlattice structure was not intentional. Simulations conducted using Epitaxy and Smoothfit software revealed a good fit between the HRXRD ω-2θ scans on samples B and sample C with $In_{0.19}Ga_{0.81}N$ (3 nm)/$In_{0.23}Ga_{0.87}N$ (3 nm) and $In_{0.26}Ga_{0.84}N$(3 nm)/$In_{0.28}Ga_{0.82}N$ (3 nm) superlattice structures, respectively. This confirmed In modulation decreased from 4% to 2% by decreasing the growth temperature, and high temperature is necessary for spinodal decomposition, which is important in the formation of SASL

to allow adatom diffusion. Lower In modulation in InGaN films grown on ZnO indicates that, in addition to the growth conditions (e.g., temperature), the strain may play a role in determining the periodicity of the superlattice structures.

Noteworthy, S. Yu Karpov et al. [140] claimed for $In_xGa_{1-x}N$ layers grown beyond the critical thickness, the relaxation begins but some residual strain in the epitaxial layer starts to be built in. This residual strain can be the origin of elevated stability of ternary compounds observed experimentally since the elastic strain is predicted to lower the critical temperature from 1135°C down to 735°C. Therefore, it is expected to observe spinodal decomposition, which can take place by suppressing phase separation. Compositional modulation in ternary alloys can occur when a high surface diffusion rate initiates the surface separation during growth [141–144]. Compositional modulation depends on growth temperature, growth rate, and surface roughness. Besides, they reported that high lattice mismatch could result in a rougher surface, which is enough to ensure partial elastic relaxation and to allow spinodal-like decomposition at the grown surface.

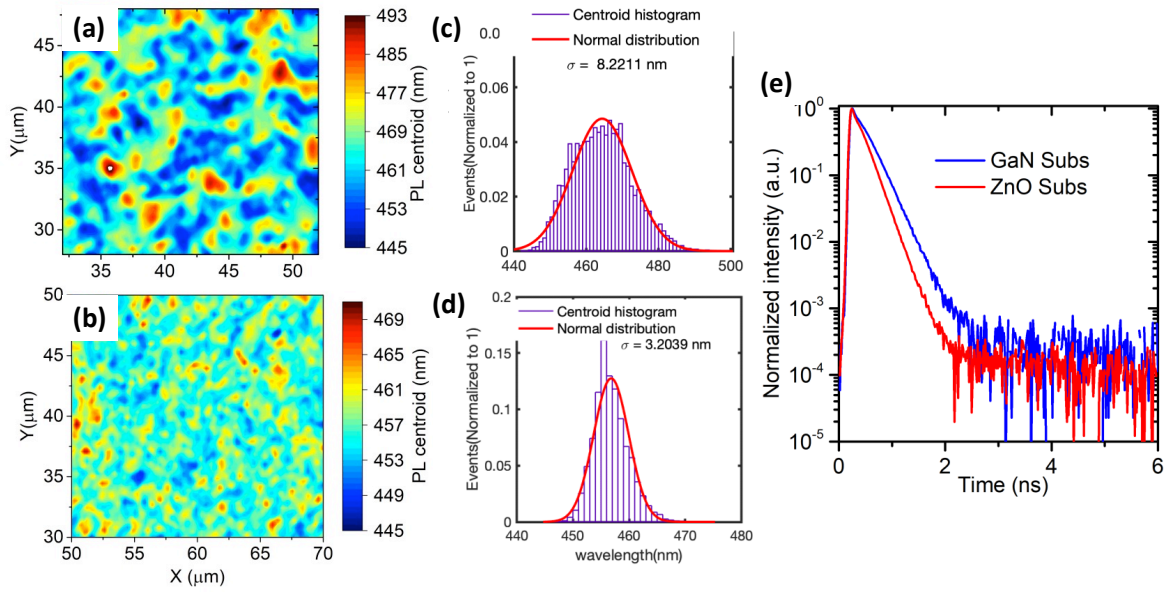

Figure 2.15 Photoluminescence (PL) intensity map of SASL structures grown on (a) GaN and (b) ZnO and Histogram plot of PL mapping of SASL structures grown on (c) GaN and (d) ZnO. (e) Time-resolved PL of the SASL structures grown on GaN and ZnO.

20x20 μm^2 PL maps were measured on the SASL structures grown on GaN (sample A) and ZnO (sample B) and are presented in **Figure 2.15 (a) and (b)** along with the histograms of PL centroid **(Figure 2.15 (c) and (d))**. The histogram shows the normalized number of events (pixels) at a specific wavelength. The scale on PL maps is varied to illustrate the lateral wavelength variation in each sample more clearly. Both samples are relatively uniform. The centroid histogram can be fitted with a unimodal bell-shaped distribution with the center wavelength and variance of 460 nm and 8.2 nm for sample A and 456 nm and 3.2 nm for sample B. A slight lateral variation in the peak wavelength is due to lateral fluctuations in the InGaN composition [145–149]. Additionally, as shown by Takeguchi et. al. [147] in InGaN/GaN quantum wells, the band structure of the quantum well changes not only by quantum dot effects but also by the additional modulation of the internal polarization electric field. However, the polarization field in $In_{0.19}Ga_{0.81}N/In_{0.23}Ga_{0.77}N$ quantum wells grown on ZnO is expected to be significantly smaller than the polarization field in $In_{0.2}Ga_{0.8}N$/GaN quantum wells grown coherently strained to GaN.

Therefore, the wavelength broadening due to fluctuations in the internal electric field is expected to be significantly less in quantum wells grown on ZnO. **Figure 2.15 (e)** shows time-resolved PL measurements on SASL grown on GaN and on ZnO. A slightly larger carrier lifetime was measured on SASL grown on GaN, which is most probably due to a lower density of threading dislocations on this sample as revealed by AFM image [150] (**Figure 2.12**). Besides, the internal polarization electric field in SL resulting from QW width and In incorporation can affect the carrier lifetime [151,152]. Polarization field in $In_{0.2}Ga_{0.8}N$/GaN SL strained to GaN is higher than that in $In_{0.19}Ga_{0.81}N/In_{0.23}Ga_{0.77}N$ SL grown on ZnO, which can also lead to a higher carrier lifetime in sample A.

2.4 Summary

In summary, spontaneous formation of $In_{0.2}Ga_{0.8}N$/GaN superlattice structure on nominal InGaN film grown on GaN by PAMBE observed. We studied the impact of strain on the superlattice formation by growing InGaN on ZnO using similar growth conditions. The self-assembled superlattice grown on ZnO showed less modulation in the In incorporation. Additionally, InGaN films grown at lower temperatures (e.g., 560 °C) did not show any superlattice structure. These observations suggest that the self-assembled superlattice structure may be due to vertical phase separation of InGaN caused by high temperature growth and intensified by strain.

Chapter 3 Self-assembled Superlattice Structure in N-polar InGaN by Plasma-assisted Molecular Beam Epitaxy

3.1 Introduction

Due to the lack of inversion symmetry in wurtzite III-nitride materials, III-nitrides can be of Ga-polar (0001) and N-polar GaN ($000\bar{1}$). The polarization direction in N-polar nitrides is opposite of that in Ga-polar nitrides, which leads to an opposite polarization-induced electric field in N-polar heterostructures compared with that in Ga-polar heterostructures. Additionally, N-polar surface is more chemically reactive, and growth dynamics on this plane are very different from that on Ga-polar. Today, commercially available GaN-based devices including light-emitting diodes (LEDs) [32,35,153], laser diodes (LDs) [89,90], and high-electron-mobility-transistors (HEMTs) [154–156] are predominantly fabricated on Ga-polar GaN. However, as will be discussed in the next two subsections N-polarity can be potentially advantageous for some electronic and optoelectronic devices.

3.1.1 Advantage of N-polarity for Electronics Applications

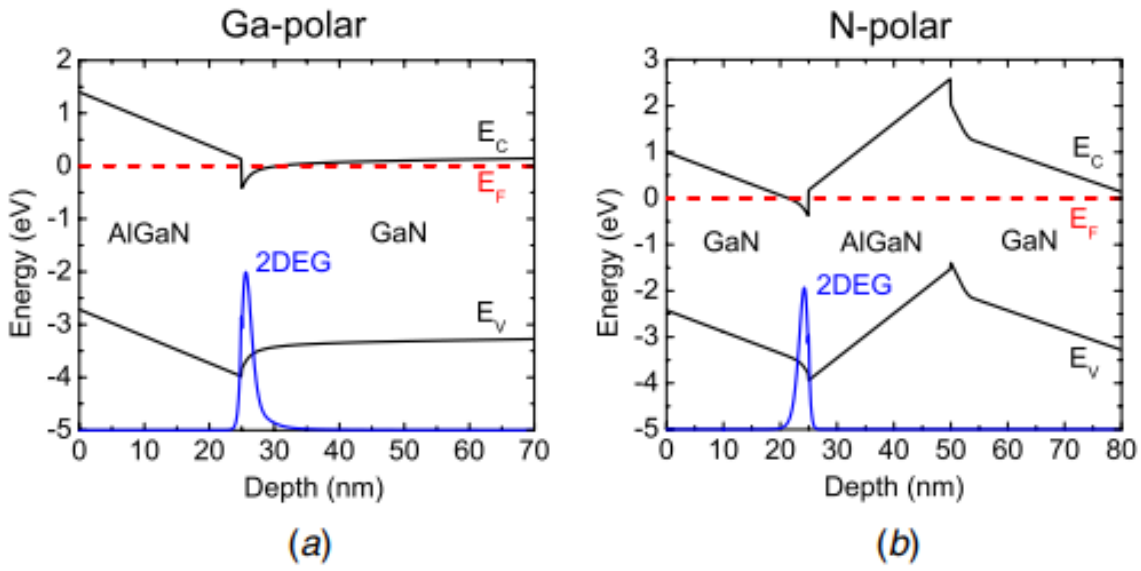

Figure 3.1 Equilibrium band diagram of generic Ga-polar (0001) (left) and N-polar $(000\bar{1})$ *(right) heterostructures* ***Courtesy: M H Wong et al. [157]***

The opposite polarization-induced field in N-polar heterostructures leads to a different band diagram [157]. Therefore, for example, in a N-polar HEMT structure, a 2DEG is formed above instead of below the wide-bandgap barrier material (**Figure 3.1**). N-polar GaN HEMTs can give scaling advantages over the existing Ga-polar GaN HEMTs for several reasons. First, due to opposite polarization direction and 2DEG above barrier layer e.g., AlGaN in AlGaN(barrier)/GaN(channel) HEMT, the barrier can be used as in-situ back barrier for electron confinement. The strong in-situ back barrier helps to reduce short-channel effects. The in-situ back barrier can also help to improve electron confinement in N-polar HEMTs. These led to an improvement in off-state pinch-off characteristics and reduced on-state output conductance.

The N-polar HEMTs can have contact through the channel layer with lower bandgap instead of barrier layer with a wider bandgap [157,158]. Moreover, this can decrease the barrier height for electrons rather than barrier layer with higher bandgap. By solving these issues for Ga-polar HEMTs, N-polar HEMTs can solve the high contact resistance issue in Ga-polar HEMTs.

Finally, N-polar GaN HEMTs can improve the scalability of GaN HEMTs by decreasing the gate length and maintaining a high aspect ratio, which requires decreasing gate-channel separation. Besides, N-polar HEMT's 2DEG forms between the gate metal and GaN/(Al,Ga)N heterointerface, and the displacement of the 2DEG in N-polar HEMT decreases the effective gate-channel distance. This showed a completely opposite effect than that of Ga-polar HEMTs. Recent results from the University of California Santa Barbara showed that N-polar GaN HEMTs can provide remarkably superior performance in W-band [159–162].

3.1.2 Advantage of N-polar for Optoelectronics Applications

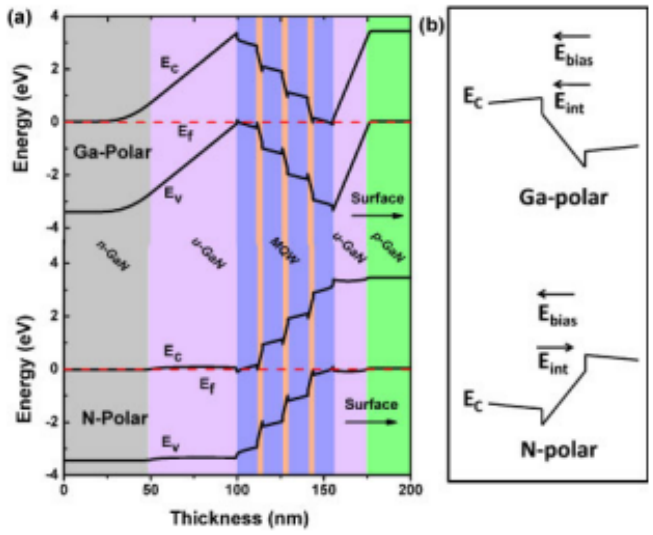

Figure 3.2 (a) Computer energy band diagrams of a typical MQW device with both polarities (b) state of the intrinsic (including spontaneous and piezoelectric polarization) and bias induced electric fields in the QWs of a typical device in both polarities ***Courtesy: F Akyol et al. [163]***

N-polar InGaN has several advantages over its Ga-polar counterparts due to opposite polarity that makes it attractive for high In composition InGaN growth. Along with electronic applications, optoelectronic applications could also potentially benefit from using the N-polar InGaN due to high crystal quality and optical properties [163]. As a reminder, the direction of spontaneous and piezoelectric polarization of N-polar is opposite from those of Ga-polar, which

can be beneficial for LED applications. **Figure 3.2 (a)** shows energy band diagrams of N- and Ga-polar typical InGaN/GaN MQW heterostructures in equilibrium using a self-consistent Schrodinger–Poisson solver that takes into account spontaneous and piezoelectric polarization [163]. In the Ga-polar LED structures, the total polarization field is in reverse direction with respect to the p–n junction depletion field, thus resulting into a wider depletion region. This wider depletion region leads to higher turn on voltage. However, the polarization fields in N-polar LED structures are in the same direction as the p–n junction depletion field, which leads to a reduction in the depletion region width and potentially a lower turn-on voltage compared with Ga-polar structures. Additionally, in a N-polar LED structure, applying a forward bias voltage helps in flattening bands in quantum wells (QWs) due to the reverse direction of polarization, therefore reducing the Stark effect **(Figure 3.2 (b))**. This is in contrast with Ga-polar LED structures, in which applying a forward bias voltage increases the field in the QWs leads to less overlap of electron and hole wave-functions in the quantum wells. The opposite direction of polarization in N-polar InGaN, therefore, is more advantageous for LED application than in the case of Ga-polar InGaN. Moreover**, as illustrated in Figure 3.2 (a) and (b)**, the injected carriers have to overcome a potential barrier for Ga-polar structure, which reduces carrier injection efficiency and results in higher turn-on voltages. In contrast, the reverse polarization direction in N-polar helps to remove the potential barrier against the carrier injection efficiency, which is advantageous for achieving a lower turn-on voltage. It is worth noting that the total polarization field increases in InGaN with increase in In content. Therefore, these effects are more prominent in applications with high In content InGaN such as long-wavelength (red/green) LEDs and LDs.

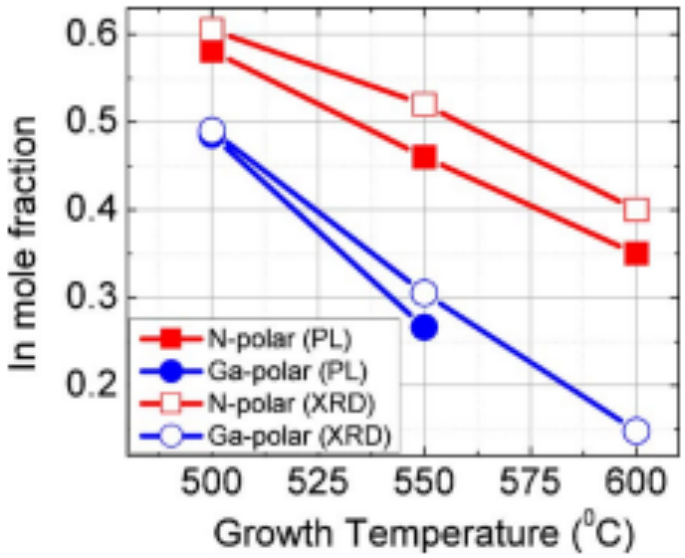

Figure 3.3 Indium mole fraction as a function of growth temperature for both Ga-polar and N-polar InGaN films as extracted from room temperature PL peaks and XRD scans ***Courtesy: D N Nath et al. [169].***

Epitaxial growths of N-polar InGaN by MOCVD [164–168] and PAMBE [169–172] have been explored extensively to use these advantages of N-polar InGaN mentioned above. In recent years, several works on N-polar InN demonstrated optimum temperature for N-polar InN is ~100 °C higher than that of Ga-polar InN because of higher stability of InN on the N-polar surface [169]. **Figure 3.3** shows a comparison between In composition in Ga-polar vs N-polar $In_xGa_{1-x}N$ films grown at different temperatures measured using room temperature PL and XRD scans with different growth temperatures. **Figure 3.3** shows In incorporation reduces with an increase in the growth temperature due to higher decomposition rate of InN at a higher temperature irrespective of polarity. Therefore, high In content N-polar InGaN can be grown at higher temperature than their Ga-polar counterparts. Due to high temperature growth and the difference in surface energies, N-polar InGaN layers can inhibit formation of structural defects and dislocations [173]. Due to

these reduction in defects and dislocations, N-polar (In,Ga)N showed drastic improvement in optical properties and photoluminescence.

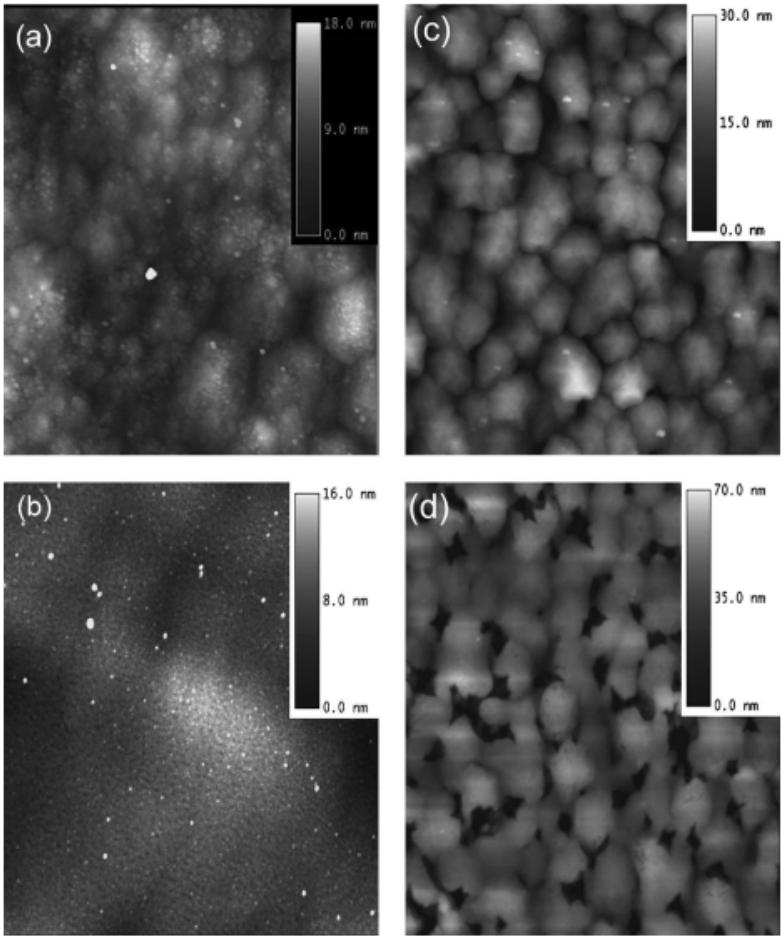

Figure 3.4AFM scans of (5x5μm²) $In_xGa_{1-x}N$ filmsl (a) Ga polar, 550 ºC, rms ~2.8 nm; (b) Ga polar, 600ºC, rms ~2.3 nm (c) N polar, 550ºC, rms 5.7nm and (d) N polar 600 ºC ~14.1nm ***Courtesy: D N Nath et al. [169]***

Figure 3.4 shows the (5μmx5μm) AFM scans for both Ga-polar **(a-b)** and N-polar **(c-d)** InGaN films grown at 550 ℃ and 600 ℃ [169]. From the AFM images, N-polar InGaN has relatively higher rms roughness than that of Ga-polar samples. Especially, the N-polar InGaN grown at 600 ℃ showed extremely high rms roughness of ~15nm. Formation of SASL structure has been also reported on Ga-polar InGaN films grown on GaN by PAMBE [127,128,174,175]. Moreover, SASL structures have been previously reported on Ga-polar InGaAlN quaternary alloys

[120]. However, to the best of our knowledge, there is no report on observation of SASL phenomenon in N-polar nominal InGaN films.

Here, it is reported on the growth of 350 nm-thick N-polar InGaN film with an average InN mole fraction of ~13% with high structural quality and sub-nm surface roughness. For the first time, spontaneous formation of superlattice structures on N-polar nominal "InGaN" films was observed. It is shown that the composition of the superlattice structure changes by varying the growth temperature. The formation of the superlattice structure can lead to a larger critical thickness of InGaN.

3.2 Observation of Self-Assembled InGaN/GaN Superlattice Structure Grown on N-polar GaN Template by Plasma-assisted Molecular Beam Epitaxy

3.2.1 Experimental Details

The samples presented here were grown in a Veeco GenXplor MBE system, equipped with conventional thermal effusion cells for Ga, and In sources and a Veeco Unibulb radio frequency (rf) plasma source. The N source consisted of ultrahigh-purity (99.9999%) N_2 gas flowing at 1 sccm through the RF-plasma source with 350 W RF power, corresponding to a growth rate of 350 nm/h for metal-rich GaN layers. All samples were grown on on-axis N-polar GaN substrates. 500nm-thick Ti was evaporated on the backside of the GaN substrates for uniform thermal coupling with the heater, which were then mounted on silicon wafers by In-bonding before being loaded in the MBE exit-entry chamber. The growth was initiated with five cycles of 10 s of Ga deposition and desorption to further clean the surface. A 200 nm thick GaN buffer layer was first grown at 730 ^{o}C using a Ga flux of 5.2×10^{-7} Torr to ensure a metal-rich growth regime. More details on epitaxial growth of GaN on N-polar GaN by PAMBE can be found in [176–178]. The substrate temperature was then reduced to a lower temperature and allowed to stabilize for 15

minutes prior to InGaN growth. A set of 350nm-thick InGaN samples were grown at a temperature varying from 600 °C to 690 °C. A Ga flux of 3.8×10^{-8} Torr was used for all samples, while In flux was increased from 1.5×10^{-7} Torr to 3×10^{-7} Torr as substrate temperature increased to maintain an In-rich growth regime.

A Bruker NanoMan atomic force microscopy (AFM) was employed to characterize the surface morphology of the samples. High-resolution x-ray diffraction (HRXRD) ω-2θ scans and (ω-2θ)-ω reciprocal space maps (RSM) were recorded on a triple-axis Philips X'pertPro Panalytical Pixel 3D materials research diffractometer. Cross-sectional specimens for transmission electron microscopy (TEM) study were prepared by in-situ focused ion beam (FIB) lift-out methods using a Thermo-Fisher G4 650 Xe Plasma-FIB (P-FIB). Utilizing a Xe plasma ion source instead of a regular Ga source prevents redistribution of Ga atoms or change of Ga concentration in InGaN films. For final thinning, a 5 keV energy and 10pA current beam were used. A JEOL JEM-3100R05 electron microscope with a cold-field emission gun equipped with both a probe and an imaging corrector was used for atom-resolved imaging that was operated in STEM mode. Both high-angle annular dark-field (HAADF) and bright-field (BF) images were taken simultaneously.

3.2.2 Results and Discussions

Surface Morphology

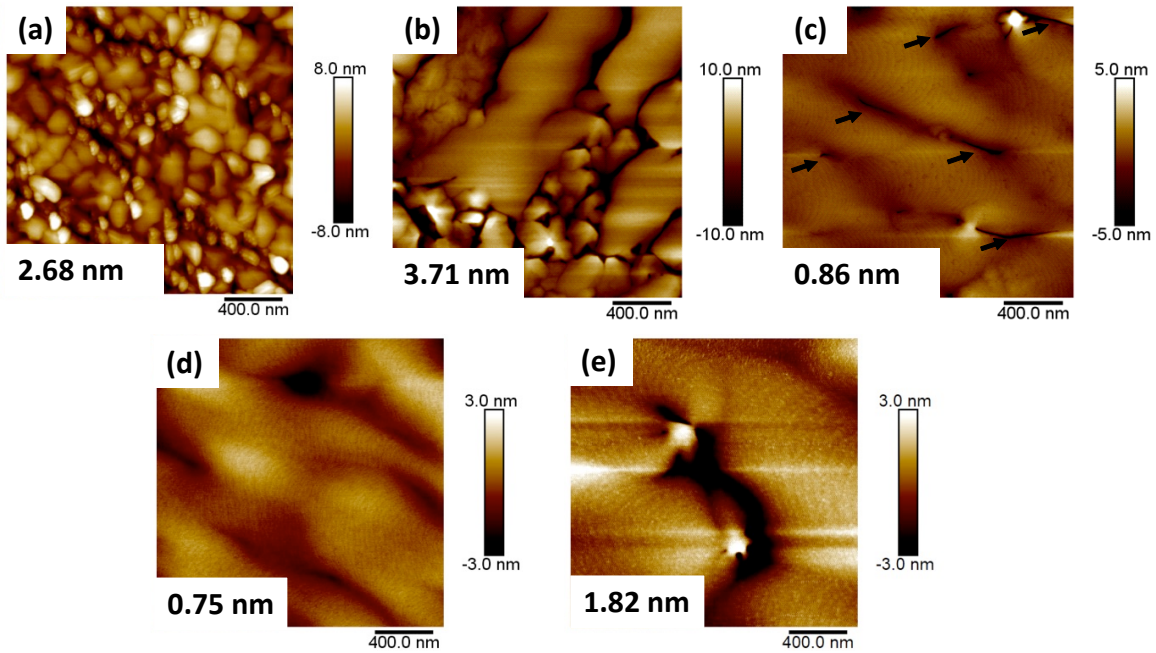

Figure 3.5 AFM image of 350 nm-thick InGaN films grown at (a) 600 °C (b) 620 °C (c) 650 °C (d) 670 °C (e) 690 °C.

Figure 3.5 shows AFM images of InGaN films grown at different substrate temperatures. Growth of InGaN at 600 °C (sample A) resulted in a rough and grain-like surface morphology. Increasing the substrate temperature improved the surface morphology. The sample grown at 650 °C (sample C) showed clear step edges and sub-nm surface root-mean-square (RMS) roughness. However, large grooves could be also observed on the surface. An excellent surface morphology with clear step edges and RMS roughness of only ~0.75 nm was achieved on sample D grown at 670 °C (sample D), indicating a step flow growth regime. This surface RMS for sample D is significantly lower than that of any previously reported N-polar InGaN films with similar In content [67,179]. A smooth surface morphology was maintained by further increasing the growth

temperature to 690 °C. The surface morphology of samples D and E is very similar to what we typically see on GaN films homoepitaxially grown on N-polar GaN substrates by PAMBE [176].

Crystal Structure by X-Ray Diffraction

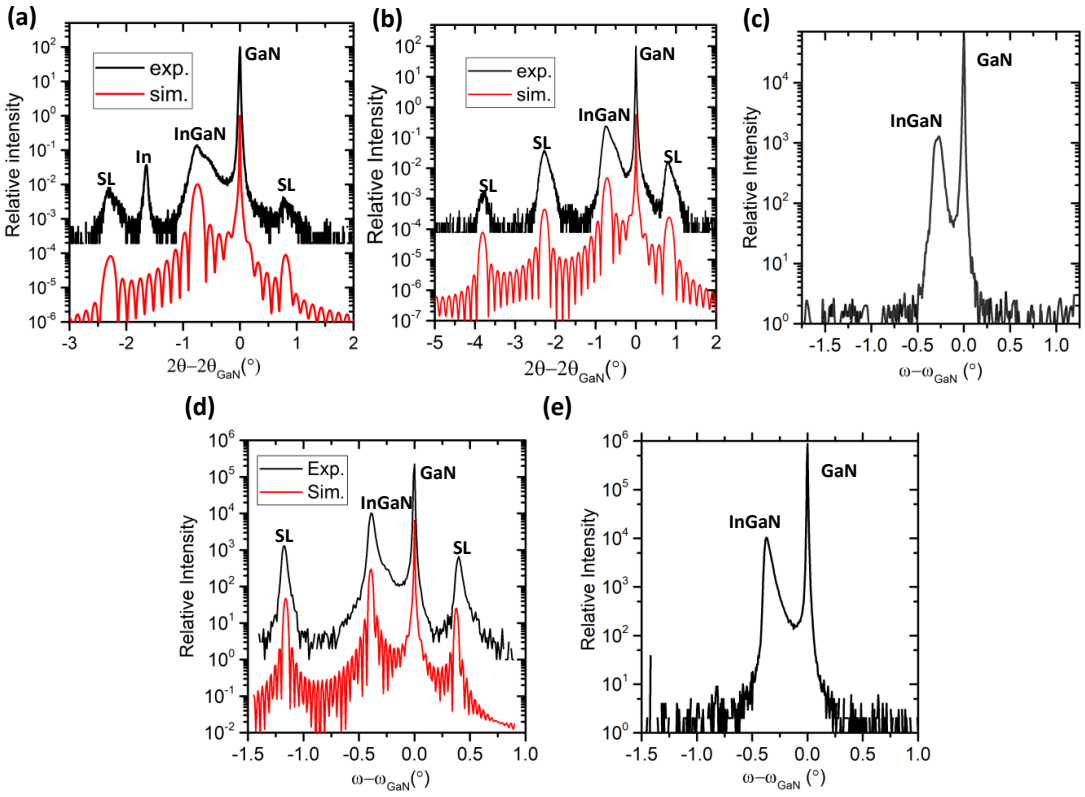

Figure 3.6 XRD ω-2θ profile of "InGaN" films grown on N-polar GaN at (a) 600 °C (b) 620 °C (c) 650 °C (d) 670 °C (e) 690 °C recorded around GaN (0002) reflection.

Figure 3.6 shows HRXRD ω-2θ profiles of all five samples recorded around GaN (0002) reflection. Unexpected SL peaks can be observed on XRD ω-2θ profiles recorded on sample A, sample B, and sample D, while ω-2θ profile of sample C and E revealed only GaN and $In_{0.13}Ga_{0.87}N$ peaks. Simulations conducted using Epitaxy and Smoothfit software revealed a good fit with the HRXRD ω-2θ profiles, assuming $In_{0.12}Ga_{0.88}N$ (4.1 nm) / $In_{0.05}Ga_{0.95}N$ (1.82 nm) superlattice structure on sample A, $In_{0.21}Ga_{0.79}N$ (2.21 nm) / $In_{0.03}Ga_{0.97}N$ (3.72 nm) superlattice structure on sample B, and $In_{0.26}Ga_{0.74}N$ (3 nm) /GaN (3 nm) superlattice structure on sample D. As mentioned

earlier, the In, Ga, and N shutters were opened once at the start and remained opened during the one hour of growth and were closed simultaneously at the end of the growth. The substrate temperature was monitored in-situ during the growth using a thermocouple. No fluctuations in the Ga/In effusion cells and substrate temperatures was observed. Therefore, observation of such SL structures on these samples from HRXRD profiles is surprising and unexpected.

Scanning Transmission Electron Microscopy (STEM)

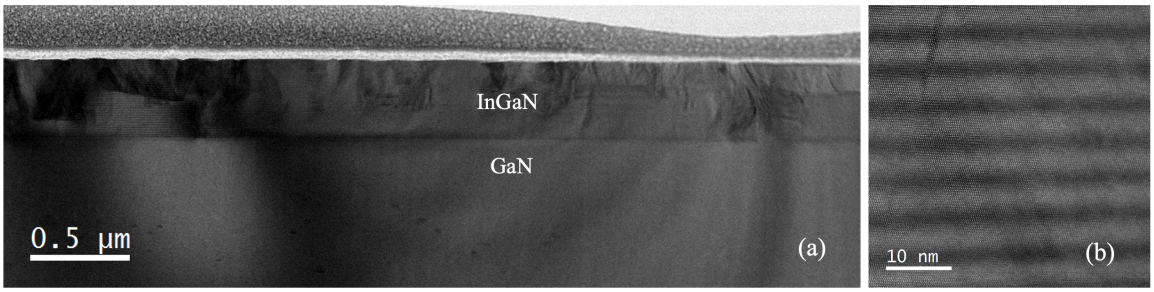

Figure 3.7 (a) STEM-BF and (b) high-resolution STEM-HAADF images of sample A (grown at 600 °C). A high density of defects and dislocations can be observed beyond a critical thickness. A SASL structure with a period of 5.9 nm was revealed from the STEM-HAADF image.

To further analyze their structural properties, STEM was performed on all five samples. STEM image taken from the InGaN film grown at 600 °C (sample A) along $< 2\bar{1}\bar{1}0 >$ is shown in **Figure 3.7**. The low magnification STEM-BF image (**Figure 3.7 (a)**) revealed the generation of a large density of defects and dislocations in InGaN layer beyond a critical thickness. This agrees with the rough surface morphology observed from the AFM image of this sample (**Figure 3.5 (a)**). The high-magnification STEM-HAADF image on this sample (**Figure 3.7 (b)**) revealed a SL structure with a period of ~5.9 nm, which is similar to that extracted from the HRXRD ω-2θ profile. Additionally, the thicknesses of low In and high In content layers are in agreement with that extracted by simulating the HRXRD ω-2θ profile.

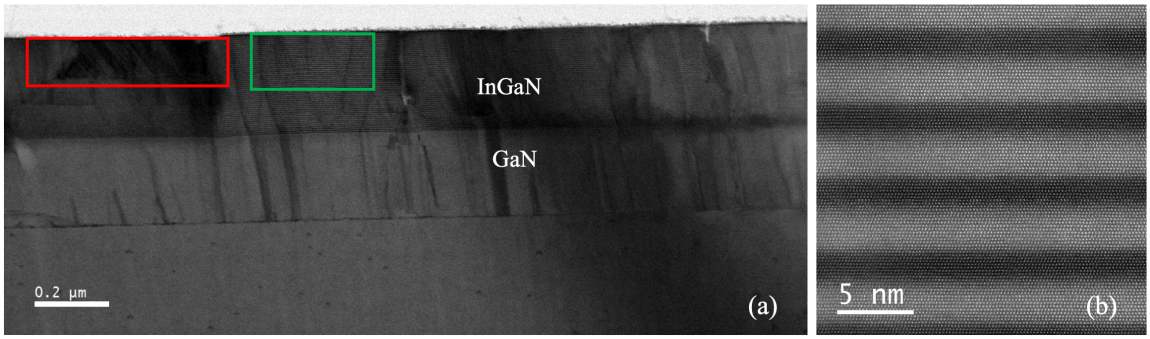

Figure 3.9 (a) STEM-BF and (b) high magnification STEM-HAADF images of sample B (grown at 620 °C). The red box shows an area with a high density of defects and dislocations, whereas the green box shows a region of InGaN layer with higher structural quality that can be observed beyond a critical thickness. A SASL structure with a period of 5.9 nm was revealed from the STEM-HAADF image.

STEM-BF image of sample B along $< 2\bar{1}\bar{1}0 >$ (**Figure 3.9(a)**) indicates areas with higher structural quality (green box) and areas with a large density of defects and dislocations (red box). This agrees with the AFM image taken on this sample (**Figure 3.5 (b)**), which shows areas with smooth surface and step edges, indicating a step-flow growth, and areas with rough and grainy surface morphology. The high-magnification STEM-HAADF image on this sample (**Figure 3.9 (b)**) also revealed a SL structure with a period similar to that of sample A (~5.9 nm), which is also similar to that extracted by simulating the HRXRD ω-2θ profile. The SL structure was observed in both areas with higher structural quality (green box) and areas with lower structural quality (red box).

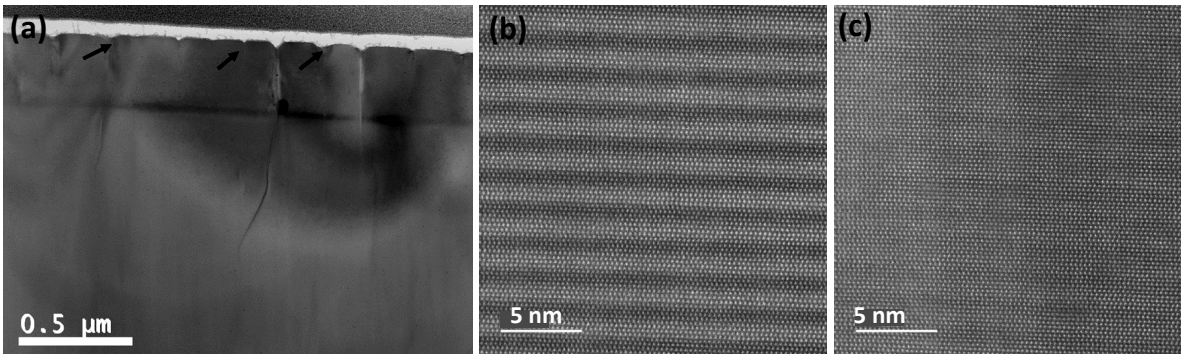

Figure 3.8 (a) STEM-BF image and (b) and (c) high-magnification STEM-HAADF images taken from two different regions of sample C (grown at 650 °C);

The STEM-BF taken from sample C along $< 2\bar{1}\bar{1}0 >$ (**Figure 3.8 (a)**) revealed significantly improved structural quality compared with that of sample A and sample B. Some deep grooves can be observed as shown by arrows, which are consistent with dark pits, as pointed by black arrows, in the AFM image of this sample (**Figure 3.5 (c)**). In contrast to sample A and sample B that have uniform SL structure all over the samples, high magnification STEM-HAADF on different areas of sample C revealed SL structure with sharp and well-defined interfaces in some regions (**Figure 3.8 (b)**), but only slight traces of In modulation in the other regions (**Figure 3.8 (c)**). This nonuniformity in the formation of SL structure can explain the absence of SL peaks in the HRXRD ω-2θ profile of sample C. The reason behind the anomalous nonuniformity in this sample is not understood. However, it can be speculated that it could be due to inconsistency in commercially available N-polar GaN substrates. For instance, the miscut angle of these N-polar GaN substrates varies between 0.25° to 0.56° on different substrates, which can affect the formation of SASL structure. Moreover, a technique to achieve a consistently smooth surface on N-polar surface prior to the epitaxial growth has not yet been developed. Further studies are needed to understand the impact of the substrate on the nonuniformity of SASL structures.

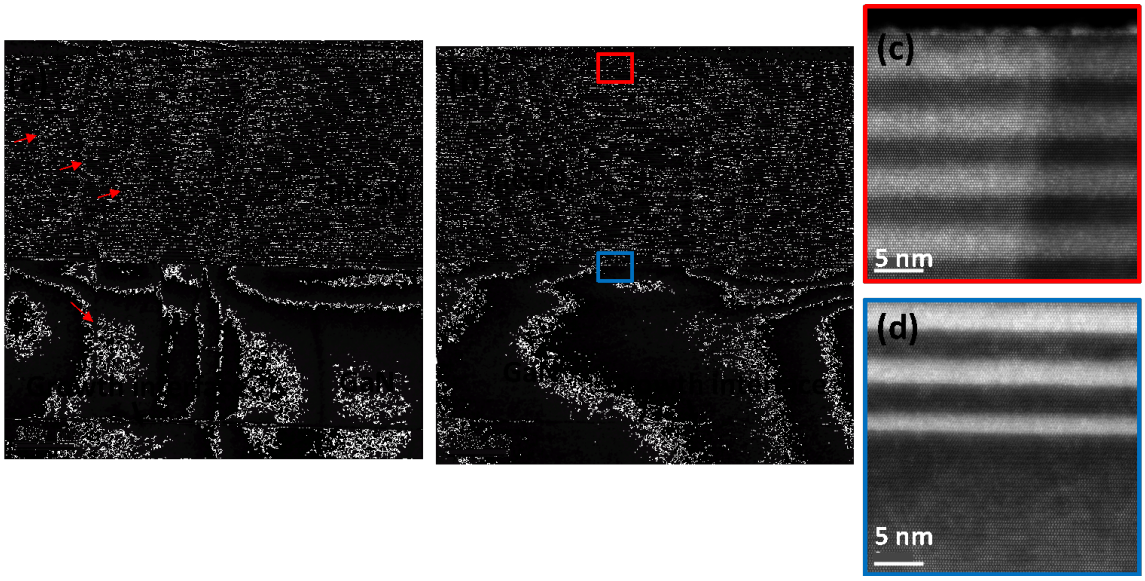

Figure 3.10 (a) STEM-BF and (b) STEM-HAADF images taken on two different regions of sample D (grown at 670 °C). (c) and (d) enlarged high-resolution STEM-HAADF images from the two outlined regions marked in b showing high-quality self-assembled InGaN-GaN SL structure

STEM-BF images taken from sample D along $< 2\bar{1}\bar{1}\ 0 >$ direction (**Figure 3.10 (a) and (b)**) revealed a film with high structural quality with these films again belonging in the family of experimental observations. The STEM-BF image in **Figure 3.8 (a)** was taken from a region where there are a few dislocations in the MBE-grown GaN. The formation of dislocations at the homoepitaxial growth interface is due to intrusive particles remaining on the GaN substrate due to unoptimized surface polishing. Newly generated dislocations can be observed in the InGaN film, originating from the dislocations propagated from the underlying GaN. In contrast, the STEM-BF image taken from the area with no dislocation density in the GaN layer revealed no new dislocations generated in the InGaN film. This observation indicates that if a surface pretreatment technology is developed to improve substrate surface such that generation of dislocations in MBE-grown GaN can be suppressed. The generation of more dislocations in the InGaN film can potentially be suppressed as well. The magnified STEM-HAADF image taken on this sample

revealed a well-defined superlattice structure with a period of ~6nm, which is in perfect agreement with the period extracted from the HRXRD ω-2θ profile of sample D.

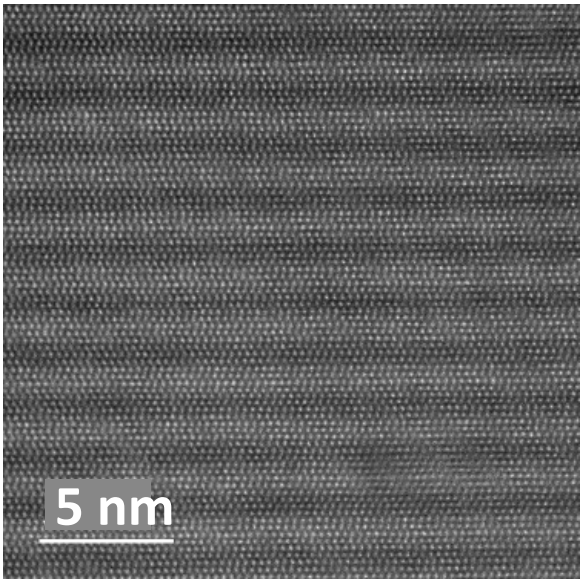

Figure 3.11High magnification STEM-HAADF images of sample E (grown at 690 °C).

Despite absence of SL peaks from the HRXRD profile taken on sample E, the magnified STEM-HAADF image taken on this sample (**Figure 3.11**) also revealed a SL structure. Further investigation is required to understand why SL peaks are sometimes missing in the HRXRD profile. The periodicity of SL structure on this sample is only ~2nm, which is less than half of the SL periodicity observed on the other samples grown at lower temperatures. This indicates the possibility of tuning the SL periodicity by changing the growth temperature. These results revealed that as the growth temperature increased, the magnitude of variation in the In layer in two layers increased such that growth at 670 °C led to a $In_{0.26}Ga_{0.84}$/GaN superlattice structure, with one layer being pure GaN as estimated by simulating HRXRD ω-2θ profile.

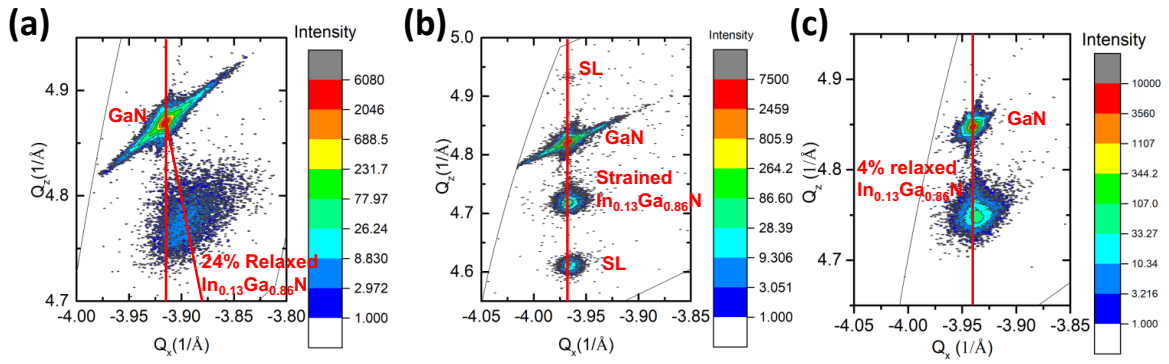

Figure 3.12 XRD-RSM scan around GaN ($\bar{1}\bar{1}24$) reflection recorded on (a) InGaN grown at 650 °C (sample C) (b) InGaN grown at 670 °C (sample D) (c) InGaN grown at 690 °C (sample E).

XRD-RSM scans recorded around the GaN ($\bar{1}\bar{1}24$) reflection on samples C, D, and E are shown in **Figure 3.12 (a)**, **(b)**, and **(c)**, respectively. Interestingly, the average InN mole fraction was measured to be ~13% on all three samples. This is somewhat unexpected as In incorporation tends to reduce as growth temperature increases [170]. $In_{0.13}Ga_{0.86}N$ film in sample C is partially relaxed, while the nominal "$In_{0.13}Ga_{0.86}N$" film in sample D remained coherently strained to GaN, and the InGaN film in sample E is only 4% relaxed. This observation indicates that uniform growth of SL structures can be employed to increase the critical thickness of InGaN films grown on GaN. However, intentional epitaxial growth of such thick superlattices is challenging. First, it requires frequent opening/closing of In/Ga shutters, which can reduce the lifetime of shutters. Additionally, and more importantly, the optimized growth temperature of InGaN and GaN is conventionally very different. While GaN is typically grown at ~730 °C, InGaN requires lower growth temperatures to suppress decomposition. This means that the growth of InGaN/GaN SL requires a constant change of growth temperature, which significantly increases the growth time. Besides, frequent growth interruptions can lead to unintentional impurity incorporation at the InGaN/GaN interfaces, leading to poor optical and electrical quality SLs. Alternatively, one could grow the

GaN layer at the same temperature as the InGaN layer, which also results in poor-quality GaN films. In contrast, growth conditions presented here naturally lead to the formation of a superlattice structure. Additionally, the content and periodicity of SASL structures reported here are very similar to quantum well structures embedded in GaN-based LEDs and LDs, and photovoltaic cells, and, therefore, can potentially be useful for these applications [119,180–182].

Stablity of Self-assembled Superlattice

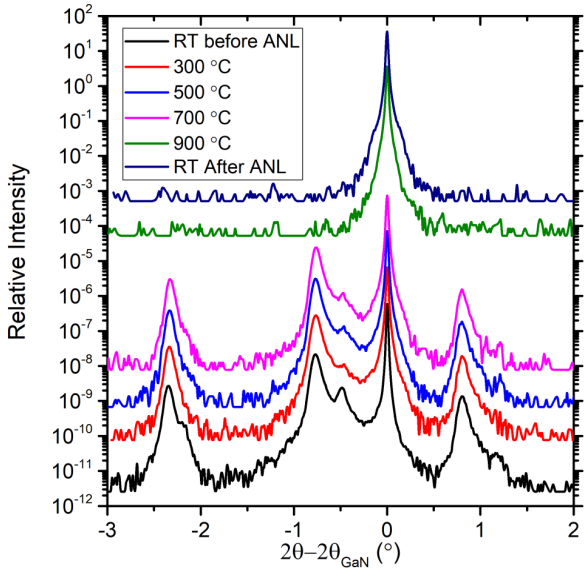

Figure 3.13In-situ HRXRD ω-2θ profile of sample D recorded around GaN (0002) reflection at different temperatures showing that SL is stable up to at least 700 °C.

To understand the thermal stability of these SASL structures, in-situ XRD measurements were conducted while heating up sample D in ambient. In this experiment, the XRD stage, on which the sample was mounted, was heated up with a ramp rate of 20 °C/min and XRD ω-2θ profiles were recorded at room temperature, 300 °C, 500 °C, 700 °C, and 900 °C. The stage was held at each specific temperature for about an hour for aligning the sample and recording XRD ω-2θ profile. XRD ω-2θ profiles shown in **Figure 3.13** revealed that the InGaN film maintained its SL structure up to at least 700 °C. At 900 °C, however, the InGaN and the SL peaks disappeared,

indicating that not only the SL structure was annihilated but also the InGaN film lost its crystalline structure most probably due to the decomposition of InGaN layers. White powder-like substance could be observed on the sample surface after annealing at 900 °C.

3.3 Summary

Spontaneous formation of superlattice structure in nominal InGaN film grown on N-polar GaN was observed. An increase in the growth temperature led to a magnification of the variation in the In content in two layers of SL such that growth at 670 °C resulted in $In_{0.26}Ga_{0.84}$/GaN superlattice structure. Moreover, it was demonstrated that the SL periodicity reduced by further increasing the growth temperature to 690 °C. Further studies are required to fully understand the impact of In content, growth regime, and In/Ga flux on the formation and periodicity of self-assembled superlattice structures. Nevertheless, the formation of a uniform SL structure increased the critical thickness of InGaN. 350 nm-thick InGaN film with an average InN mole fraction of 13%, excellent structural quality, and sub-nm surface roughness was demonstrated. The thermal stability of the SASL structure was also investigated by heating up the sample in ambient while performing in-situ XRD measurements. These structures are stable up to at least 700 °C. Many devices, including hot electron transistors (HETs) [1], InGaN-channel HEMTs, LEDs, solar cells, and detectors, could potentially benefit from relatively high temperature (690 °C) growth of high-quality InGaN and spontaneous formation of InGaN/GaN superlattice structure.

Chapter 4 Ga-polar InGaN Growth on ZnO Substrate

4.1 Introduction

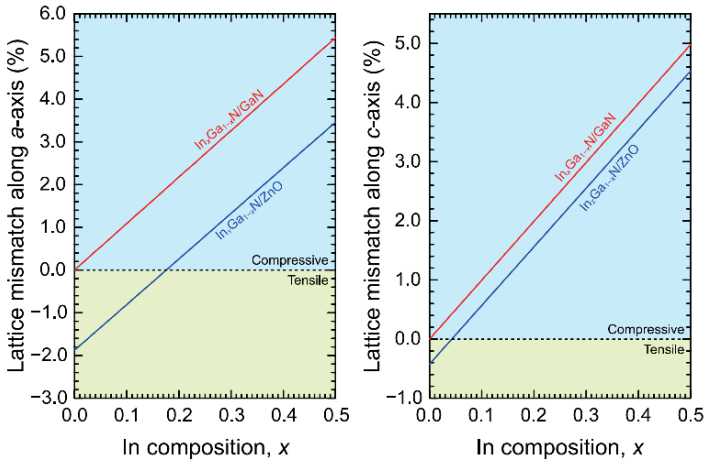

Figure 4.1 In-plane lattice mismatches of m-plane InGaN/ZnO and InGaN/GaN showing $In_xGa_{1-x}N$ is lattice matched with ZnO substrate for In composition 0.18 and 0.06 along along a-axis and c-axis, respectively. The lattice constants of InGaN were calculated according to the Vegard's Law ***Courtesy A Kobayashi et al. [183]***

ZnO has been proposed as a promising substrate for high quality relaxed InGaN pseudo-substrates growth since $In_{0.2}Ga_{0.8}N$ is lattice matched to the ZnO substrate in the in-plane direction (a-plane) **(Figure 4.1(left))** [183] and has a similar thermal coefficient as ZnO substrate. ZnO has the same wurtzite crystal structure, and ZnO and InGaN are isomorphic in stacking order [184–186]

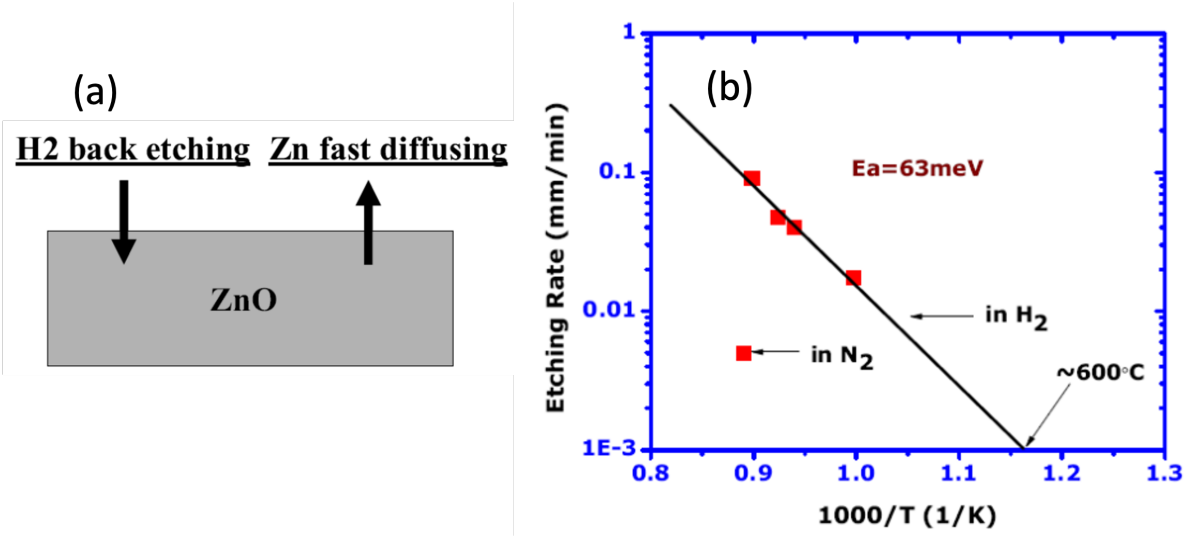

Figure 4.2 (a) Issues related to growth of GaN by MOCVD on ZnO substrates shows H_2 back etching into substrate and Zn diffusing into epilayers, both causing poor epilayer growth of GaN. (b) Arrhenius plot for the H2 etching rate (mm/min) of ZnO versus temperature (1/T) ***Courtesy: N Li (2009) [193].***

ZnO was studied as a potential substrate for epitaxial growth of (In,Ga)N via both MBE [187–189] and MOCVD [75,190–192] in the early years of developing nitrides due to in-plane lattice matching of $In_{0.2}Ga_{0.8}N$ and ZnO [9,44]. However, InGaN growths on ZnO substrates have a long history of disappointing results. The main challenges that hindered ZnO from emerging as the common substrate for the InGaN growth were the out diffusion of Zn from the substrate into the epilayer and interfacial reaction between nitrides and the ZnO at high temperature due to the thermal stability of the ZnO substrate (**Figure 4.2 (a)**) [193]. In addition to the thermal stability issue at high temperature, H_2 in MOCVD reactors back etches substrate at high temperatures [75]. As the temperature increases, the H_2 etching rate results in damaging the substrate before the epilayer growth **(Figure 4.2 (b))** [193]. Ammonia (NH_3), which is the source that supplies N in MOCVD of III-nitrides is the source of H_2 during the growth. At low temperature (~500 °C), the contribution of H_2 is too small to cause damage to the substrate surface. However, the NH_3 cracking efficiency decreases with reducing the growth temperature below 600 °C. ZnO was used as a substrate to grow $In_{0.2}Ga_{0.8}N$ films for the first time in 1992 with the MOVPE technique by

Matsuoka et al [194]. They concluded that growing on the lattice-matched substrate (ZnO) helps to improve the InGaN film quality. However, at the time, ZnO substrates were not commercially available. Moreover, there was no well-developed pretreatment technique available to remove the surface damage caused by slicing the ZnO substrate. *A substrate treatment process for both O-face and Zn-face ZnO by annealing followed by ozone treatment and BHF etching was developed and* ***described in section 4.2.***

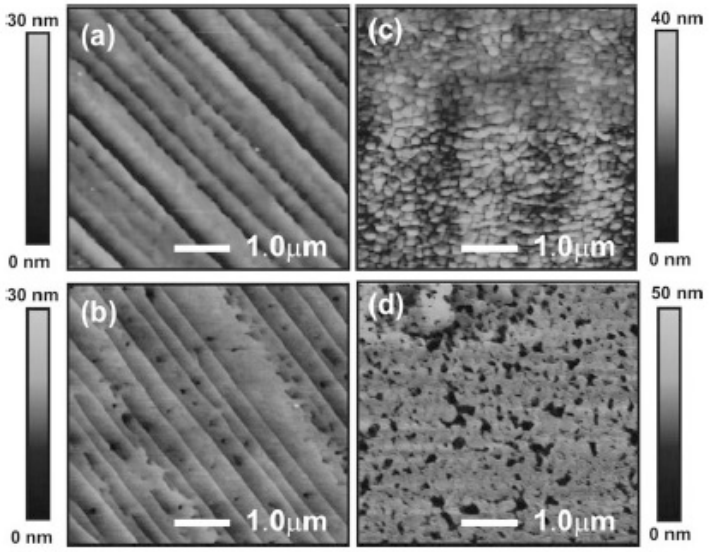

Figure 4.3 AFM images of GaN epilayers before and after H_3PO_4 etching on vicinal and singular ZnO substrate. GaN epilayers (a) before and (b) after etching on vicinal ZnO, and GaN epilayers (c) before and (d) after etching on on-axis ZnO ***Courtesy: G Namkoong et al. [196].***

Later, other groups also attempted to grow GaN on ZnO substrates using PAMBE since the MBE growth temperature for (In,Ga)N is lower than that of MOCVD [186,195]. Namkoong et al. [196] were able to reduce the dislocation density of GaN films by two orders of magnitude using miscut ZnO substrates as opposed to on-axis ZnO substrates. **Figure 4.3** shows the GaN surface before and after H_3PO_4 etching to reveal dislocations/pits on miscut substrate (**Figure 4.3 (a) and (b)**) and on on-axis substrate (**Figure 4.3 (c) and (d)**). This figure shows that the density of pits caused by etching is two orders of magnitude smaller on the miscut substrate in comparison

with that on on-axis substrate. Nevertheless, it has been proven to be difficult to achieve high-quality GaN on ZnO due to a reaction between GaN and ZnO at elevated temperatures. E.S. Hellman et al. reported that in MBE growth of GaN on ZnO, ZnO reacts with Ga in GaN at high temperature and forms Ga_2ZnO_4, an oxide with the spinel structure [197].

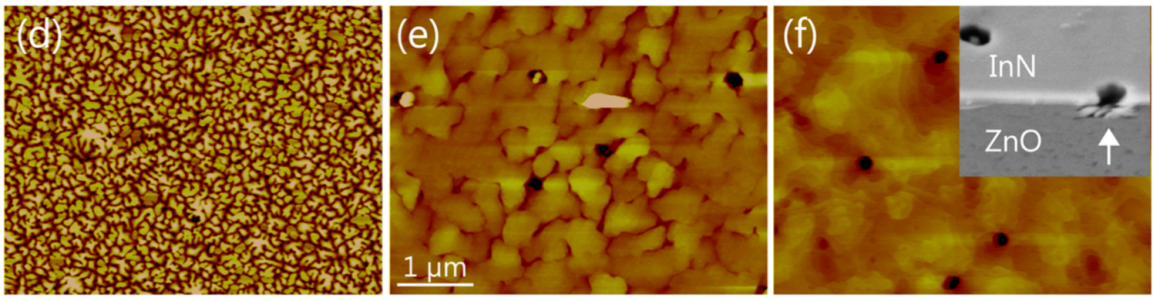

Figure 4.4 AFM [(a)–(c)] of thin InN films grown at different temperature: 350 ºC, 450 ºC, 550 ºC, respectively. The inset in (c) shows a bird's eye view SEM micrograph of the surface of the sample. The arrow indicates a hexagonal pit ***Courtesy: Y Cho et al. [198]****.*

Recently, successful growth of high-quality InN on O-face ZnO substrates was demonstrated by Cho et. al using PAMBE [198]. ZnO is isomorphic to InN with a lattice mismatch of 8%. Although this lattice mismatch is smaller than that between GaN and InN (11%), it is still relatively large. Moreover, due to the interaction between oxygen and InN at elevated temperatures, In_2O_3 forms at the interface. Cho et al. [198] were able to eliminate the ZnO and InN reaction at the interface by growing at temperatures below 550 °C while maintaining a relatively high-quality surface morphology (**Figure 4.4**). In their work, InN films were grown on O-face ZnO. However, the polarity of InN films is not mentioned here. Additionally, they showed that even a small amount of Ga incorporation leads to inversion domains at the interface, and, therefore, degrades the film's quality. Ernst et al. [199] studied low temperature growth of InN and GaN on ZnO and demonstrated step flow growth for films thinner than 2 monolayers (MLs). However, three-dimensional (3D) structures started to form for GaN thickness beyond 3.1 MLs.

They concluded that the growth of InN/GaN multiple quantum wells (MQWs) and InN/GaN superlattices (SPSLs) may not be possible on ZnO under the growth conditions they investigated.

The interfacial reaction between III-nitride and ZnO forms an intermediate phase with poor crystalline quality and eliminates the advantage of the lattice-matched ZnO substrate with $In_{0.2}Ga_{0.8}N$. Kobayashi et al. demonstrated growth of high-quality m-plane GaN on m-plane ZnO substrates using the pulsed laser deposition (PLD) technique [200]. They initiated the growth with a thin GaN layer grown at room temperature to suppress the reaction between ZnO and GaN. As mentioned earlier, there is an 8% lattice mismatch between InN and ZnO crystal structures, whereas $In_{0.2}Ga_{0.8}N$ is perfectly lattice matched to ZnO.

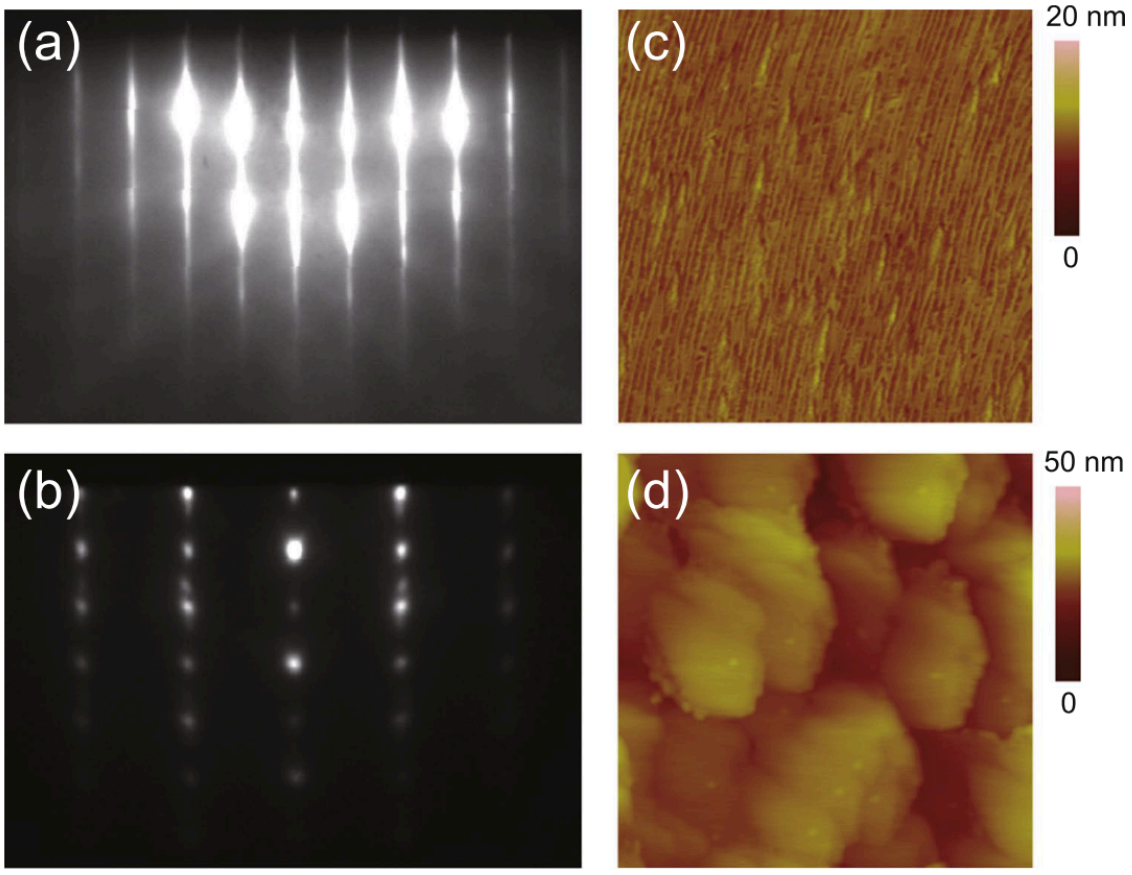

Figure 4.5 RHEED patterns [(a) and (b)] and AFM images 1 µm x1 µm [(c) and (d)] of GaN films grown on m-plane ZnO substrates at 340 ºC [(a) and (c)] and 540 ºC [(b) and (d)] ***Courtesy: A Kobayashi et al. [183]***

Recently, Kobayashi et. al [183] successfully grew m-plane GaN and lattice-matched InGaN films on m-plane ZnO at 350 ºC using pulsed sputtering deposition (PSD). **Figure 4.5 (a) and (b)** show a streaky RHEED pattern and smooth surface morphology, respectively, on the GaN film grown at 340 ºC. In contrast, the RHEED pattern on the sample grown at 540 ºC is spotty (**Figure 4.5 (c)**), implying a rough surface, which agrees with the AFM image on this sample (**Figure 4.5 (d)**).

To attain ZnO substrates surfaces with step edges, different substrate treatment methods have been studied and explained ***section 4.2****. Different substrate treatments, e.g., wet etching, ozone treatment and annealing in different environment have been investigated extensively. An ozone treatment with BHF wet etching followed by annealing in ambient for an hour improved the surface morphology drastically. A low temperature GaN buffer layer grown by metal enhanced epitaxy (MEE) using a shutter modulation scheme has been explored to prevent formation of the interfacial layer and* ***is discussed in section 4.3.*** *A two monolayer (ML) thick GaN layer grown by MEE was successful in stopping the interfacial interaction between InGaN and ZnO at high growth temperature. InGaN growths on ZnO initiated with a 2ML thick GaN layer were grown at different growth temperatures, and the dependence of surface morphology and luminescence of InGaN on growth temperature were studied and described in section 4.4.*

4.2 ZnO Substrate Treatment

4.2.1 Introduction

ZnO is an attractive substrate for (In,Ga)N growth because it is isomorphic to (In,Ga)N and lattice-matched to the $In_{0.18}Ga_{0.82}N$. One of the important factors that can affect quality of (In,Ga)N films grown on ZnO substrate is the surface quality and morphology of the ZnO substrate [201]. The substrate surface needs to be atomically flat and free of particles (e.g., metallic impurity,

contaminants). The difficulties of using a non-conventional substrate, ZnO, are primarily related to the unavailability of any established surface preparation method prior to the growth, as well as the stability of the substrate surface during high-temperature growth [202–205]. In addition, ZnO single-crystal substrates for growth have various issues due to their high cost, short supply, Li contamination and so on. The surface of the ZnO substrate has contaminants from silica (SiO_x) particles due to chemo-mechanical polishing and the formation of $Zn(OH)_2$ gel [201]. To solve all these issues and obtain a smooth surface on ZnO substrate ready for epitaxial growth, thermal annealing, wet-chemical etching and plasma treatments have been explored for substrate treatments [75,201,202,206,207].

Attempts have been made to remove the damaged layer due to polishing with thermal annealing in different environments e.g., ambient, N_2, O_2 or high vacuum [201,203–205,207]. Annealing ZnO substrates at a low temperature (~650 °C) resulted in relatively low surface roughness with a decrease in the number of scratches, without any step edges and terraces. An increase in annealing temperature resulted in an accumulation of nucleation islands with a height of a lattice constant and developed regular steps (including some irregularities). An O-face ZnO $(000\bar{1})$ substrate annealed at 1150 °C for 3h can remove all the damage induced by sawing and the residual scratches from mechanical polishing[195,207]. The annealing can help to attain an atomically flat, terrace-like surface. However, Ernst et al. [199] reported annealing in O_2 showed that some three-dimensional protrusions occurred. However, these clusters can be removed by rinsing the samples in de-ionized water under sonication and re-annealing the samples. Besides, high-temperature annealing of ZnO decreases the amount of residual Li from the substrate [202].

Electrochemical etching has been proposed instead of annealing by several research groups as a surface treatment method [201,208]. They have explored HCl, HNO_3, HF, and BHF for

etching both O-face and Zn-face ZnO substrates [201,208]. S. Akasaka et al. demonstrated that dipping the Zn-face ZnO substrates in an HCl solution (HCl: H_2O=7:200) for 30s results in an epitaxy-ready surface with great reproducibility [201]. After exposing the Zn-face ZnO to HCl solution, the Zn-face ZnO substrate exhibited as a flat surface showing some steps and terraces. With an increase in etching time to 6 min, the Zn-face ZnO showed island-shape morphology with a high step height of 3.5 nm. With an etching time of 13min, the Zn-face ZnO surface led to the island-shape structure. Furthermore, etching in HCl solution can decrease the residue of silica particles from the chemo-mechanically polished surfaces. Besides, Zn-face and O-face ZnO substrates showed different morphology after etching for two minutes in nitric acid (61 wt%) at room temperature [75]. Zn-face ZnO surface was showing smooth surface morphology with some grooves coming from slicing and polishing. In contrast, the O-face ZnO showed rough surface morphology after the nitric acid wet etching treatment. The etching rate for O-face ZnO is one order of magnitude higher than that of Zn-face ZnO. Additionally, T. Nakamura et al. [208] introduced UV-ozone treatment before wet chemical etching to eliminate the inorganic particles from the surface. They studied the impact of the pH value of NH_4F buffered HF solution on Zn-face ZnO substrates. The wet chemical etching by BHF results in the formation of the step and terraces in the ZnO substrate surface. However, BHF with a higher pH value leads to etch-pits at the surface. They showed lowering the pH of the BHF solution decreases the etching rate of the ZnO and can reduce the pit density on the surface. T. Nakamura et al. [208] showed atomically flat substrates without any etch pits can be successfully obtained by etching ZnO by BHF solution with pH=5 following UV-ozone treatment. However, most of the studies were focused on Zn-face

ZnO substrates, and there have been only a few studies comparing substrate treatment for both Zn-face and O-face ZnO substrates.

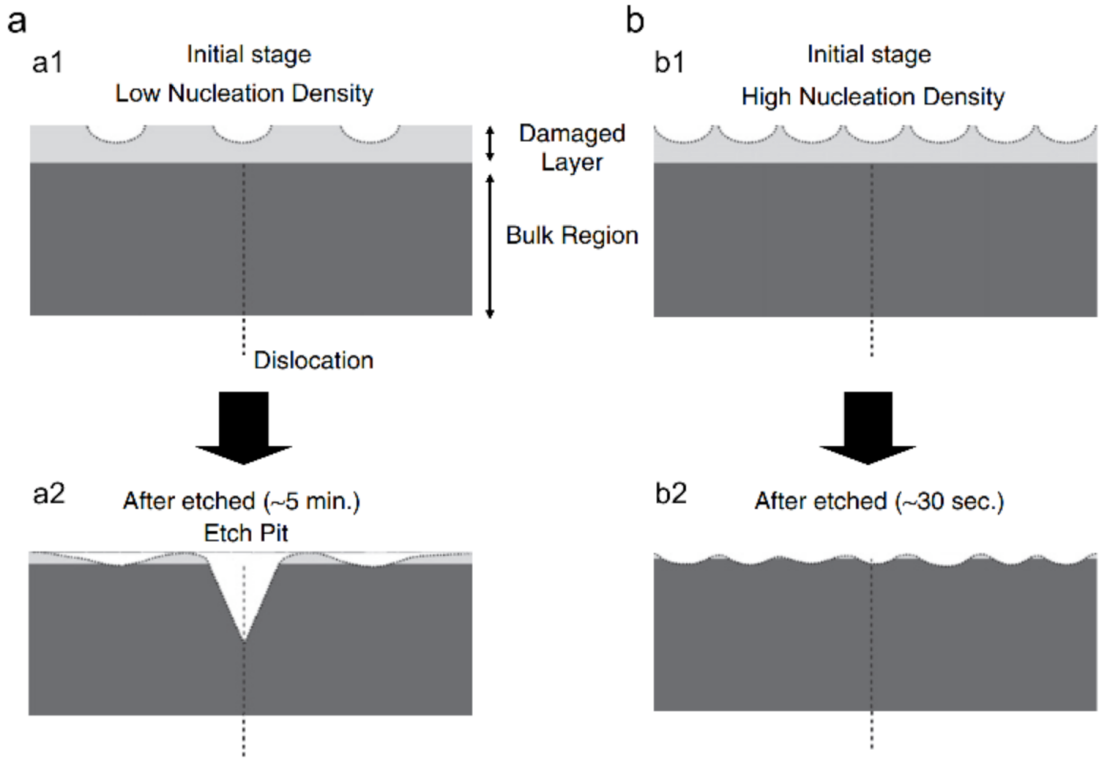

Figure 4.6 Schematic diagram of BHF etching process for cross sectional view of the Zn-face ZnO substrate. The pH values of the BHF are (a) ~6.5 and (b) ~5 ***Courtesy: T. Nakamura et al. [208]***

The most important parameters are etching time and using BHF with low pH for obtaining a surface morphology with step edges and no pyramid shaped pits. The mechanism of BHF etching can be explained by a theory proposed by J.R. Heffelfinger et al. [209]. Usually, Zn-face ZnO substrates have an amorphous damaged layer at the top [208]. At the first step of the BHF etching, the topmost amorphous layer is usually etched (**Figure 4.6 a(1)**). Later, nuclei of the pits forms at the edge of dislocation. These nuclei of the pits extend as the faceted pits during the etching process **(Figure 4.6 a(2))** and with an increase in the etching time, the depth of the faceted pits increases. The etched regions in the amorphous layer coalesce together with time, leading to a removal of the amorphous layer and formation of a smooth morphology with step edges. During the etching

process, the nuclei for the pits can also grow due to exposure to BHF over a long time or BHF with high pH value. These can lead to over-etching of the surface, which can result in etch pit formation in ZnO substrate and inhomogeneous step structure. Therefore, a BHF solution with low concentration was preferred so that uniform etching of the amorphous layer without any faceted etch bits can be obtained **(Figure 4.6b(1) & b(2))** [22]. In this thesis, the impacts of wet etching, ozone treatment and annealing on both Zn-face and O-face ZnO substrates are studied.

4.2.2 Wet Etching of ZnO Substrates

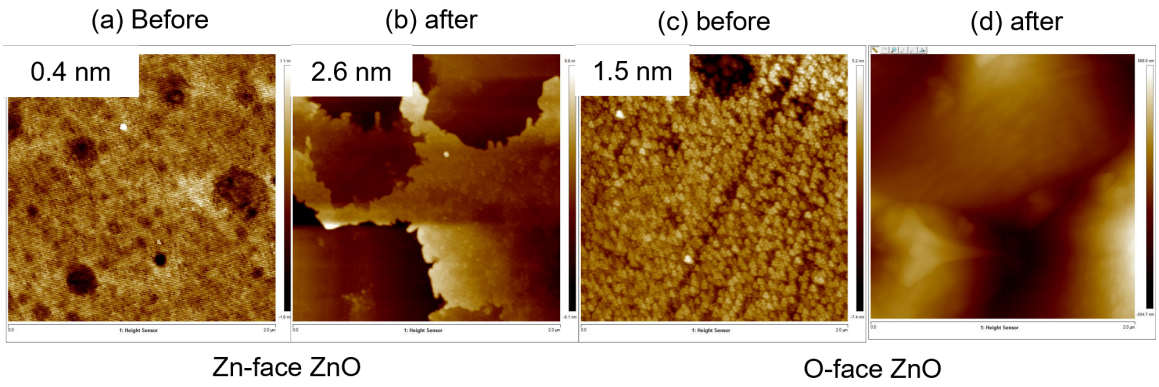

Figure 4.7 2μm x 2μm AFM scan of Zn-face ZnO substrate (a) before cleaning (b) after 20% HNO_3 treatment for 2 min; O-face ZnO substrate (c) before cleaning (d) after 20% HNO_3 treatment for 2 min.

Wet etching of Zn-face and O-face ZnO substrates by HNO_3, HCl, BHF was investigated. **Figure 4.7 (a), (b) and (c), (d)** show change in surface morphology of Zn-face and O-face ZnO substrate due to 20% HNO_3 treatment for 2 min, respectively. Etching ZnO substrate by 20% HNO_3 led to a rough surface for both Zn-face and O-face. Zn-face ZnO substrate showed an increase in surface roughness from 0.4 nm to 2.6 nm due to HNO_3 wet etching, and large pits were observed in the substrate surface. The O-face ZnO substrate lost its morphology, and the substrate roughness increased two orders of magnitude. This corroborates previous results shown by other research groups that Zn-face ZnO substrate shows more resistance to wet-etching than O-face ZnO

[75]. The etching rate of O-face ZnO by HNO_3 and HCl is an order of magnitude higher than that of Zn-face ZnO.

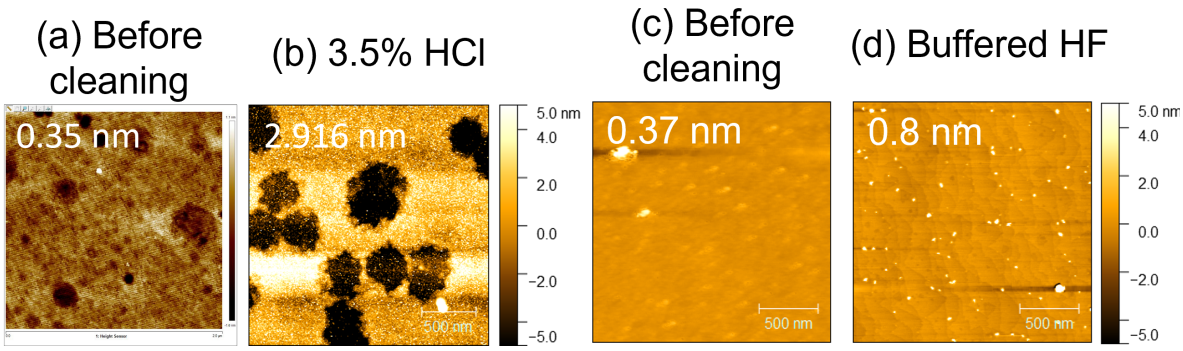

Figure 4.8 2µm x 2µm AFM scan of Zn-face ZnO substrate (a) before cleaning (b) after 3.5% HCl treatment for 30s (c) Before cleaning (d) after buffered HF treatment for 30s.

Etching of Zn-face ZnO by 3.5% HCl for 30s results in a drastic increase in the pit size **(Figure 4.8 (a) and (b))**. Large pits are non-ideal and detrimental for further epitaxial growth and device fabrication. After etching Zn-face ZnO by buffered HF for 30s, the surface morphology of Zn-face ZnO improved with clear step edges on the substrate surface (**Figure 4.8** (c) and (d)). However, the surface morphology slightly increased due to appearance of small particles on the surface. Therefore, UV-ozone treatment was developed to remove these particles as discussed in the next section.-In contrast, the surface morphology of O-face ZnO was damaged severely by wet etching of 3.5% HCl and BHF (similar to surface morphology shown in **Figure 4.7(d)).**

4.2.3 UV-Ozone Treatment of ZnO Substrate

A Senlights PL16 Deep UV exposure tool was used in this experiment as a source of ozone cleaning. It has a power density of approximately 15 MW/cm^2 at 30 mm of 254 nm and 185 nm UV light. A light source with a wavelength of 185 nm UV light was used for ozone generation,

and the concentration of ozone was relatively low in the range of 20-200 ppm for this experiment. After UV-ozone treatment, the substrate went through DI water cleaning for 2 min.

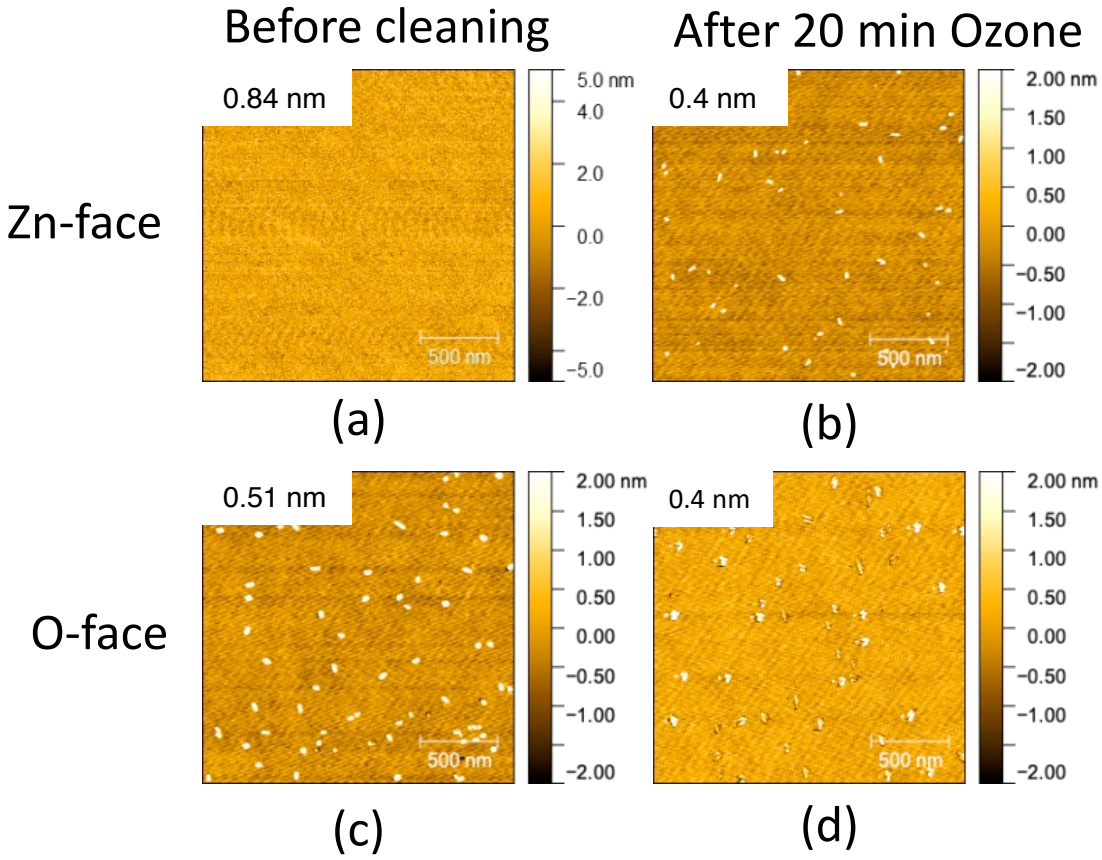

Figure 4.9 2µm x 2µm AFM scan of Zn-face ZnO substrate (a) before cleaning (b) after 15 min UV-ozone treatment showing worse substrate morphology (c) after 20 min UV-ozone treatment showing smooth surface morphology with surface roughness of 0.35nm; O-face ZnO substrate (d) before cleaning (e) after 20 min UV-ozone treatment showing smooth surface morphology with a surface roughness of 0.36 nm

UV-ozone treatment was explored as a technique for substrate treatment for both Zn-face and O-face ZnO. Zn-face ZnO substrate was exposed to a UV ozone environment for 20 min, **(Figure 4.9 (b))**. UV-ozone exposure for 20 min led to a smooth surface with a sub-nm surface roughness (0.35nm). Similarly, treating O-face ZnO substrate for 20 min resulted in a smooth surface with sub-nm RMS roughness **(Figure 4.9 (d))**.

Although UV-ozone exposure led to a smooth surface morphology on both O-face and Zn-face surfaces, step edges did not appear on the surface. Step-edges on the substrate surface help with step flow growth mode by MBE. Therefore, ozone treatment followed by BHF etching was explored on Zn-face ZnO substrate. The ozone-treated Zn-face ZnO substrate was then wet etched by BHF for 30s. This BHF wet etching following the ozone treatment was repeated three times for removal of 3D protrusions on the substrate surface. It is suspected that these 3D protrusions on the substrate surface came from the organics remaining from the substrate surface preparation. The substrate surface after the BHF treatment following ozone treatment for three times showed a sub-nm root mean square (RMS) roughness of 0.27 nm and a smooth surface with step edges (**Figure 4.10**). On the other hand, as mentioned before in **section 4.2.2**, BHF treatment can completely damage the O-face ZnO surface morphology. Therefore, BHF treatment followed by UV-ozone treatment cannot be pursued for O-face ZnO substrates.

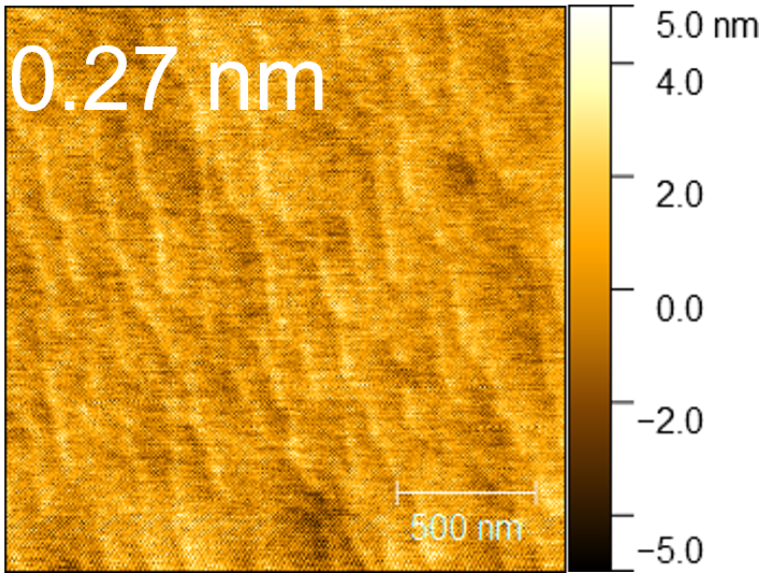

Figure 4.10: 2µm x 2µm AFM scans of Zn-face ZnO substrate after BHF treatment for 30s following UV-ozone treatment showing a surface roughness of 0.27 nm.

4.2.4 Annealing of ZnO Substrate in Ambient Environment

A Tempress diffusion system and A FB1300 model furnace were used for annealing the substrates. Similar experiments were conducted using both systems, which resulted in similar outcomes. A FB1300 model used a single three-section resistant heater embedded in a refractory material for heating the substrate. The chamber used a ceramic fiber for insulation. The temperature is controlled by an electronic control and measured by thermocouple. In contrast to the Tempress diffusion system, the wafers were placed flat on the boats directly for heating up the samples.

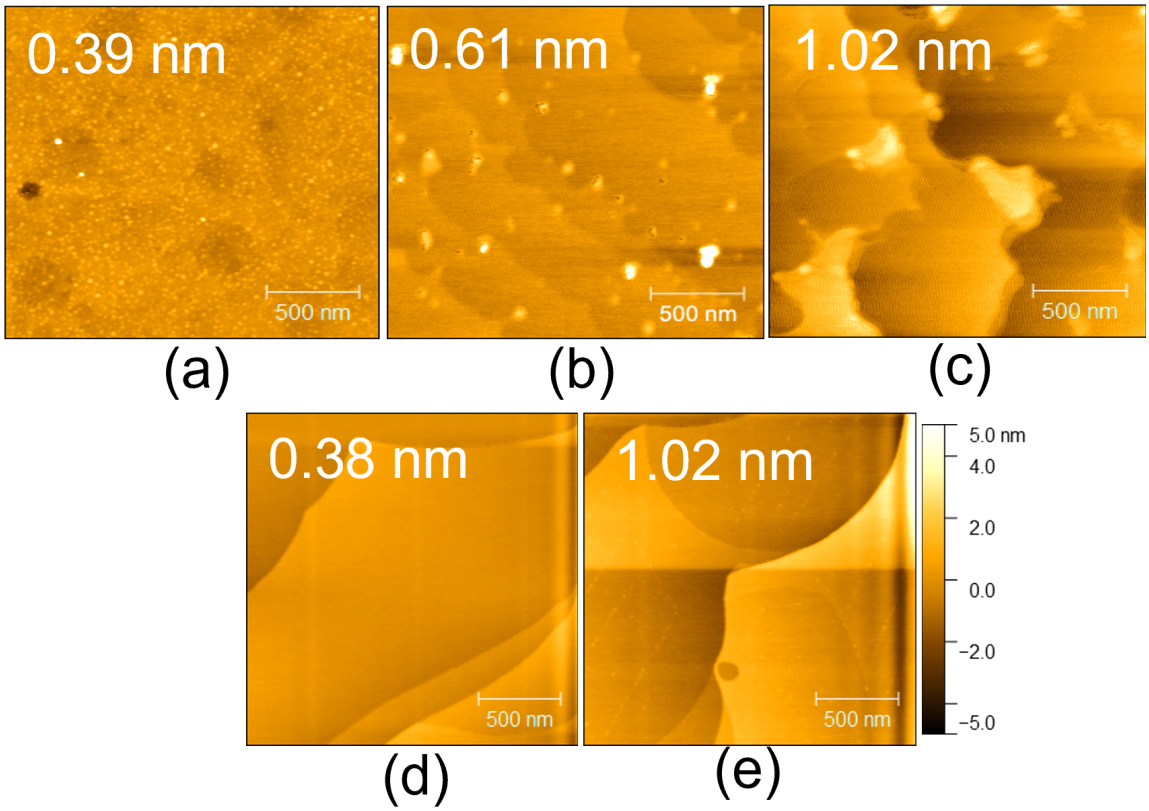

Figure 4.11 AFM scans of 2µmx2µm area of Zn-face ZnO substrate (a) before annealing (b) after annealing at 950 °C for 30 min (c) after annealing at 950 °C for 2h (d) after annealing at 1050 °C for 30 min (e) after annealing at 1050 °C for 1h

Annealing of Zn-face and O-face ZnO substrate in an ambient environment was conducted at different temperatures ranging from 950 °C to 1050 °C for 30 min to 2h. The surface morphology of Zn-face ZnO substrate after annealing at 950 °C for 30 min to 2h showed irregular steps and unclear step edges **(Figure 4.11 (b) and (c))**. An increase in annealing temperature to 1050 °C for 30 min and 60 min improved the surface morphology. The surface morphology showed clear step edges with relatively low RMS roughness (~1nm) **(**

Figure 4.11 **(d) and (e)).** Though the surface showed clear step edges and low roughness, the surface morphology did not show regularity in step height and step edges. This can be related to the surface morphology before treatment.

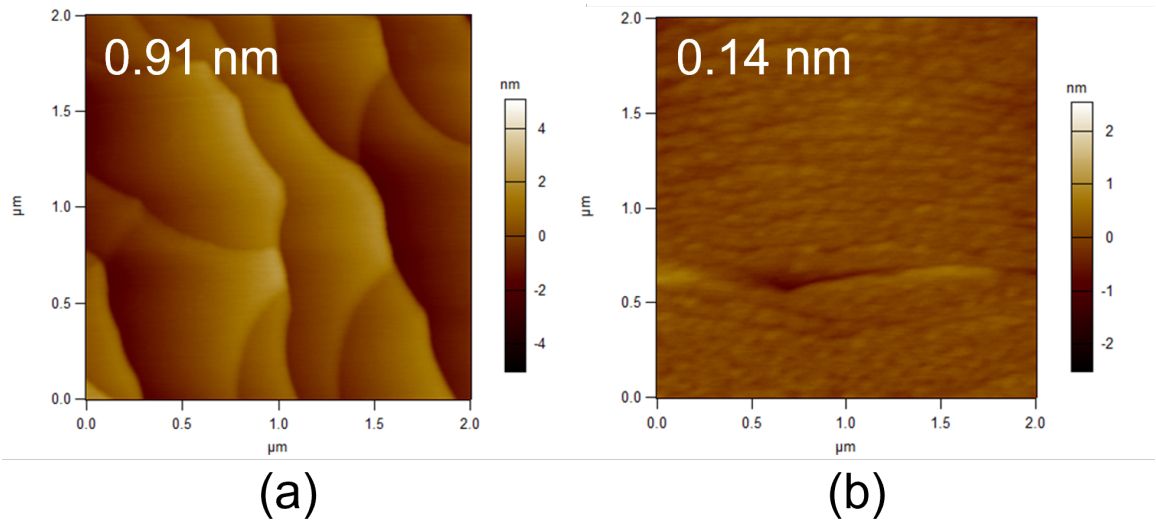

Figure 4.12 AFM scans of Zn-face ZnO substrate (a) after annealing at 1050 °C for 1h following by Ozone treatment (b) after annealing at 1050 °C for 1h with keeping two Zn-face ZnO substrate face to face following ozone and BHF treatment.

The surface morphology after annealing following the ozone treatment shows irregular step edges with relatively high step height (**Figure 4.12 (a)),** which makes step flow growth by MBE challenging. This issue was resolved by introducing an ozone treatment followed by BHF wet etching before the annealing. Additionally, substrates were placed face to face in the furnace in this case to increase Zn vapor pressure and prevent ZnO from dissociation. The BHF and ozone

treatment followed by annealing at 1050 °C for an hour with two substrates placed face to face shows sub-nm RMS surface roughness of 0.14 nm **(Figure 4.12 (b))**.

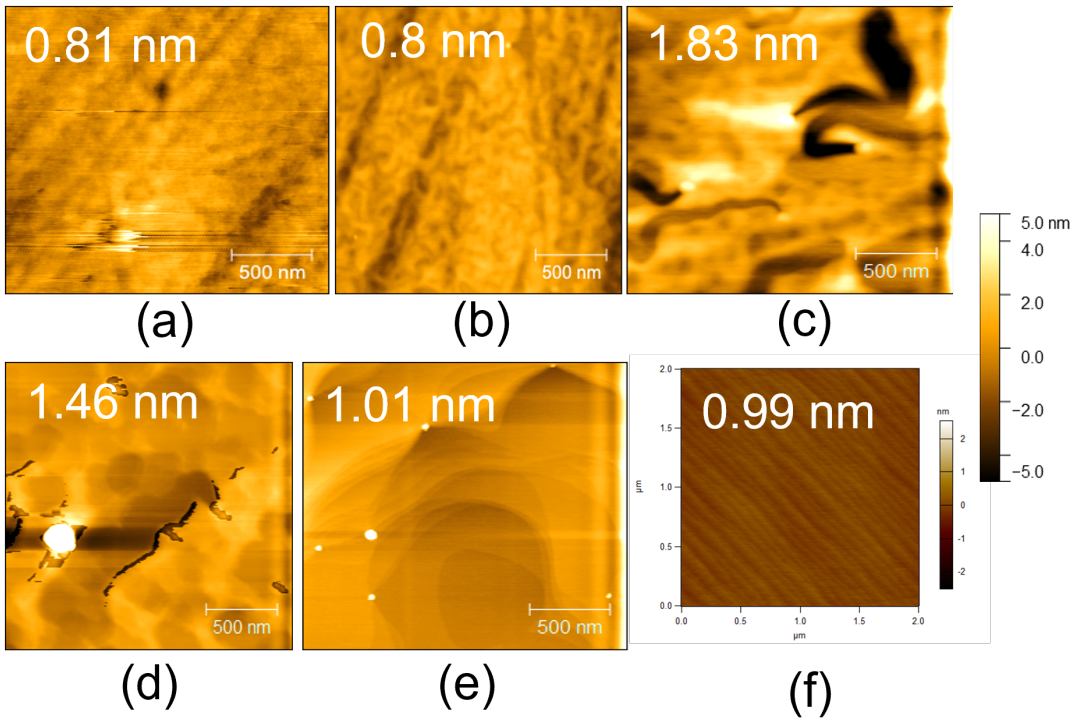

Figure 4.13 AFM scans of 2µmx2µm area of O-face ZnO substrate (a) before annealing (b) after annealing at 950 °C for 30 min (c) after annealing at 950 °C for 2h (d) after annealing at 1050 °C for 30 min (e) after annealing at 1050 °C for 1h (f) after ozone treatment followed by annealing in ambient at 1050 °C for 1h.

Furthermore, the annealing of O-face ZnO substrate was explored similar to Zn-face ZnO substrate. The O-face ZnO substrate was annealed in an ambient environment at different temperatures ranging from 950 °C to 1050 °C for 30 min to 2h. **Figure 4.13 (b) and (c)** show the annealing of O-face ZnO substrate for 30 min and 2h. The surface morphology did not improve after 30 min annealing in ambient, and annealing for 2h in ambient at 950 °C introduced pits in the O-face ZnO substrate surface. This can be related to the ZnO decomposition. The O-face ZnO substrate was annealed at a higher temperature of 1050 °C for 30min (**Figure 4.13(d)**). The surface did not show any drastic improvement. Annealing O-face ZnO substrate at 1050 °C for 1h resulted in irregular step edges (**Figure 4.13 (e)**). O-face ZnO cannot be exposed to BHF etching due to

the high etching rate and high reactivity of O-face ZnO substrate. Therefore, an ozone treatment before the annealing at 1050 °C for 1h was introduced. Furthermore, to stop the decomposition of the O-face ZnO substrate due to the high temperature, the substrates were placed face to face. This led to a smooth surface morphology with clear step edges and ultra-low RMS roughness of ~1nm (**Figure 4.13 (f)).**

Since, the optimum growth conditions for on O-face and Zn-face are different, O-face ZnO substrates for InGaN growths became the research focus of this thesis. One of the main reasons is because O-face showed similar step edges, which is important for epitaxial growths.

4.3 Low Temperature Metal-enhanced Epitaxy of III-Nitrides

One of the main challenges that hindered ZnO from emerging as the common substrate for the growth of nitrides is the interfacial reaction between nitrides and the ZnO [197,198,210]. More recently, high-quality nitride films [211–214] have been achieved on ZnO using pulsed laser deposition (PLD), as this growth technique allows for growth temperatures as low as room temperature, and, therefore, interfacial reaction of nitrides with ZnO can be fully suppressed. On the contrary, the optimum growth temperature for InGaN via MBE is typically between 500 °C and 600 °C. F. Hamdani et al. [185] showed a low temperature thin buffer layer of GaN and $In_{0.2}Ga_{0.8}N$ can help to prevent the interfacial reaction between III-nitride and ZnO.

Epitaxial growth refers to a process where atoms deposit randomly on the growing substrate surface in a properly arranged manner according to the perfect equilibrium atomic configuration. Any deviation from the perfect configuration leads to crystal defects and imperfections. Therefore, lateral diffusion of deposited atoms on the surface is essential for growing high-quality films by MBE. To grow high-quality films, attaining a sufficiently high substrate temperature is important to ensure the diffusivity of metal. The low temperature growth

can lead to 3D island-like structures. A technique called metal enhanced epitaxy (MEE) or metal modulated epitaxy (MME) has been developed previously to allow for lower growth temperatures. In this work, MEE of (In,Ga)N by MBE is performed by alternating between metal (Ga/In) and nitrogen shutters[215–217]. This provides the group III metal atoms enough time to migrate to energetically favorable sites by adatom surface diffusion before reacting with active nitrogen, which can improve the crystal quality of the film grown at low-temperature and decrease the surface roughness. The impact of MEE technique would be negligible for high-temperature growths.

4.3.1 Experimental Details

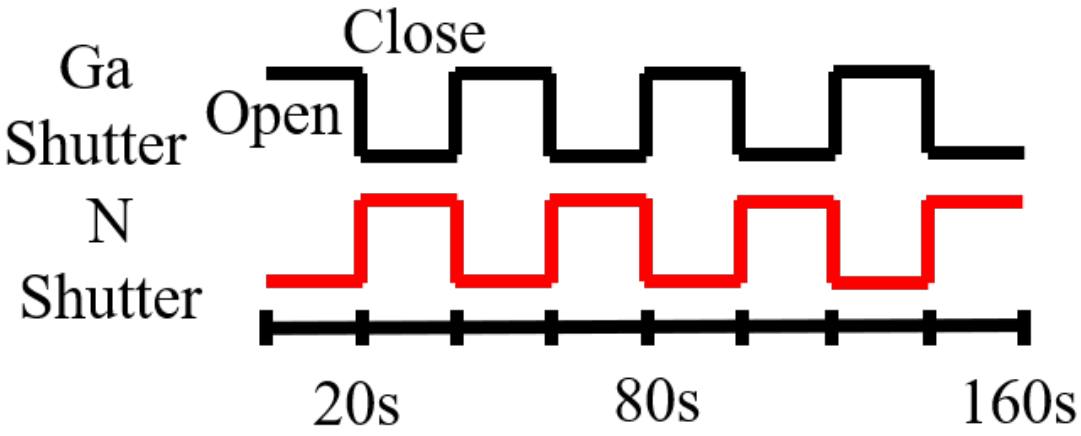

Figure 4.14 Shutter modulation scheme showing Ga and N shutter close and open scheme during the growth period of 160 nm

500 nm- thick Ti was then deposited on the backside of the ZnO substrate via e-beam evaporation to ensure uniform temperature during the growth. Substrates were then cut into ~5 mm x 5mm pieces. All the ZnO substrates were solvent cleaned (acetone, methanol and isopropanol for 4 min each) to remove organic residues from the surface. They were then mounted on a Si substrate by In-bonding, loaded in the MBE exit-entry chamber and baked for 1 hour at

400 °C in the buffer chamber to remove water prior to transferring to the growth chamber. All the growths discussed here were performed in a Veeco GENxplor system equipped with Al, Ga, and In effusion cells and a radio-frequency (RF) plasma source to supply active nitrogen. A plasma power of 350W and N_2 flow of 0.3 sccm were used for the growth. The growth rate with this condition was 150 nm/ hour or ~2.5nm/min at metal rich or intermediate growth regime. The substrate temperature was measured with a thermocouple. For the GaN growth by MEE, a Ga and In beam equivalent flux (BEF) of $4x10^{-8}$ was used. A shutter modulation scheme of 20 s metal shutter open time and 20 s nitrogen shutter open time was used as shown in **Figure 4.14.**

4.3.2 GaN *on ZnO by MEE*

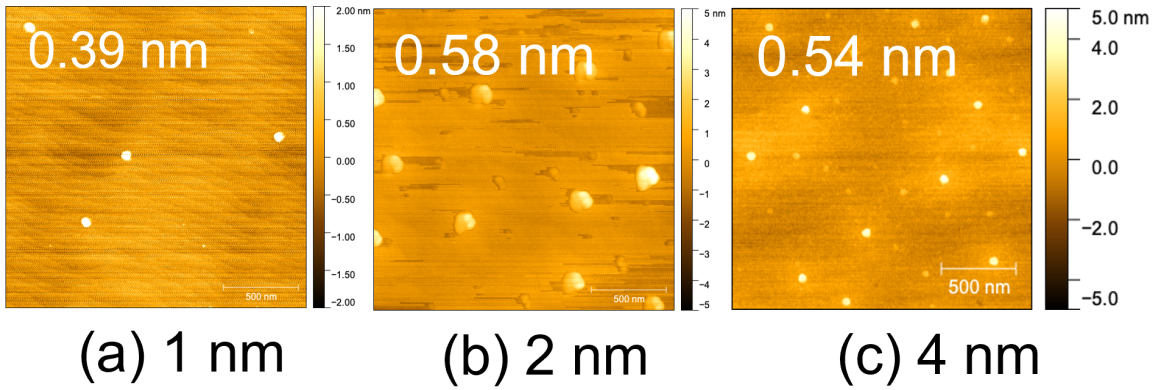

Figure 4.15: 2 µm×2 µm AFM images of GaN thin films grown on O face ZnO (0001) substrates via MEE with a thickness of (a) 1 nm, (b) 2 nm , (c) 4nm showing RMS roughness of 0.39 nm, 0.58 nm and 0.58 nm

Figure 4.15 shows AFM images of GaN samples grown at 450 °C for different thicknesses from 1 nm to 4 nm. Surface morphology of 1 nm GaN showed smooth surface morphology with step edges and RMS roughness of 0.39 nm. With an increase in thickness, the Ga droplets started to appear and surface roughness increased. Furthermore, with an increase in thickness up to 4 nm,

the surface step edges disappeared. Therefore, 1 nm GaN by MEE is the optimum thickness for use as a nucleation layer for InGaN growth on O-face ZnO substrates.

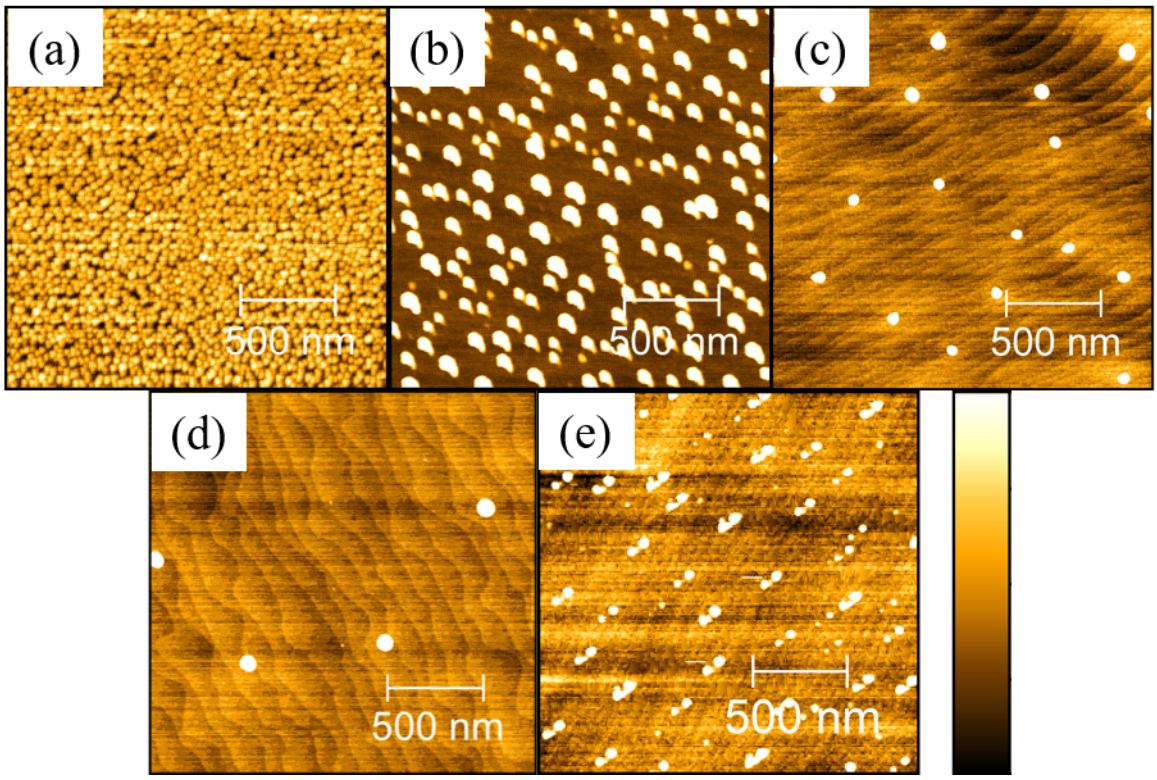

Figure 4.16 2 µm×2 µm AFM images of GaN thin films grown on O face ZnO (0001) substrates via MEE at (a) 350 °C, (b) 400 °C , (c) 430 °C, (d) 450 °C and (e) 460 °C showing RMS roughness of 0.93 nm, 2.6 nm, 1.3 nm, 0.9 nm and 0.57 nm. Scale bar from -3 to 3 nm for (a), and (b) and -1 to 1 nm for (c), (d), (e).

Figure 4.16 ((a)-(e)) shows the AFM image of samples grown at different temperatures. Growing at temperatures below 430 °C led to 3D growth due to very low adatom mobility on the surface, which cannot be overcome via MEE. It is suspected that these 3D features are GaN since increasing the substrate temperature did not remove them as would have been expected for Ga-droplets and instead changed in their shape from circular to a rectangular. Step edges were observed on samples grown at temperatures ranging from 430 °C to 450 °C, confirming a step flow growth. The number of 3D features on the surface also reduced by increasing substrate temperature from 430 °C to 450 °C. By further increasing the temperature to 460 °C, the surface

morphology degraded and more dots appeared, most probably due to a chemical reaction between Ga atoms and the ZnO surface at higher temperatures.

For the rest of samples discussed in this thesis, the growth was initiated with a ~2 MLs-thick GaN layer grown at 440 °C using MEE. The substrate temperature was then raised to a particular temperature to grow 300 nm-thick (In,Ga)N films. Growth of a thin GaN film at low temperature helps to (i) prevent the reaction between Ga/In atoms and the ZnO surface and (ii) reduce ZnO decomposition at elevated temperatures and, consequently, diffusion of Zn atoms in (In,Ga)N films.

4.4 InGaN Growth on O-face ZnO Substrate by PAMBE

4.4.1 Experimental Details

Using this thin layer as the buffer layer as described in **section 4.3**, 300 nm-thick (In,Ga)N films were grown at temperatures ranging from 575 °C to 730 °C. A plasma power of 350W and N_2 flow of 1.0 sccm were used for the growth. The growth rate with this condition was 350 nm/hour or ~5.8nm/min at the metal rich or intermediate growth regime. Samples were analyzed in-situ via RHEED. After growth, high-resolution X-ray diffraction (HRXRD) by automated multipurpose Smartlab X-ray diffractometer was employed. Moreover, surface morphology was measured by a Bruker NanoMan AFM. The polarity of the GaN film was determined by a non-contact, non-destructive Kelvin probe force microscopy (KPFM) technique. Photoluminescence (PL) measurements were performed with the excitation at 325 nm provided by a He-Cd laser. The PL data were analyzed by an Acton Spectrometer with a resolution of 1.0 nm. The room temperature PL spectrum was measured with an excitation intensity of 150 kW/cm^2.

4.4.2 Results and Discussions

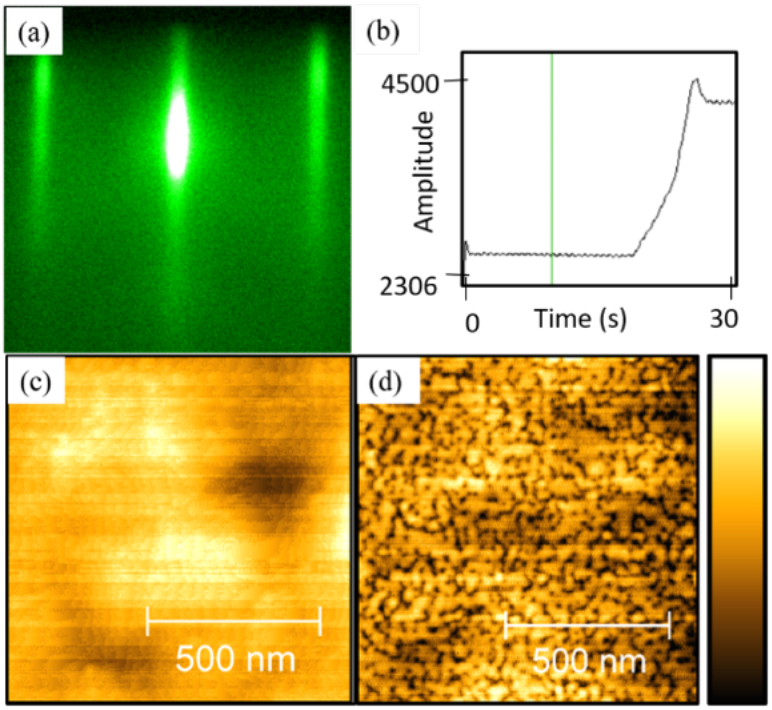

Figure 4.17 Figure 4: (a) RHEED image and (b) intensity amplitude vs time(s) diagram of 300 nm-thick GaN films grown at 730 °C on O-face ZnO substrate. AFM images (1 μm × 1 μm) of the same GaN film taken (c) 2 hours and (d) 2 days after unloading from the MBE chamber. The surface roughness remained relatively constant (~0.57 nm), but the surface morphology degraded significantly. Scale bar from -2 to 2 nm.

Using metal-enhanced epitaxy (MEE), step-flow growth of atomically smooth GaN thin layers on O-face ZnO substrate was demonstrated. In the next step, a 300 nm-thick GaN at 730 °C was grown. N_2 gas flow was set at 1 sccm through the RF-plasma source with 350 W RF power, corresponding to a growth rate of 5 nm/min. The growth was performed in the metal-rich growth regime using a Ga Flux BEP of 4.1 x 10^{-7} Torr, to ensure step flow growth [51,218,219]. **Figure 4.17 (a)** demonstrates a streaky RHEED pattern during and after the growth was completed, confirming atomically smooth GaN film. Growth was interrupted every 20 min to desorb the excess Ga from the surface by closing the Ga shutter and keeping the N shutter open for ~30 s [218,220]. A full desorption of excess Ga was confirmed by a rise in RHEED intensity as shown in **Figure 4.17 (b)**. The sample was taken out of the ultra-high vacuum environment of the MBE

system two days after the growth, and the surface morphology was immediately characterized by AFM. As shown in **Figure 4.17 (c)**, a smooth surface with rms roughness of ~ 0.57 nm was achieved. Spiral hillocks, which are associated with mixed (edge and screw) dislocations, were observed [130]. However, to our surprise, the surface morphology drastically changed after the sample was kept in a N_2 dry box for two days (**Figure 4.17 (d)**). This surface degradation is due to strain because of a 1.8% lattice mismatch between GaN and ZnO and is facilitated by exposure to the ambient environment. Detailed study will be performed in the future to fully understand the onset of this drastic change in surface morphology.

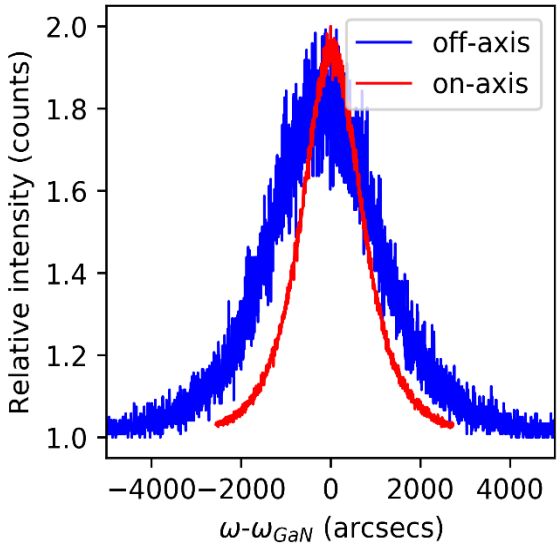

Figure 4.18 X-ray diffraction (XRD) on axis and off-axis rocking curve of 300nm GaN thin films at a high temperature (730 °C) by ω-scans across (0002) and ($10\bar{1}2$) reflections, respectively. The full width at half maximum (FWHM) of on-axis rocking curve is much smaller than that of off-axis rocking curve of GaN thin films.

In order to further analyze the film quality, rocking curves (ω scans) were taken across the on-axis (0002) and off-axis ($10\bar{1}2$) GaN reflections and are shown **in Figure 4.18**. Full width at half maximum (FWHM) of 1589 arcsecs and 2862 arcsecs were measured from on-axis and off-axis ω scans, respectively. The screw and edge dislocations were estimated from these measurements following the method described in [15] to be ~2.45x10^9 cm^{-2} and ~2.1x10^{10} cm^{-2},

respectively. The threading dislocation density is comparable to those previously measured on GaN films grown on ZnO or SiC by PAMBE [158,196]. However, We believe, the eventual degradation of GaN film quality can be mitigated by either passivating the surface or removing the ZnO substrate immediately after the growth by etching in HF [75], which could be integrated into the process flow for flexible electronics [75]. A Platinum-Iridium (Pt-Ir) coated electrically conductive tip was used for the KPFM measurements, and a surface potential profile was obtained in the lift mode by lifting the tip at a 30 nm distance from the sample surface. A surface potential of 0.9 eV was measured on this sample employing KPFM, corresponding to a Ga-polar surface [221].

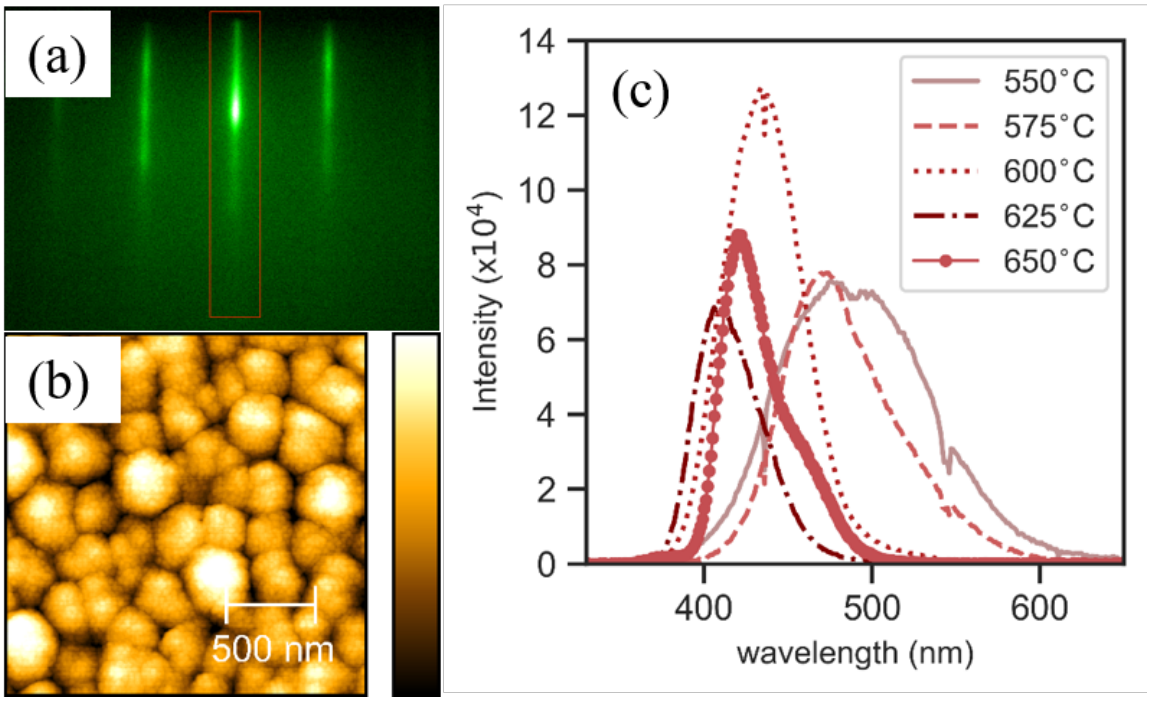

Figure 4.19 (a) RHEED pattern, (b) AFM image (2 µm × 2 µm) of InGaN films grown at 600 °C and (c) room temperature photo-luminescence (PL) spectra of InGaN films grown at different temperatures on GaN/O-face ZnO (0001). AFM scale bar is from -6 to 6 nm.

In the next step, a set of 300 nm-thick InGaN samples was grown, varying substrate temperature from 550 °C to 650 °C while keeping N_2 flow and plasma power constant at 1.0 sccm and 350 W, respectively. As a reminder, for all the samples presented here, the growth was initiated with a ~2 MLs-thick GaN layer grown at 440 °C using MEE. Ga and In fluxes were changed accordingly to maintain a metal-rich growth regime. An atomically smooth surface morphology was achieved as confirmed by a streaky RHEED pattern as shown in **Figure 4.19 (a) and (b),** which show a representative AFM image on these samples indicating a RMS roughness of 2.3nm. As opposed to the GaN sample, the surface morphology on the InGaN films did not degrade over time due to significantly lower lattice mismatch between InGaN and ZnO. Indium content of these films was verified via photoluminescence (PL) measurements at room temperature as shown in **Figure 4.19 (c)** and was varied from 11% to 23% by reducing substrate temperature.

4.4.3 Summary

In summary, ozone treatment followed by annealing at 1050 °C in ambient was proven to be an effective substrate treatment for O-face ZnO substrate. MEE technique was used to enable low temperature growth of GaN thin films on ZnO to suppress interfacial reaction between ZnO and nitrides. We demonstrated step flow growth of 300 nm-thick GaN films showing atomically smooth surface morphology. However, the surface morphology eventually degraded due to the strain built up in GaN. Nonetheless, this result is very promising and can be of potential interest for flexible electronics and optoelectronics applications since the surface morphology degradation can be mitigated by removing the ZnO substrate immediately after the growth. InGaN films with In content ranging from 11% to 23% were also successfully demonstrated by changing substrate temperature.

4.5 Investigation of 1µm-thick InGaN Films Grown on O-face ZnO by Plasma-assisted Molecular Beam Epitaxy

In this work, We have investigated the structural and optical quality of ~1µm-thick InGaN films grown on ZnO using photoluminescence (PL), transmission electron microscopy (TEM), and secondary ion mass spectroscopy (SIMS).

4.5.1 Experimental Details

Commercial O-face ZnO (0001) substrates of size 10 × 10 mm^2 grown by the hydrothermal method were used for this study. An ultra-violet (UV) ozone treatment followed by annealing of the substrate at 1050 °C was performed to obtain atomically smooth surface morphology with step edges. The details on substrate pretreatment can be found elsewhere [139] . To ensure uniform temperature during growth, 500 nm-thick Ti was then deposited on the backside of the substrate via e-beam evaporation. Substrates were then cut into ~5 × 5 mm^2 pieces. All the substrates were solvent (acetone, methanol, and isopropanol for 4 min each) cleaned to remove organic residues from the surface. They were then mounted on a Si substrate by In-bonding, loaded in the molecular beam epitaxy (MBE) exit–entry chamber, and baked for 1h at 400 °C in the buffer chamber to remove water prior to transferring to the growth chamber. A Veeco GENxplor system equipped with Al, Ga, and In effusion cells and a radio-frequency (RF) nitrogen plasma source was employed for all the growths discussed here.

The surface morphology of the sample was recorded by a Bruker NanoMan atomic force microscopy (AFM) after growth. Cross-sectional specimens for transmission electron microscopy (TEM) study were prepared by in-situ focused ion beam (FIB) lift-out methods using a Thermo-Fisher G4 650 Xe Plasma-FIB. Utilizing a Xe plasma ion source instead of a regular Ga source

prevents redistribution of the Ga atoms and changes to the Ga concentration in InGaN films. For final thinning, a 5 keV energy and 10 pA current were used.

A JEOL JEM-3100R05 TEM with a cold-field emission gun equipped with both a probe and an imaging corrector were used for atom-resolved imaging that was operated in scanning transmission electron microscopy (STEM) mode. Both high-angle annular dark-field (HAADF) and bright field-images were taken simultaneously. For diffraction contrast imaging, a TF30F TEM was used that is operated in conventional TEM mode.

The lateral composition uniformity of the InGaN films was characterized by employing a PL spectroscopy setup with a diffraction-limited spot using 405 nm excitation at room temperature. The PL signal was collected using a 60X 0.95 NA objective (Nikon CFI Plan Apochromat Lambda 60XC) and was analyzed using a high-resolution spectrometer (Princeton Instruments IsoPlane SCT 320) coupled to a highly-sensitive CCD camera (Princeton Instruments Pixis: 400). The slit-width at the entrance of the spectrometer was kept at 250 μm with the spectrometer integration time set to 1.0 second. The PL scans were performed by keeping the laser excitation spot at a fixed position and moving the sample by a piezo-nano-positioner stage in ~200 nm steps.

4.5.2 Results and Discussions

The growth of all the samples presented here was initiated with ~2 ML-thick low-temperature GaN at 440 °C by MEE [139]. The substrate temperature was then increased for the growth of InGaN film. Samples A, B, and C were prepared with ~1μm-thick InGaN film grown at

600 °C, 580 °C, and 560 °C, respectively. In and Ga flux were tuned to achieve smooth surface morphology while also maximizing In content in the film.

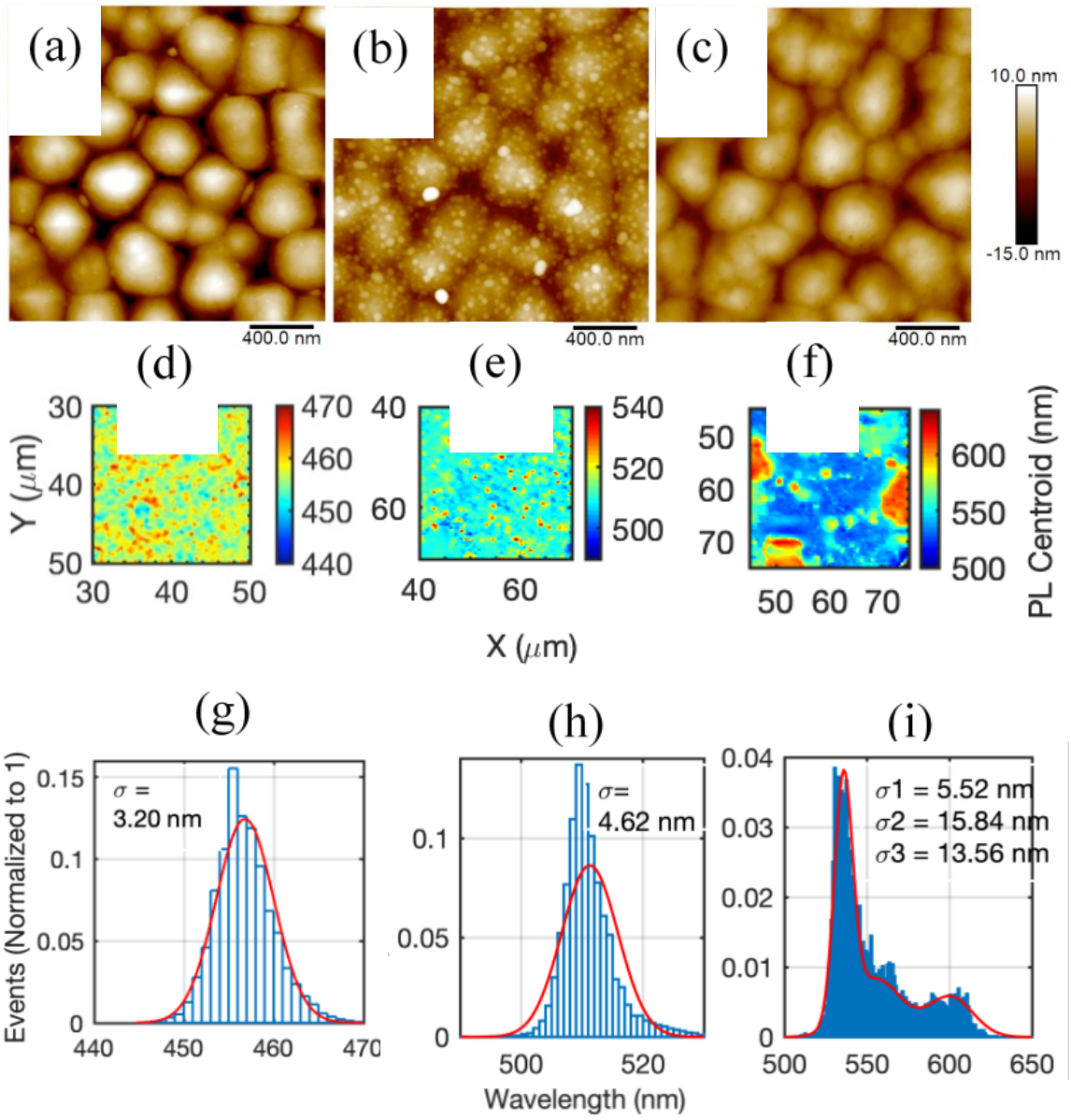

Figure 4.20 (a)-(c) Atomic force microscopy (AFM) images (2μmx2μm) of the InGaN film grown on O-face ZnO (0001) substrate with different substrate temperatures: 600 °C, 580 °C and 560 °C showing a surface roughness of 4.45 nm, 2.6 nm, 2.92 nm. (d)-(f) Photoluminescence (PL) intensity map and (g)-(i) Histogram plot of PL mapping of InGaN film grown on O-face ZnO (0001) substrate with different substrate temperatures: 600 °C, 580 °C and 560 °C showing increase in inhomogeneity in PL map and a shoulder peak at ~600nm (probably due to defects) from histogram plot of PL mapping with decrease in temperature.

Figure 4.20(a)-(c) demonstrate 2x2 μm^2 AFM images on these samples showing spiral hillocks, which are associated with mixed (screw and edge) threading dislocations [130]. Surface

root mean square (rms) roughness of 4.45 nm, 2.6 nm, and 2.92 nm were measured on samples A, B, and C, respectively. 20x20 μm^2 or 30x30 μm^2 PL centroid maps were measured on these samples and are presented in **Figure 4.20(d)-(f).** The centroid histograms of these PL maps are also plotted and shown in **Figure 4.20(g)-(i).** The histogram shows the normalized number of events (pixels) at a specific wavelength. The scales on PL maps were varied to illustrate the lateral wavelength variation in each sample more clearly. Sample A, grown at 600 °C, is relatively uniform. The centroid histogram can be fitted with a unimodal bell-shape distribution with a center wavelength and variance of 456 nm and 3.2 nm respectively. Sample B, grown at 580 °C, is also relatively uniform. The centroid histogram can also be fitted with a unimodal bell curve having center wavelength of 501 nm and a slightly higher variance of 4.6 nm. The average In incorporation was estimated from the center wavelength using equation $Eg=x\ Eg_{InN}+(1-x)\ Eg_{GaN}-1.4\ x(1-x)$. In incorporation in the film increased from 19.6% to 25% by reducing the growth temperature from 600 °C to 580 °C. In contrast, the PL map of sample C, grown at 560 °C, shows a non-uniform film with PL peak varying laterally from 530 nm to 620 nm. The non-uniformity is clearly evident from the multimodal fitting of the centroid histogram extracted from PL mapping.

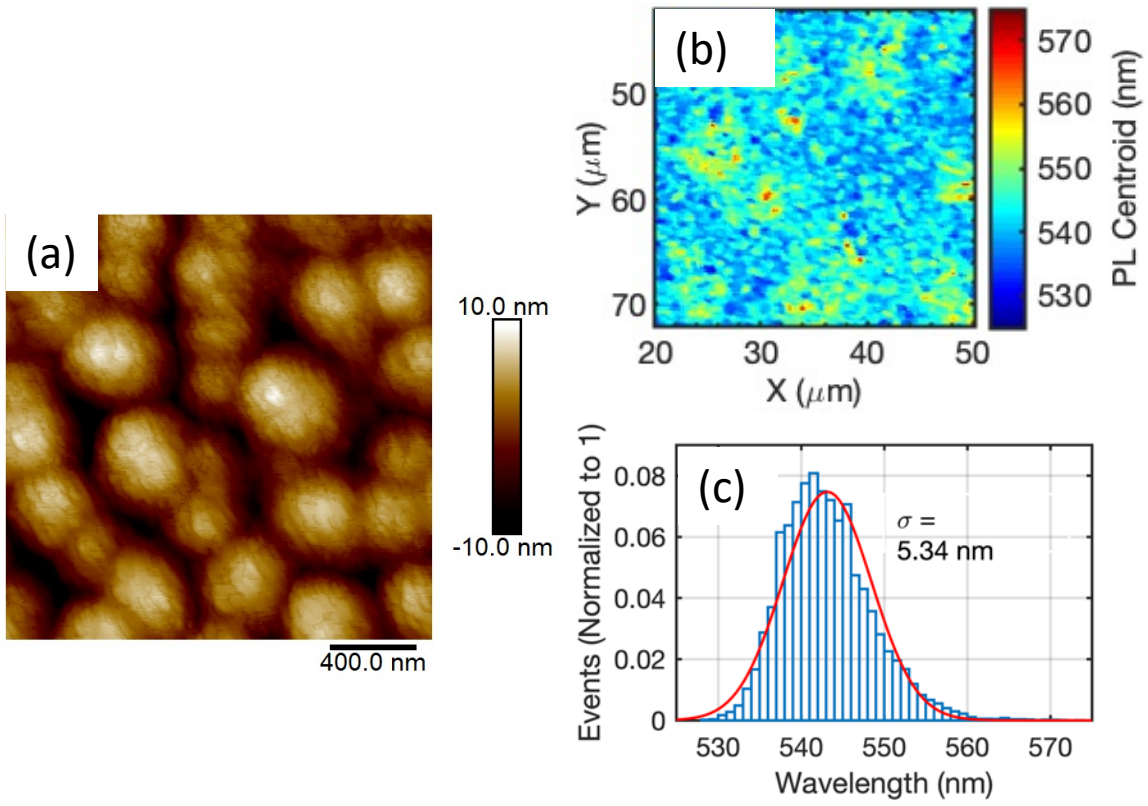

Figure 4.21 (a) AFM images (2μm x 2μm) of the InGaN film grown on O-face ZnO (0001) substrate at 560 °C with periodic annealing showing a surface roughness of 3.36 nm. (b) PL intensity map and (c) histogram plot of PL mapping of InGaN film.

In the next step, to improve the uniformity of the sample grown at 560 °C, the temperature was raised to 730 °C every 20 min (~100 nm-thick InGaN). To prevent InGaN decomposition at elevated temperatures, 2nm-thick GaN was grown before raising the temperature. After reaching to 730 °C, the sample was cooled to 560 °C to grow additional InGaN. The surface morphology was not changed significantly, and an rms roughness of 3.36 nm was measured from the AFM image recorded on this sample **(Figure 4.21(a))**. As the PL map and the histogram shown in **Figure 4.21 (b) and (c)** demonstrate, the film uniformity was improved significantly, and a PL peak around 542 nm was achieved.

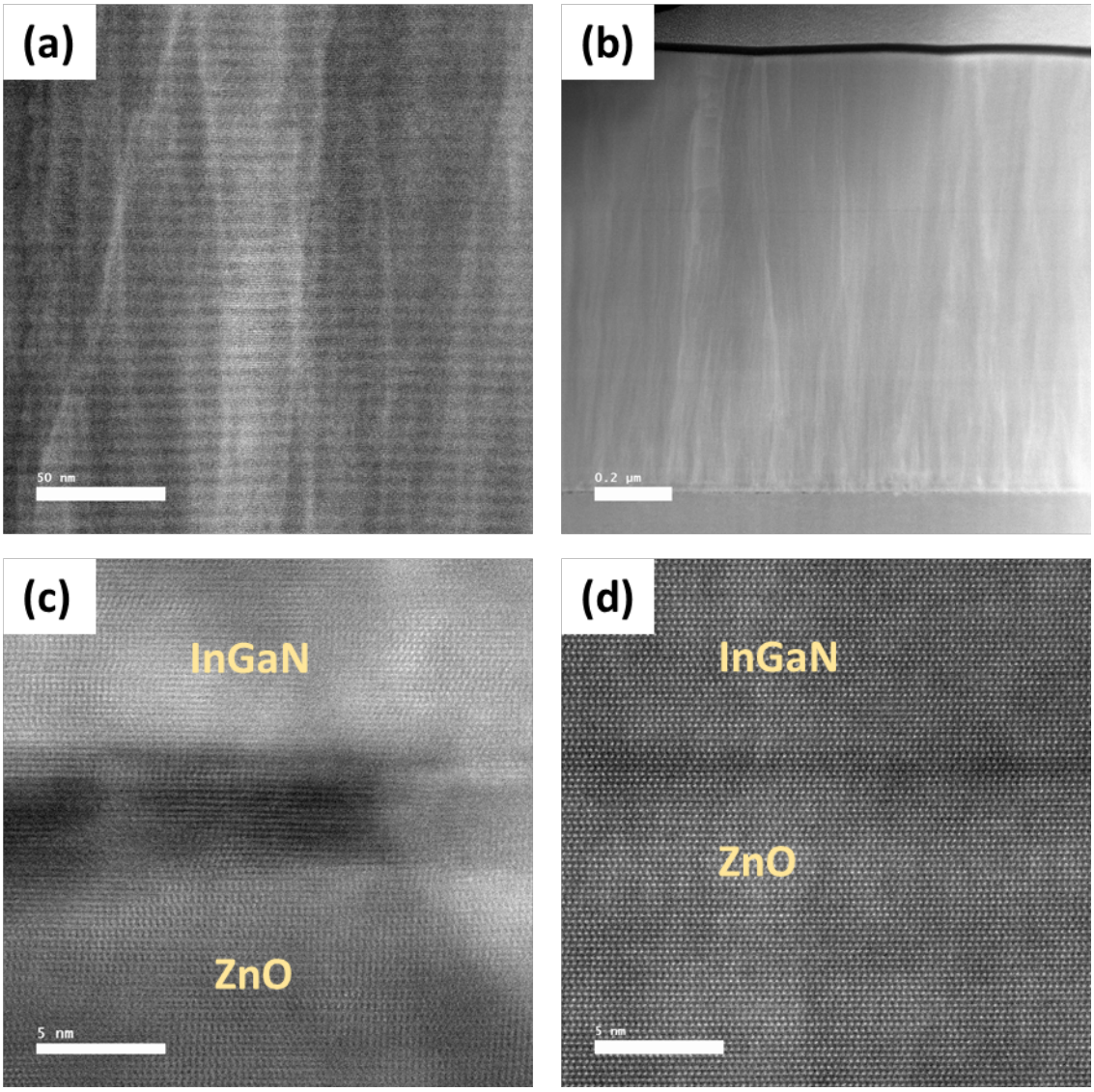

Figure 4.22 STEM-HAADF images taken from sample A showing (a) formation of a superlattice structure; (b) the dislocation coalesced with thickness to decrease the dislocation density; (c) a region with poor oxide interfacial layer formed and (d) a region without an oxide interfacial layer.

Figure 4.22 (a) is a high-resolution STEM-HAADF image taken from sample A, which confirmed the formation of a self-assembled InGaN-GaN superlattice structure. Such a phenomenon was recently reported by our group on InGaN films grown at similar growth conditions on GaN [174,175,222]. However, the self-assembled superlattice structure on GaN was composed of ~3 nm-thick GaN and ~2.4 nm-thick $In_{0.2}Ga_{0.8}N$. This indicates that, in addition to

the growth conditions, strain may play a role in determining the periodicity of the superlattice structures. As mentioned in **Chapter 2**, compositional modulation in InGaN can occur only due to high surface diffusion rate initiating the surface separation during growth due to the high substrate temperature during growth [142–144,223]. Compositional modulation in InGaN may require high lattice mismatch, which can result in a rougher surface. The rougher surface morphology is necessary to ensure partial elastic relaxation and to allow spinodal-like decomposition at the grown surface. However, further studies are required to fully understand the cause of such self-assembled superlattice structures.

A low magnification STEM-HAADF image of sample A shown in **Figure 4.22 (b)** revealed generation of a large density of threading dislocations at the interface. A large portion of the dislocations was annihilated by bending and merging as the film thickness increased, leading to a significantly lower TDD at the top layer of the 1 μm-thick InGaN. **Figure 4.22 (c) and (d)** show high-resolution STEM-HAADF images taken from two different regions of the ZnO-InGaN interface. A poor-quality interfacial layer can be observed from **Figure 4.22 (c)** due to chemical reactions between oxygen in ZnO and In/Ga adatoms at elevated temperatures. On the contrary, **Figure 4.22 (d)** shows a clean and abrupt interface. Variation in the interface quality may be attributed to the variation in the thickness of the low-temperature (LT) GaN grown using MEE technique. 2 ML-thick LT GaN may not be thick enough to fully cover the ZnO surface. Hence, in the areas that are not capped with a thin GaN film, an interfacial poor-quality oxide film grows at elevated temperatures. Initiating the growth with a thicker LT GaN may be beneficial to maintain an abrupt interface throughout the sample.

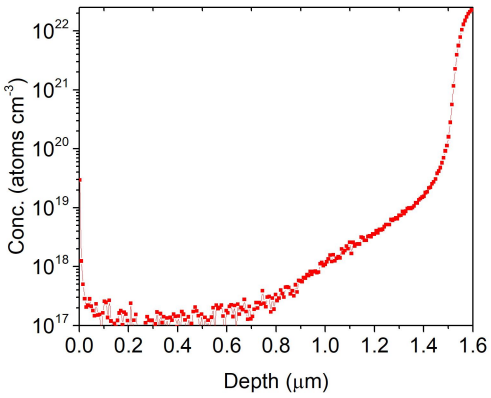

Figure 4.23 Zn profile in GaN/InGaN layers on ZnO substrate SIMS data showing the Zn diffusion through the InGaN films.

SIMS analysis (**Figure 4.23**) of a sample grown at similar conditions as sample A showed a significant diffusion of Zn atoms into InGaN film, which was eventually reduced to $1x10^{17}$ cm^{-3} as the film thickness increased. This may be due to an exponential increase in Zn atoms diffusion coefficient beyond 300-400 °C and a relatively high growth temperature of 610 °C. Zn substituting Ga sites (Zn_{Ga}) can be a possible acceptor in III-nitrides [224–226]. Zn_{Ga} is predicted to be an acceptor with a binding energy of 330-400meV with first principle calculation and experimental values deducted from optical spectroscopy. Later calculations determined this value to 450 meV, which is higher than the ionization energy of Mg acceptor. However, Zn substituting N-site (Zn_N) was proposed to explain the high resistive nature of Zn doped III-nitrides and Zn can bond with three electrons from the nearest donors resulting in a semi-insulating III-nitride. Therefore, Zn diffusing to InGaN can be a candidate to make semi-insulating InGaN as a pseudo-substrate. Additionally, growth of a thicker LT GaN could also help with the reduction of Zn diffusion and will be studied in the future.

4.5.3 Summary

In summary, successful growth of high-quality 1μm-thick InGaN with In content ranging from 19.5% to 30.5% on ZnO substrate by plasma-assisted molecular beam epitaxy was

demonstrated. PL analysis showed a relatively uniform InGaN composition spatially on samples grown at 600 °C and 580 °C. Lowering the growth temperature to 560 °C led to clusters with higher In content. The composition uniformity was recovered on this sample by periodically raising in the temperature during the growth. High-resolution STEM-HAADF image taken from sample grown at 600 °C confirmed the formation of a self-assembled InGaN-GaN superlattice structure. Although STEM image showed a high threading dislocation density generated at the substrate interface, TDD reduced significantly through annihilation of dislocations as InGaN thickness was increased. A significant diffusion of Zn was also observed in the InGaN, which was eventually reduced to $1x10^{17}$ cm^{-3} as InGaN thickness increased.

Chapter 5 Relaxation of InGaN on Ga-polar Porous GaN on Si Substrate

5.1 Introduction

As discussed in the earlier chapters, one of the daunting challenges to achieve amber and particularly red LEDs is the growth of InGaN with high In content with good structural and optical properties. The difficulty of high-In-content InGaN quantum wells is due to the large lattice mismatch (10%) and different thermal stability between InN and GaN [50,227]. Another phenomenon that makes achieving efficient amber/red InGaN LEDs difficult is quantum confined stark effect (QCSE), which will be discussed below. A relaxed InGaN pseudo-substrate can help to overcome these issues as discussed earlier. For this purpose, we investigated growth of InGaN on porousified GaN compliant template, which will be discussed in this chapter.

5.1.1 Quantum Confined Stark Effect (QCSE)

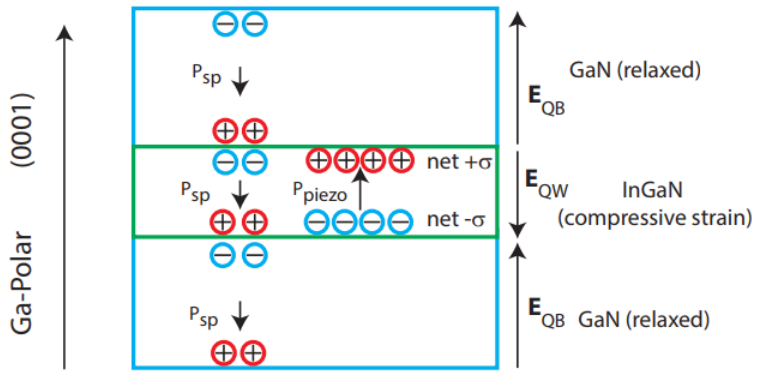

Figure 5.1 Schematic of the spontaneous and piezoelectric induced polarization directions, and resultant electric field in a single InGaN quantum wellbetween two GaN barriers. The InGaN is compressively strained and the GaN layers are taken to be relaxed ***Courtesy: M. Wallace (2016) [228, 229]***

The use of QWs in LEDs enables carrier confinement into a small fraction of the device, known as an active layer. Besides, the light emission wavelength can be varied by tuning the alloy composition of the confined QW layer. The effect of strong net polarization resulting from spontaneous and piezoelectric polarization in an InGaN/GaN QW is shown in **Figure 5.1** [228,229]. In the relaxed GaN layers, there is only spontaneous polarization due to absence of strain, while in the InGaN layer both spontaneous and piezoelectric polarizations exist. As a result, in InGaN/GaN QWs, the strong net polarization charge at the interface results in large electric fields, in the range of 1.5-3 $MVcm^{-1}$ [230–232]. The relationship between the electric field and polarization can be determined by the following Equation 5-1

$$F_{qw} = \frac{P_{sp,b} - P_{sp,qw}}{\varepsilon_{e,qw}\,\varepsilon_0} - \frac{P_{pz,qw}}{\varepsilon_{e,qw}\,\varepsilon_0}$$

Equation 5-1

Where $P_{sp,b}$ is the spontaneous polarization of the barrier, and $\varepsilon_{e,qw}$ is the relative dielectric permittivity of the QW material.

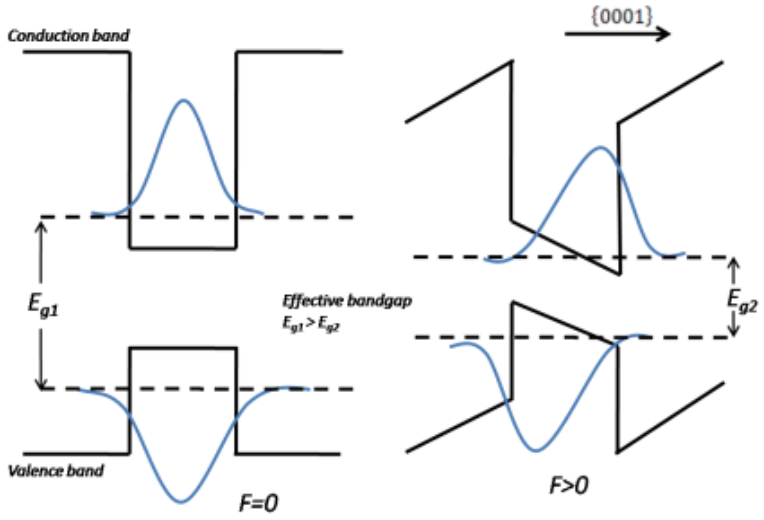

Figure 5.2 Quantum confined stark effect: QW without electric field (left) and with electric field (right) ***Courtesy: S. Alam [235]***

The polarization-induced electric field can introduce an inclination of the valence band and conduction band edges in the QW [233,234]. Therefore, with the tilt in the valence and conduction band, electrons are driven to the lower corner of the conduction band, and holes are driven to the upper corner of the valence band. This leads to spatial separation of electrons and holes, resulting in a decrease in an overlap of the respective wave functions, which is called the quantum confined stark effect (QCSE) **(Figure 5.2)** [235]. This can reduce the recombination probability in the active region. With higher In content, the strain increases due to the increase in lattice constant, leading to an increase in the piezoelectric field and exacerbation of QCSE.

Therefore, to resolve these issues, introducing a relaxed $In_xGa_{1-x}N$ film on porous GaN layer as a pseudo-substrate (PS) for the growth of $In_zGa_{1-z}N$-based structure z>x has been proposed [236]. This decreases the lattice mismatch between the $In_zGa_{1-z}N$ layer and $In_xGa_{1-x}N$ PS as compared to the lattice mismatch between $In_zGa_{1-z}N$ layer and GaN substrate.

5.1.2 Porous GaN

A porous medium or material is a medium or material consisting of voids or pores instead of being solid [237]. The term nano-porous material usually refers broadly to a material with a pore size of 100nm or less. Depending on the characteristics length (d) of pores, nano-porous materials can be classified as macroporous (d<2nm), mesoporous (2nm<d<50nm) and microporous (d>50nm) materials. Porosifying a bulk solid material can affect its materials and physical properties drastically. Micro-porous and mesoporous materials have been widely

explored for catalysis applications due to their surface-to-volume ratio [238]. Porous Si has been pursued extensively due to its unexpected light emission from low dimensional structures [239].

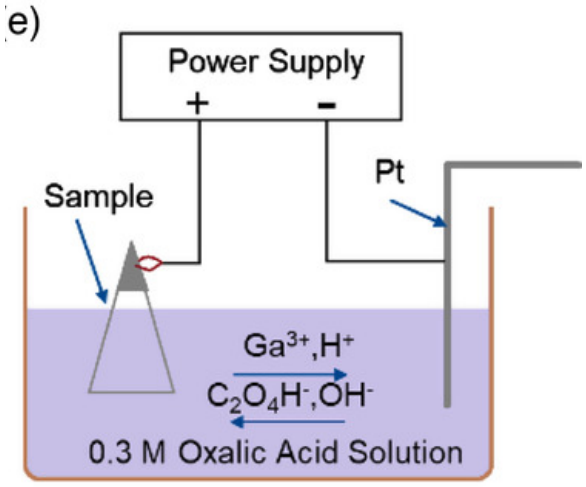

Figure 5.3 Schematic of the electrochemical cell. ***Courtesy: S. Keller et al. [83]***

Recently, Han research group at Yale University reported nano-porous-GaN by electrochemically etching [240,241]. Porous GaN maintains its single crystalline behavior while it shows different unique characteristics [237]. Nano-porous-GaN introduces optical inhomogeneity in a way that visible light gets scattered during its propagation. Enhancement in scattering can enhance light emitting diode (LED) performance e.g., external quantum efficiency (EQE). Patterned mesoporous GaN can engineer the index of refraction of GaN. The elastic modulus and hardness of nano-porous-GaN can be reduced with an increase in porosity akin to porous Si.

The basic setup for electrochemical etching consists of **(Figure 5.3)**:

1) A nitride-based sample which will be porosified connected to the anode.
2) An inert electrode, connected to the cathode, usually platinum
3) An electrolyte, forming an ionic conduction path between the electrodes, e.g, oxalic acid

4) An applied bias between the anode and cathode from a voltage or current source [83]

Within this basic setup there are variety of choices that can be made of nitride-based sample structures, electrolytes, and applied potential. There can be differences in physical setup, e.g. adding a known reference electrode (e.g. Ag/AgCl) or the use of a stirrer or pump to continuously flow the electrolyte [6].

When a positive bias (anode) is applied to the n+ type GaN sample dipped in an acid-based electrolyte (e.g., Oxalic acid), the n+ GaN becomes oxidized by the holes in the surface inversion layer [237,240–242]. The oxidation of GaN is an electrochemical reaction driven by holes and can be expressed as Equation 5-2

$$2GaN + 6h^{+} \rightarrow 2Ga^{3+} + N_2$$

Equation 5-2

The oxide layer in the surface (Ga^{3+} ions) is then dissolved in a suitable electrolyte [243]. This is now accepted as the mechanism for electrochemical etching of nitrides [244,245]. Besides, it has also been reported that if pure water is used as an electrolyte for the same electrochemical

etching (EC) etching, the surface is oxidized but the oxide cannot be dissolved, leading to no porosification of the nitrides [246] .

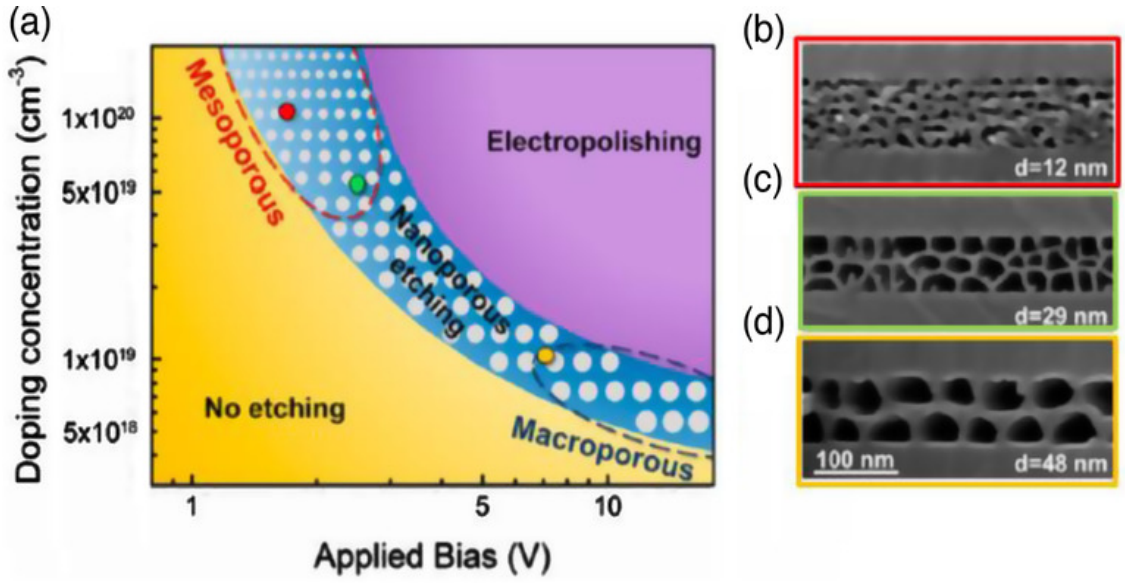

Figure 5.4 a) Processing phase diagram for EC etching. b–d) Cross-sectional SEM images of u.i.d. GaN/GaN:Si/u.i.d. GaN structures with different Si doping in the GaN:Si layer after porosification according to the conditions marked by the red (b), green (c), and yellow (d) points in (a). The GaN:Si layers reacted in the electrochemical cell under formation of porous GaN, whereas the u.i.d. layers were unaffected ***Courtesy: C. Zhang et al.*** *[237]*

For an EC etching, there are two important parameters: the anodic bias and conductivity of the layers (doping concentrations) [237]. An etching phase diagram is illustrated in **Figure 5.4 (a)** showing three regions of porosification depending on these two essential parameters. **Figure 5.4 (b-d)** shows the dependency where the doping concentration was varied from $1x1^{19}$ to $1x10^{20}$ cm^{-3}, corresponding to the red, green and yellow dots in **Figure 5.4 (a).** The nano-porous-GaN can show morphologies ranging from microporous (d~50nm; **Figure 5.4(d))** to mesoporous (d~30nm; **Figure 5.4(c)**) and approaching microporous (d~10nm; **Figure 5.4b)** in the upper left portion of the phase diagram [237,242]. When applied bias voltage or the doping concentration is low, no chemical reaction in GaN happens, and GaN remains intact (yellow region). With an increase in the applied bias or the doping concentration, the electrostatic break starts with the injection of

holes into certain localized hot spots, leading to porosification of the structures through localized dissolution (blue region). At a higher applied bias or doping concentration, electropolishing or complete etching occurs (purple region) [237,242]

5.1.3 Relaxed InGaN on Porous GaN by MOCVD

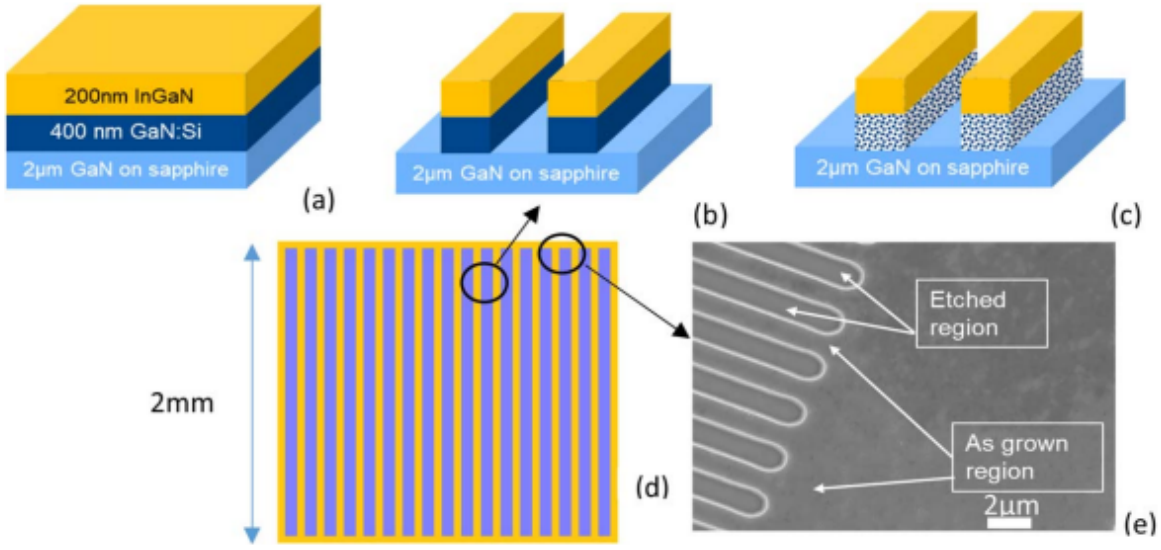

Figure 5.5 . (a) Sample consisting of 200 nm $In_xGa_{1-x}N$ ($x \geq .08$) on top of 400 nm of GaN:Si with a doping of 5 × 10^{18} cm^{-3} , on 2 µm thick u.i.d. GaN base layers on sapphire substrate. (b) Sample structure after patterning into 2, 5, or 10 µm wide and 2 mm long fins, (c) followed by a doping selective electrochemical etch, leading to porosification of the GaN:Si layer. (d) Top view representative schematic (not to scale) of the 2 mm × 2 mm die after patterning and dry etch, (e) SEM image of the edge of the die. ***Courtesy: S. S. Pasayat [78]***

Recently S. S. Pasayat et al. [78,79] reported a novel technique, which can enable elastic uniaxial and biaxial relaxation of a GaN stripe and tiles buried underneath InGaN, respectively, in the micron regime (1-10 µm) without substrate transfer and with the capability of using conventional substrates e.g., SiC, sapphire and Si etc. They developed a recipe to porosify the GaN:Si interlayer to allow relaxation of (In,Ga)N layer on top of it, which was biaxially strained to GaN before porosification (**Figure 5.5**) [78]. The porous GaN mechanical stiffness reduces with an increase in porosity due to high surface-to-volume ratio. The degree of relaxation of the top InGaN layer is strongly dependent on the nano-stripe width in addition to the applied voltage in

the EC cell. In addition, the InGaN relaxation was confirmed to increase with increasing degree of porosification of the embedded porous GaN layer and decreasing tile size [78]. The relaxation perpendicular to stripe direction increased with a decrease in nano-stripe width. Interestingly, a small relaxation (~10%) was observed along the stripe direction as well (**Figure 5.6**). These observations corroborated the importance of free sidewall surface for the relaxation process. With the narrower stripe, the top InGaN layer can expand perpendicular to the stripe direction, leading to relaxation of InGaN by releasing strain. Since a decrease in stripe-width increases relaxation, it shows higher relaxation at a higher aspect ratio similar to nanostructures e.g., nanopillars and nanostrips. Similarly, decreasing the tile size of the PS of relaxed InGaN regrowth leads to higher relaxation. **Figure 5.6** shows that with an increase in porosification voltage, the relaxation of the InGaN top layers increased [78]. This shows the comparison of relaxation parallel and perpendicular to the fin [78–80] .

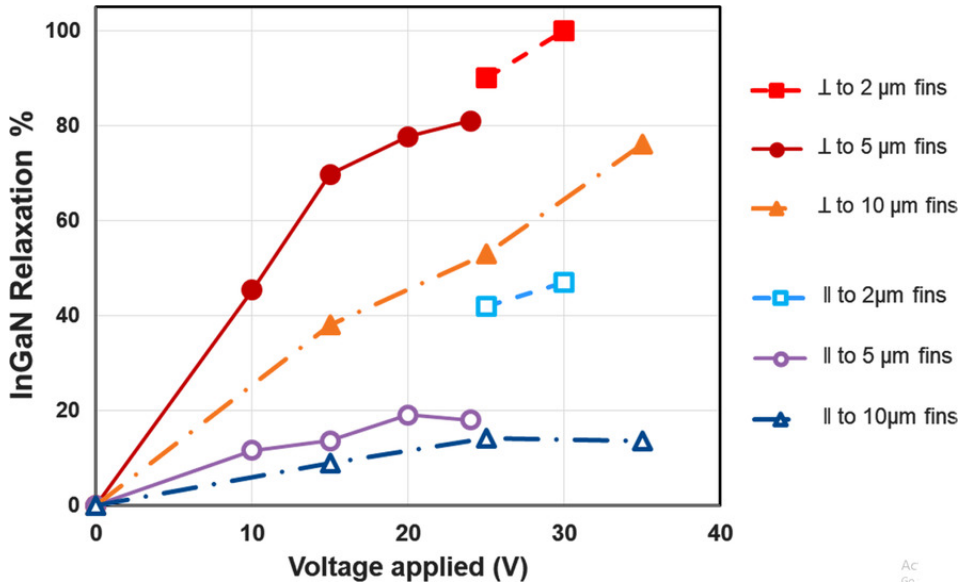

Figure 5.6 Degree of relaxation perpendicular and parallel to the fins versus applied voltage for samples with varying fin widths ***Courtesy: S. S. Pasayat [78]***

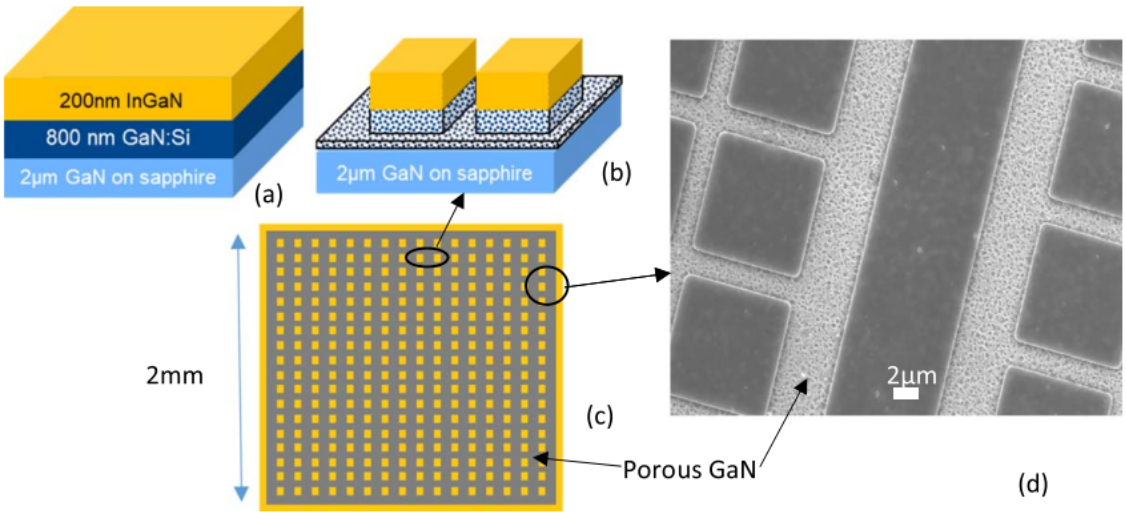

Figure 5.7 (a) Sample consisting of 200 nm $In_xGa_{1-x}N$ (x = 0.08) on top of 800 nm of GaN:Si with a doping of 5 × 10^{18} cm^{-3} , on 2 µm thick u.i.d. GaN base layers on sapphire substrate. (b) Sample structure after patterning into 10 µm × 10 µm square tiles, followed by a doping selective electrochemical etch, leading to porosification of the GaN:Si layer.(c) Top view representative schematic (not to scale) of the 2 mm × 2 mm die after patterning and dry etch, (d) SEM image of the edge of the die. ***Courtesy: S. S. Pasayat [78]***

A fin structure showed primarily in uni-axial relaxation and then the pattern was modified to 10 µm × 10 µm square tiles (µLED regime) to enable bi-axial relaxation. They also reported the compliant nature of the $In_xGa_{1-x}N$ PS on porosified GaN:Si tiles (**shown in Figure 5.7**), which can enable elastic relaxation instead of plastic relaxation of bulk $In_zGa_{1-z}N$ regrowth by metal organic chemical vapor deposition (MOCVD) on relaxed $In_xGa_{1-x}N$ on porous GaN PS [78,79,86]. InGaN/GaN MQWs regrown on porous PS with tiled geometry resulted in a redshift of 45nm with respect to MQWs grown on reference planar GaN on sapphire. However, V-defects were observed on InGaN on GaN PS, which are very typical for InGaN films grown by MOCVD [247]. These surface V-defects can cause issues with scalability and reliability.

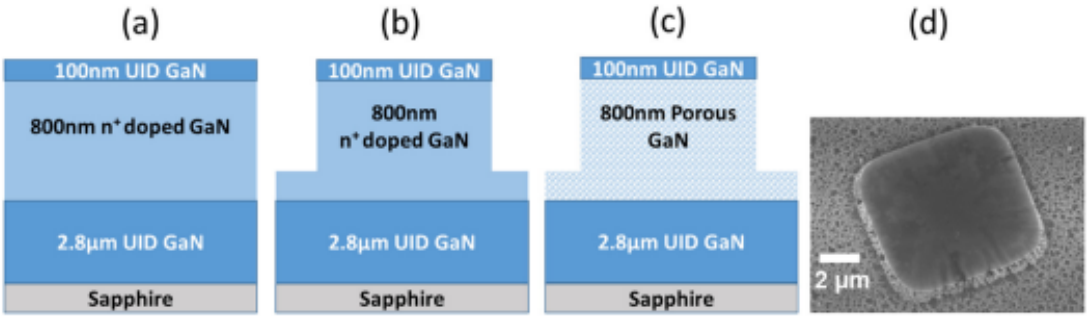

Figure 5.8 (a) Sample consisting of 200 nm $In_xGa_{1-x}N$ (x = 0.08) on top of 800 nm of GaN:Si with a doping of 5 × 10^{18} cm^{-3} , on 2 µm thick u.i.d. GaN base layers on sapphire substrate. (b) Sample structure after patterning into 10 µm × 10 µm square tiles, followed by a doping selective electrochemical etch, leading to porosification of the GaN:Si layer.(c) Top view representative schematic (not to scale) of the 2 mm × 2 mm die after patterning and dry etch, (d) SEM image of the edge of the die ***Courtesy: S. S. Pasayat [85]***

After observing the compliant nature of the thin (In,Ga)N layer above porous GaN tiles, recently, they have substituted a square patterned compliant (In,Ga)N by GaN to improve the surface morphology and decrease the V-defects (**Figure 5.8**) [85]. Compliant GaN on porous GaN pseudo-substrates (PS) can be used an universal substrate for growth of relaxed (In,Ga,Al)N materials. The higher In or Al incorporation in these (In,Ga,Al)N films is higher than that of GaN on sapphire substrate due to composition pulling effect [248]. Recently, there have been several attempts to regrow relaxed or partially relaxed InGaN or AlGaN layers on these compliant GaN on porous GaN pseudo-substrates by MOCVD [78,83–86,249,250]. By growing InGaN on UID GaN on porous GaN tiles by metal-organic chemical vapor deposition (MOCVD), Pasayat et al. [86], demonstrated 65% relaxed $In_{0.11}Ga_{0.89}N$ corresponding to fully relaxed $In_{0.07}Ga_{0.93}N$. However, MOCVD growth of thick InGaN layers is challenging due to the high vapor pressure of nitrogen over InGaN and its low thermal stability. In addition, MOCVD InGaN films often exhibit V-defects. InGaN regrowth on porous GaN by molecular beam epitaxy was recently reported by

Wurm et al. [251]. An extensive study of InGaN regrowth on porous GaN by MBE is still to be performed.

5.2 Demonstration of 82% Relaxed $In_{0.18}Ga_{0.82}N$ on Porous GaN Pseudo-substrate by PAMBE

In this work, the impact of film thickness on relaxation was studied along with different types of compositionally graded InGaN epi-structures [68]. The surface morphology and crystal structure of regrown InGaN were studied by atomic force microscopy (AFM). Strain relaxation and In-content in InGaN were studied by off-axis X-ray diffraction reciprocal space mapping (XRD-RSM). The MBE InGaN films exhibited spiral surface morphology free of V-defects. $In_xGa_{1-x}N/In_yGa_{1-y}N$ multi-quantum wells (MQWs) grown on the PAMBE-grown InGaN-on-porous- GaN tiles by MOCVD showed a clear 85nm redshift in comparison to those grown on planar InGaN on GaN. Additionally, the impact of the degree of porosification on the dislocation density of regrown InGaN was studied by scanning transmission electron microscopy (STEM).

5.2.1 Experimental Details

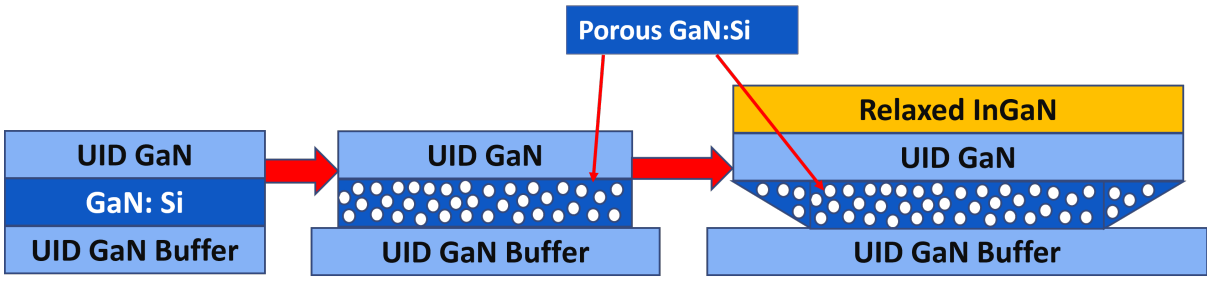

Figure 5.9 Shchematic of Porosification and regrowth of InGaN on porous GaN on GaN PS by MBE

For simplicity, GaN-on-porous GaN tiled pseudo-substrates will be referred to as "PS". Commercially grown GaN/GaN:Si/GaN (2 μm/0.8 μm/0.1 μm) on Si substrates were used in this

study. The process flow to obtain the final relaxed InGaN layers grown on PS (**Figure 5.9**) is laid out as such: (i) patterning of 10 μm × 10 μm tiles and 6 μm × 6 μm tiles of GaN on Si substrates; (ii) porosification of GaN:Si layer by EC etching; and (iii) PAMBE growth of GaN/InGaN. 10 × 10 μm^2 and 6 × 6 μm^2 tiles with 2 μm and 1 μm spacing between them, respectively, were defined by reactive ion etching (RIE) using a 100 W BCl_3/Cl_2 etch chemistry. The RIE etch defining the tiles went through the top 0.1 μm GaN:UID layer and approximately 0.45 μm into the GaN:Si layer. Porosification of the GaN:Si layers was done in a 0.3M oxalic acid solution, where the GaN:Si layer acted as the anode and a Pt wire in the solution acted as the cathode. It is important to note that the top 100 nm UID GaN layers are not porosified as they are meant to provide a smooth surface for subsequent MBE regrowth. Doping and electro-chemical etch conditions in this study were similar to past work from Pasayat et. al. [78], which resulted in 50%–60% porosification of the GaN:Si layer. Following porosification, the samples were subjected to a solvent clean and hydrofluoric acid (HF) dip prior to MBE growth.

In this study PAMBE growth was carried out using a Veeco GENxplor MBE system equipped with conventional Ga, Al, In effusion cells and a radio frequency (RF) plasma source to supply activated nitrogen. The substrates were first solvent cleaned (acetone, methanol, and isopropanol for 4 min each) to remove organic residues from the surface, and then mounted on a Si substrate using molten In before being loaded in the MBE exit-entry chamber. An hour of baking in the load lock chamber was performed at 200 °C followed by an hour of baking at 400 °C in the buffer chamber to remove any water prior to transferring the substrate to the growth chamber. During the growth, the substrate temperature was measured and monitored using a thermocouple. The growth was monitored in situ via reflection high-energy electron diffraction (RHEED). 1 SCCM of 99.9995% pure N2 was supplied via an RF plasma source powered at 350 W, which

corresponds to a growth rate of ~5.8 nm/min for GaN in a metal-rich growth regime. Background pressure in the chamber during growth was approximately 1 x 10^{-5} Torr.

To attain uniform surface morphology for InGaN regrowth by PAMBE, all growths in this study were initiated with a 30 nm thick GaN buffer layer grown at 740 °C with a Ga beam equivalent pressure (BEP) of 6.4 x 10^{-7} T, which corresponds metal (Ga)-rich conditions. Excess Ga was desorbed after GaN growth by closing the Ga shutter while keeping the N-shutter open. Following the initial GaN growth, the substrate temperature was lowered to approximately 610 °C while interrupting the growth for 20 min to allow for temperature stabilization [218,252]. InGaN growth was then carried out under metal (In)-rich conditions [175,222]. Following InGaN growth, the sample was capped with approximately 4 nm of GaN grown at 610 °C to protect the InGaN layer during the regrowth of high-temperature $In_xGa_{1-x}N/In_yGa_{1-y}N$ MQW by MOCVD. A streaky RHEED pattern was recorded on the sample during and after the growth ended, confirming an atomically smooth surface morphology.

Several InGaN samples were first grown on planar substrates for calibration. Afterward, several samples were grown to study surface morphology, composition, strain, and relaxation of InGaN films grown on GaN PS and to optimize the growth parameters and porosification of tiles. MQW regrowth on the MBE InGaN base layer was performed by atmospheric pressure MOCVD using triethylgallium (TEG), trimethylindium (TMI), and triethylindium (TEI) as group-III precursors and ammonia as the nitrogen precursor. The regrown MQW structure consisted of 3 InGaN QWs, which were grown at 810 °C with TMI as the In precursor, and $In_{0.05}Ga_{0.95}N$ barriers grown at 830 °C with TEI. All layers were deposited using N_2 as the carrier gas.

The surface morphology of every sample was characterized post-growth by atomic force microscopy (AFM) using a Bruker NanoMan atomic force microscopy (AFM) tool. Off-axis,

$[\bar{1}\bar{1}24]$ reflection, and x-ray diffraction (XRD) (ω-2θ)-ω reciprocal space map (RSM) scans were also carried out using a Philips X'PERT MPD X-ray source, which has a Philips high intensity ceramic sealed 3kW tube that produces a wavelength of 1.5405 Å for Cu Ka. Composition and relaxation were determined from the experimental XRD–RSM data using X-Pert Epitaxy software. The new in-plane lattice constant (a_{new}) was calculated from Equation 5-3 Vegard's law taken from S. Pereira et. al. [253]

$$a_{new} = 3.1893 \times \left\{1 - \left(x_{In} \times \frac{R}{100}\right)\right\} + 3.538 \times x_{In} \times \frac{R}{100}$$

Equation 5-3

where 3:1893 Å and 3:538 Å are the relaxed in-plane lattice constants for GaN and InN, respectively. x_{In} and R refer to the In-composition and relaxation values extracted from the RSM scans respectively. In determining a_{new} from Eq. (1) using the R and x_{In} values extracted from XRD–RSM data, the equivalent fully relaxed In composition ($x_{In,equiv.}$) can be determined by setting R = 100%, $x_{In} = x_{In,equiv.}$ in Eq. (1) and solving for $x_{In,equiv.}$.

Scanning transmission electron microscopy (STEM) study on a cross-sectional specimen was prepared on the sample with the thickest (~1 μm) InGaN on PS. STEM sample prep was performed using an in situ focused ion beam (FIB) lift-out method performed using FEI Helios 450 and was thinned to electron transparency. A Hitachi HD2300 STEM system was used for imaging the microstructures of the specimen. The microscope was operated at 200 keV in STEM mode with lens settings that define a probe smaller than 0.1 nm. Annular dark-field (HAADF) imaging was performed together with bright-field (BF) imaging simultaneously.

To examine light emission from active regions grown on relaxed PS, room temperature photoluminescence (RT PL) was carried out on samples with MOCVD grown MQWs using a 325 nm He-Cd laser source.

5.2.2 Results and Discussions

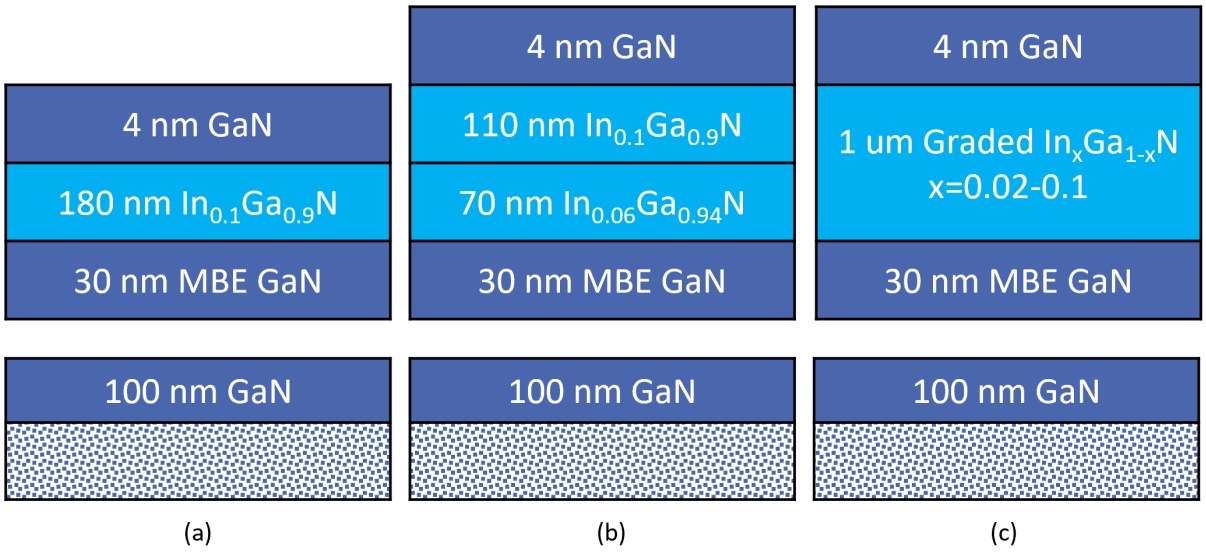

Figure 5.10: Schematic of GaN/InGaN/GaN grown on GaN PS with different tiles size of 10 µm x 10 µm (sample A1-A3) and 6 µm x 6 µm(sample B1-B3) for samples A1, B1 (a), samples A2, B2 (b) and samples A3, B3 (c).

Schematics of epi-structure grown in this study are shown in **Figure 5.10**. For samples A1-A3 InGaN films were grown on PS GaN with 10 µm x 10 µm tiles spaced 2 µm apart whereas for sample B1-B3, InGaN films were grown on PS GaN with 6 µm x 6 µm tiles spaced 1 µm apart. For both samples A1 and B1, $In_{0.1}Ga_{0.9}N$ (180 nm) films were grown on GaN PS and for samples A2 and B2, $In_{0.1}Ga_{0.9}N$ (110 nm)/ $In_{0.06}Ga_{0.94}N$ (70 nm) films were grown on GaN PS at a substrate temperature of 610 °C. In incorporation was changed from $In_{0.06}Ga_{0.94}N$ (70 nm) to $In_{0.1}Ga_{0.9}N$ (110nm) by decreasing the Ga flux gradually with a decrease in Ga cell temperature with 1 °C/min ramp rate. For samples A3 and B3, a 1 µm $In_xGa_{1-x}N$ layer was grown where x_{In} was graded from 0% to 20% by decreasing Ga flux by reducing Ga cell temperature and increasing In flux by increasing the In cell temperature with a 1 °C/min ramp rate.

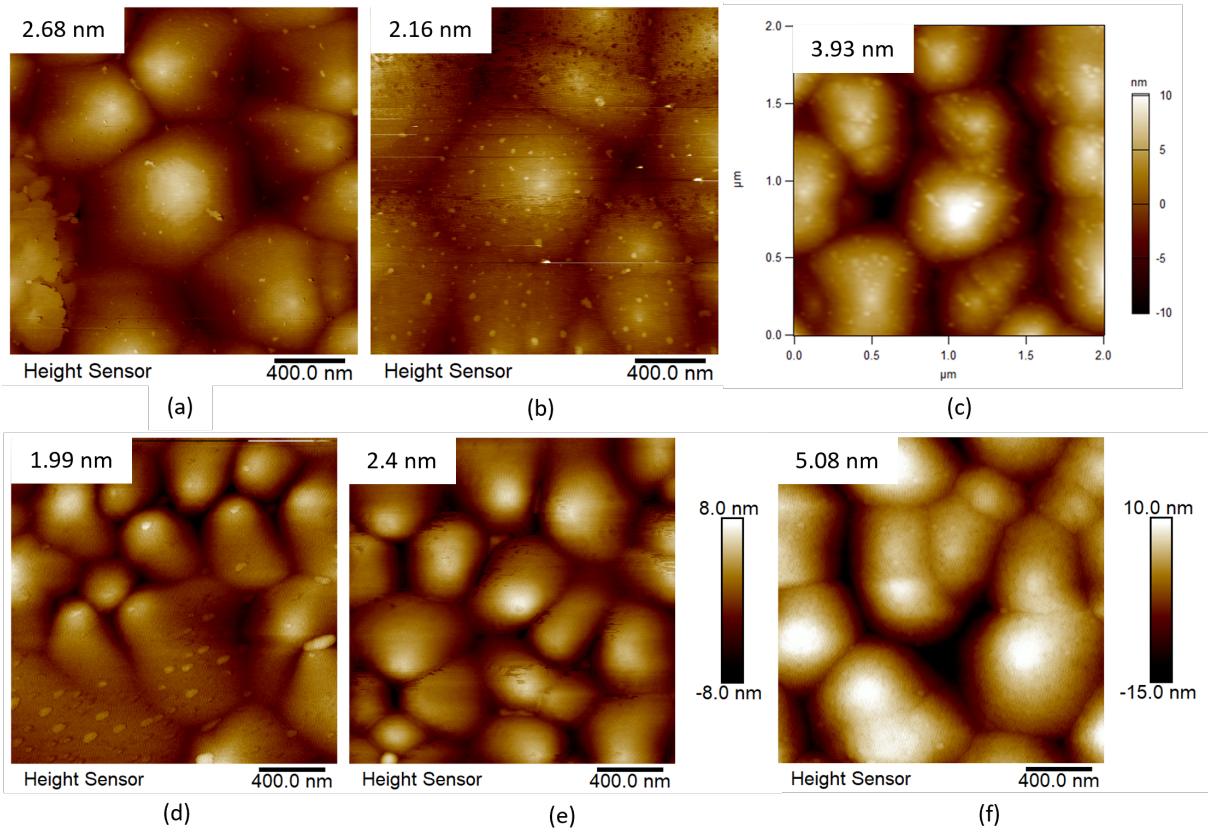

Figure 5.11: 2 µm x 2 µm AFM images of (a-c) InGaN grown on GaN PS for sample A1-A3 with tiles size of 10 µm x 10 µm and (d-f) sample B1-B3 with tiles size of 6 µm x 6 µm. Sample A1 (a), sample A2 (b) and sample A3(c) show surface roughness of 2.68 nm, 2.16 nm and 3.93 nm, respectively. Sample B1 (d), sample B2 (e) and sample B3 (f) show surface roughness of 1.99 nm, 2.4 nm and 5.08 nm, respectively. The RMS roughness shows that with increase in grading and thickness, surface roughness and dislocation density increases.

Figure 5.11 (a-c) and (d-f) show the surface morphology of InGaN films grown on GaN PS with 10 µm x 10 µm tiles (sample A1-A3) and 6 µm x 6 µm tiles (sample B1-B3), respectively. The surface root mean square (RMS) roughness extracted from AFM for samples A1, A2, and A3 were found to be 2.7 nm, 2.2 nm, and 3.9 nm, respectively. The surface RMS roughness on samples B1, B2, and B3 were found to be 2 nm, 2.4 nm, and 5.1 nm, respectively. All of the samples exhibited spiral hillocks, which radiate around screw and mixed-type dislocations, which is characteristic of III-nitride growth in the metal-rich growth regime [130,254]. Samples with a total thickness of 180 nm (samples A1, A2, B1, and B2) showed smooth surface morphology with clear step edges as observed by the AFM images. On the other hand, samples with ~1µm-thick

InGaN (samples A3 and B3) showed an increase in spiral hillock density, indicating an increase in the dislocation density. Interestingly, none of the samples showed V-defects, pits or cross-hatching like features on the surface, which were observed previously in InGaN films grown on GaN PS by MOCVD or PAMBE [84,251].

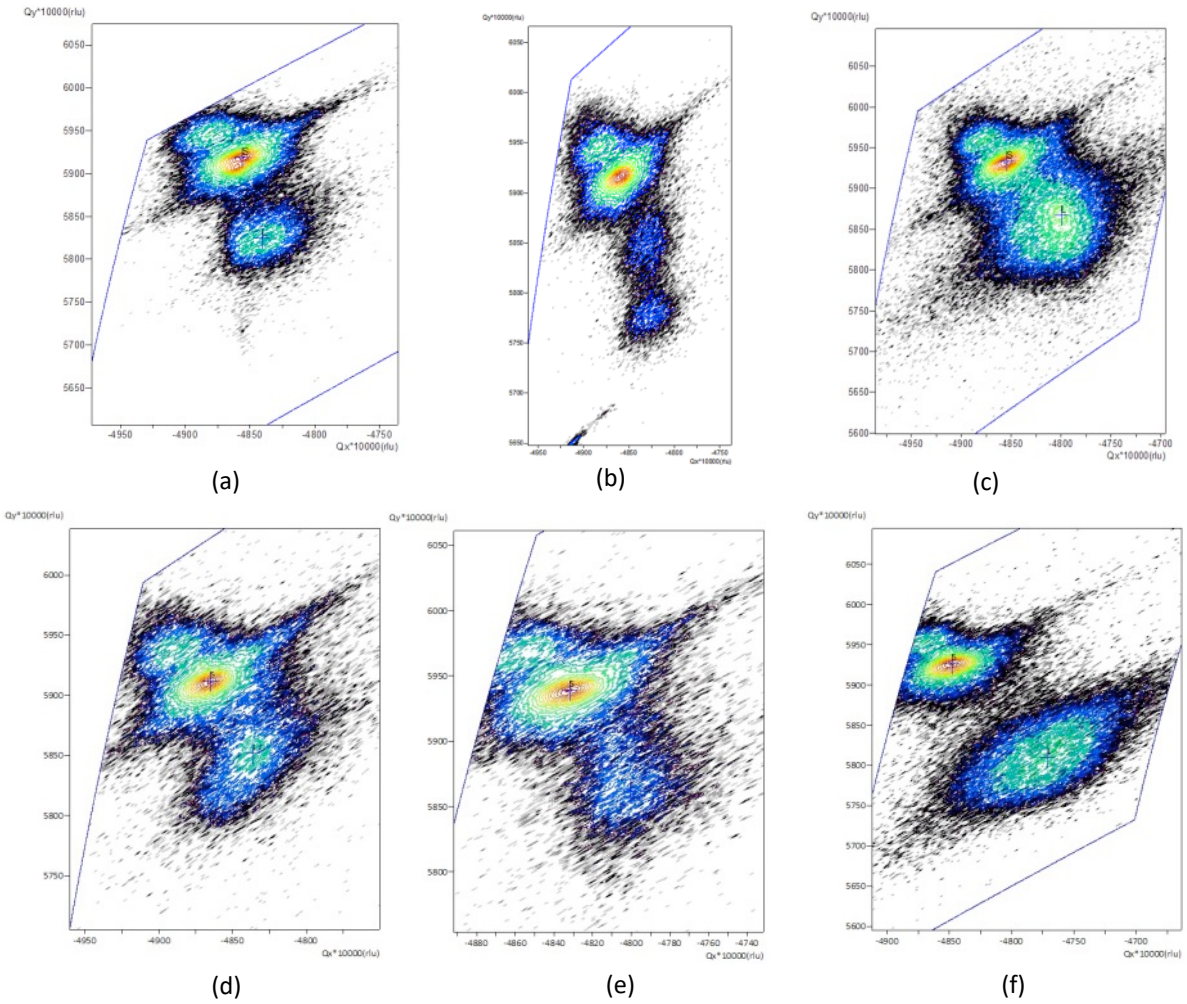

Figure 5.12 X-ray diffraction-reciprocal space mapping (XRD-RSM) scans toward $[\bar{1}\bar{1}24]$ *direction for (a-c) sample A1-A3, InGaN grown on GaN PS with 10 µm x 10 µm tiles size and (d-f) sample B1-B3, InGaN grown on GaN PS with 6 µm x 6 µm. The vertical dashed line running down from the GaN peak shows the strain line while the other tilted dashed line is the fully relaxed line.*

Figure 5.12 shows the XRD-RSM toward the $[\bar{1}\bar{1}24]$ direction for all of the samples discussed earlier. The relaxation for samples A1, A2, and A3 were calculated to be 26.1%, 35.7%, and 95.1%, respectively, corresponding to an $x_{In,equiv.}$ of 2.94%, 6.12%, and 10.43%, respectively.

Table 5-1 Sample information and results for each sample in this study. From left to right, each column corresponds to the sample name, tiles size, InGaN thickness, extracted In incorporation from XRD-RSM, relaxation, new in-plane lattice constant, equivalent relaxed In composition calculated from Equation 5-3and surface roughness value extracted from 2 µm x 2 µm AFM scans. Tiles size correspond to the size of each of the tiles after EC.

Sample Name	Tile size (µm x µm)	Thickness (nm)	X_{In}(%)	R (%)	a_{new} (Å)	$X_{In,\ equiv}$ (%)	RMS (nm)
A1	10 x 10	180	11.3	26.1	3.2	2.94	2.68
A2	10 x 10	180	17.2	35.7	3.211	6.12	2.16
A3	10 x 10	1000	11	95.1	3.226	10.43	3.93
B1	6 x 6	180	9.5	53.6	3.207	5.08	1.99
B2	6 x 6	180	10.5	56.7	3.21	5.93	2.4
B3	6 x 6	1000	18.1	81.2	3.241	14.6	5.08

To study the impact of tile size on relaxation and In incorporation in InGaN, similar structure samples B1-B3 were grown on GaN PS with a tile size of 6 µm x 6 µm. The relaxation for samples B1, B2, and B3 were calculated to be 53.6%, 56.7%, and 81.2%, respectively, corresponding to an $x_{In,equiv.}$ of 5.08%, 5.93%, and 14.6%, respectively. The detailed and

systematic comparison of all of the samples in this study are given in **Table 5-1.**

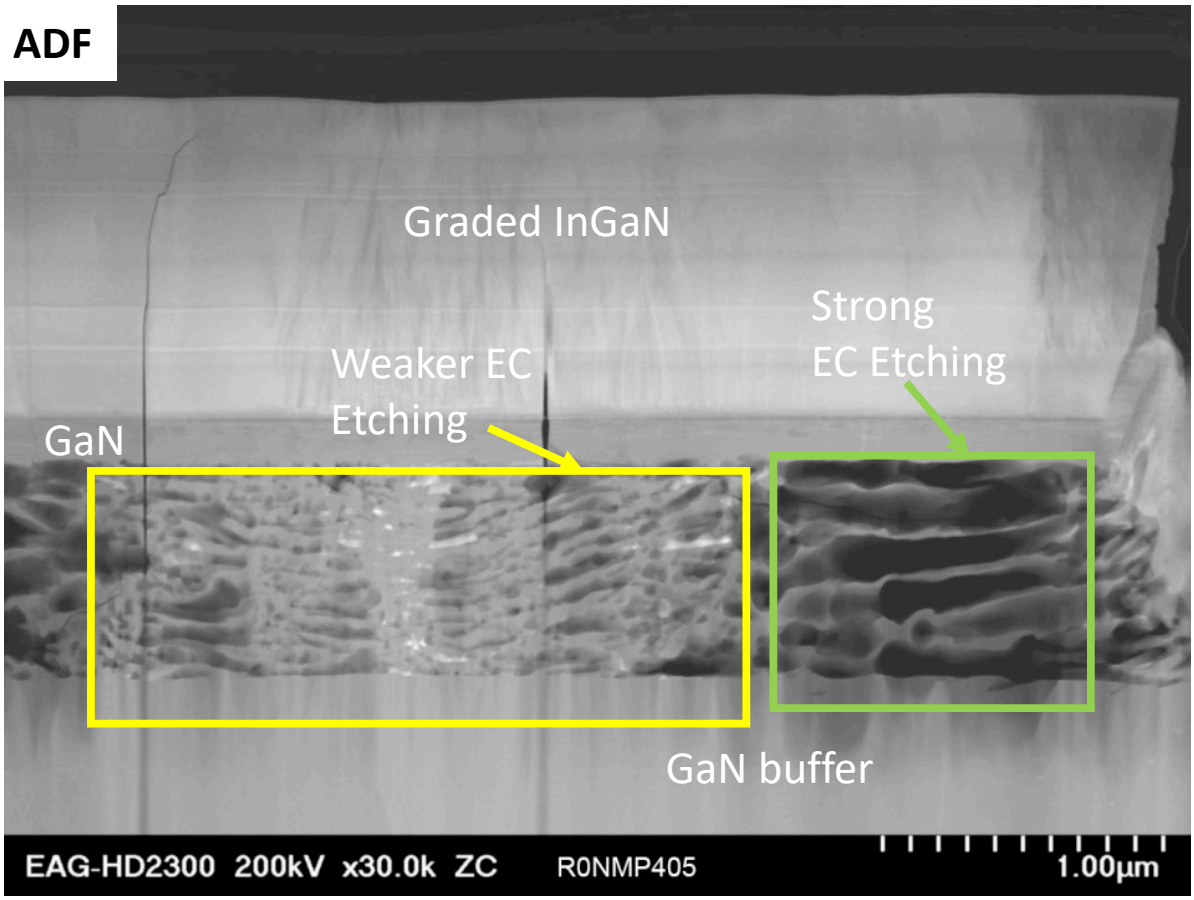

Figure 5.13: Annular dark field (ADF) Scanning transmission electron microscopy (STEM) image of graded InGaN grown on GaN PS. The yellow region shows incomplete porosification in GaN:Si layer whereas the green region shows complete porosification in GaN:Si layer. The 1 ~µm thick InGaN shows the InGaN grown on the green region shows less dislocation whereas InGaN grown on the yellow region shows a lot more dislocation due to incomplete porosification.

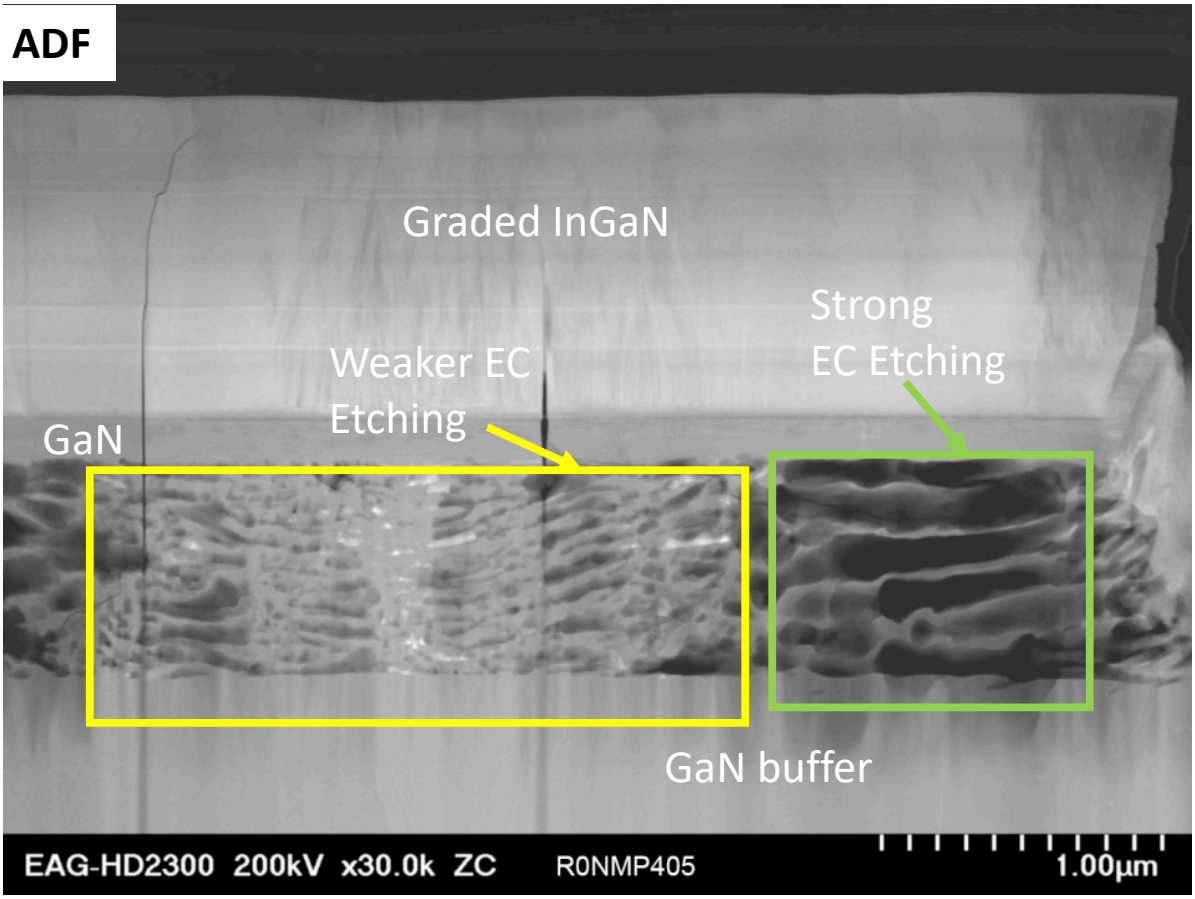

Figure 5.13 shows the ADF STEM image recorded on sample B3 showing stronger EC in the edge region compared to center region. This non-uniform EC may be related to the EC conditions. The InGaN layer above the porosified regions with strong EC etching showed negligible dislocation generation whereas the InGaN near the center of the tile with weaker EC etching exhibited a high density of dislocations. These dislocations may lead to the large number of spiral hillocks in the surface morphology on sample B3 (**Figure 5.11 (f)).** The surface morphology and dislocation density may be decreased by optimizing the porosification conditions, making the porous GaN layer more uniform.

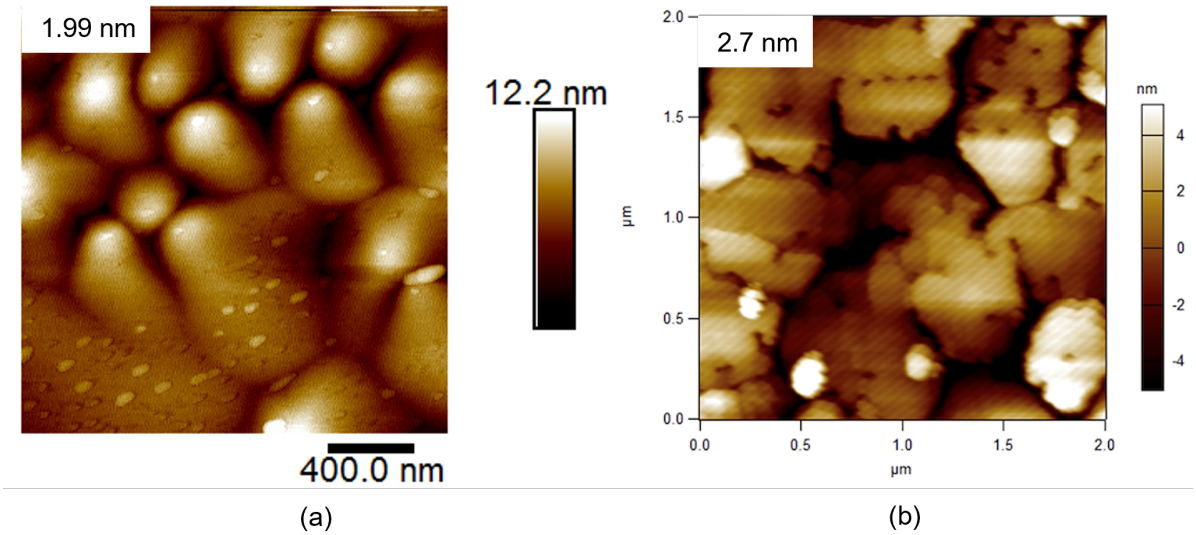

Figure 5.14: 2 µm x 2 µm AFM images of (a) InGaN on GaN PS with 6 µm x 6 µm tiles size (sample B1) (b) GaN/InGaN MQW grown by MOCVD on relaxed InGaN re-grown on GaN PS with 6 µm x 6 µm tiles size. The surface morphology showed a small increase in RMS roughness from 1.99 nm to 2.7 nm.

Figure 5.14 (a) shows 2 µm x 2 µm AFM images of sample B1 (InGaN grown on 6 µm x 6 µm tiles), which showed relatively smooth surface morphology and step edges. Subsequent MOCVD-growth of GaN/InGaN MQWs on a sample grown under the same conditions as B1 was carried out. The GaN/InGaN MQW structure growth is described above. A planar GaN on sapphire template wafer was co-loaded for reference. **Figure 5.14 (b)** shows the AFM images of the MQW structure, which exhibited a somewhat increased surface roughness compared to B1 (RMS value went from 2.0 nm to 2.7 nm after MQW growth). However, no significant V-defect formation after the InGaN/GaN MQW was observed, showing that the fabrication of relaxed InGaN films on GaN PS by PAMBE can be useful for growing InGaN/GaN MQW for LED applications [250].

Figure 5.15 shows the RT PL emission from the MQWs grown on InGaN on GaN PS in comparison with blue reference MQW and MQW grown on planar InGaN on GaN. The GaN/InGaN MQW grown on relaxed InGaN on GaN PS with 6 µm x 6 µm tiles showed bright luminescence at 565 nm. As shown in **Figure 5.15**, the peak PL intensity of the MQWs grown on

InGaN on PS (black solid curve) is comparable to standard MOCVD grown blue MQWs (blue curve). The wider FWHM of the PL spectra from MQW on InGaN on GaN PS is likely due to the presence of spiral hillocks leading to lateral variation in In incorporation [255–257]. The MQWs grown on InGaN tiles showed an 85 nm redshift from MQWs grown on planar GaN. The MQWs grown on planar InGaN on GaN exhibited a peak PL intensity 5 times lower than MQW grown on tiles. The decrease in emission from the MQWs on planar InGaN can be related to the defect formation due to plastic relaxation of planar InGaN on GaN template [258–260] . However, determining the reason is beyond the scope of this manuscript. Therefore, for the MQWs grown by MOCVD, In-incorporation in InGaN QWs was increased on the InGaN-on-GaN PS due to the partial relaxation of the InGaN base layer grown by PAMBE. The enhanced In-incorporation and

redshift is due to the partially relaxed InGaN base layer with a new in-plane lattice constant higher than that of GaN.

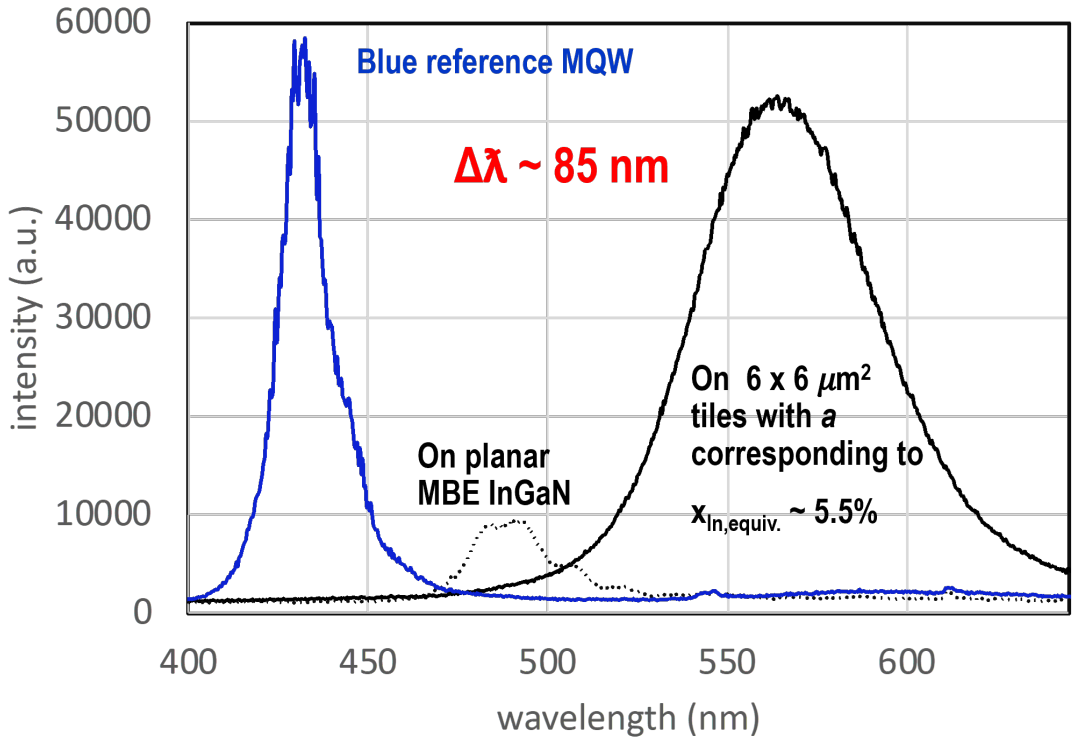

Figure 5.15: The black line shows strong photo-luminescence (PL) from the MQW grown on InGaN on GaN PS with 6 μm x 6 μm square tiles size. The black dashed line shows PL from the MQW on MBE planar InGaN on GaN. The blue line shows PL from a blue reference MQW.

5.3 **Summary**

In conclusion, the influence of InGaN film thickness and various graded layers with different composition on the relaxation of InGaN layers, which were grown by PAMBE on GaN-on-porous-GaN PSs was investigated. 1μm thick $In_{0.18}Ga_{0.82}N$ with grading showed 82% relaxation, which is equivalent to 15% fully relaxed In incorporation. It was also observed that high-quality InGaN growth is associated with the degree of porosification of the GaN:Si layer. MOCVD grown MQWs on InGaN on porous GaN redshifted ~85 nm in comparison with MQWs grown on planar GaN. The developed method is an attractive pathway for the fabrication of high

In content InGaN layer structures for efficient red-LEDs and especially micro-LEDs for future displays.

Chapter 6 Selective Area Growth of III-Nitride Nanowires (NWs)

6.1 Introduction

III-nitride nanowires (NWs) can be grown without the formation of defects and dislocations [261–263]. Due to their significantly small dimensions, III-nitride NWs can be utilized for scaling down future electronic and optoelectronic devices e.g., field effect transistors (FET)s [264–266], gate all-around field effect transistors (GAAFET), Fin-FETs [267,268], junction-less nanowire transistors (JNTs) [269,270], photodetectors [266], μ-LED [271], etc. GaN nanowires (NWs) have attracted interest as they can be grown dislocation- and strain-free on foreign substrates such as Si (100), (111) as well as Al_2O_3 in a self-assembled (SA) way by molecular beam epitaxy (MBE) [272–274] and metal organic chemical vapor deposition (MOCVD) [275–281]. The term "self-assembled" means the formation of NWs does not need a foreign catalyst. SA GaN NWs are usually grown under N-rich conditions at a growth temperature beyond the onset of GaN decomposition temperature. They typically grow axially toward the c-direction and form a hexagonal cross-section with m-plane side facets. SA GaN NWs grown on foreign substrates (e.g. sapphire and silicon) have better structural and optical properties compared with thin films grown on these substrates. Since NWs are intrinsically strain free, NWs are usually defect free and have large surface to volume ratio [282–284]. Moreover, InGaN/GaN superlattices grown on GaN NWs can accommodate a higher amount of strain than those grown on GaN films due to strain relief by lateral relaxation without the formation of dislocations and defects [132,285].

Despite these advantages, SA InGaN/GaN NWs suffer from inhomogeneity in axial and radial In incorporation as well as geometry dispersion and inherent In composition fluctuations

due to localizations, which result in random polychromatic emission in optoelectronics devices such as light-emitting diodes (LEDs). Additionally, LEDs based on InGaN/GaN NWs suffer from

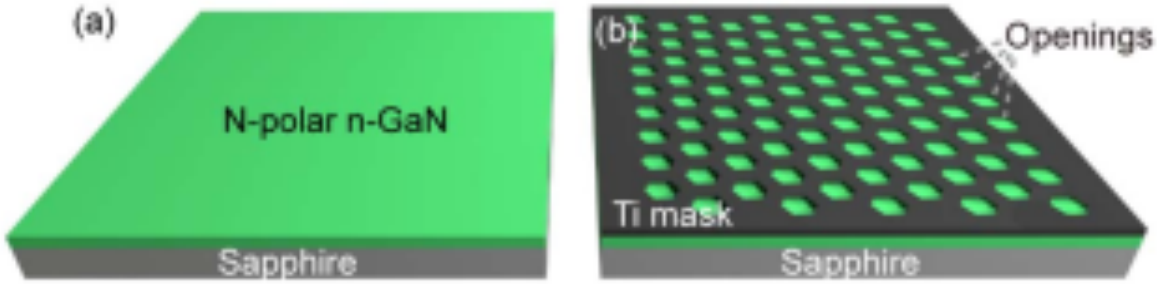

Figure 6.1 (a) Schematic of a N-polar GaN template grown on sapphire substrate. (b) Schematic of a patterned N-polar n-GaN template on sapphire using Ti mask. ***Courtesy: X. Liu et al. [297].***

electric dispersion mostly because of fluctuations in the diameter of and spacing between SA NWs.

To address these issues, selective area growth (SAG) has been developed, which allows precise control of size and position of the NWs [286–288]. Therefore, a densely packed geometrical array of high aspect ratio NWs without any surface, structural or optical dispersion can be achieved using this technique. Additionally, precise control over the NW's diameter allows for tuning the emission wavelength of optoelectronic devices [289–293]. In order to attain selectivity, the Ga atoms reaching the mask surface should either desorb from the mask or diffuse to the nearest hole to contribute to the NW's growth. SiN_x, SiO_2, Ti and Mo have been successfully used as mask materials for SAG growth of GaN NWs [287,288,294–296]. A schematic of the patterning process is shown in **Figure 6.1 (a) and (b)** [297]. After patterning the substrate using lithography [287,297–304], the mask is etched using reactive ion etch (RIE) followed by several wet and dry-cleaning processes to remove residual photoresist, organic contaminants, and native oxide [297,298]. When Ti is used as the mask, the growth initiates with nitridation and TiN is used to achieve selectivity of NWs [287].

Although SA GaN NWs grown on Si (111) by MBE typically have N-polarity, SAG of GaN NWs have been mostly studied on Ga-polar GaN templates [289,291,301,305,306] while SAG of N-polar GaN NWs has been less explored. Recently, it was shown that LEDs based on N-polar NWs demonstrated improvement in performance in comparison with Ga-polar nanostructures [297,307]. The better performance of LEDs based on N-polar NWs is probably because they can be grown at relatively higher temperatures than Ga-polar NWs, which can help to reduce point defects and improve crystal quality [308–312]. Reduction of point defects is critical for increasing emission efficiency in the optoelectronic devices ranging from the deep UV region to the infrared (IR) region [313]. Additionally, N polar NWs have a flat top surface, whereas pyramids form on top of Ga-polar NWs [314]. The flat top surface on N-polar NWs can be potentially helpful for some devices such as FETs. In addition, since better selectivity can be achieved in SAG of N-polar NWs, larger pitch spacings can be obtained in SAG of N-polar NWs compared with that in Ga-polar NWs [315], which also enables less shadowing effect. Moreover, N-polarity can potentially lead to reduced electron overflow, lower stark effect, and lower turn-on voltage in LEDs [171].

Brubaker et. al. [298] showed SAG of N-polar GaN NWs on an N-polar GaN/AlN template on Si (111) grown by MBE. For this purpose, they first grew an N-polar AlN nucleation layer in a Al-rich growth regime by introducing a planar boundary and inversion layers [298,316–318], followed by growth of N-polar GaN film. This required precise control of the Al-Si eutectic formation to enable perfect planar polarity inversions [317,318]. However, defects coming from Al-Si eutectic formation and inversion domains were present in N-polar nanowires.

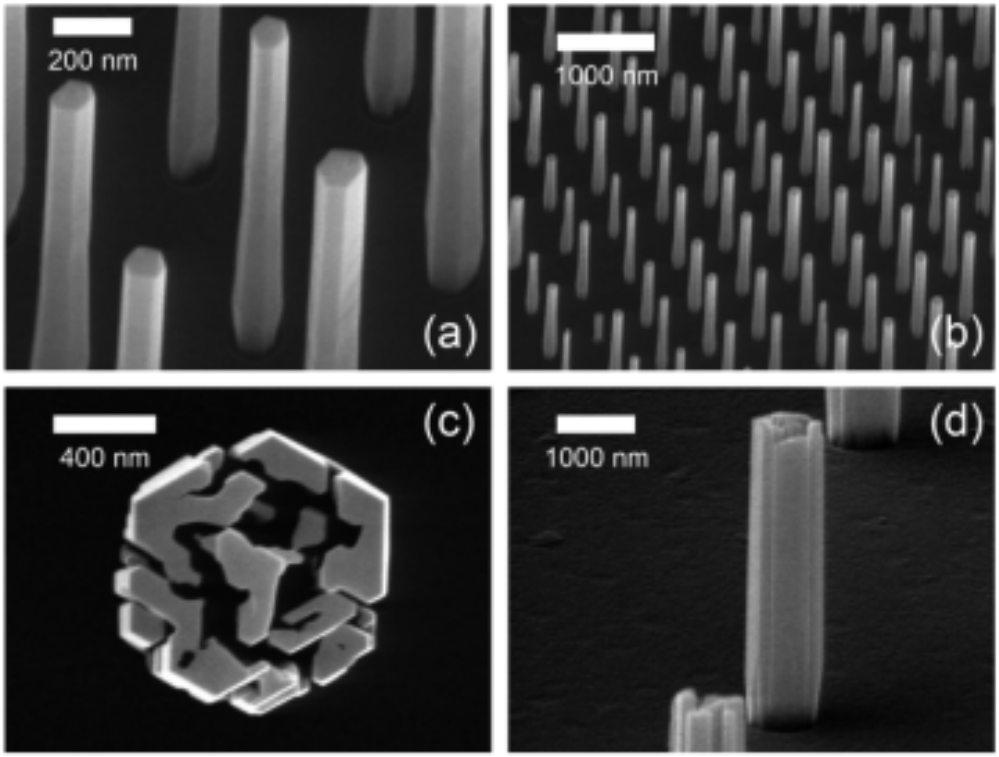

Figure 6.2 Selective-area NW growths on N-polar GaN/AlN/Si(111) templates. The nucleation layer polarity was verified by a 3 ×3 RHEED pattern after growth and prior to removal from the MBE system for mask fabrication. Nanowires with flat c-plane tips and mplane sidewall facets are produced in smaller mask openings (0.5 μm pitch, 100 nm diameter) patterned by e-beam lithography (a,b). Interior void regions are observed in larger mask . openings with circular (c, d) ***Courtesy: M. D. Brubaker et al. [320].***

The N-polar GaN template was then used as the template and patterned for the subsequent SAG NWs. [298,319]. A 70nm-thick SiN_x film was used as the growth mask for SAG in this work. High-quality NWs were produced with a mask opening of 500nm pitch and 100nm diameter, whereas NWs with larger diameter presented irregular facets and interior voids (**Figure 6.2**) [320].

This was attributed to an increase in decomposition and suppressed growth rate at grain boundary regions. N polar NWs showed long range selectivity than Ga-polar, which may be due to high growth rate of N-polar GaN NWs than that of Ga-polar counterparts. Besides, the growth rate of N-polar NWs was similar to the growth rate of planar GaN films, whereas significantly lower growth rate was observed for Ga-polar NWs compared to their planar counterparts [298]. The higher growth rate for N-polar GaN NWs may be related to low surface decomposition processes at high growth temperature for N-polar.

6.2 Selective-area Growth of GaN and AlGaN Nanowires on N-polar GaN Templates with 4° Miscut by Plasma-assisted Molecular Beam Epitaxy

There have been few studies about SAG of N-polar GaN NWs, and all of them were grown directly on on-axis Si and sapphire substrates [298,316,317,320,321]. The main challenge of growing N-polar NWs was unavailability of N-polar GaN templates. In this study, MOCVD grown N-polar GaN-on-sapphire templates were used for SAG of N-polar (Al,Ga)N NWs. Since high-quality growth of N-polar GaN templates by MOCVD requires miscut substrates [322–325], the templates used in this study have 4° miscut toward the sapphire a-plane, which leads to GaN miscut toward the a-plane ($\{1\bar{1}00\}$) and surface steps parallel to the GaN <$11\bar{2}0$> direction. The impact of growth temperature on the growth rate (both axial and radial) and growth selectivity was investigated and compared to NWs grown on Ga-polar GaN templates.

6.2.1 Experimental Details

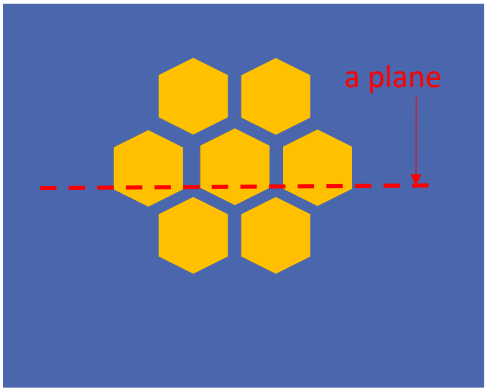

Figure 6.3 Direction of E-beam lithography pattern, which is necessary for coalescing of sidewalls and uniform growth

Ga-polar and N-polar GaN-on-sapphire templates were used for SAG of NWs. First, 500 nm Ti was evaporated on the backside of the template to ensure uniform temperature during the growth. Then, 10 nm Ti was deposited on the frontside of the template as a mask. The sample was then cleaned with solvents (acetone, methanol, and isopropanol) for 4 mins each and hydrochloric acid (HCl) for 10 mins. Next, PMMA950 A4 was spin-coated on the sample and baked at 180 °C for 3 mins, followed by the E-beam lithography using JEOL JBX-6300FS System. The hexagonal patterns need to be toward the specific direction shown in **Figure 6.3**. The direction is important for coalescing of the hexagonal nanowires and for promoting lateral growth. The NW patterns have different diameters (h) and spacings (a), including h = 75 nm and a = 125 nm; h= 100 nm and a = 150 nm; h =150 nm, a = 200 nm; h = 200 nm, a =250 nm. Nine 50 µm x 50 µm dices with different diameters and spacings were patterned in 5 mmx5 mm pieces of both Ga-polar and N-polar GaN templates (**Figure 6.4)**. After that, the sample was developed in the MIPK/IPA for 90 seconds. Then 10 nm-thick Ti was etched via fluorine-based chemistry using LAM9400 for 240s

and soaked in AZ 400T for 2.5 hrs at 80 °C. After the sample inspection under SEM and measurement of patterned Ti mask size, the sample was cleaned again with HCl for 10 mins.

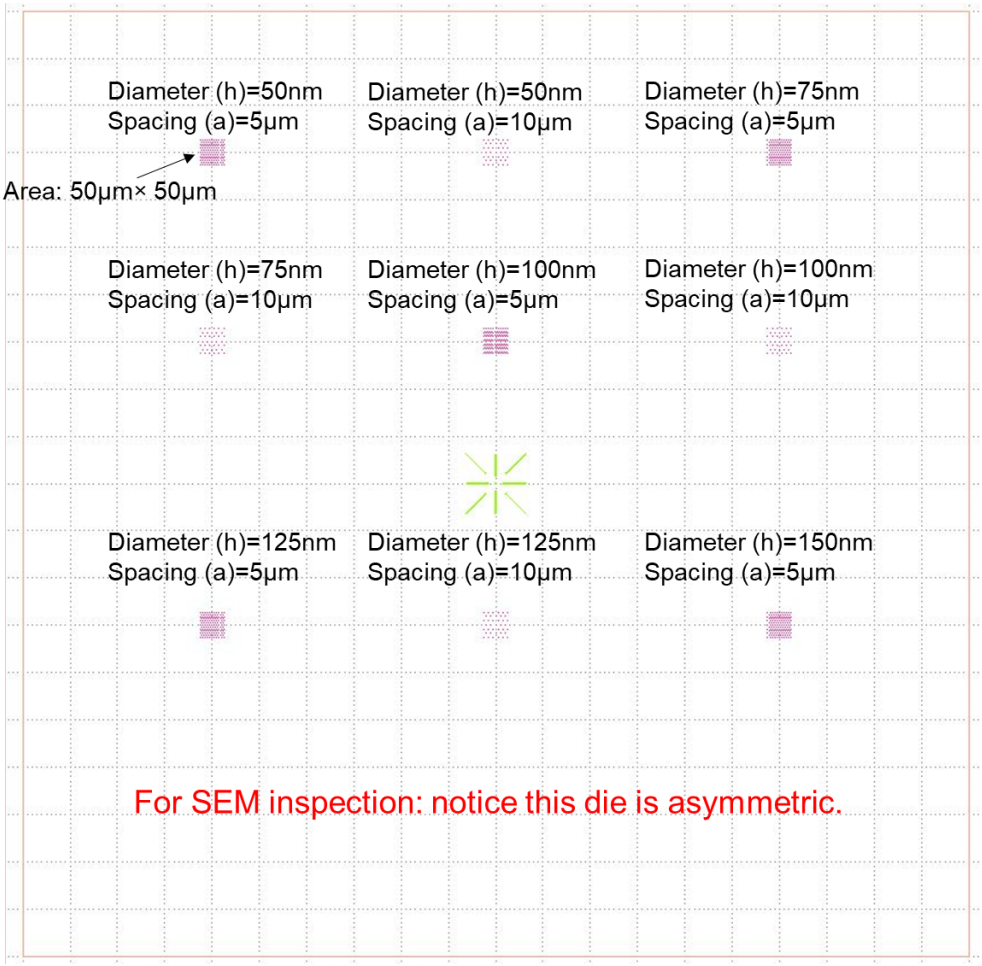

Figure 6.4: Schematic of 50 μm x 50 μm dice with different diameters and spacings. The die is asymmetric, which was used for SEM inspection of the pattern.

All samples were grown by a Veeco GENxplor MBE system equipped with conventional Ga, Al, In effusion cells and a radio frequency (RF) plasma source to supply activated nitrogen. The substrates were first solvent cleaned (acetone, methanol, and isopropanol for 4 min each) to remove organic residues from the surface, and then mounted on a Si substrate by In bonding before being loaded in the MBE exit-entry chamber. An hour of baking in the load lock chamber was performed at 200 °C to remove residue contamination from cassette and wafer blocks. An hour of

baking was performed at 400 °C in a buffer chamber to remove any water prior to transferring the substrate to the growth chamber. During the growth, the substrate temperature was measured and monitored using a thermocouple. The growth was monitored in situ via reflection high-energy electron diffraction (RHEED). Active nitrogen was supplied by 0.3 SCCM of 99.9995% pure N_2 via a VEECO RF plasma source powered at 350 W.

The patterned substrate with Ti mask was first nitridated in-situ at 400 °C for 10 min to avoid crack formation in the Ti mask during growth. GaN was then grown for 6 h using Ga beam equivalent pressure (BEP) of 2 x 10^{-7} Torr and the plasma condition mentioned above at different temperatures ranging from 800 ℃ to 880 ℃. Five different samples were grown starting with a growth temperature of 800 ℃, 820 ℃, 830 ℃, 850 ℃, and 880 ℃, which will be referred to as samples A, B, C, D, and E, respectively. For all samples, the growth temperature was increased by 10 ℃ every 2h. Therefore, the final growth temperatures for samples A, B, C, D, and E were 820 ℃, 840 ℃, 850 ℃, 870 ℃, and 900 ℃, respectively. Under optimized conditions with specific substrate temperature and Ga flux, epitaxy of GaN was suppressed on the surface of Ti mask due to the high desorption rate of Ga adatoms, thereby allowing for growth only in the mask openings.

After the initial 6 hours of GaN growth, the substrate temperature was lowered 20 °C from the final GaN growth temperature for the subsequent AlGaN growth. The AlGaN growth temperatures for samples A, B, C, D, and E were 800 ℃, 820 ℃, 830 ℃, 850 ℃, and 880 ℃, respectively. The AlGaN layer was grown for 30 min with Ga and Al BEP of 1.7 x 10^{-7} Torr and 3 x 10^{-8} Torr, respectively. Samples were then characterized by Hitachi SU 8000 In-line FE-SEM, which has top-down and 45° tilted views. Cross-sectional specimens for transmission electron microscopy (TEM) study were prepared by in situ focused ion beam (FIB) lift-out methods using a Thermo-Fisher G4 650 Xe Plasma-FIB (P-FIB). For final thinning, a 5-keV energy and 10-pA

current beam were used. A Thermo-Fisher Talos 200F transmission electron microscope was used, operating in scanning transmission electron microscopy (STEM) mode. Both high-angle annular dark-field (HAADF) and bright-field (BF) images were taken simultaneously.

6.2.2 Results and Discussions

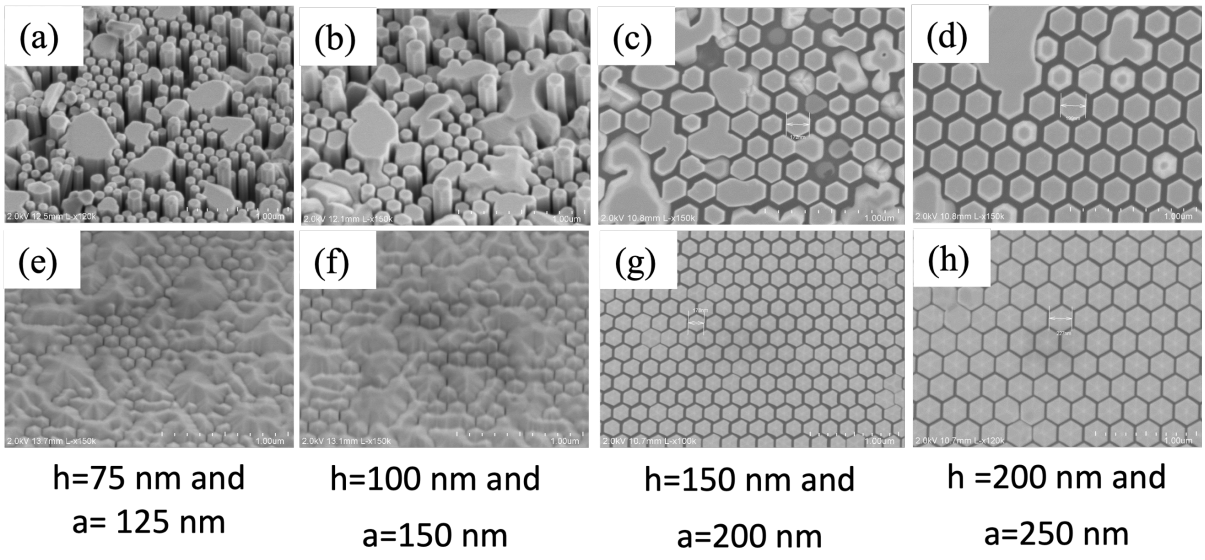

Figure 6.5: SEM images of the GaN grown for 6 hrs with NWs for sample A with different diameters (h) and spacings (a): (a), (e) h=75 nm and a= 125 nm; (b), (f) h=100 nm and a=150 nm; (c), (g) h=150 nm, a=200 nm; (d), (h) h =200 nm, a=250 nm. (a)-(d) and (e)-(h) show N-polar and Ga-polar GaN NWs, respectively. This shows Ga-polar NWs show homogeneity even for smaller diameter.

Figure 6.5 shows SEM images of N-polar (a-d) and Ga-polar (e-h) GaN NWs with different diameter (h) and spacing (a) for sample A after 6 hours of GaN growth. SEM images **in Figure 6.5 (a-d)** shows that with a decrease in diameter the homogeneity decreased for N-polar and with diameter below 100 nm, the N-polar NWs became completely irregular and sparse. In contrast, Ga-polar NWs showed homogeneity for all the diameters ranging from 75 nm to 200 nm **(Figure 6.5 (e-h)).** Interestingly, the lower diameter (75 nm and 100 nm) Ga-polar NWs started to show some coalescence below 100 nm.

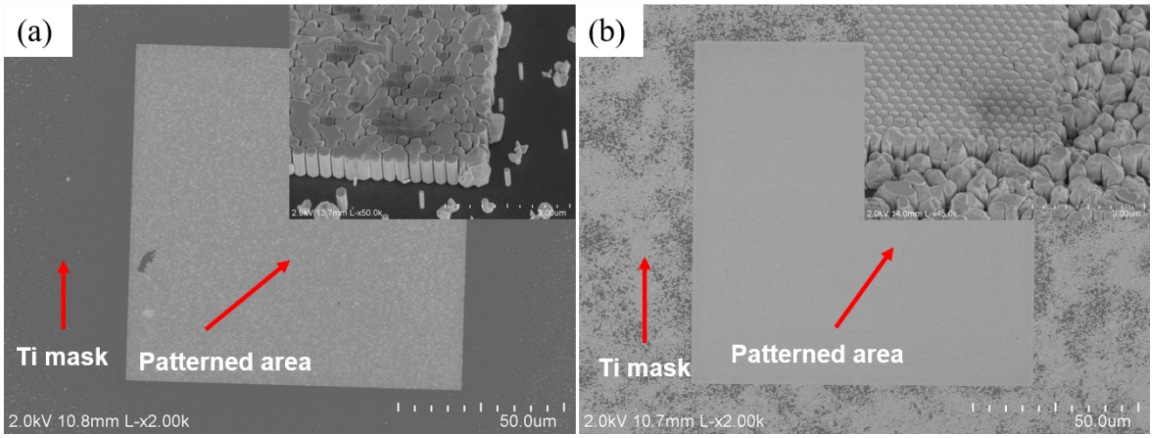

Figure 6.6 SEM images of the (a) N-polar and (b) Ga-polar polar GaN NW grown for 6h showing the hawk-eye image of the Ti mask and patterned area. The inset images show 45° angle image. Both images confirm N-polar NW shows much better selectivity and less junk than Ga-polar.

Figure 6.6 shows SEM images of N-polar (a) and Ga-polar (b) GaN NWs after 6 h of growth showing both the Ti mask region and patterned region to determine selectivity. In the inset, 45° angle images are shown, confirming that significantly better selectivity can be achieved for SAG of N-polar NWs than Ga-polar NWs.

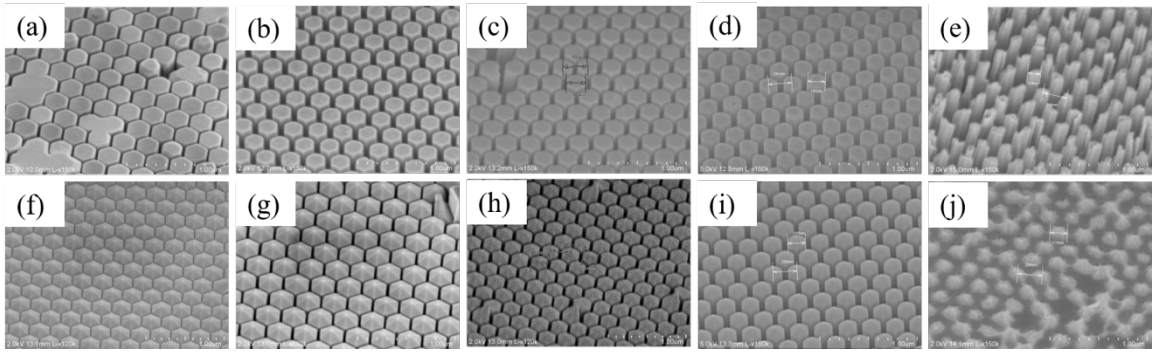

Figure 6.7 SEM image of N-polar (a)-(e) and (f)-(j) Ga polar SA grown GaN NWs after 6h of growth with different temperatures: (a), (f) sample A (800 °C); (b), (g) sample B (820 °C); (c), (h) sample C(830 °C); (d), (i) sample D (850 °C) and (e), (j) sample E (880 °C). This shows with an increase in substrate temperature, lateral growth rate decreases.

Figure 6.7 shows SEM images of N-polar (a)-(e) and Ga-polar (f)-(j) GaN NWs after 6h of growth at different growth temperatures. **Figure 6.7** shows SEM images of (a), (f) sample A (800 °C); (b), (g) sample B (820 °C); (c), (h) sample C (830 °C); (b), (g) sample D (850 °C); (b), (g) sample E (880 °C). **Figure 6.7** clearly shows that with an increase in substrate temperature, the lateral growth decreases drastically for both N-polar (a)-(e) and Ga-polar (f)-(j). For extreme high growth temperature e.g., 880 °C, the NWs almost showed negative lateral growth, which means

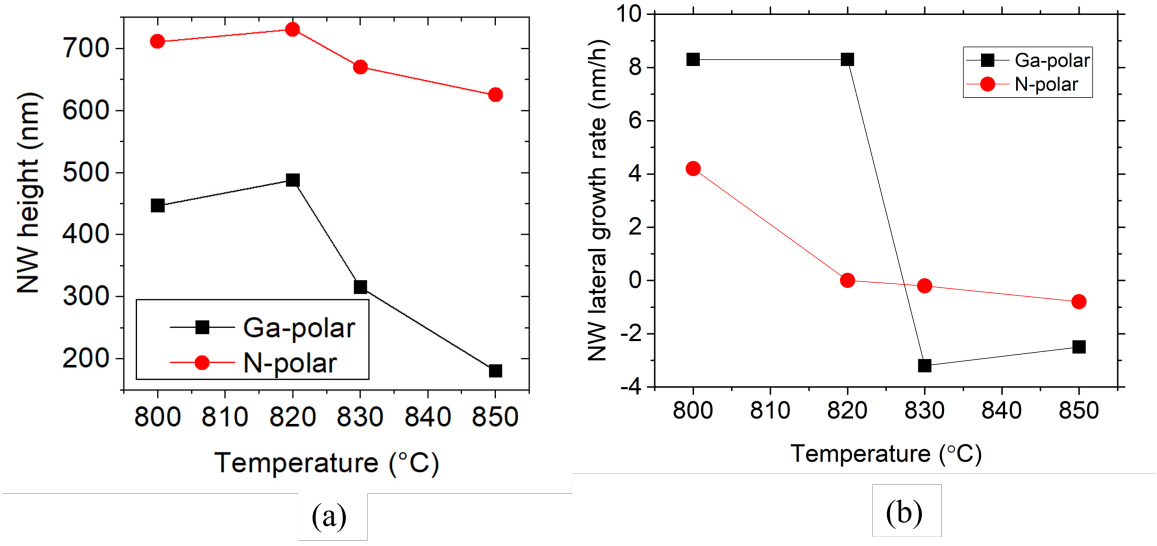

Figure 6.8 Comparison between N-polar and Ga-polar NWs (a) height (nm) and (b) lateral growth rate (nm/h) after 6h growth. Ga polar NWs growth rate decreases abruptly with an increase in temperature.

the nanowire diameter is smaller compared to their pattern diameter. This also showed that the growth temperature for sample A and sample B (800-820 °C) is the optimum temperature.

Figure 6.8 shows a comparison between the height of N-polar and Ga-polar NWs after 6h of GaN growth at different temperatures. Higher growth rates were achieved on N-polar GaN NWs compared with that on Ga-polar GaN NWs. Moreover, the growth rate of N-polar NWs remained relatively constant over a large range of growth temperatures, whereas the growth rate of Ga-polar NWs decreased abruptly as growth temperature increased (**Figure 6.8 (a)**). The lateral growth rate of Ga-polar NWs was shown to be much higher than that for N-polar NWs and decreased abruptly with increase in substrate temperature (**Figure 6.8 (b)**).

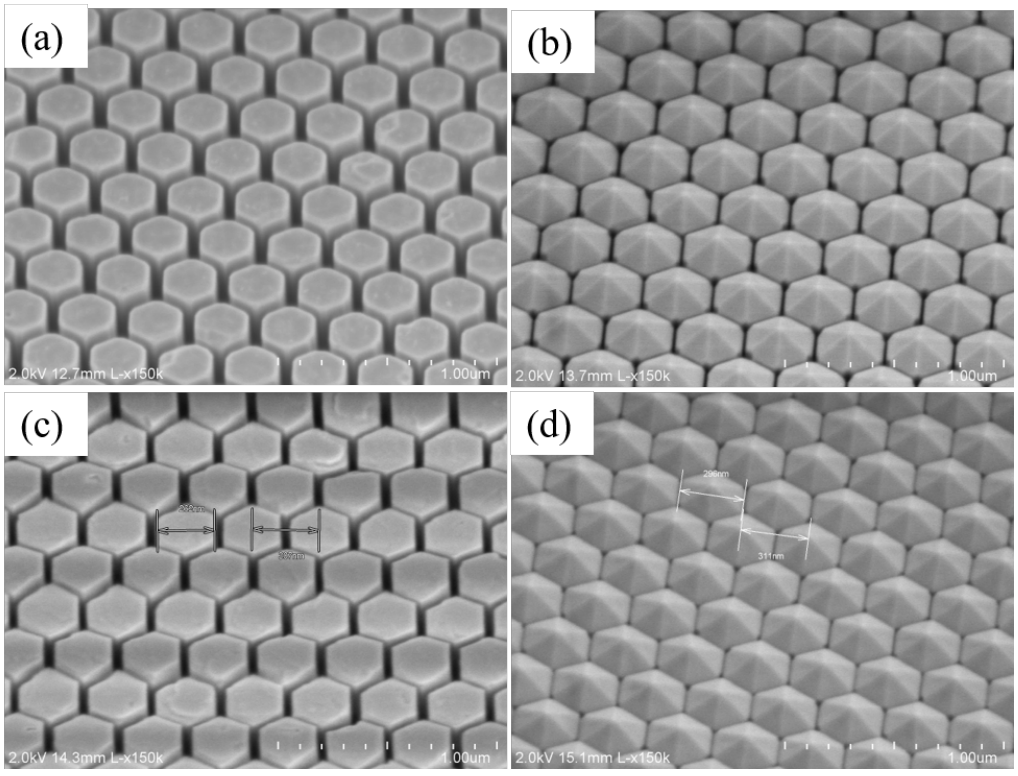

Figure 6.9 SEM images of sample B as a representative of GaN SA grown NWs. (a), (b) after 6h of growth; (c), (d) after additional 1h of AlGaN growths for N-polar and Ga-polar, respectively. This showing Alloying GaN with Al promotes lateral growth on Ga-polar SAG of NWs helping to coalesce whereas does not affect N-polar GaN NWs significantly.

Top view SEM images of sample B are shown in **Figure 6.9 (a), (b)** as a representation after 6h growth of GaN NWs and **Figure 6.9 (c), (d)** as a representation after 1h growth of AlGaN

for N-polar and Ga polar, respectively. As can be observed in these images, alloying GaN with AlN did not change the lateral growth of N-polar NWs (**Figure 6.9 (a) and (c)**), whereas it increased the lateral growth of Ga-polar NWs (**Figure 6.9 (b) and (d)**).

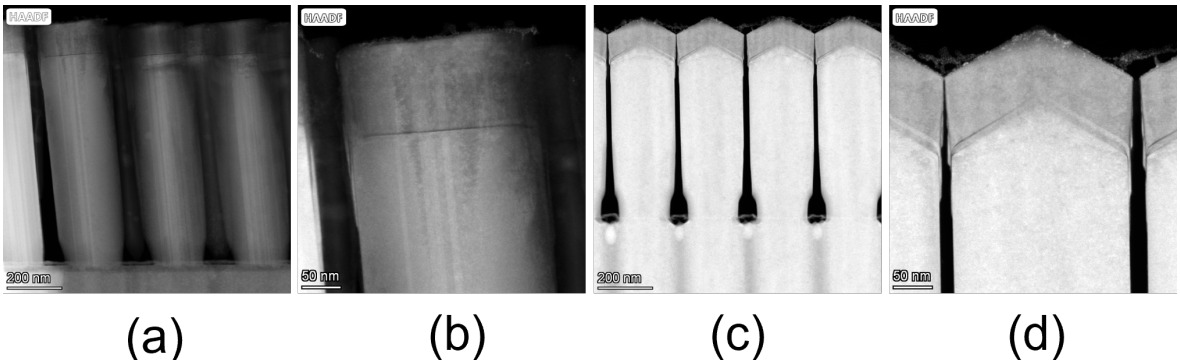

Figure 6.10 Low-magnification STEM HAADF images of AlGaN/GaN NWs by SAG with 250 nm nanowire diameter as a representative of other nanowire diameters e.g. 100 nm and 150 nm for N-polar (a-b) and Ga-polar(c-d). The N-polar NWs showed 4° tilt than vertical direction probably due to 4° miscut in N-polar GaN template on sapphire substrate. The N-polar GaN NWs showed flat top surface whereas Ga-polar showed pyramidal structure on the top surface.

Figure 6.10 shows (a), (c) low-resolution and (b), (d) high-resolution STEM images of AlGaN/GaN NWs with diameter of 250 nm for N polar (a-b) and Ga-polar (c-d). The N-polar NWs showed 4° tilt with respect to the vertical direction due to 4° miscut in the N-polar GaN template on sapphire substrate, which shows that growth only occurs along the c-direction. N-polar GaN NWs showed flat top surfaces whereas Ga-polar NWs showed pyramidal structure on the top surfaces, similar to previous reports on self-assembled and SAG of GaN NWs [314,320,326,327]. A sharp AlGaN/GaN interface was achieved as evidenced by high-resolution STEM images. To compare the Al content in N-polar and Ga-polar AlGaN SA grown NWs, energy dispersive spectra was performed.

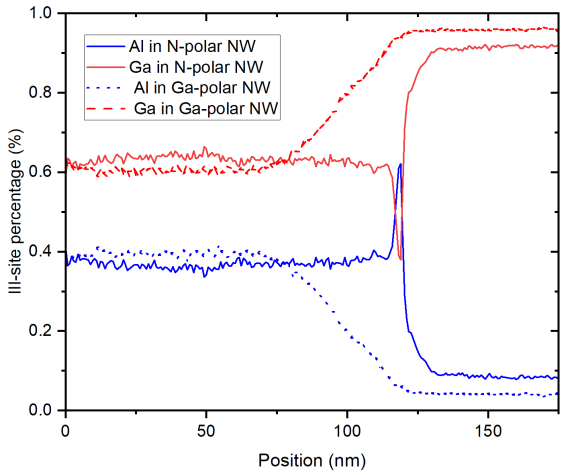

Figure 6.11 Energy dispersive spectra (EDS) shows Al and Ga site percentage with different position for N-polar and Ga-polar AlGaN/GaN NWs by SAG. Both N-polar and Ga-polar AlGaN/GaN showed similar Al incorporation for similar growth condition.

Figure 6.11 shows EDS of AlGaN/GaN NWs with Al and Ga-site percentage with different position for N-polar and Ga-polar SA grown AlGaN/GaN NWs for sample B (GaN NWs grown at 820 °C). Interestingly, N-polar and Ga-polar AlGaN/GaN showed similar Al incorporation at similar growth conditions for different NWs diameters. The gradual change of Al content in the interface is related to the pyramidal structure of Ga-polar AlGaN/GaN NWs since EDS measurement averages Al or Ga content over a specific area.

6.3 Summary

In summary, higher growth rate and improved selectivity was observed for SAG of N-polar GaN NWs compared to Ga-polar GaN NWs. Additionally, significantly higher lateral growth rate for Ga-polar GaN NWs was observed, which can lead to the coalescence of nanowires, especially in the dense patterns needed for LEDs or lasers. Alloying with Al further increased the lateral growth rate of Ga-polar NWs, whereas it did not impact the lateral growth rate of N-polar NWs. The N-polar NWs showed 4° tilt with respect to substrate surface, likely due to the 4° miscut in N-polar GaN template on sapphire substrate. Al incorporation of ~40% was achieved on both N-

polar and Ga-polar AlGaN NWs irrespective of NW diameters. Due to improvement in selectivity and the increase in growth rate by N-polar III-nitride based NWs compared to their Ga-polar counterparts, N-polar NWs can be utilized for various next-generation optoelectronics and electronics applications in near future.

Chapter 7 Conclusions and Future Works

7.1 Conclusions

In this thesis, a spontaneous formation of $In_xGa_{1-x}N/In_yGa_{1-y}N$ SASL structure on nominal InGaN film grown on both Ga-polar and N-polar GaN by PAMBE was reported. These results confirmed formation of SASL is independent of GaN substrate polarity. The formation SASL on both Ga-polar and N-polar InGaN enabled growth of InGaN films beyond critical thickness without any formation of dislocation and defects. Besides, it was observed that SASL did not form when grown below a critical growth temperature.

A substrate treatment method was developed to obtain smooth surface with step edges on ZnO substrates. A low temperature MEE technique was introduced to grow a thin layer of GaN film on ZnO, which is necessary to suppress interfacial reaction between ZnO and InGaN. InGaN films with In content ranging from 11% to 23% were also successfully grown on ZnO. InGaN films grown on ZnO also showed SASL structure, however with significantly lower In modulation, which indicates strain plays a role in the SL formation.

Additionally, in this thesis, relaxed InGaN films were developed on compliant porosified GaN templates. ~1μm thick $In_{0.18}Ga_{0.82}N$ with grading showed 82% relaxation, which is equivalent to 15% fully relaxed In incorporation. It was shown that high-quality InGaN growth and InGaN uniformity are associated with the degree of porosification of the GaN:Si layer. MOCVD grown MQWs on InGaN on porous GaN redshifted ~85 nm in comparison with MQWs grown on planar GaN.

SAG growth of GaN and AlGaN nanowires were also studied on N-polar GaN template. Higher growth rate and improved selectivity were observed for SAG of N-polar GaN NWs compared to Ga-polar GaN NWs. Significantly higher lateral growth rate for Ga-polar GaN NWs was observed. Alloying with Al further increased the lateral growth rate of Ga-polar NWs, whereas it did not impact the lateral growth rate of N-polar NWs. Al incorporation of ~40% was achieved on both N-polar and Ga-polar AlGaN NWs irrespective of NW diameters.

7.2 Future Works

Spontaneous formation of InGaN/GaN SA structures is intriguing and there are several questions remaining that could be studied in the future. It would be interesting to explore impact of strain on formation, period, and compositional modulation of SASL. For this purpose, once could grow InGaN films with different compositions by changing Ga flux while maintaining the growth temperature constant. Additionally, further studies are required to fully understand the impact of substrate rotation, In content, growth regime (metal-rich vs N-rich), growth temperature, and In/Ga flux on the formation and periodicity of self-assembled superlattice structures. Besides, the impact of miscut angles in substrates in formation of SASL can also be explored. Moreover, in the future, a robust substrate treatment method for N-polar GaN should be developed to prevent formation of dislocation in N-polar GaN buffer layer.

There can be several applications for these SASL in photovoltaic cells (solar cells), LEDs and etc. Additionally, many devices including hot electron transistors (HETs) [1], InGaN-channel HEMTs, LEDs, solar cells, and detectors could potentially benefit from relatively high temperature (690 °C) growth of high-quality InGaN and spontaneous formation of InGaN/GaN superlattice structure.

This study showed that while high-quality GaN was initially achieved on ZnO. the surface morphology of GaN on ZnO eventually degraded probably due to the strain built up in GaN. The surface morphology degradation can be mitigated by removing the ZnO substrate immediately after the growth or passivating the GaN Substrate after growth. Moreover, it would be interesting to study InGaN growth on ZnO using thicker low temperature GaN interlayer to ensure suppressing formation of low-quality interfacial layer.

The developed method of regrowing InGaN on porous GaN is an attractive technique for the fabrication of high In content InGaN layer structures for efficient red-LEDs and especially micro-LEDs for future displays. Studying growth of AlGaN on porosified tiles can be useful for UV applications. Besides, studying relaxed (In,Al,Ga)N on fully porosified tiles with different sizes can be of another promising direction.

The higher lateral growth rate of Ga-polar AlGaN can lead to the coalescence of nanowires, especially in the dense patterns needed for LEDs or lasers. Due to improvement in selectivity and the increase in growth rate by N-polar III-nitride based NWs compared to their Ga-polar counterparts, N-polar NWs can be utilized for various next-generation optoelectronics and electronics applications in near future.

Bibliography

[1] Gupta G, Ahmadi E, Suntrup D J and Mishra U K 2018 Establishment of design space for high current gain in III-N hot electron transistors *Semicond Sci Technol* **33** 015018

[2] Jain S C, Willander M, Narayan J and Van Overstraeten R 2000 III–nitrides: Growth, characterization, and properties *J Appl Phys* **87** 965

[3] Strite S and Morkoç H 1998 GaN, AlN, and InN: A review *Journal of Vacuum Science & Technology B: Microelectronics and Nanometer Structures Processing, Measurement, and Phenomena* **10** 1237

[4] Kour R, Arya S, Verma S, Singh A, Mahajan P and Khosla A 2020 Review—Recent Advances and Challenges in Indium Gallium Nitride (In x Ga 1-x N) Materials for Solid State Lighting *ECS Journal of Solid State Science and Technology* **9** 015011

[5] Bhuiyan A G, Sugita K, Hashimoto A and Yamamoto A 2012 InGaN Solar Cells: Present State of the Art and Important Challenges *IEEE J Photovolt* **2** 276

[6] Fritsch D, Schmidt H and Grundmann M 2004 Band dispersion relations of zinc-blende and wurtzite InN *Phys Rev B* **69** 165204

[7] Hsiao C L, Liu T W, Wu C T, Hsu H C, Hsu G M, Chen L C, Shiao W Y, Yang C C, Gällström A, Holtz P O, Chen C C and Chen K H 2008 High-phase-purity zinc-blende InN on r-plane sapphire substrate with controlled nitridation pretreatment *Appl Phys Lett* **92** 111914

[8] Ahmadi E 2015 *PhD Dissertation, Growth Optimization of III-N Electronic Devices by Plasma-Assisted Molecular Beam Epitaxy*

[9] Wojciech M. Linhart 2009 *Electron accumulation and doping in InN and InGaN alloys* (Georgia Institute of Technology)

[10] Mishra U K and Singh J Electronic levels in semiconductors *Semiconductor Device Physics and Design* (Dordrecht: Springer Netherlands) pp 28–91

[11] Guo Q X, Tanaka T, Nishio M, Ogawa H, Pu X D and Shen W Z 2005 Observation of visible luminescence from indium nitride at room temperature *Appl Phys Lett* **86** 231913

[12] Specht P, Ho J C, Xu X, Armitage R, Weber E R, Erni R and Kisielowski C 2005 Band transitions in wurtzite GaN and InN determined by valence electron energy loss spectroscopy *Solid State Commun* **135** 340–4

[13] Wu J, Walukiewicz W, Shan W, Yu K M, Ager J W, Li S X, Haller E E, Lu H and Schaff W J 2003 Temperature dependence of the fundamental band gap of InN *J Appl Phys* **94** 4457

[14] Sparavigna A C and Sparavigna A C 2014 Light-Emitting Diodes in the Solid-State Lighting Systems *Int J Sci* **3** 9–17

[15] Moram M A and Vickers M E 2009 X-ray diffraction of III-nitrides *Reports on Progress in Physics* **72** 36502

[16] Scholz F *Compound Semiconductors : Physics, Technology, and Device Concepts*

[17] Hu S M 1998 Misfit dislocations and critical thickness of heteroepitaxy *J Appl Phys* **69** 7901

[18] Holec D, Costa P M F J, Kappers M J and Humphreys C J 2007 Critical thickness calculations for InGaN/GaN *J Cryst Growth* **303** 314–7

[19] Holec D, Zhang Y, Rao D V S, Kappers M J, McAleese C and Humphreys C J 2008 Equilibrium critical thickness for misfit dislocations in III-nitrides *J Appl Phys* **104** 123514

[20] Leyer M, Stellmach J, Meissner C, Pristovsek M and Kneissl M 2008 The critical thickness of InGaN on (0 0 0 1)GaN *J Cryst Growth* **310** 4913–5

[21] People R and Bean J C 1998 Calculation of critical layer thickness versus lattice mismatch for GexSi1−x/Si strained-layer heterostructures *Appl Phys Lett* **47** 322

[22] Mishra U K and Singh J *Semiconductor Device Physics and Design*

[23] Ho I H and Stringfellow G B 1996 Solid phase immiscibility in GaInN *Appl Phys Lett* **69** 2701–3

[24] El-Masry N A, Piner E L, Liu S X and Bedair S M 1998 Phase separation in InGaN grown by metalorganic chemical vapor deposition *Appl Phys Lett* **72** 40

[25] Singh R, Doppalapudi D, Moustakas T D and Romano L T 1998 Phase separation in InGaN thick films and formation of InGaN/GaN double heterostructures in the entire alloy composition *Appl Phys Lett* **70** 1089

[26] Ho I-H and Stringfellow G B 1997 Solubility of nitrogen in binary III-V systems *J Cryst Growth* **178** 1–7

[27] Stringfellow G B 2010 Microstructures produced during the epitaxial growth of InGaN alloys *J Cryst Growth* **312** 735–49

[28] Bergh A, Craford G, Duggal A and Haitz R 2001 The promise and challenge of solid-state lighting *Phys Today* **54** 42–7

[29] Tsao J Y, Crawford M H, Coltrin M E, Fischer A J, Koleske D D, Subramania G S, Wang G T, Wierer J J, Karlicek Jr J Y Tsao R F, Crawford M H, Coltrin M E, Fischer A J, Koleske D D, Subramania G S, Wierer J J and Karlicek Jr R F 2014 Toward Smart and Ultra-efficient Solid-State Lighting *Adv Opt Mater* **2** 809–36

[30] Krames M R, Shchekin O B, Mueller-Mach R, Mueller G O, Zhou L, Harbers G and Craford M G 2007 Status and future of high-power light-emitting diodes for solid-state lighting *IEEE/OSA Journal of Display Technology* **3** 160–75

[31] Crawford M H 2009 LEDs for Solid-State Lighting: Performance Challenges and Recent Advances *IEEE JOURNAL OF SELECTED TOPICS IN QUANTUM ELECTRONICS* **15** 1028–40

[32] Pimputkar S, Speck J S, DenBaars S P and Nakamura S 2009 Prospects for LED lighting *Nat Photonics* **3** 180–2

[33] Bergh A, Craford G, Duggal A and Haitz R 2001 The promise and challenge of solid-state lighting *Phys Today* **54** 42–7

[34] Jiang H X, Lin J Y, Jin S X, Li J, Li J Z, Microdisk G, Shakya J, Fan Z Y, Ao J P, Sato H, Mizobuchi T, Morioka K, Kawano S, Muramoto Y, Lee Y B, Sato D, Ohno Y, Day J, Lie D, Bradford C, D McKendry J J, Rae B R, Gong Z, Muir K R, Guilhabert B, Massoubre D, Gu E, Renshaw D, Dawson M D and Henderson R K 2013 Nitride micro-LEDs and beyond - a decade progress review *Optics Express, Vol. 21, Issue S3, pp. A475-A484* **21** A475–84

[35] DenBaars S P, Feezell D, Kelchner K, Pimputkar S, Pan C-C, Yen C-C, Tanaka S, Zhao Y, Pfaff N, Farrell R, Iza M, Keller S, Mishra U, Speck J S and Nakamura S 2013 Development of gallium-nitride-based light-emitting diodes (LEDs) and laser diodes for energy-efficient lighting and displays *Acta Mater* **61** 945–51

[36] Nakamura S 2015 Nobel Lecture :Background story of the invention of efficient blue InGaN light emitting diodes *Ann Phys* **87** 335–49

[37] Chen H W, Lee J H, Lin B Y, Chen S and Wu S T 2017 Liquid crystal display and organic light-emitting diode display: present status and future perspectives *Light: Science & Applications 2018 7:3* **7** 17168–17168

[38] Jung T, Choi J H, Jang S H and Han S J 2019 Review of micro-light-emitting-diode technology for micro-display applications *Dig Tech Pap* **50** 442–6

[39] Lin J Y and Jiang H X 2020 Development of microLED *Appl Phys Lett* **116** 100502

[40] Jiang H and Lin J 2021 Development of nitride microLEDs and displays *Semiconductors and Semimetals* **106** 1–56

[41] Park J, Kim J, Kim S Y, Cheong W H, Jang J, Park Y G, Na K, Kim Y T, Heo J H, Lee C Y, Lee J H, Bien F and Park J U 2018 Soft, smart contact lenses with integrations of wireless circuits, glucose sensors, and displays *Sci Adv* **4**

[42] He J, Nuzzo R G and Rogers J A 2015 Inorganic materials and assembly techniques for flexible and stretchable electronics *Proceedings of the IEEE* **103** 619–32

[43] Lingley A R, Ali M, Liao Y, Mirjalili R, Klonner M, Sopanen M, Suihkonen S, Shen T, Otis B P, Lipsanen H and Parviz B A 2011 A single-pixel wireless contact lens display *Journal of Micromechanics and Microengineering* **21** 125014

[44] Poher V, Grossman N, Kennedy G T, Nikolic K, Zhang H X, Gong Z, Drakakis E M, Gu E, Dawson M D, French P M W, Degenaar P and Neil M A A 2008 Micro-LED arrays: a tool for two-dimensional neuron stimulation *J Phys D Appl Phys* **41** 094014

[45] Yoshimoto N, Matsuoka T, Sasaki T and Katsui A 1991 Photoluminescence of InGaN films grown at high temperature by metalorganic vapor phase epitaxy *Appl Phys Lett* **59** 2251–3

[46] Nakamura S, Mukai T and Senoh M 1994 Candela class high brightness InGaN/AlGaN double-heterostructure blue light emitting diodes *Appl. Phys. Lett* **64** 1687

[47] Nakamura S and Mukai T 1992 High-quality ingan films grown on gan films *Jpn J Appl Phys* **31** L1457–9

[48] Auf Der Maur M, Pecchia A, Penazzi G, Rodrigues W and Di Carlo A 2016 Efficiency Drop in Green InGaN/GaN Light Emitting Diodes: The Role of Random Alloy Fluctuations *Phys Rev Lett* **116** 027401

[49] Doppalapudi D, Basu S N, Ludwig K F and Moustakas T D 1998 Phase separation and ordering in InGaN alloys grown by molecular beam epitaxy *J Appl Phys* **84** 1389–95

[50] Hestroffer K, Lund C, Li H, Keller S, Speck J S and Mishra U K 2016 Plasma-assisted molecular beam epitaxy growth diagram of InGaN on (0001)GaN for the optimized synthesis of InGaN compositional grades *Phys Status Solidi B Basic Res* **253** 626–9

[51] Heying B, Averbeck R, Chen L F, Haus E, Riechert H and Speck J S 2000 Control of GaN surface morphologies using plasma-assisted molecular beam epitaxy *J Appl Phys* **1855** 1855–60

[52] Valdueza-Felip S, Bellet-Amalric E, Núñez-Cascajero A, Wang Y, Chauvat M-P, Ruterana P, Pouget S, Lorenz K, Alves E and Monroy E 2014 High In-content InGaN layers synthesized by plasma-assisted molecular-beam epitaxy: Growth conditions, strain relaxation, and In incorporation kinetics *J Appl Phys* **116** 233504

[53] Keller B P, Keller S, Kapolnek D, Kato M, Masui H, Imagi S, Mishra U K and DenBaars S P 1995 Effect of atmospheric pressure MOCVD growth conditions on UV band-edge photoluminescence in GaN thin films *Electron Lett* **31** 1102–3

[54] Sharma T K and Towe E 2010 Application-oriented nitride substrates: The key to long-wavelength nitride lasers beyond 500 nm *J Appl Phys* **107** 024516

[55] Even A, Laval G, Ledoux O, Ferret P, Sotta D, Guiot E, Levy F, Robin I C and Dussaigne A 2017 Enhanced In incorporation in full InGaN heterostructure grown on relaxed InGaN pseudo-substrate *Appl Phys Lett* **110** 262103

[56] Johnson E 1965 Physical limitations on frequency and power parameters of transistors *1958 IRE International Convention Record* vol 13 pp 27–34

[57] Polyakov V M and Schwierz F 2006 Low-field electron mobility in wurtzite InN *Appl Phys Lett* **88** 032101

[58] Matsuno T, Masato H, Ryoji A and Inoue K 1993 Mobilities of a two-dimensional electron gas in pseudomorphic and strain-free InAlAs/InGaAs HEMT structures. *Institute of Physics Conference Series* pp 729–234

[59] Yarar Z, Ozdemir B and Ozdemir M 2007 Transport and Mobility Properties of Bulk Indium Nitride (InN) and a Two-Dimensional Electron Gas in an InGaN/GaN Quantum Well *Journal of Elec Material* **36**

[60] Fehlberg T B, Umana-Membreno G A, Nener B D, Parish G, Gallinat C S, Koblmüller G, Rajan S, Bernardis S and Speck J S 2006 Characterisation of multiple carrier transport in indium nitride grown by molecular beam epitaxy *Japanese Journal of Applied Physics, Part 2: Letters* **45** L1090

[61] Zhang Y, Zhang T, Zhou H, Li Y, Xu S, Bao W, Zhang J and Hao Y 2018 InGaN-channel high-electron-mobility transistor with enhanced linearity and high-temperature performance *Applied Physics Express* **11** 94101

[62] Okamoto N, Hoshino K, Hara N, Takikawa M and Arakawa Y 2004 MOCVD-grown InGaN-channel HEMT structures with electron mobility of over 1000cm2/Vs *J Cryst Growth* **272** 278–84

[63] Laboutin O, Cao Y, Johnson W, Wang R, Li G, Jena D and Xing H 2012 InGaN channel high electron mobility transistor structures grown by metal organic chemical vapor deposition *Appl Phys Lett* **100** 121909

[64] Wang R, Li G, Karbasian G, Guo J, Faria F, Hu Z, Yue Y, Verma J, Laboutin O, Cao Y, Johnson W, Snider G, Fay P, Jena D and Xing H 2013 InGaN channel high-electron-mobility transistors with InAlGaN barrier and fT/fmax of 260/220 GHz *Applied Physics Express* **6** 016503

[65] Hsin Y M, Hsu H T, Chuo C C and Chyi J I 2001 Device characteristics of the GaN/InGaN-doped channel HFETs *IEEE Electron Device Letters* **22** 501–3

[66] Hestroffer K, Wu F, Li H, Lund C, Keller S, Speck J S and Mishra U K 2015 Relaxed c-plane InGaN layers for the growth of strain-reduced InGaN quantum wells *Semicond Sci Technol* **30**

[67] Hestroffer K, Lund C, Koksaldi O, Li H, Schmidt G, Trippel M, Veit P, Bertram F, Lu N, Wang Q, Christen J, Kim M J, Mishra U K and Keller S 2017 Compositionally graded InGaN layers grown on vicinal N-face GaN substrates by plasma-assisted molecular beam epitaxy *J Cryst Growth* **465** 55–9

[68] Keller S, Lund C, Whyland T, Hu Y, Neufeld C, Chan S, Wienecke S, Wu F, Nakamura S, Speck J S, Denbaars S P and Mishra U K 2015 InGaN lattice constant engineering via growth on (In,Ga)N/GaN nanostripe arrays *Semicond Sci Technol* **30**

[69] Keller S, Schaake C, Fichtenbaum N A, Neufeld C J, Wu Y, McGroddy K, David A, Denbaars S P, Weisbuch C, Speck J S and Mishra U K 2006 Optical and structural properties of GaN nanopillar and nanostripe arrays with embedded InGaN/GaN multi-quantum wells *J Appl Phys* **100** 054314

[70] Evangeline H *Disruptive Substrate Technology for Direct Green and Red Micro LEDs*

[71] Chan P, DenBaars S P and Nakamura S 2021 Growth of highly relaxed InGaN pseudo-substrates over full 2-in. wafers *Appl Phys Lett* **119** 131106

[72] Wang S J, Li N, Yu H B, Feng Z C, Summers C and Ferguson I 2009 Metalorganic chemical vapour deposition of GaN layers on ZnO substrates using α-Al2O3 as a transition layer *J Phys D Appl Phys* **42**

[73] Kobayashi A, Ohta J and Fujioka H 2006 Low temperature epitaxial growth of In0.25Ga0.75N on lattice-matched ZnO by pulsed laser deposition *J Appl Phys* **99** 1–5

[74] Cho Y, Korytov M, Albrecht M, Riechert H and Brandt O 2012 Effects of Ga on the growth of InN on O-face ZnO (000 1) by plasma-assisted molecular beam epitaxy *Appl Phys Lett* **101** 10–4

[75] Matsuoka T, Yoshimoto N, Sasaki T and Katsui A 1992 Wide-gap semiconductor InGaN and InGaAln grown by MOVPE *J Electron Mater* **21** 157–63

[76] Ozaki T, Funato M and Kawakami Y 2015 InGaN-based visible light-emitting diodes on ScAlMgO $_4$ (0001) substrates *Applied Physics Express* **8** 062101

[77] Ozaki T, Takagi Y, Nishinaka J, Funato M and Kawakami Y 2014 Metalorganic vapor phase epitaxy of GaN and lattice-matched InGaN on ScAlMgO4(0001) substrates *Applied Physics Express* **7** 4–7

[78] Pasayat S, Gupta C, Acker-James D, Cohen D, DenBaars S P, Nakamura S, Keller S and Mishra U K 2019 Fabrication of relaxed InGaN pseudo-substrates composed of micron-sized pattern arrays with high fill factors using porous GaN *Semicond Sci Technol*

[79] Pasayat S S, Gupta C, Wang Y, DenBaars S P, Nakamura S, Keller S and Mishra U K 2020 Compliant micron-sized patterned ingan pseudo-substrates utilizing porous GaN *Materials* **13** 6–15

[80] Keller S, Pasayat S S, Gupta C, DenBaars S P, Nakamura S and Mishra U K 2021 Patterned III-Nitrides on Porous GaN: Extending Elastic Relaxation from the Nano- to the Micrometer Scale *physica status solidi (RRL) – Rapid Research Letters* **15** 2100234

[81] Buzza D W, Alkire R C, Griffin P H and Oliver R A 2020 Porous nitride semiconductors reviewed *J Phys D Appl Phys* **53** 383002

[82] Zhang C, Park S H, Chen D, Lin D W, Xiong W, Kuo H C, Lin C F, Cao H and Han J 2015 Mesoporous GaN for Photonic Engineering-Highly Reflective GaN Mirrors as an Example *ACS Photonics* **2** 980–6

[83] Keller S, Pasayat S S, Gupta C, DenBaars S P, Nakamura S and Mishra U K 2021 Patterned III-Nitrides on Porous GaN: Extending Elastic Relaxation from the Nano- to the Micrometer Scale *Physica Status Solidi - Rapid Research Letters* **15**

[84] Pasayat S S, Gupta C, Wang Y, DenBaars S P, Nakamura S, Keller S and Mishra U K 2020 Compliant micron-sized patterned ingan pseudo-substrates utilizing porous GaN *Materials* **13** 6–15

[85] Pasayat S S, Hatui N, Li W, Gupta C, Nakamura S, Denbaars S P, Keller S and Mishra U K 2020 Method of growing elastically relaxed crack-free AlGaN on GaN as substrates for ultra-wide bandgap devices using porous GaN *Appl Phys Lett* **117** 0–6

[86] Pasayat S S, Gupta C, Wong M S, Wang Y, Nakamura S, Denbaars S P, Keller S and Mishra U K 2020 Growth of strain-relaxed InGaN on micrometer-sized patterned compliant GaN pseudo-substrates *Appl Phys Lett* **116**

[87] Wurm C, Collins H, Hatui N, Li W, Pasayat S, Hamwey R, Sun K, Sayed I, Khan K, Ahmadi E, Keller S and Mishra U 2022 Demonstration of device-quality 60% relaxed In0.2Ga0.8N on porous GaN pseudo-substrates grown by PAMBE *J Appl Phys* **131** 015701

[88] Nakamura S, Senoh M, Nagahama S, Iwasa N, Yamada T, Matsushita T, Hiroyuki Kiyoku A and Sugimoto Y 1996 Characteristics of InGaN multi-quantum- well-structure laser diodes *Appl Phys Lett* **68** 3269–71

[89] Nakamura S, Senoh M, Nagahama S, Iwasa N, Yamada T, Matsushita T, Sugimoto Y and Kiyoku H 1997 Room-temperature continuous-wave operation of InGaN multi-quantum-well- structure laser diodes with a long lifetime *Appl. Phys. Lett* **868** 5–8

[90] Nakamura S, Senoh M, Nagahama S I, Iwasa N, Yamada T, Matshushita T, Kiyoku H and Sugimoto Y 1997 InGaN-Based Multi-Quantum-Well-Structure Laser Diodes *Jpn J Appl Phys* **35** L74

[91] Denbaars S P, Feezell D, Kelchner K, Pimputkar S, Pan C C, Yen C C, Tanaka S, Zhao Y, Pfaff N, Farrell R, Iza M, Keller S, Mishra U, Speck J S and Nakamura S 2013 Development of gallium-nitride-based light-emitting diodes (LEDs) and laser diodes for energy-efficient lighting and displays *Acta Mater* **61** 945–51

[92] Chakraborty A, Haskell B A, Keller S, Speck J S, Denbaars S P, Nakamura S and Mishra U K 2005 Demonstration of nonpolar m-plane InGaN/GaN light-emitting diodes on free-standing m-plane GaN substrates *Japanese Journal of Applied Physics, Part 2: Letters* **44** L173

[93] Dahal R, Pantha B, Li J, Lin J Y and Jiang H X 2009 InGaN/GaN multiple quantum well solar cells with long operating wavelengths *Appl Phys Lett* **94** 063505

[94] Neufeld C J, Toledo N G, Cruz S C, Iza M, DenBaars S P and Mishra U K 2008 High quantum efficiency InGaN/GaN solar cells with 2.95 eV band gap *Appl Phys Lett* **93** 143502

[95] Bhuiyan A G, Sugita K, Hashimoto A and Yamamoto A 2012 InGaN solar cells: Present state of the art and important challenges *IEEE J Photovolt* **2** 276–93

[96] Wu J, Walukiewicz W, Yu K M, Shan W, Ager J W, Haller E E, Lu H, Schaff W J, Metzger W K and Kurtz S 2003 Superior radiation resistance of In 1-xGa xN alloys: Full-solar-spectrum photovoltaic material system *J Appl Phys* **94** 6477–82

[97] Chiou Y Z, Su Y K, Chang S J, Gong J, Lin Y C, Liu S H and Chang C S 2003 High detectivity InGaN-GaN multiquantum well p-n junction photodiodes *IEEE J Quantum Electron* **39** 681–5

[98] Muñoz E 2007 (Al,In,Ga)N-based photodetectors. Some materials issues *Phys Status Solidi B Basic Res* **244** 2859–77

[99] Sang L, Liao M, Sumiya M, Yang X and Shen B 2021 High-pressure MOCVD growth of InGaN thick films toward the photovoltaic applications *Fundamental Research*

[100] Sang L, Liao M, Koide Y and Sumiya M 2015 InGaN-based thin film solar cells: Epitaxy, structural design, and photovoltaic properties *J Appl Phys* **117** 105706

[101] Wu J, Walukiewicz W, Yu K M, Shan W, Ager J W, Haller E E, Lu H, Schaff W J, Metzger W K and Kurtz S 2003 Superior radiation resistance of In1−xGaxN alloys: Full-solar-spectrum photovoltaic material system *J Appl Phys* **94** 6477

[102] Tao T, Zhang Z, Liu L, Su H, Xie Z, Zhang R, Liu B, Xiu X, Li Y, Han P, Shi Y and Zheng Y 2011 Surface morphology and composition studies in InGaN/GaN film grown by MOCVD *Journal of Semiconductors* **32** 083002

[103] Sharma N, Thomas P, Tricker D and Humphreys C 2000 Chemical mapping and formation of V-defects in InGaN multiple quantum wells *Appl Phys Lett* **77** 1274–6

[104] Egawa T, Zhang B and Ishikawa H 2005 High performance of InGaN LEDs on (111) silicon substrates grown by MOCVD *IEEE Electron Device Letters* **26** 169–71

[105] Massabuau F C P, Sahonta S L, Trinh-Xuan L, Rhode S, Puchtler T J, Kappers M J, Humphreys C J and Oliver R A 2012 Morphological, structural, and emission characterization of trench defects in InGaN/GaN quantum well structures *Appl Phys Lett* **101** 212107

[106] Schulz T, Lymperakis L, Anikeeva M, Siekacz M, Wolny P, Markurt T and Albrecht M 2020 Influence of strain on the indium incorporation in (0001) GaN

[107] Jahnen B, Albrecht M, Dorsch W, Christiansen S, Strunk H P, Hanser D and Davis R F 1998 Pinholes, dislocations and strain relaxation in InGaN *MRS Internet Journal of Nitride Semiconductor Research* **3** 39

[108] Srinivasan S, Geng L, Liu R, Ponce F A, Narukawa Y and Tanaka S 2003 Slip systems and misfit dislocations in InGaN epilayers *Appl Phys Lett* **83** 5187–9

[109] Liu R, Mei J, Srinivasan S, Ponce F A, Omiya H, Narukawa Y and Mukai T 2006 Generation of misfit dislocations by basal-plane slip in InGaN/GaN heterostructures *Appl Phys Lett* **89** 201911

[110] Mei J, Liu R, Ponce F A, Omiya H and Mukai T 2007 Basal-plane slip in InGaNGaN heterostructures in the presence of threading dislocations *Appl Phys Lett* **90** 171922

[111] Holec D, Costa P M F J, Kappers M J and Humphreys C J 2007 Critical thickness calculations for InGaN/GaN *J Cryst Growth* **303** 314–7

[112] Lobanova A v., Kolesnikova A L, Romanov A E, Karpov S Y, Rudinsky M E and Yakovlev E v. 2013 Mechanism of stress relaxation in (0001) InGaN/GaN via formation of V-shaped dislocation half-loops *Appl Phys Lett* **103** 152106

[113] Fischer A M, Wei Y O, Ponce F A, Moseley M, Gunning B and Doolittle W A 2013 Highly luminescent, high-indium-content InGaN film with uniform composition and full misfit-strain relaxation *Appl Phys Lett* **103** 1–5

[114] Norman A G, Seong T-Y, Ferguson I T, Booker G R and Joyce B A 1993 Structural studies of natural superlattices in group III-V alloy epitaxial layers *Semicond Sci Technol* **8** S9

[115] Ferguson I T, Norman A G, Joyce B A, Seong T Y, Booker G R, Thomas R H, Phillips C C and Stradling R A 1991 Molecular beam epitaxial growth of InAsSb strained layer superlattices. Can nature do it better? *Appl Phys Lett* **59** 3324–6

[116] Jani O, Ferguson I, Honsberg C and Kurtz S 2007 Design and characterization of GaNInGaN solar cells *Appl Phys Lett* **91** 132117

[117] Dahal R, Pantha B, Li J, Lin J Y and Jiang H X 2009 InGaN/GaN multiple quantum well solar cells with long operating wavelengths *Appl Phys Lett* **94** 063505

[118] Neufeld C J, Toledo N G, Cruz S C, Iza M, DenBaars S P and Mishra U K 2008 High quantum efficiency InGaN/GaN solar cells with 2.95 eV band gap *Appl Phys Lett* **93** 143502

[119] Sheu J K, Yang C C, Tu S J, Chang K H, Lee M L, Lai W C and Peng L C 2009 Demonstration of GaN-based solar cells with GaN/InGaN superlattice absorption layers *IEEE Electron Device Letters* **30** 225–7

[120] El-Masry N A, Behbehani M K, LeBoeuf S F, Aumer M E, Roberts J C and Bedair S M 2001 Self-assembled AlInGaN quaternary superlattice structures *Appl Phys Lett* **79** 1616–8

[121] Teles L K, Marques M, Scolfaro L M R, Leite J R and Ferreira L G 2004 Phase Separation and Ordering in Group-III Nitride Alloys *Brazilian Journal of Physics* **34**

[122] Behbehani M K, Piner E L, Liu S X, El-Masry N A and Bedair S M 1999 Phase separation and ordering coexisting in InxGa1-xN grown by metal organic chemical vapor deposition *Appl Phys Lett* **75** 2202–4

[123] Gao M, Bradley S T, Cao Y, Jena D, Lin Y, Ringel S A, Hwang J, Schaff W J and Brillson L J 2006 Compositional modulation and optical emission in AlGaN epitaxial films *J Appl Phys* **100** 1–12

[124] Northrup J E, Romano L T and Neugebauer J 1999 Surface energetics, pit formation, and chemical ordering in InGaN alloys *Appl Phys Lett* **74** 2319

[125] Northrup J E 2009 GaN and InGaN(11$\bar{2}$2) surfaces: Group-III adlayers and indium incorporation *Appl Phys Lett* **95** 133107

[126] Teles L K, Marques M, Scolfaro L M R, Leite J R and Ferreira L G 2004 Phase Separation and Ordering in Group-III Nitride Alloys *Brazilian Journal of Physics* **34**

[127] Wu Z H, Kawai Y, Fang Y Y, Chen C Q, Kondo H, Hori M, Honda Y, Yamaguchi M and Amano H 2011 Spontaneous formation of highly regular superlattice structure in InGaN epilayers grown by molecular beam epitaxy *Appl Phys Lett* **98** 141905

[128] Zheng X T, Wang T, Wang P, Sun X X, Wang D, Chen Z Y, Quach P, Wang Y X, Yang X L, Xu F J, Qin Z X, Yu T J, Ge W K, Shen B and Wang X Q 2020 Full-composition-graded InxGa1-xN films grown by molecular beam epitaxy *Appl Phys Lett* **117**

[129] Kaun S W, Wong M H, Mishra U K and Speck J S 2013 Molecular beam epitaxy for high-performance Ga-face GaN electron devices Related content N-polar GaN epitaxy and high electron mobility transistors *Semicond. Sci. Technol* **28** 74001

[130] Heying B, Tarsa E J, Elsass C R, Fini P, DenBaars S P and Speck J S 1999 Dislocation mediated surface morphology of GaN *J Appl Phys* **85** 6470–6

[131] Holec D, Costa P M F J, Kappers M J and Humphreys C J 2007 Critical thickness calculations for InGaN/GaN *J Cryst Growth* **303** 314–7

[132] Ertekin E, Greaney P A and Chrzan D C 2005 Equilibrium limits of coherency in strained nanowire heterostructures *J. Appl. Phys* **97** 114325

[133] Stankevič T, Dzhigaev D and Bi Z 2015 Strain mapping in an InGaN/GaN nanowire using a nano-focused x-ray beam *Appl. Phys. Lett* **107** 103101

[134] Iliopoulos E, Ludwig K F and Moustakas T D 2003 Complex ordering in ternary wurtzite nitride alloys *Journal of Physics and Chemistry of Solids* **64** 1525–32

[135] Iliopoulos E, Ludwig K F, Moustakas T D, Komninou P, Karakostas T, Nouet G and Chu S N G 2001 Epitaxial growth and self-organized superlattice structures in AlGaN films grown by plasma assisted molecular beam epitaxy *Materials Science and Engineering: B* **87** 227–36

[136] Behbehani M K, Piner E L, Liu S X, El-Masry N A and Bedair S M 1999 Phase separation and ordering coexisting in InxGa1−xN grown by metal organic chemical vapor deposition *Appl Phys Lett* **75** 2202

[137] Tersoff J 1997 Spinodal decomposition during step-flow growth *Phys Rev B* **56** 56

[138] Grenet G, Gendry M, Oustric M, Robach Y, Porte L, Hollinger G, Marty O, Pitaval M and Priester C 1998 Surface spinodal decomposition in low temperature Al0.48In0.52As grown on InP(001) by molecular beam epitaxy

[139] Khan K, Biswas M and Ahmadi E 2020 Growth of high quality (In,Ga)N films on O-face ZnO substrates by plasma-assisted molecular beam epitaxy *AIP Adv* **10** 075120

[140] Karpov S Y 1998 Suppression of phase separation in InGaN due to elastic strain *MRS Internet J. Nitride Semicond. Res* **3** 16

[141] Anon 2002 Phase separation suppression in InGaN epitaxial layers due to biaxial strain

[142] Tessarek C, Figge S, Aschenbrenner T, Bley S, Rosenauer A, Seyfried M, Kalden J, Sebald K, Gutowski J and Hommel D 2011 Strong phase separation of strained In x Ga 1−x N layers due to spinodal and binodal decomposition: Formation of stable quantum dots *Phys Rev B* **83** 115316

[143] Bartel T, Kisielowski C and Specht P 1927 Spinodal Decomposition in Thick InGaN Layers Studied by Strain Field Analysis *Microsc Microanal* **12**

[144] Mbaye A A, Wood ' D M and Zunger A Stability of bulk and yseudomoryhic epitaxial semiconductors and their alloys *PHYSICAL REVIEWER* **8** 15–1988

[145] Sun C-K, Chiu T-L, Keller S, Wang G, Minsky M S, DenBaars S P and Bowers J E 1998 Time-resolved photoluminescence studies of InGaN/GaN single-quantum-wells at room temperature *Appl Phys Lett* **71** 425

[146] Lefebvre P, Morel A, Gallart M, Taliercio T, Allègre J, Gil B, Mathieu H, Damilano B, Grandjean N and Massies J 2001 High internal electric field in a graded-width InGaN/GaN quantum well: Accurate determination by time-resolved photoluminescence spectroscopy *Appl Phys Lett* **78** 1252

[147] Takeguchi M, McCartney M R and Smith D J 2004 Mapping In concentration, strain, and internal electric field in InGaN/GaN quantum well structure *Appl Phys Lett* **84** 2103

[148] Minsky M S, Fleischer S B, Abare A C, Bowers J E, Hu E L, Keller S and Denbaars S P 1998 Characterization of high-quality InGaN/GaN multiquantum wells with time-resolved photoluminescence *Appl Phys Lett* **72** 1066

[149] Pophristic M, Long F H, Tran C, Ferguson I T and Karlicek R F 1999 Time-resolved photoluminescence measurements of quantum dots in InGaN multiple quantum wells and light-emitting diodes *J Appl Phys* **86** 1114

[150] Kurtz A D, Kulin S A and Averbach B L 1956 Effect of Dislocations on the Minority Carrier Lifetime in Semiconductors* *Phys. Rev.* **101** 1285

[151] Im J S, Kollmer H, Off J, Sohmer A, Scholz F and Hangleiter A 1998 Reduction of oscillator strength due to piezoelectric fields in GaN/Al x Ga 1x N quantum wells *Phys Rev B* **57** R9435

[152] Berkowicz E, Gershoni D, Bahir G, Lakin E, Shilo D and Zolotoyabko E 2000 Measured and calculated radiative lifetime and optical absorption of quantum structures *Phys Rev B Condens Matter Mater Phys* **61** 10994–1008

[153] Nakamura S, Senoh M, Iwasa N and Nagahama S I 1995 High-Brightness InGaN Blue , Green and Yellow Light-Emitting Diodes with Quantum Well Structures *Jpn J Appl Phys* **34** 797–9

[154] Wu Y F, Saxler A, Moore M, Smith R P, Sheppard S, Chavarkar P M, Wisleder T, Mishra U K and Parikh P 2004 30-W/mm GaN HEMTs by Field Plate Optimization *IEEE Electron Device Letters* **25** 117–9

[155] Mishra U K, Shen Likun, Kazior T E and Yi-Feng Wu 2008 GaN-Based RF Power Devices and Amplifiers *Proceedings of the IEEE* **96** 287–305

[156] Mishra U K, Parikh P and Wu Y F 2002 AlGaN/GaN HEMTs - An overview of device operation and applications *Proceedings of the IEEE* **90** 1022–31

[157] Wong M H, Keller S, Dasgupta N S, Denninghoff D J, Kolluri S, Brown D F, Lu J, Fichtenbaum N A, Ahmadi E, Singisetti U, Chini A, Rajan S, Denbaars S P, Speck J S and Mishra U K 2013 N-polar GaN epitaxy and high electron mobility transistors *Semicond Sci Technol* **28**

[158] Wong M H 2009 *N-face GaN-based Materials and Microwave Transistors by Plasma-Assisted Molecular Beam Epitaxy* (University of California, Santabarba)

[159] Romanczyk B, Wienecke S, Guidry M, Li H, Hestroffer K, Ahmadi E, Zheng X, Keller S and Mishra U K 2016 mm-Wave N-polar GaN MISHEMT with a self-aligned recessed gate exhibiting record 4.2 W/mm at 94 GHz on Sapphire *2016 74th Annual Device Research Conference (DRC)* (IEEE) pp 1–2

[160] Romanczyk B, Mishra U K, Zheng X, Guidry M, Li H, Hatui N, Wurm C, Krishna A, Ahmadi E and Keller S 2020 W-Band Power Performance of SiN-Passivated N-Polar GaN Deep Recess HEMTs *IEEE Electron Device Letters* **41** 349–52

[161] Romanczyk B, Wienecke S, Guidry M, Li H, Ahmadi E, Zheng X, Keller S and Mishra U K 2018 Demonstration of Constant 8 W/mm Power Density at 10, 30, and 94 GHz in State-of-the-Art Millimeter-Wave N-Polar GaN MISHEMTs *IEEE Trans Electron Devices* **65** 45–50

[162] Liu W, Romanczyk B, Guidry M, Hatui N, Wurm C, Li W, Shrestha P, Zheng X, Keller S and Mishra U K 2021 6.2 W/mm and Record 33.8% PAE at 94 GHz from N-polar GaN Deep Recess MIS-HEMTs with ALD Ru Gates *IEEE Microwave and Wireless Components Letters* 1–1

[163] Akyol F, Nath D N, Gür E, Park P S and Rajan S 2011 N-polar III-nitride green (540 nm) light emitting diode *Jpn J Appl Phys* **50** 052101

[164] Lund C, Nakamura S, DenBaars S P, Mishra U K and Keller S 2017 Growth of high purity N-polar (In,Ga)N films *J Cryst Growth* **464** 127–31

[165] Lund C, Nakamura S, Denbaars S P, Mishra U K and Keller S 2019 Properties of N-polar InGaN/GaN quantum wells grown with triethyl gallium and triethyl indium as precursors *Semicond Sci Technol* **34** 075017

[166] Pasayat S S, Lund C, Tsukada Y, Catalano M, Wang L, Kim M J, Nakamura S, Keller S and Mishra U K 2020 Optimization of Digital Growth of Thick N-Polar InGaN by MOCVD *J Electron Mater* **49** 3450–4

[167] al Balushi Z Y and Redwing J M 2017 The effect of polarity on MOCVD growth of thick InGaN *Appl Phys Lett* **110** 022101

[168] Bansal A, Redwing J M and al Balushi Z Y 2020 Cathodoluminescence spatially resolves optical transitions in thick group-III and N-polar InGaN films *J Appl Phys* **128**

[169] Nath D N, Gür E, Ringel S A and Rajan S 2011 Growth model for plasma-assisted molecular beam epitaxy of N-polar and Ga-polar InxGa1−xN *Journal of Vacuum Science & Technology B* **29** 021206

[170] Nath D N, Gür E, Ringel S A and Rajan S 2010 Molecular beam epitaxy of N-polar InGaN *Appl Phys Lett* **97** 13–6

[171] Akyol F, Nath D N, Krishnamoorthy S, Park P S and Rajan S 2012 Suppression of electron overflow and efficiency droop in N-polar GaN green light emitting diodes *Appl Phys Lett* **100** 111118

[172] Akyol F, Nath D N, Gür E, Park P S and Rajan S 2011 N-polar III-nitride green (540 nm) light emitting diode *Jpn J Appl Phys* **50** 052101

[173] Northrup J E and Neugebauer J 1999 Indium-induced changes in GaN(0001) surface morphology *Phys Rev B* **60** R8473

[174] Khan K, Sun K, Wurm C and Ahmadi E 2022 Impact of In flux on self-assembled InGaN / GaN superlattice grown on GaN template by plasma-assisted molecular beam epitaxy **98** 141905

[175] Khan K, Sun K, Wurm C, Datta K, Deotare P B and Ahmadi E 2021 Strain-induced formation of self-assembled InGaN/GaN superlattices in nominal InGaN films grown by plasma-assisted molecular beam epitaxy *Phys Rev Mater* **5** 124606

[176] Diez S, Mohanty S, Kurdak C and Ahmadi E 2020 Record high electron mobility and low sheet resistance on scaled-channel N-polar GaN/AlN heterostructures grown on on-axis N-polar GaN substrates by plasma-assisted molecular beam epitaxy *Appl Phys Lett* **117** 042102

[177] Pasayat S S, Ahmadi E, Romanczyk B, Koksaldi O, Agarwal A, Guidry M, Gupta C, Wurm C, Keller S and Mishra U K 2019 First demonstration of RF N-polar GaN MIS-HEMTs grown on bulk GaN using PAMBE *Semicond Sci Technol* **34** 045009

[178] Wurm C, Ahmadi E, Wu F, Hatui N, Keller S, Speck J and Mishra U 2020 Growth of high-quality N-polar GaN on bulk GaN by plasma-assisted molecular beam epitaxy *Solid State Commun* **305** 113763

[179] Yang F, Zhang Y T, Han X, Li P C, Jiang J Y, Huang Z, Yin J Z, Zhao D G, Zhang B L and Du G T 2016 Growth parametric study of N-polar InGaN films by metalorganic chemical vapor deposition *Superlattices Microstruct* **91** 259–68

[180] Vampola K J, Iza M, Keller S, DenBaars S P and Nakamura S 2009 Measurement of electron overflow in 450 nm InGaN light-emitting diode structures *Appl Phys Lett* **94** 061116

[181] Xie J, Ni X, Fan Q, Shimada R, Özgür Ü and Morkoç H 2008 On the efficiency droop in InGaN multiple quantum well blue light emitting diodes and its reduction with p-doped quantum well barriers *Appl Phys Lett* **93** 121107

[182] Shiojiri M, Čeh M, Šturm S, Chuo C C, Hsu J T, Yang J R and Saijo H 2006 Structural and compositional analyses of a strained superlattice *J. Appl. Phys* **100** 13110

[183] Kobayashi A, Ohta J and Fujioka H 2017 Pulsed sputtering epitaxial growth of m-plane InGaN lattice-matched to ZnO *Sci Rep* **7** 1–6

[184] Hamdani F, Yeadon M, Smith D J, Tang H, Kim W, Salvador A, Botchkarev A E, Gibson J M, Polyakov A Y, Skowronski M and Morkoç H 1998 Microstructure and optical properties of epitaxial GaN on ZnO (0001) grown by reactive molecular beam epitaxy *J Appl Phys* **83** 983–90

[185] Hamdani F, Botchkarev A E, Tang H, Kim W and Morkoç H 1997 Effect of buffer layer and substrate surface polarity on the growth by molecular beam epitaxy of GaN on ZnO *Appl Phys Lett* **71** 3111–3

[186] Hamdani F, Botchkarev A, Kim W, Morkoç H, Yeadon M and Morkoc H 1997 Optical properties of GaN grown on ZnO by reactive molecular beam epitaxy **467** 226–9

[187] Hamdani F, Botchkarev A E, Tang H, Kim W and Morkoç H 1997 Effect of buffer layer and substrate surface polarity on the growth by molecular beam epitaxy of GaN on ZnO *Appl Phys Lett* **71** 3111–3

[188] Hamdani F, Yeadon M, Smith D J, Tang H, Kim W, Salvador A, Botchkarev A E, Gibson J M, Polyakov A Y, Skowronski M and Morkoç H 1998 Microstructure and optical properties of epitaxial GaN on ZnO (0001) grown by reactive molecular beam epitaxy *J Appl Phys* **83** 983–90

[189] Gu X, Sabuktagin S, Teke A, Johnstone D, Morkoç H, Nemeth B and Nause J 2004 Effect of thermal treatment on ZnO substrate for epitaxial growth *Journal of Materials Science: Materials in Electronics* **15** 373–8

[190] Wang S J, Li N, Yu H B, Feng Z C, Summers C and Ferguson I 2009 Metalorganic chemical vapour deposition of GaN layers on ZnO substrates using α-Al2O3 as a transition layer *J Phys D Appl Phys* **42**

[191] Wang S J, Li N, Park E H, Feng Z C, Valencia A, Nause J, Kane M, Summers C and Ferguson I 2008 MOCVD growth of GaN-based materials on ZnO substrates *Physica Status Solidi (C) Current Topics in Solid State Physics* **5** 1736–9

[192] Li N, Wang S, Park E, Chuan Z, Tsai H, Yang J, Ferguson I and Sapphire B 2009 Suppression of phase separation in InGaN layers grown on lattice-matched ZnO substrates *J Cryst Growth* **311** 4628–31

[193] Li N 2009 *GaN on ZnO: a new approach to solid state lighting*

[194] Matsuoka T, Yoshimoto N, Sasaki T and Katsui A 1992 Wide-Gap Semiconductor InGaN and InGaAIN Grown by MOVPE *J. Electronic. Mater.* **21** 157–63

[195] Gu X, Reshchikov M A, Teke A, Johnstone D, Morkoç H, Nemeth B and Nause J 2004 GaN epitaxy on thermally treated c-plane bulk ZnO substrates with O and Zn faces *Appl Phys Lett* **84** 2268–70

[196] Namkoong G, Burnham S, Lee K K, Trybus E, Doolittle W A, Losurdo M, Capezzuto P, Bruno G, Nemeth B and Nause J 2005 III-nitrides on oxygen- and zinc-face ZnO substrates *Appl Phys Lett* **87** 1–3

[197] Hellman E S, Buchanan D N E, Wiesmann D, Brener I, Laboratories B and Technologies L 1996 Internet Journal *MRS internet Journal of Nitride Semiconductor Research* **1** 13(4pp)

[198] Cho Y, Brandt O, Korytov M, Albrecht M, Kaganer V M, Ramsteiner M and Riechert H 2012 Structural properties of InN films grown on O-face ZnO (000$\bar{1}$) by plasma-assisted molecular beam epitaxy *Appl Phys Lett* **100**

[199] Ernst T, Chèze C and Calarco R 2018 InN and GaN/InN monolayers grown on ZnO(000 1) and ZnO(0001) *J Appl Phys* **124**

[200] Kobayashi A, Kawano S, Kawaguchi Y, Ohta J and Fujioka H 2007 Room temperature epitaxial growth of m -plane GaN on lattice-matched ZnO substrates *Appl Phys Lett* **90** 1–4

[201] Akasaka S, Nakahara K, Yuji H, Tsukazaki A, Ohtomo A and Kawasaki M 2011 Preparation of an epitaxy-ready surface of a ZnO(0001) substrate *Applied Physics Express* **4** 12–4

[202] Kozuka Y, Tsukazaki A and Kawasaki M 2014 Challenges and opportunities of ZnO-related single crystalline heterostructures *Appl Phys Rev* **1**

[203] Cho M W, Harada C, Suzuki H, Minegishi T, Yao T, Ko H, Maeda K and Nikura I 2005 Issues in ZnO homoepitaxy *Superlattices Microstruct* **38** 349–63

[204] Grasza K, ŁUsakowska E, Skupiński P, Kopalko K, Bąk-Misiuk J and Mycielski A 2007 Effect of annealing atmosphere on the quality of ZnO crystal surface *Phys Status Solidi B Basic Res* **244** 1468–72

[205] Grasza K, Łusakowska E, Skupinski P, Sakowska H and Mycielski A 2007 Thermal annealing of ZnO substrates *Superlattices Microstruct* **42** 290–3

[206] Neumann C, Lautenschläger S, Graubner S, Sann J, Volbers N, Meyer B K, Bläsing J, Krost A, Bertram F and Christen J 2007 Homoepitaxy of ZnO: From the substrates to doping *Phys Status Solidi B Basic Res* **244** 1451–7

[207] Graubner S, Neumann C, Volbers N, Meyer B K, Bläsing J and Krost A 2007 Preparation of ZnO substrates for epitaxy: Structural, surface, and electrical properties *Appl Phys Lett* **90** 88–91

[208] Nakamura T, Masuko K, Ashida A, Yoshimura T and Fujimura N 2011 Surface preparation of ZnO single-crystal substrate for the epitaxial growth of ZnO thin films *J Cryst Growth* **318** 516–8

[209] Heffelfinger J R and Carter C B 1997 Mechanisms of surface faceting and coarsening *Surf Sci* **389** 188–200

[210] Ohgaki T 2009 Interface structure and polarity of GaN / ZnO heterostructure *The 62th CerSJ Awards for Advancements in Ceramic Science and Technology: Review* **117** 475–81

[211] Kobayashi A, Fujioka H, Ohta J and Oshima M 2004 Room Temperature Layer by Layer Growth of GaN on Atomically Flat ZnO *Japanese Journal of Applied Physics, Part 2: Letters* **43** 2–5

[212] Shimomoto K, Kobayashi A, Mitamura K, Ueno K, Ohta J, Oshima M and Fujioka H 2010 Characteristics of m-Plane InN films grown on ZnO substrates at room temperature by pulsed laser deposition *Jpn J Appl Phys* **49** 2–5

[213] Ueno K, Kobayashi A, Ohta J and Fujioka H 2006 Layer-by-layer growth of AlN on ZnO(0001) substrates at room temperature *Japanese Journal of Applied Physics, Part 2: Letters* **45**

[214] Oshima M, Ueno K, Kajima T, Ohta J, Fujii T, Kobayashi A, Fujioka H and Shimomoto K 2010 Room-Temperature Epitaxial Growth of High-Quality m -Plane InAlN Films on Nearly Lattice-Matched ZnO Substrates *Jpn J Appl Phys* **49** 070202

[215] Butcher K S A, Alexandrov D, Terziyska P, Georgiev V and Georgieva D 2012 Initial experiments in the migration enhanced afterglow growth of gallium and indium nitride *Physica Status Solidi (C) Current Topics in Solid State Physics* **9** 1070–3

[216] Yamaguchi T, Muto D, Araki T, Maeda N and Nanishi Y 2009 Novel InN growth method under In-rich condition on GaN/Al2O3 (0001) templates *physica status solidi c* **6** S360–3

[217] Trybus E, Namkoong G, Henderson W, Burnham S, Doolittle W A, Cheung M and Cartwright A 2006 InN: A material with photovoltaic promise and challenges *J Cryst Growth* **288** 218–24

[218] Koblmüller G, Fernández-Garrido S, Calleja E and Speck J S 2007 In situ investigation of growth modes during plasma-assisted molecular beam epitaxy of (0001) GaN *Appl Phys Lett* **91** 16–8

[219] Poblenz C, Waltereit P and Speck J S 2005 Uniformity and control of surface morphology during growth of GaN by molecular beam epitaxy *Journal of Vacuum Science and Technology B: Microelectronics and Nanometer Structures* **23** 1379–85

[220] Adelmann C, Brault J, Jalabert D, Gentile P, Mariette H, Mula G and Daudin B 2002 Dynamically stable gallium surface coverages during plasma-assisted molecular-beam epitaxy of (0001) GaN *J Appl Phys* **91** 9638–45

[221] Foussekis M, Ferguson J D, McNamara J D, Baski A A and Reshchikov M A 2012 Effects of polarity and surface treatment on Ga- and N-polar bulk GaN *Journal of Vacuum Science & Technology B, Nanotechnology and Microelectronics: Materials, Processing, Measurement, and Phenomena* **30** 051210

[222] Khan K, Diez S, Sun K, Wurm C, Mishra U K and Ahmadi E 2021 Observation of self-assembled InGaN/GaN superlattice structure grown on N-polar GaN by plasma-assisted molecular beam epitaxy *APL Mater* **9** 121114

[223] Tabata A, Teles L K, Scolfaro L M R, Leite J R, Kharchenko A, Frey T, As D J, Schikora D, Lischka K, Furthmüller J and Bechstedt F 2002 Phase separation suppression in InGaN epitaxial layers due to biaxial strain *Appl Phys Lett* **80** 769

[224] Sekiguchi H, Sasaki Y C, Lyons J L, Janotti A and van de Walle C G Impact of Group-II Acceptors on the Electrical and Optical Properties of GaN *Jpn J Appl Phys*

[225] Janicki Ł, Mohajerani M S, Hartmann J, Zdanowicz E, Wehmann H H, Waag A and Kudrawiec R 2018 Zn acceptor position in GaN:Zn probed by contactless electroreflectance spectroscopy *Appl Phys Lett* **113** 032109

[226] Zajac M, Konczewicz L, Litwin-Staszewska E, Iwinska M, Kucharski R, Juillaguet S and Contreras S 2021 p-type conductivity in GaN:Zn monocrystals grown by ammonothermal method *J Appl Phys* **129** 135702

[227] Hestroffer K, Wu F, Li H, Lund C, Keller S, Speck J S and Mishra U K 2015 Relaxed c-plane InGaN layers for the growth of strain-reduced InGaN quantum wells *Semicond Sci Technol* **30**

[228] Wallace M 2016 Optoelectronic study of InGaN/GaN LEDs

[229] Ambacher O, Dimitrov R, Stutzmann M, Foutz B E, Murphy M J, Smart J A, Shealy J R, Weimann N G, Chu K, Chumbes M, Green B, Sierakowski A J, Schaff W J and Eastman L F 1999 Role of

Spontaneous and Piezoelectric Polarization Induced Effects in Group-III Nitride Based Heterostructures and Devices *phys. stat. sol. (b)* **216**

[230] Feneberg M and Thonke K 2007 Polarization fields of III-nitrides grown in different crystal orientations *Journal of Physics: Condensed Matter* **19** 403201

[231] Bernardini F, Fiorentini V and Vanderbilt D 1997 Spontaneous polarization and piezoelectric constants of III-V nitrides *Phys Rev B* **56** R10024

[232] Bernardini F and Fiorentini V 1999 Spontaneous versus Piezoelectric Polarization in III±V Nitrides: Conceptual Aspects and Practical Consequences *phys. stat. sol. (b)* **216** 391

[233] Takeuchi T, Sota S, Katsuragawa M, Komori M, Takeuchi H, Amano H A H and Akasaki I A I 1997 Quantum-Confined Stark Effect due to Piezoelectric Fields in GaInN Strained Quantum Wells *Jpn J Appl Phys* **36** L382

[234] Miller D A B, Chemla D S, Damen T C, Gossard A C, Wiegmann W, Wood T H and Burrus C A 1984 Band-Edge Electroabsorption in Quantum Well Structures: The Quantum-Confined Stark Effect *Phys Rev Lett* **53** 2173

[235] Alam S *High Indium Concentration InGaN Multi-Quantum-Well-Based Blue-Green Light-Emitting Diodes Grown on InGaN "Semi-Bulk" Buffer*

[236] Sharma T K and Towe E 2010 Application-oriented nitride substrates: The key to long-wavelength nitride lasers beyond 500 nm *J Appl Phys* **107** 024516

[237] Zhang C, Park S H, Chen D, Lin D W, Xiong W, Kuo H C, Lin C F, Cao H and Han J 2015 Mesoporous GaN for Photonic Engineering-Highly Reflective GaN Mirrors as an Example *ACS Photonics* **2** 980–6

[238] Davis M E 2002 Ordered porous materials for emerging applications *Nature 2002 417:6891* **417** 813–21

[239] Cullis A G, Canham L T and Calcott P D J 1998 The structural and luminescence properties of porous silicon *J Appl Phys* **82** 909

[240] Zhang Y, Ryu S-W, Yerino C, Leung B, Sun Q, Song Q, Cao H and Han J 2010 A conductivity-based selective etching for next generation GaN devices *physica status solidi (a)* **247** 1713

[241] Chen D, Xiao H and Han J 2012 Nanopores in GaN by electrochemical anodization in hydrofluoric acid: Formation and mechanism *J Appl Phys* **112** 064303

[242] Griffin P H and Oliver R A 2020 Porous nitride semiconductors reviewed *J Phys D Appl Phys* **53**

[243] Tseng W J, Van Dorp D H, Lieten R R, Vereecken P M and Borghs G 2014 Anodic etching of n-GaN epilayer into porous GaN and its photoelectrochemical properties *Journal of Physical Chemistry C* **118** 29492–8

[244] Vajpeyi A P, Tripathy S, Chua S J and Fitzgerald E A 2005 Investigation of optical properties of nanoporous GaN films *Physica E Low Dimens Syst Nanostruct* **28** 141–9

[245] Chen D, Xiao H and Han J 2012 Nanopores in GaN by electrochemical anodization in hydrofluoric acid: Formation and mechanism *J Appl Phys* **112** 064303

[246] Lin C F, Zheng J H, Yang Z J, Dai J J, Lin D Y, Chang C Y, Lai Z X and Hong C S 2006 High-efficiency InGaN-based light-emitting diodes with nanoporous GaN:Mg structure *Appl Phys Lett* **88** 083121

[247] Won D, Weng X and Redwing J M 2010 Effect of indium surfactant on stress relaxation by V-defect formation in GaN epilayers grown by metalorganic chemical vapor deposition *J Appl Phys* **108** 093511

[248] Hiramatsu K, Kawaguchi Y, Shimizu M, Sawaki N, Zheleva T, Davis R F, Tsuda H, Taki W, Kuwano N and Oki K 1997 The Composition Pulling Effect in MOVPE Grown InGaN on GaN and AlGaN and its TEM Characterization *Materials Research Society Internet Journal of Nitride Semiconductor Research* **2**

[249] Collins H, Sayed I, Liu W, Pasayat S S, Taylor A A, Li W, Keller S and Mishra U K 2021 Investigation and optimization of N-polar GaN porosification for regrowth of smooth hillocks-free GaN films *Appl Phys Lett* **119**

[250] Pasayat S S, Gupta C, Wong M S, Wang Y, Nakamura S, Denbaars S P, Keller S and Mishra U K 2020 Growth of strain-relaxed InGaN on micrometer-sized patterned compliant GaN pseudo-substrates *Appl Phys Lett* **116** 111101

[251] Wurm C, Collins H, Hatui N, Li W, Pasayat S, Hamwey R, Sun K, Sayed I, Khan K, Ahmadi E, Keller S and Mishra U 2022 Demonstration of device-quality 60% relaxed In0.2Ga0.8N on porous GaN pseudo-substrates grown by PAMBE *J Appl Phys* **131** 015701

[252] Koblmüller G, Wu F, Mates T, Speck J S, Fernández-Garrido S and Calleja E 2007 High electron mobility GaN grown under N-rich conditions by plasma-assisted molecular beam epitaxy *Appl Phys Lett* **91** 221905

[253] Pereira S, Correia M R and Pereira E 2002 Strain and composition distributions in wurtzite InGaN/GaN layers extracted from x-ray reciprocal space mapping *Appl. Phys. Lett* **80** 3913

[254] Tarsa E, Heying B, Wu X, Fini P, DenBaars S and Speck J 1997 Homoepitaxial growth of GaN under Ga-stable and N-stable conditions by plasma-assisted molecular beam epitaxy *J Appl Phys* **82** 5472

[255] Jeong H, Jeong H J, Oh H M, Hong C H, Suh E K, Lerondel G and Jeong M S 2015 Carrier localization in In-rich InGaN/GaN multiple quantum wells for green light-emitting diodes *Sci Rep* **5**

[256] Valdueza-Felip S, Rigutti L, Naranjo F B, Ruterana P, Mangeney J, Julien F H, González-Herráez M and Monroy E 2012 Carrier localization in InN/InGaN multiple-quantum wells with high In-content *Appl Phys Lett* **101** 062109

[257] Naranjo F B, Sánchez-García M A, Calle F, Calleja E, Jenichen B and Ploog K H 2002 Strong localization in InGaN layers with high In content grown by molecular-beam epitaxy *Appl Phys Lett* **80** 231

[258] Wu C-J, Kuo C-Y, Wang C-J, Chang W-E, Tsai C-L, Lin C-F and Han J 2020 Deep-UV Porous AlGaN Distributed Bragg Reflectors for Deep Ultraviolet Light-Emitting Diodes and Laser Diodes

[259] Griffin P, Zhu T and Oliver R 2018 Porous AlGaN-Based Ultraviolet Distributed Bragg Reflectors *Materials* **11**

[260] Zhao C, Yang X, Wei B, Liu J, Chen R, Luan C and Xiao H 2020 Enhancement in light-emission efficiency of InGaN/GaN multiple quantum well layer by a porous-GaN mirror *Vacuum* **182**

[261] Calleja E, Sá Nchez-Garcí M A, Sá Nchez F J, Calle F, Naranjo F B, Muñ Oz E, Jahn U and Ploog K Luminescence properties and defects in GaN nanocolumns grown by molecular beam epitaxy

[262] Ristić J, Calleja E, Fernández-Garrido S, Cerutti L, Trampert A, Jahn U and Ploog K H 2008 On the mechanisms of spontaneous growth of III-nitride nanocolumns by plasma-assisted molecular beam epitaxy *J Cryst Growth* **310** 4035–45

[263] Calarco R, Meijers R J, Debnath R K, Stoical T, Sutter E and Lüth H 2007 Nucleation and growth of GaN nanowires on Si(111) performed by molecular beam epitaxy *Nano Lett* **7** 2248–51

[264] Legallais M, Nguyen T T T, Mouis M, Salem B, Robin E, Chenevier P and Ternon C 2018 An innovative large scale integration of silicon nanowire-based field effect transistors *Solid State Electron* **143** 97–102

[265] Mu L, Chang Y, Sawtelle S D, Wipf M, Duan X and Reed M A 2015 Silicon nanowire field-effect transistors - A versatile class of potentiometric nanobiosensors *IEEE Access* **3** 287–302

[266] Shaygan M, Davami K, Kheirabi N, Baek C K, Cuniberti G, Meyyappan M and Lee J S 2014 Single-crystalline CdTe nanowire field effect transistors as nanowire-based photodetector *Physical Chemistry Chemical Physics* **16** 22687–93

[267] Schmidt V, Riel H, Senz S, Karg S, Riess W and Gösele U 2006 Realization of a Silicon Nanowire Vertical Surround-Gate Field-Effect Transistor *Small* **2** 85–8

[268] Larrieu G and Han X L 2013 Vertical nanowire array-based field effect transistors for ultimate scaling *Nanoscale* **5** 2437–41

[269] Yu R, Georgiev Y M, Das S, Hobbs R G, Povey I M, Petkov N, Shayesteh M, O'Connell D, Holmes J D and Duffy R 2014 Junctionless nanowire transistor fabricated with high mobility Ge channel *physica status solidi (RRL) – Rapid Research Letters* **8** 65–8

[270] Kranti A, Yan R, Lee C W, Ferain I, Yu R, Akhavan N D, Razavi P and Colinge J P 2010 Junctionless nanowire transistor (JNT): Properties and design guidelines *2010 Proceedings of the European Solid State Device Research Conference, ESSDERC 2010* 357–60

[271] Bui H Q T, Velpula R T, Jain B, Aref O H, Nguyen H-D, Lenka T R and Nguyen H P T 2019 Full-Color InGaN/AlGaN Nanowire Micro Light-Emitting Diodes Grown by Molecular Beam Epitaxy: A Promising Candidate for Next Generation Micro Displays *Micromachines (Basel)* **10** 492

[272] Cerutti L, Ristić J, Fernández-Garrido S, Calleja E, Trampert A, Ploog K H, Lazic S and Calleja J M 2006 Wurtzite GaN nanocolumns grown on Si(001) by molecular beam epitaxy *Appl Phys Lett* **88**

[273] Sanchez-Garcia M A, Calleja E, Monroy E, Sanchez F J, Calle F, Muñoz E and Beresford R 1998 The effect of the III/V ratio and substrate temperature on the morphology and properties of GaN- and AlN-layers grown by molecular beam epitaxy on Si(1 1 1) *J Cryst Growth* **183** 23–30

[274] Yoshizawa M, Kikuchi A, Mori M, Fujita N and Kishino K 1997 Growth of self-organized GaN nanostructures on Al2O3(0001) by RF-radical source molecular beam epitaxy *Japanese Journal of Applied Physics, Part 2: Letters* **36**

[275] Craven M D, Lim S H, Wu F, J.S. Speck and S.P. DenBaars 2002 Structural characterization of nonpolar (1120) a-plane GaN thin films grown on (1102)r-plane sapphire *Appl. Phys. Lett* **81** 469

[276] Han J, Ng T-B and Biefeld R M 1997 The effect of on morphology evolution during GaN metalorganic chemical vapor deposition *Appl. Phys. Lett* **71** 3114

[277] Jain A, Weng X, Raghavan S, Vanmil B L, Myers T and Redwing J M 2008 Effect of polarity on the growth of InN films by metalorganic chemical vapor deposition *J Appl Phys* **104** 053112

[278] Bergbauer W, Strassburg M, Kölper C H, Linder N, Roder C, Lähnemann J, Trampert A, Fündling S, Li S F, Wehmann H H and Waag A 2010 Continuous-flux MOVPE growth of position-controlled N-face GaN nanorods and embedded InGaN quantum wells *Nanotechnology* **21** 1–6

[279] Bergbauer W, Strassburg M, Klper C, Linder N, Roder C, Lhnemann J, Trampert A, Fndling S, Li S F, Wehmann H H and Waag A A 2011 N-face GaN nanorods: Continuous-flux MOVPE growth and morphological properties *J Cryst Growth* **315** 164–7

[280] Li S F, Fuendling S, Wang X, Merzsch S, Al-Suleiman M A M, Wei J D, Wehmann H H, Waag A, Bergbauer W and Strassburg M 2011 Polarity and its influence on growth mechanism during MOVPE growth of GaN sub-micrometer rods *Cryst Growth Des* **11** 1573–7

[281] Li S, Wang X, Mohajerani M S, Fündling S, Erenburg M, Wei J, Wehmann H H, Waag A, Mandl M, Bergbauer W and Strassburg M 2013 Dependence of N-polar GaN rod morphology on growth parameters during selective area growth by MOVPE *J Cryst Growth* **364** 149–54

[282] Calleja E, Sanchez-Garcia A, Sanchez F J, Calle F, Naranjo F B and Munoz E 2000 Luminescenc properties and defects in GaN nanocolumn grown by molecular beam epitaxy *Phys Rev B* **62** 826–34

[283] Thillosen N, Sebald K, Hardtdegen H, Meijers R, Calarco R, Montanari S, Kaluza N, Gutowski J and Lüth H 2006 The state of strain in single GaN nanocolumns as derived from micro-photoluminescence measurements *Nano Lett* **6** 704–8

[284] Park Y S, Park C M, Fu D J, Kang T W and Oh J E 2004 Photoluminescence studies of GaN nanorods on Si (111) substrates grown by molecular-beam epitaxy *Appl Phys Lett* **85** 5718

[285] Oto T, Mizuno Y, Yanagihara A, Miyagawa R, Kano T, Yoshida J, Sakakibara N and Kishino K 2016 Influence of GaN column diameter on structural properties for InGaN nanocolumns grown on top of GaN nanocolumns *AIP Adv* **6** 115214

[286] Bengoechea-Encabo A, Barbagini F, Fernandez-Garrido S, Grandal J, Ristic J, Sanchez-Garcia M A, Calleja E, Jahn U, Luna E and Trampert A 2011 Understanding the selective area growth of GaN nanocolumns by MBE using Ti nanomasks *J Cryst Growth* **325** 89–92

[287] Kishino K, Sekiguchi H and Kikuchi A 2009 Improved Ti-mask selective-area growth (SAG) by rf-plasma-assisted molecular beam epitaxy demonstrating extremely uniform GaN nanocolumn arrays *J Cryst Growth* **311** 2063–8

[288] Sekiguchi H, Kishino K and Kikuchi A 2008 Ti-mask selective-area growth of GaN by RF-plasma-assisted molecular-beam epitaxy for fabricating regularly arranged InGaN/GaN nanocolumns *Applied Physics Express* **1** 1240021–3

[289] Sekiguchi H, Kishino K and Kikuchi A 2010 Emission color control from blue to red with nanocolumn diameter of InGaN/GaN nanocolumn arrays grown on same substrate *Appl Phys Lett* **96** 96–9

[290] Kishino K, Nagashima K and Yamano K 2013 Monolithic integration of InGaN-based nanocolumn light-emitting diodes with different emission colors *Applied Physics Express* **6** 2–5

[291] Albert S, Bengoechea-Encabo A, Kong X, Sanchez-Garcia M A, Calleja E and Trampert A 2013 Monolithic integration of InGaN segments emitting in the blue, green, and red spectral range in single ordered nanocolumns *Appl Phys Lett* **102** 6–10

[292] Albert S, Bengoechea-Encabo A, Kong X, Sánchez-Garcia M A, Trampert A and Calleja E 2015 Correlation among growth conditions, morphology, and optical properties of nanocolumnar InGaN/GaN heterostructures selectively grown by molecular beam epitaxy *Cryst Growth Des* **15** 2661–6

[293] Albert S, Bengoechea-Encabo A M, Sánchez-García M and Calleja E 2017 Selective Area Growth of InGaN/GaN Nanocolumnar Heterostructures by Plasma-Assisted Molecular Beam Epitaxy *Semiconductors and Semimetals* **96** 231–66

[294] Bertness K A, Sanders A W, Rourke D M, Harvey T E, Roshko A, Schlager J B and Sanford N A 2010 Controlled Nucleation of GaN Nanowires Grown with Molecular Beam Epitaxy *Adv Funct Mater* **20** 2911–5

[295] Calleja E, Ristić J, Fernández-Garrido S, Cerutti L, Sánchez-García M A, Grandal J, Trampert A, Jahn U, Sánchez G, Griol A and Sánchez B 2007 Growth, morphology, and structural properties of group-III-nitride nanocolumns and nanodisks *Phys Status Solidi B Basic Res* **244** 2816–37

[296] Kozlowski G, Corbett B, Schulz - S, Zhao Y, Farrell R M, Wu Y-R, - A, GaN Photoanode Hyojung Bae S, Kim E, Urban A, Malindretos J, Klein-Wiele J, Simon P and Rizzi A 2013 Ga-polar GaN nanocolumn arrays with semipolar faceted tips *New J Phys* **15** 053045

[297] Liu X, Liu X, Sun Y, Malhotra Y, Pandey A, Wang P, Wu Y, Sun K and Mi Z 2022 N-polar InGaN nanowires: breaking the efficiency bottleneck of nano and micro LEDs *Photonics Research, Vol. 10, Issue 2, pp. 587-593* **10** 587–93

[298] Brubaker M D, Duff S M, Harvey T E, Blanchard P T, Roshko A, Sanders A W, Sanford N A and Bertness K A 2016 Polarity-Controlled GaN/AlN Nucleation Layers for Selective-Area Growth of GaN Nanowire Arrays on Si(111) Substrates by Molecular Beam Epitaxy *Cryst Growth Des* **16** 596–604

[299] Ishizawa S, Kishino K and Kikuchi A 2008 Selective-area growth of gan nanocolumns on si(111)Substrates using nitrided al nanopatterns by rf-plasma-assisted molecular-beam epitaxy *Applied Physics Express* **1**

[300] Le B H, Zhao S, Liu X, Woo S Y, Botton G A and Mi Z 2016 Controlled Coalescence of AlGaN Nanowire Arrays: An Architecture for Nearly Dislocation-Free Planar Ultraviolet Photonic Device Applications *Advanced Materials* **28** 8446–54

[301] Bengoechea-Encabo A, Albert S, Sanchez-Garcia M A, López L L, Estradé S, Rebled J M, Peiró F, Nataf G, de Mierry P, Zuniga-Perez J and Calleja E 2012 Selective area growth of a- and c-plane GaN nanocolumns by molecular beam epitaxy using colloidal nanolithography *J Cryst Growth* **353** 1–4

[302] Schumann T, Gotschke T, Limbach F, Stoica T and Calarco R 2011 Selective-area catalyst-free MBE growth of GaN nanowires using a patterned oxide layer *Nanotechnology* **22**

[303] Sanchez-Garcia M A, Albert S, Bengoechea-Encabo A M, Barbagini F and Calleja E 2014 Selective Area Growth of GaN Nanowires by Plasma-Assisted Molecular Beam Epitaxy *Wide Band Gap Semiconductor Nanowires 1: Low-Dimensionality Related Effects and Growth* **9781848215** 215–43

[304] Kishino K and Ishizawa S 2015 Selective-area growth of GaN nanocolumns on Si(111) substrates for application to nanocolumn emitters with systematic analysis of dislocation filtering effect of nanocolumns *Nanotechnology* **26**

[305] Albert S, Bengoechea-Encabo A, Sánchez-García M A, Kong X, Trampert A and Calleja E 2013 Selective area growth of In(Ga)N/GaN nanocolumns by molecular beam epitaxy on GaN-buffered Si(111): From ultraviolet to infrared emission *Nanotechnology* **24**

[306] Albert S, Bengoechea-Encabo A, Sanchez-Garcia M A, Calleja E and Jahn U 2013 Selective area growth and characterization of InGaN nanocolumns for phosphor-free white light emission *J Appl Phys* **113** 1–6

[307] Brubaker M, Spann B, Genter K, Roshko A, Blanchard P, Harvey T, Bertness K and Weber J 2018 Core-shell p-i-n GaN nanowire LEDs by N-polar selective area growth **1072502** 1

[308] Uedono A, Shojiki K, Uesugi K, Chichibu S F, Ishibashi S, Dickmann M, Egger W, Hugenschmidt C and Miyake H 2020 Annealing behaviors of vacancy-type defects in AlN deposited by radio-frequency sputtering and metalorganic vapor phase epitaxy studied using monoenergetic positron beams *J Appl Phys* **128** 085704

[309] Uesugi K, Hayashi Y, Shojiki K and Miyake H 2019 Reduction of threading dislocation density and suppression of cracking in sputter-deposited AlN templates annealed at high temperatures *Applied Physics Express* **12** 065501

[310] Liu Z, Guo Y, Yan J, - A, Mogami Y, Motegi S, Osawa A, Alfaraj N, Min J-W, Hong Kang C, Liu S, Yuan Y, Sheng S, Wang T, Zhang J, Huang L, Zhang X, Kang J, Luo W, Li Y, Wang H, Wang W, Xiao C, Liu Y, Wang Q, Wang X, Liu S F, Yuan Y, Sheng S S, Wang T, Zhang J, Huang L J, Zhang X H, Kang J J, Luo W, Li Y D, Wang H J, Wang W Y, Xiao C, Liu Y P, Wang Q and Wang X Q 2021 Four-inch high quality crack-free AlN layer grown on a high-temperature annealed AlN template by MOCVD *Journal of Semiconductors* **42** 122804

[311] Wang M X, Xu F J and Xie N 2019 High-temperature annealing induced evolution of strain in AlN epitaxial films grown on sapphire substrates *Appl. Phys. Lett* **114** 112105

[312] Brunner F, Cancellara L, Hagedorn S, Albrecht M and and Weyers M 2020 High-temperature annealing of AlN films grown on 4H-SiC *AIP Adv* **10** 125303

[313] Uedono A, Shojiki K, Uesugi K, Chichibu S F, Ishibashi S, Dickmann M, Egger W, Hugenschmidt C and Miyake H 2020 Annealing behaviors of vacancy-type defects in AlN deposited by radio-frequency sputtering and metalorganic vapor phase epitaxy studied using monoenergetic positron beams *J Appl Phys* **128** 085704

[314] Hestroffer K, Leclere C, Bougerol C, Renevier H and Daudin B 2011 Polarity of GaN nanowires grown by plasma-assisted molecular beam epitaxy on Si(111) *Phys Rev B Condens Matter Mater Phys* **84** 1–6

[315] Brubaker M D, Genter K L, Roshko A, Blanchard P T, Spann B T, Harvey T E and Bertness K A 2019 UV LEDs based on p-i-n core-shell AlGaN/GaN nanowire heterostructures grown by N-polar selective area epitaxy *Nanotechnology* **30**

[316] Roshko A, Brubaker M D, Blanchard P T, Harvey T E and Bertness K A 2020 Eutectic Formation, V/III Ratio, and Controlled Polarity Inversion in Nitrides on Silicon *Phys Status Solidi B Basic Res* **257** 1–8

[317] Roshko A, Brubaker M, Blanchard P, Harvey T and Bertness K 2019 The role of Si in GaN/AlN/Si(111) plasma assisted molecular beam epitaxy: Polarity and inversion *Jpn J Appl Phys* **58**

[318] Dasgupta S, Wu F, Speck J S and Mishra U K 2009 Growth of high quality N-polar AlN($000\bar{1}$) on Si(111) by plasma assisted molecular beam epitaxy *Appl Phys Lett* **94** 151906

[319] Yoshikawa A and Xu K 2003 In situ investigation for polarity-controlled epitaxy processes of GaN and AlN in MBE and MOVPE growth *Opt Mater (Amst)* **23** 7–14

[320] Brubaker M D, Levin I and Davydov A v 2011 Effect of AlN buffer layer properties on the morphology and polarity of GaN nanowires grown by molecular beam epitaxy *J. Appl. Phys* **110** 53506

[321] Roshko A, Brubaker M, Blanchard P, Harvey T and Bertness K A 2018 Selective Area Growth and Structural Characterization of GaN Nanostructures on Si(111) Substrates *Crystals (Basel)* **8**

[322] Zauner A R A, Weyher J L, Plomp M, Kirilyuk V, Grzegory I, van Enckevort W J P, Schermer J J, Hageman P R and Larsen P K 2000 Homo-epitaxial GaN growth on exact and misoriented single crystals: suppression of hillock formation *J Cryst Growth* **210** 435–43

[323] Keller S, Fichtenbaum N A, Furukawa M, Speck J S, Denbaars S P and Mishra U K 2007 Growth and characterization of N-polar InGaN/GaN multiquantum wells *Appl Phys Lett* **90** 191908

[324] Wong M H, Keller S, Dasgupta N S, Denninghoff D J, Kolluri S, Brown D F, Lu J, Fichtenbaum N A, Ahmadi E, Singisetti U, Chini A, Rajan S, Denbaars S P, Speck J S and Mishra U K 2013 N-polar GaN epitaxy and high electron mobility transistors *Semicond Sci Technol* **28** 074009

[325] Keller S, Fichtenbaum N A, Wu F, Brown D, Rosales A, Denbaars S P, Speck J S and Mishra U K 2007 Influence of the substrate misorientation on the properties of N-polar GaN films grown by metal organic chemical vapor deposition *J Appl Phys* **102** 083546

[326] Jindal V and Shahedipour-Sandvik F 2009 Theoretical prediction of GaN nanostructure equilibrium and nonequilibrium shapes *J Appl Phys* **106** 083115

[327] Li H, Geelhaar L, Riechert H and Draxl C 2015 Computing Equilibrium Shapes of Wurtzite Crystals: The Example of GaN *Phys Rev Lett* **115**